

Koldo Almandoz Forcén

Advanced Characterization and Resistance to Failure of Novel Electron Beam Physical Vapour Deposited Thermal Barrier Coatings for Net Zero: An Experimental Study.

School of Aerospace, Transport and Manufacturing
Sustainable Materials and Manufacturing

EngD
Academic Year: 2019–2024

Supervisor: Dr. Christine Chalk
Associate Supervisors: A/Prof. Tara Schiller and Prof. John R. Nicholls
June 2024



School of Aerospace, Transport and Manufacturing
Sustainable Materials and Manufacturing

EngD

Academic Year: 2019–2024

Koldo Almandoz Forcén

Advanced Characterization and Resistance to Failure of Novel Electron Beam Physical Vapour Deposited Thermal Barrier Coatings for Net Zero: An Experimental Study.

Supervisor: Dr. Christine Chalk
Associate Supervisors: A/Prof. Tara Schiller and Prof. John R. Nicholls

June 2024

This thesis is submitted in partial fulfilment of the requirements for the degree of EngD.

© Cranfield University 2024. All rights reserved. No part of this publication may be reproduced without the written permission of the copyright owner.

Academic Integrity Declaration

I declare that:

- the thesis submitted has been written by me alone.
- the thesis submitted has not been previously submitted to this university or any other.
- that all content, including primary and/or secondary data, is true to the best of my knowledge.
- that all quotations and references have been duly acknowledged according to the requirements of academic research.

I understand that to knowingly submit work in violation of the above statement will be considered by examiners as academic misconduct.

Abstract

The efficiency of aeroengines is of paramount importance to reduce the environmental impact and operating costs of the aviation industry. The attainable efficiency gains are limited by the durability of the components in the hot section of the engine, the turbine.

Thermal Barrier Coatings (TBCs) are ceramic layers protecting the metallic components in the hot section of the engine. Improvements to the thermal capability of these coatings translates to overall efficiency gains. However, achieving them is a steep challenge, due to the harsh environment in which TBCs operate. Overcoming this challenge requires a deep understanding of the links between manufacturing process, resulting microstructure and behaviour of TBCs, as well as their failure modes.

Electron Beam Physical Vapour Deposition (EB-PVD) was used to deposit TBCs with a range of microstructures. Their microstructural features were quantified through a method developed to that end. This analysis was complemented through the advanced crystallographic study of the TBCs using Electron Back Scattered Diffraction (EBSD).

The characterized systems were tested for life-limiting failure modes: CMAS[1] attack, erosion and cyclic oxidation. The response of the TBCs to CMAS infiltration and the effect of the microstructural features was studied. A method for the quantification of CMAS infiltration depth was developed and validated using isothermal and thermal gradient exposures. This method allowed for identifying of a previously unreported two-stage mechanism for CMAS infiltration in EB-PVD TBCs.

The erosion resistance of the produced coatings was investigated through high velocity particle impact testing. The morphology of damage was observed and material loss

[1] after its constituents, Calcia, Magnesia, Alumina, Silica

mechanisms were proposed based on the microstructural and crystalline characteristics of each coating.

The proposed methods will help accelerate the development of novel TBCs by laying the foundations for a mechanistic understanding of coating characteristics and their effect on failure behaviour.

Keywords:
7YSZ; Yttria Stabilized Zirconia; Gadolinium Zirconate; GZO; CMAS; Erosion; Cyclic oxidation; Image analysis; Infiltration;

Acknowledgements

I would like to start these acknowledgements by thanking all parties supporting this EngD project: the EPSRC centre for doctoral training in Sustainable Materials and Manufacturing, as a partnership between Cranfield University, Warwick Manufacturing Group within The University of Warwick and University of Exeter, and Rolls-Royce plc as the industrial sponsor. My deep appreciation goes to Alan Johnstone, Dr. Gyaneshwara Brewster and Dr. Robert Jones for their time, patience and insight, which have undoubtedly improved the quality of my work.

I am especially thankful for the trust and support from Dr. Christine Chalk, whose supervision, constant encouragement and guidance have been key in shaping the project and this report. To A/Prof. Tara Schiller, I extend my gratitude for the reassurance and for helping me keep focus in the final throes of writing up this portfolio. I would also like to recognize and thank Prof. John Nicholls for the trust placed in me, the probing questions and interesting discussions.

This project would not have been possible without the help of a multitude of technicians, and academic staff at Cranfield University, too many to be fully listed here. Among the many who contributed are Tony Gray, Tim Pryor, Tracey Roberts, Jim Hurley, Arturo Vara Herrera, Kris Bramley and many others in the Surface Engineering and Precision Centre, the Composites and Advanced Materials Centre and Microscopy Services in Cranfield University.

A very special thanks goes to the people who made space for fun even in the thick of it, **especially** in the thick of it. Thank you, Joana, Aabid, Gabriele, and Roger. Thanks Herbert, for all the coffee and Tratsch. And a huge thank you to Luis for helping me keep (some of) my sanity going through it.

Last, but not least, a huge thanks to my family. Ama, Aita, I feel incredibly privileged for the unwavering support and love you have always shown me. Ana, I am really grateful to have you as a sister. To Paula and Carmela, you have been my joy during this journey and my motivation to complete it, and I can only promise to make up for all the time I owe you both.

A Adrián, allá donde estés.

Table of Contents

Academic Integrity Declaration i

Abstract ii

Acknowledgements iv

Table of Contents v

List of Figures ix

List of Tables xv

List of Abbreviations xvii

1 Introduction: TBC durability 1
- 1.1 Research questions . . . 2
  - 1.1.1 Problem Statement . . . 2
  - 1.1.2 Project scope definition . . . 2
  - 1.1.3 Research questions: . . . 3
- 1.2 Aim and Objectives . . . 4
- 1.3 Contribution to Innovation . . . 4
- 1.4 Contribution to Knowledge . . . 5
- 1.5 Portfolio layout . . . 7
- 1.6 Structure of the Innovation Report . . . 8

2 Review of the literature 9
- 2.1 TBC form and function . . . 10
  - 2.1.1 Brief summary of TBC development . . . 11
  - 2.1.2 TBC deposition modes and EB-PVD microstructure . . . 12
    - 2.1.2.1 APS . . . 12
    - 2.1.2.2 SPS . . . 12
    - 2.1.2.3 SPPS . . . 13
    - 2.1.2.4 PS-PVD . . . 13
    - 2.1.2.5 EB-PVD . . . 13
  - 2.1.3 Methods for the quantitative characterisation of TBC microstructures 15
- 2.2 TBC failure modes . . . 19
  - 2.2.1 Sintering . . . 19

2.2.2 Phase transformation of 7YSZ . . . 20
2.2.3 Intrinsic delamination . . . 20
2.2.3.1 Test methods for intrinsic delamination . . . 21
2.2.4 Particle impact . . . 21
2.2.4.1 Methods for evaluating TBC particle impact resistance . 23
2.2.5 CMAS attack . . . 24
2.2.5.1 Testing . . . 25
2.2.5.2 Methods for quantifying CMAS infiltration . . . 25

3 Deposition of model TBCs **28**
3.1 Experimental Methodology . . . 28
3.1.1 Experimental Materials . . . 28
3.1.1.1 Substrate materials . . . 28
3.1.1.2 Bond coat materials . . . 29
3.1.1.3 Top coat materials . . . 29
3.1.1.4 Consumable testing materials . . . 29
3.1.1.5 Ancillary materials . . . 29
3.1.2 Experimental equipment . . . 30
3.1.2.1 Deposition and preparation equipment . . . 30
3.1.2.2 Coating endurance testing equipment . . . 31
3.1.2.3 Analytical equipment . . . 31
3.1.3 Summary of tested samples and experimental conditions. . . . 32
3.2 Model TBCs . . . 33
3.2.1 Viable EB-PVD materials . . . 34
3.2.1.1 Rare Earth Oxide doped PYSZ - LowK . . . 35
3.2.1.2 GZO . . . 35
3.2.1.3 GZO to LowK comparison . . . 37
3.2.2 Experimental matrix . . . 37
3.3 LowK & GZO coatings . . . 39
3.4 Model TBC microstructures . . . 39
3.4.1 Qualitative assessment of model TBC microstructures . . . 40
3.4.1.1 LowK Systems . . . 40
3.4.1.2 GZO Systems . . . 44
3.4.2 Quantitative analysis of model TBC microstructures . . . 48
3.4.2.1 Quantitative analysis of LowK model TBCs . . . 49
3.4.2.2 Quantitative analysis of GZO model TBCs . . . 53
3.4.3 Crystallographic study of model TBCs . . . 56
3.4.3.1 LowK model TBCs . . . 57
3.4.3.2 GZO model TBCs . . . 68
3.5 Considerations regarding modelling . . . 73
3.6 Conclusions . . . 74

4 CMAS testing **77**
4.1 CMAS infiltration depth determination . . . 78
4.1.1 Isothermal tests . . . 79
4.1.2 Thermal gradient tests . . . 80
4.2 Effect of microstructure on CMAS infiltration . . . 81

4.2.1 Isothermal tests . . . 81
4.2.1.1 Non-reactive system - LowK . . . 82
4.2.1.2 Reactive system - GZO . . . 87
4.2.2 Thermal gradient tests . . . 91
4.2.2.1 Temperature determination . . . 95
4.2.2.2 CMAS segregation and crystallization . . . 97
4.2.2.2.1 Elemental mapping . . . 98
4.2.2.2.2 EBSD mapping of crystalline nature of Deposits. . . . 100
4.2.2.3 Phase diagrams and Equilibrium calculations . . . 101
4.3 Summary of findings and conclusions . . . 103

5 Erosion of model TBCs 106
5.1 LowK TBC systems . . . 106
5.2 GZO TBC systems . . . 110
5.3 Summary of findings . . . 113

6 Cyclic oxidation 115
6.1 Failure analysis models and criteria setting . . . 116
6.1.1 Descriptive statistics . . . 118
6.1.2 Lifetime distributions . . . 118
6.1.2.1 LowK systems . . . 119
6.1.2.2 GZO coatings . . . 124
6.1.2.3 Comparison of the coating systems to 7YSZ . . . 129
6.2 Conclusions . . . 129

7 Research impact 131
7.1 Methodology for the determination of CMAS infiltration . . . 131
7.2 Algorithm for column measurement . . . 132
7.3 CMAS testing methodology . . . 132
7.3.1 Isothermal testing . . . 132
7.3.2 Gradient rig testing . . . 132
7.3.2.1 Script for probing the surface temperature . . . 133
7.4 TBC durability data . . . 133
7.5 EB-PVD TBCs - A crystallographic study . . . 134

8 Conclusions and future perspectives 135
8.1 Conclusions . . . 136
8.1.1 Deposition methods and failure modes of TBCs . . . 136
8.1.2 Deposition and characterization of model TBCs . . . 136
8.1.3 Functional testing . . . 138
8.1.3.1 CMAS infiltration . . . 138
8.1.3.2 Erosion resistance . . . 139
8.1.3.3 Cyclic oxidation . . . 139
8.1.3.4 Summary of the performance of the coating systems tested . . . 141
8.2 Future perspectives . . . 141

8.2.1 TBC systems and materials 142
8.2.2 Quantitative coating characterization 143
8.2.2.1 Analytical techniques 143
8.2.2.2 Data analysis 143
8.2.3 Reproducibility and Replicability 144
8.2.4 Integrated Computational Materials Engineering 144

References **146**

A Ethical Approval Letter **169**

B EBSD maps of model TBC systems. **171**

C Enlarged images of erosion damage. **187**

List of Figures

2.1 Evolution of maximum TET over the years and materials and technologies contributing to it. Adapted from (1) 10
2.2 Diagram showing the layers in a TBC system, including typical thicknesses for each layer. Reproduced with permission from (2) 11
2.3 Typical EB-PVD TBC microstructure displaying ceramic columns separated by vertical pores. Work of the author. 15
2.4 Type and distribution of porosity in typical EB-PVD columnar microstructures. Reproduced with permission from (3). 15
2.5 Type and distribution of porosity in typical EB-PVD columnar microstructures. Reproduced with permission from (4). 17
2.6 Schematic diagrams for Mode I and Mode II fracture modes respectively. (c) Edge delamination mechanism, mode II. Work of the author based on (5). 21
2.7 Particle impact damage mechanism zones as a function of particle size and velocity, reproduced with permission from (6). 22
2.8 Diagram of the phases of the attack of TBC by CMAS. Work of the author. 24

3.1 ZrO_2-$GdO_{1.5}$ diagram showing the narrow Pyrochlore field, stable at the stoichiometric composition at room temperature, reproduced with permission from (7) - L = Liquid, F = Fluorite, P = Pyrochlore, M = Monoclinic ZrO_2, C = Cubic Gd_2O_3 36
3.2 Schematic structures of Fluorite and Pyrochlore Rare Earth Zirconates, including order-disorder transition energetics, from (8), based on data from (9, 10). Also depicted the Weberite - Defect Fluorite transition of Fluorite-related structures with nominal composition A_3BO_7 (B = Ta, A = RE). 36
3.3 Substrate temperature, corrected according to the method detailed in Submission 3, based on thermal survey data. 41
3.4 Cross section and surface SEM images for the LowK-LLT systems deposited on different substrates 41
3.5 Coating surface SEM images for the different LowK systems deposited on Alumina discs - inset images show higher magnification details. 42
3.6 SEM micrographs of cross sections for the different LowK systems deposited on Alumina discs. 43
3.7 Coating surface SEM images for the different LowK systems deposited on N75 substrates. 44

3.8 SEM micrographs of cross sections for the different LowK systems deposited on N75 substrates. 44
3.9 Corrected substrate temperature for the depositions of GZO coatings. . . . 45
3.10 SEM micrographs of cross sections for the different GZO systems deposited on Alumina discs. 45
3.11 Coating surface SEM images for the different GZO systems deposited on Alumina discs. The artefacts in (b) are a consequence of SEM charging. . 46
3.12 SEM micrographs of cross sections for the different GZO systems deposited on N75 substrates. 47
3.13 Coating surface SEM images for the different GZO systems deposited on N75 substrate. 48
3.14 Diagram showing the steps in the quantitative evaluation of column width (CoCo). FIJI (11), WEKA (12) and Python were uses at different steps of the project, as indicated by their corresponding logos. 49
3.15 Example image sections used for manual appraisal of number of columns. 49
3.16 Image section used in the manual appraisal of the number of columns for LowK-LT deposited on N75, at 10% of the thickness. 51
3.17 Automatic through-thickness column width measurement results for LowK TBC coatings deposited on Alumina discs. 53
3.18 Automatic through-thickness column width measurement results for LowK TBC coatings deposited on N75 metallic substrates. 53
3.19 Automatic through-thickness column width measurement results for GZO TBC coatings deposited on Alumina discs. 54
3.20 Automatic through-thickness column width measurement results for GZO TBC coatings deposited on N75 metallic substrates. 55
3.21 Orientation map (Y axis Inverse Pole Figure) of tetragonal zirconia for the LowK-LT system deposited on N75. The legend at the bottom left provides a guide to the crystallographic orientation colour code and sample coordinate system. 57
3.22 Grain boundary map for LowK-LT coating on N75, constructed using the EBSD data presented in Figure 3.21. 58
3.23 Column width result for LowK systems deposited on N75, determined using CoCo. 59
3.24 Column widths measured using the automated method developed and EBSD-grain boundary data, deposited on different substrate materials. The profile is corrected based on an interpolation of the upper envelope of the profiles shown in Figure 3.23. 60
3.25 Column widths determined manually vs. using CoCo. 62
3.26 Kernel Density Estimations for the grain size of LowK systems deposited on different substrates. 63
3.27 Orientation map of tetragonal zirconia for the LowK-LT system deposited on AD. 64
3.28 Inverse Pole Figures for LowK coatings deposited on Alumina discs. . . . 65
3.29 Inverse Pole Figures for LowK coatings deposited on N75. 66
3.30 Detail of LowK-LLT map for the coating deposited on Alumina showing the large unresolved area around the nucleation zone. 67

3.31 KDE of LowK systems on N75 recalculated filtering for small grains in LowK-LT . . . 68
3.32 IPF (Y axis projection) map for the GZO-LT coating deposited on an N75 substrate. . . . 69
3.33 Column widths measured by CoCo using EBSD grain boundary data for GZO systems. . . . 70
3.34 Kernel Density Estimations for the grain size of GZO systems deposited on different substrates. . . . 71
3.35 Inverse Pole Figures for GZO layer on coatings. . . . 72

4.1 Topographic parameters used for peak detection. . . . 78
4.2 Infiltration profile of partially infiltrated sample, with break points highlighted. The diagram underneath shows the meaning of the points in an infiltrated TBC. . . . 79
4.3 CMAS infiltration profile for LowK-Nom exposed for 30s. Note the logarithmic and linear y-axis on the top and bottom subplots, respectively. . . . 82
4.4 Combined Ca, Mg, Al and Si elemental maps (all elements coloured yellow to show combined infiltration) for selected model LowK TBCs exposed at 1250°C for different times, showing full or partial infiltration. Red lines indicate infiltration front. . . . 83
4.5 CMAS infiltration depth for LowK systems tested at 1250°C. Shaded areas correspond to 95% Confidence intervals, σ = 1.96. . . . 84
4.6 Combined Ca, Mg, Al and Si elemental map showing infiltration through large vertical crack and lateral transport of CMAS in coating LowK-LLT. 85
4.7 CMAS saturation for LowK systems. Shaded areas correspond to 95% Confidence intervals, σ = 1.96. . . . 86
4.8 CMAS saturation profile for GZO-Nom exposed at 1300°C for 360 s. . . . 87
4.9 CMAS infiltration depth for GZO systems exposed at 1250°C. Shaded areas correspond to 95% Confidence intervals, σ = 1.96. . . . 88
4.10 CMAS saturation level (at. % of metals basis proportion) for GZO systems exposed at 1250°C. Shaded areas correspond to 95% Confidence intervals. . . . 88
4.11 Combined Ca, Mg, Al and Si elemental maps for model GZO TBCs exposed for 360s at 1250°C, showing no infiltration. . . . 89
4.12 Detail of reaction zones for GZO-LTLR, a) BSE image exhibiting reaction product morphology and b) EDS map for CMAS elements, showing limited infiltration beyond reaction zone. . . . 89
4.13 Thickness of reaction zone for the GZO model coatings exposed for different times at 1250°C. Error bars represent 95% Confidence Intervals - σ = 1.96. . . . 90
4.14 Thickness of reaction zone for the GZO model coatings exposed for 360s at different temperatures. . . . 90
4.15 Arrhenius plot for the reaction zone thickness growth in the GZO TBC systems . . . 91
4.16 Cross section images for (a) 7YSZ-Nom and (b) 7YSZ-LT coating systems tested under gradient conditions. . . . 92

4.17 a) Infiltration depth and b) saturation radial profiles for the TBC coatings tested under gradient conditions. 93
4.18 Extent of delamination across different radial positions. Positive values of X correspond to areas to the right of the cross section centre, and negative values correspond to the left. 94
4.19 Method for probing the surface temperature at different locations in the sample surface. The blue squares correspond to an the area constrained to the inscribed rectangle, and the red trapezium shows a better fit to the circular substrate edge. X and Y axes in pixels - actual diameter of sample 30 mm. 96
4.20 Radial temperature distribution for a virtual "probe". 96
4.21 Emissivity spectra for CMAS recorded at different temperatures during the heating up and cool down cycle performed. Temperatures in K. K-D indicates measurements during cool-down. 97
4.22 Surface image for sample Nom-6', showing a 'glassy' deposit. 98
4.23 BSE micrograph of sample PTC-2 in radial positions a) x = 0.5mm and b) x = 7.5mm. 99
4.24 Micrographs of sample PTC-1 showing a) Forward Scattered Diode image, b) Aluminium EDS map for deposit overlaid on band contrast image - captured by EBSD camera. 99
4.25 Large area map montages of sample Nom-6' showing a) Forward Scattered Diode image, b) Aluminium EDS map for deposit overlaid on band contrast image for TBC. 100
4.26 EBSD map of Åkermanite mapped over band contrast image for sample Nom-6'. Interpretation of the colour scheme as per Figure 4.27. 101
4.27 IPF sets for Åkermanite and tetragonal Zirconia for the EBSD map in Figure 4.26. The multiple of uniform density values demonstrate a stronger texture in Zirconia relative to Åkermanite, particularly in the Y1/<110> direction. 101
4.28 EBSD map of Åkermanite mapped over band contrast image for sample PTC-1. Inverse Pole Figure (IPF) colour code for projection on Y coordinate are inset. 102
4.29 1300°C Liquidus fields for different Alumina content isopleths projected in CaO-MgO-SiO2 ternary diagram. 102
4.30 Phase evolution of the C33 composition melt under Scheil-Gulliver cooling conditions, calculated between 1300°C and 1100°C. 103

5.1 Erosion rates of LowK systems. The erosion rate of nominal 7YSZ EB-PVD TBCs is included as a benchmark. Error bars represent 95% Confidence Interval, σ = 1.96. 107
5.2 Selected micrographs of model LowK TBCs, (a)-(c) correspond to LowK-Nom, (d)-(f) LowK-LR, (g)-(i) LowK-LT & (j)-(l) LowK-LTLR. Micrographs correspond to representative damage morphologies at different magnifications and are not arranged by radial position. 108
5.3 Erosion rates of GZO systems. The erosion rate of nominal 7YSZ EB-PVD TBCs is included as a benchmark. 110

5.4 Micrographs of model GZO TBCs, (a)-(c) correspond to GZO-Nom, (d)-(f) GZO-LR, (g)-(i) GZO-LT & (j)-(l) GZO-LTLR. Criteria for selection of images and their position as per 5.2. 111

6.1 SEM (a-c) and optical microscope (d-e) micrographs showing: (a,d) Pressure Side, (b,e) Suction side, and (e,f) Leading edge. 117
6.2 Optical microscope micrograph of a turbine blade section with areas B-O overlaid. The colour coding refers to the areas used to assess the Pressure Side (red), Leading Edge (green) and suction side (blue). Note area A is absent from the picture. 117
6.3 Weibull (a) and likelihood (b) plots for the cyclic life LowK coatings exposed to 1190°C in 3 h cycles, corresponding to the pressure side. The inner contour in the reliability plot corresponds to a 90% level of confidence, and the outer to a 95%. 120
6.4 Weibull and likelihood plots corresponding to the suction side for LowK systems exposed to 1190°C in 3 h cycles. 121
6.5 Weibull and likelihood plot for LowK systems exposed to 1190°C in 3 h cycles, corresponding to the leading edge 123
6.6 Weibull plot for the GZO coatings, corresponding to the pressure side. Note the infant failure for GZO-LR 124
6.7 Weibull and confidence interval plots for the GZO coatings exposed to 1190°C in 3 h cycles, corresponding to the pressure side. The inner contour in the reliability plot corresponds to a 90% level of confidence, and the outer to a 95%. 126
6.8 Weibull and likelihood plots corresponding to the suction side for GZO systems exposed to 1190°C in 3 h cycles 127
6.9 Weibull and likelihood plot for GZO systems exposed to 1190°C in 3 h cycles, corresponding to the leading edge 128
6.10 a) Weibull plot and b) likelihood plot for Weibull parameters for the cyclic life of 7YSZ, LowK and GZO nominal coatings exposed to 1190°C in 3 h cycles, evaluated for the suction surface. 130

B.1 LowK-Nom AD 171
B.2 LowK-Nom N75 172
B.3 LowK-LR AD 173
B.4 LowK-LR N75 174
B.5 LowK-LT AD 175
B.6 LowK-LT N75 176
B.7 LowK-LTLR AD 177
B.8 LowK-LTLR N75 178
B.9 LowK-LLT AD 179
B.10 LowK-LLT N75 180
B.11 GZO-LR AD 181
B.12 GZO-LR N75 182
B.13 GZO-LT AD 183
B.14 GZO-LT N75 184
B.15 GZO-LTLR AD 185

B.16 GZO-LTLR N75 186

C.1 LowK-Nom. cracked. 188
C.2 LowK-Nom. cracked & densified. 188
C.3 LowK-Nom. cracked & delaminated. 189
C.4 LowK-LR. cracks. 189
C.5 LowK-LR. cracks. 190
C.6 LowK-LR. cracks & densified. 190
C.7 LowK-LT. cracks & densification. 191
C.8 LowK-LT. delamination 191
C.9 LowK-LT. interface delamination 192
C.10 LowK-LTLR. delaminated. 192
C.11 LowK-LTLR. cracked & delaminated. 193
C.12 LowK-LTLR. erosion scar edge. 193
C.13 GZO-Nom. damage overview. 194
C.14 GZO-Nom. cracked 194
C.15 GZO-Nom. extensively cracked 195
C.16 GZO-LR delaminated 195
C.17 GZO-LR densification 196
C.18 GZO-LR damage detail 196
C.19 GZO-LT cracked 197
C.20 GZO-LT cracked at interface 197
C.21 GZO-LT delaminated 198
C.22 GZO-LTLR - damage overview 198
C.23 GZO-LTLR - cracked 199
C.24 GZO-LTLR delaminated 199

List of Tables

1.1 Description of sub-objectives, motivation and methodology 4

3.1 CMAS powder composition 29
3.2 List of analytical equipment 31
3.3 List of material system and substrate combinations used in results presented in each chapter. † refers to historic data. 32
3.4 Summary of test conditions for each type of test, including relevant Chapter within the present report where test results are discussed, and related Portfolio Submissions 32
3.5 List of material candidates considered as a replacement for 7YSZ, including whether deposition via EB-PVD has been reported, and compositional segregation/banding has been observed. 34
3.6 Crystallographic characterization of Pyrochlore and Defect Fluorite GZO, including site occupancy and coordination of the Gd and Zr cations, based on data from (8). For interpretation of Wyckoff points, the reader is referred to (13). 37
3.7 Properties of model EB-PVD TBCs, measured at room temperature. The crystallographic phase for 7YSZ corresponds to the metastable tetragonal, and GZO to the pyrochlore. * SERR refers to Strain Energy Release Rate. † data from erosion testing at Cranfield University. § this work, for GZO-Nom - see Chapter 5. ‡ See Chapter 6 for an explanation of normalized cyclic oxidation life, 7YSZ value based on historic data from cyclic testing at Cranfield university. 38
3.8 Test matrix for the deposition of TBCs. Each dot represents an EB-PVD run on those conditions, for either LowK (magenta) or GZO (grey). The black dot represents pre-existing data for GZO. 38
3.9 Nomenclature and deposition conditions explored in the deposition of LowK and GZO coatings. 39
3.10 LowK coating porosity and column widths at different relative positions in the coating thickness, determined manually. NaN refers to cases where neither of the appraisers was able to resolve and count the columns in the given image. * Means that one of the appraisers could not count any columns. 50
3.11 Counting of columns using different criteria by the same appraiser and minimum cluster size 51

3.12 Values used for peak detection in the analysis of model TBC systems. *MAD refers to median average deviation. Height and prominence are calculated for each gray value profile (horizontal line) where peaks are to be detected. 52
3.13 Coating porosity and manually determined column widths at different relative thicknesses for GZO coatings. Interpretation as per Table 3.10 . . . 54
3.14 Comparison of column measurement results, evaluated at 90% of the coating thickness for the LowK model TBCs. 61
3.15 Preferred orientations and intensities obtained for tetragonal zirconia from IPFs for LowK coating systems and corresponding J-index for crystallographic texture. 67
3.16 Preferred orientations and intensities obtained for Pyrochlore Gadolinium Zirconate from IPFs for GZO coating systems and corresponding J-index for crystallographic texture. 73

4.1 Number of samples tested for the LowK model TBCs. 82
4.2 Number of samples tested for the GZO systems. *Due to the limited samples available, no GZO-Nom systems were tested at these conditions. 87
4.3 Activation energy for the reaction zone thickness growth of GZO systems, determined from Arrhenius plot in Figure 4.15. Note that the asymmetric confidence intervals are a result of the assumed normal distribution of reaction zone thicknesses. 91
4.4 Exposure times for the tests conducted in the gradient rig at FZJ. 92
4.5 Experimental conditions for the exploration of shorter high temperature exposure times to induce partial infiltration, and resulting dosage 98

6.1 Systems whose cyclic oxidation performance is presented and clarification of systems tested as part of the research project and pre-existing data. 116
6.2 Characteristic life and beta values for LowK systems. 7YSZ-Nom included as a reference. Numbers **in bold** correspond to highest values for the corresponding zone of interest. 124
6.3 Characteristic life and beta values for GZO coatings. 7YSZ-Nom included as a reference. 129

8.1 Relative performance ranking of tested systems. 142
8.2 Criteria used in the determination of performance ranking presented in Table 8.1. †Profile drop refers to the sharp infiltration depth transition from the uninfiltrated to the fully infiltrated/plateaued infiltration in the radial distribution profiles - see Figure 4.17a. 142

List of Abbreviations

7YSZ	7 wt.% Yttria Stabilized Zirconia
APS	Atmospheric plasma spray or Air plasma spray
BC	Bond coat
BI	Basicity Index
BSE	Back-Scattered Electron
CALPHAD	Calculation of phase diagrams
CAS	Calcia Alumina and Silica
CFMAS	Calcia Iron Oxide Magnesia Alumina and Silica
CIMM	CMAS Infiltration Measurement Method
CMAS	Calcia Magnesia Alumina and Silica
CMSX-4	Cannon Muskegon Single Crystal 4
CoCo	Column Counter - algorithm developed to quantify column width
CT	Computed Tomography
CTE	Coefficient of thermal expansion
CVD	Chemical Vapour Deposition
DT	Deformation temperature
EBSD	Electron BackScattered Diffraction
EBSP	Electron BackScattered Pattern
EB-PVD	Electron beam physical vapour deposition
EDS	Energy Dispersive x-ray Spectroscopy
EELS	Electron Energy Loss Spectroscopy
FOD	Foreign object damage
FT	Flow temperature
GD-OES	Glow Discharge-Optical Emission Spectroscopy
GRD	Giordano-Russel-Dingwell
GZO	Gadolinium Zirconate $Gd_2Zr_2O_7$
HAADF	High-Angle Annular Dark Field
HP	High Pressure
HPTB	High Pressure Turbine Blade
HT	Hemisphere temperature
HTLA	High Temperature Low Activity
ICME	Integrated Computational Materials Engineering
IDR	Intrinsic Dissolution Rate
IPS	Inertial particulate separators
KDE	Kernel Density Estimation
LCF	Low cycle fatigue
LEV	Local Exhaust Ventilation

L.E.	Leading Edge
LTHA	Low Temperature High Activity
MCrAlY	Metal - Cobalt or Nickel - Chromium Aluminium and Yttrium
MOM	Method of Manufacture
MP	Megapixel
N75	Nimonic-75
NBO/T	Non-Bridging Oxygen per Tetrahedron
OB	Optical Basicity
PM	Particulate matter
P.S.	Pressure Side
PS-PVD	Plasma Sprayed - Physical Vapour Deposition
PtAl	Platinum Aluminide
PYSZ	Partially Yttria-stabilized Zirconia
RE	Rare Earth
REE	Rare Earth Element
REO	Rare Earth Oxide
SATM	School of Aerospace, Technology and Manufacturing
SE	Secondary Electron
SFC	Specific fuel consumption
SFT	Stagnant Film Theory
SEM	Scanning Electron Microscope
SEPC	Surface Engineering and Precision Centre
SPPS	Suspension Precursor Plasma Spray
SPS	Suspension Plasma Spray
ST	Shrinkage temperature
STEM-EDS	Scanning Transmission Electron Microscopy - Energy Dispersive X-ray Spectroscopy
S.S.	Suction Side
SX	Single crystal
TBC	Thermal Barrier Coating
TBO	Thermal barrier Oxide
TC	Top coat
TET	Turbine entry temperature
TGO	Thermally grown oxide
TKD	Transmission Kikuchi Diffraction
UCSB	University of California in Santa Barbara

Chapter 1

Introduction: Thermal Barrier Coating durability and performance

The air transport sector is undertaking significant decarbonization efforts globally. Thermal Barrier Coatings (TBCs), low conductivity ceramic coatings used to protect components in the hot end of the engine, are one of the material systems that have played a pivotal role in the history of efficient engine development. They are also a critical technology for the continuous improvement of aeroengine efficiency required to achieve an accelerated path to a net zero aviation. TBCs are subject to a variety of failure modes as a result of the extreme conditions they are subjected to. The resilience of TBCs to failure is highly dependent on their microstructure. TBCs are deposited through a variety of coating methods, depending on the component and surface being protected, which results in a variety of microstructures. TBCs deposited via EB-PVD exhibit a characteristic columnar microstructure, which provide the ceramic coating with enough compliance to withstand high thermomechanical loads. The aim of the present project is to contribute to the decarbonisation of air transport by understanding the links between the EB-PVD process parameters, resulting TBC microstructure and its durability.

This innovation report provides an executive summary of the research conducted in pursuance of this understanding. The results of the investigation are reported in three different blocks. The first is an investigation into TBC systems, the deposition techniques used in their manufacture and the failure modes affecting them. The second concerns the deposition and characterization of "model" TBCs whose durability with regard to the different failure modes is analysed in the third and final block. Supporting documents provide a more comprehensive review of TBC systems, their production and failure, as well as the evaluation methods developed in the course of the present project for the evaluation of the produced TBCs. This innovation report concludes with a summary of the impact of the research impact and concluding remarks including the author's perspective on TBC development, trying to answer the question "What is to be done?".

1.1 Problem statement, project scope, and research questions.

There are a variety of properties that affect the performance of TBC systems in gas turbine environments, namely: strain compliance, thermal conductivity, compatibility with Bond Coat (BC) material, phase stability at high temperature, toughness and resistance to fluxing attack by environmental debris (CMAS[1]). Among these properties, phase stability, toughness and CMAS resistance are recognised as the key barriers with regards to the life and/or temperature capability of current TBC systems. CMAS resistance in particular poses a considerable challenge, due to the multi-modal failure mode induced by CMAS attack, with coupled chemical, thermal and mechanical effects. Some TBC material compositions have been shown to increase CMAS resistance and high temperature phase stability. However, in most cases, the resulting toughness of the TBC is compromised on these candidate systems, resulting in a coating life reduction.

Overcoming the durability limits imposed by the temperature capability of the current TBCs would allow for achieving significant environmental and economic benefits:

1. Increased aeroengine competitiveness due to relatively lower fuel consumption and associated cost.

2. Reduced emissions resulting in compliance with increasingly stringent environmental policies, and, more generally, contributing to abate the effects of anthropogenic climate change.

3. Extended turbine component durability, with subsequent reduction on the required number of components throughout engine life-cycle, material and processing costs and strain on supply chain capacity.

Note that item number 3 would also result in a significant environmental footprint reduction, by reducing the consumption of alloying elements used in the manufacture of the turbine components protected by the TBCs.

1.1.1 Problem Statement

Summing up the problem both from the technical and the economic perspective, it could be articulated as:
Advancing the understanding of the links between the EB-PVD process parameters, TBC microstructure and TBC durability to support the deployment of advanced TBC systems with increased operational (thermal and endurance) capability in gas turbine environments relative to baseline systems while minimising the complexity and operational burden introduced during their manufacturing process.

1.1.2 Project scope definition

To frame the approach selected to address the problem statement, the following definition of the research scope was established at the outset of the project:

[1] shorthand for Calcia, Magnesia, Alumina and Silica, the main constituent oxides

1. In scope:
    - Depositing TBCs via EB-PVD, to utilize coating capabilities at Cranfield University.
    - Exploring EB-PVD deposition parameter, to produce coatings with varying microstructures.
    - Investigating different TBC top coat compositions, to account for intrinsic material property effects.
        - Compositions already in operation are favoured.
    - Testing the produced TBCs for CMAS, cyclic oxidation and particle impact resistance.
2. Out of scope:
    - Depositing TBCs via other manufacturing methods
    - Investigating the effect of substrate composition on TBC durability
    - Investigating the effect of different BC composition on TBC microstructure and durability
    - Testing the produced TBCs for CMAS, cyclic oxidation and particle impact resistance.
3. Potentially in scope[2]:
    - Exploring novel compositions not currently in service
    - Testing the produced TBCs for their thermal insulation capability

1.1.3 Research questions:

The research questions investigated in response to the problem statement were:

- How do deposition temperature and rotation speed affect the TBC microstructure and crystalline texture for the selected coating materials?
- What analytical techniques and methods can accurately quantify relevant microstructural features of produced TBC systems?
- How much can the severity of CMAS attack be reduced through modifying the TBC microstructure?
- How do the different microstructures produced degrade when exposed to particle impacts?
- Does the difference in microstructure have a significant effect on cyclic oxidation life?

[2]Depending on time and resource availability

1.2 Aim and Objectives

The aim of the study is to review the microstructural factors of EB-PVD TBCs, and how they influence the life-limiting failure modes. This is understood as a necessary building block in order to propose modelling tools that enable rapid design of TBCs for optimum manufacturability and performance in high temperature gas turbine applications, in line with Integrated Computational Materials Engineering (ICME) principles.
The ultimate goal is to accelerate the development of TBC system designs with improved capabilities relative to 7 wt.% Yttria Stabilized Zirconia (7YSZ), which is proposed as a baseline for comparison. This objective can be further broken down into four sub-objectives detailed in Table 1.1.

Table 1.1: Description of sub-objectives, motivation and methodology

	Motivation	Methodology
Manufacturing: Manufacture EB-PVD TBCs in a variety of deposition conditions	Provide a more comprehensive parameter exploration, to understand the trade-offs and limits of EB-PVD deposition of different materials	Physical deposition experiments using the EB-PVD coating equipment in Cranfield University
Characterization: Develop a quantitative understanding of the links between process parameters and TBC durability.	Enable the model led design of advanced, resilient TBCs .	Quantification of morphological features of the deposited coatings, using the appropriate analytical techniques available.
Durability: Design and validate methods to evaluate the degradation of TBCs.	Underpin the validation of existing TBC degradation models.	Testing the degradation modes of the produced TBCs with different microstructures.

1.3 Contribution to Innovation

A novel method was developed for the for the quantification of EB-PVD TBC column width. While quantification of the microstructural features of TBCs has been performed and reported before, the developed method relies on automated rather than manual measurement of the column width. This approach offers two benefits. On the one hand, the subjectivity of the measurement process is reduced. On the other hand, the method is published and can be replicated, allowing for its independent evaluation and improvement.

The developed method has been compared to manual quantification of TBC column width, providing a benchmark for its relative accuracy and reliability. Additionally, the effect of using secondary electron images vs. Electron Back Scattered Diffraction (EBSD) image data on the results obtained has been evaluated.

The method developed has been used to evaluate the microstructural differences of model coating systems. The deposition of these model TBCs has covered a range of conditions seldom investigated in EB-PVD. This, coupled with the comprehensive functional testing, has provided a broad spectrum of condition-performance correlations. The obtained results provide a wider view of the engineering compromises possible with EB-PVD.

The method developed for the quantification of the CMAS infiltration depth allows for accurate determination of the CMAS infiltration front and the level of saturation. The original method developed correctly identifies the location of the infiltration front in partially infiltrated samples, even if the attempted automatic detection of the infiltration depth has, to date yielded inaccurate results. The application of this method enables a like-for-like comparison of the depth of infiltration of samples tested by different research groups, which so far has depended on subjectively determined infiltration depths. This method and its subsequent refinements possess significant potential for the validation or correction of analytical or numerical models of CMAS infiltration.

Gradient testing was performed as part of the development of the CMAS infiltration depth measurement method and its validation. Guidelines for performing infiltration kinematic studies in thermal gradient conditions were developed. Furthermore, code has been developed for performing advanced analysis of the surface temperature on thermal gradient test coupons. This enables detailed correlations of post-test analysis results to the test conditions local to the area of interest in the test coupon.

1.4 Contribution to Knowledge

The model TBCs deposited have resulted in microstructural morphologies reported for the first time for EB-PVD TBCs. The quantitative morphological analysis using the method developed has been coupled with comprehensive crystallographic analysis of the model TBCs. This analysis showed a significantly different effect of the deposition parameters on column width, crystal size, preferential growth orientation and texture depending on substrate material.

This effect was not previously reported in the discussion of Structure Zone Models. However, given the significantly different microstructures observed suggest this effect could be leveraged in the coordinated development of superalloy-BC-TBC systems. For that reason, the author suggests that the mechanism causing the observed differences should be investigated

The results expand on the “column” based framework for analysing EB-PVD TBC, by including grain size and texture analysis. This expanded framework is proposed to be applicable to other columnar or column-like TBCs

The developed method for the quantification of the CMAS infiltration depth has led to the identification of a two-stage mechanism for CMAS infiltration in columnar EB-PVD TBCs. This mechanism has been observed in both isothermal and gradient rig CMAS exposures, as demonstrated in this project.

In addition to this, the slower infiltration speed in TBCs with fine columns, as compared to nominally thick columns, was confirmed both in isothermal and thermal gradient conditions. To the knowledge of the author, this is the first time that these two aspects of the CMAS infiltration kinematics have been experimentally observed together.

This thesis has shown significant crystallization occurred within the CMAS deposit when exposed under gradient conditions. This behaviour, observed in engine operation, had previously not been reported in the literature for gradient rig testing. The obtained

evidence coupled with the thermochemical studies opens potential avenues for inducing infiltration-limiting intrinsic crystallization and protect TBCs from this failure mode, extending their life.

High velocity particle erosion testing was conducted on the model TBCs produced. The results from the erosion tests show that column width alone can not explain the erosion rates observed, in contrast with previous observations. The detailed crystallographic studies conducted provide evidence that support the effect of crystal size and texture on the impact damage resistance of ceramic coatings. This finding has significant implications for the development of future TBCs in applications where impact resistance is critical to component survival.

The mechanism for erosive damage was also investigated beyond the mass loss, looking at the mechanism for the loss of coating mass and thickness. The differences in crack propagation mechanisms observed could be exploited to design coatings that, despite having inherently lower erosion resistance, retain a sufficiently large coating thickness to remain effective in protecting the underlying substrate.

1.5 Portfolio layout

The research portfolio comprises all the work produced in the fulfilment of the requirements for the Sustainable Materials and Manufacturing Engineering Doctorate (international). The present document - the innovation report - represents the culmination of the research project undertaken in pursuance of the EngD, while the rest of the portfolio includes both the supporting Submissions for the research project, and work submitted as part of the MSc in sustainable materials and manufacturing. The layout of the portfolio is as follows:

- Research project Submissions
    1. Review of failure modes affecting Thermal Barrier Coatings
    2. Methodology of physical experiments
    3. Method for the quantification of EB-PVD TBC microstructural features
    4. International research visit - ForschungsZentrum Jülich
    5. Method for the determination of CMAS infiltration depth
- Sustainable Materials and Manufacturing MSc: Assignments and prior work
    1. Module - Introduction to manufacturing, materials and research techniques
    2. Module - Whole system design
    3. Module - Advanced materials and processes
    4. Module - Sustainable energy and the environment
    5. Module - Business model generation
    6. Module - Circular waste management: resource, recovery and disposal
    7. Module - Product design and development management
    8. Module - Mechanics of materials
    9. Module - Computational modelling
- Published papers: Journal articles and conference presentations
    1. Journal article - Modelling the evaporation of EB-PVD TBCs
    2. Presentation abstract - International Symposium for Hot Oxidation and Corrosion. Takamatsu, Japan, October 2022
    3. Presentation abstract - International Conference on Surface Science, Engineering & Technology - Manchester 16-19 September 2024

1.6 Structure of the Innovation Report

The present document follows the structure provided in the table of contents. However, a narrative summary of the Innovation Report structure, is provided below, to aid in the interpretation and navigation of the present document. Additionally, the aim of this Section is to establish the high-level relationship between the constituent parts of the report and the stated research question, aims and objectives, discussed in Section 1.2.
In Chapter 2, a brief review of the development of Thermal Barrier Coatings is provided. This review covers the relevant modes of deposition, focusing on the Electron-Beam Physical Vapour Deposition technique. The functional requirements and failure modes, and the characterisation techniques relevant to their understanding are also discussed in Chapter 2. This Chapter is supported by Submissions 1, 2 and 3.
Chapter 3 discusses the deposition of TBCs produced in this study to unveil the links between deposition process and material, and the resulting coating morphology and durability. The method developed for the quantification of a microstructural feature of note - the column width - discussed in Submission 3, is used for the evaluation of the produced microstructures, and compared to alternative methods of microstructure quantification.
Once the microstructural features have been analysed and quantified when possible, the endurance of the produced thermal barrier coating against different failure modes is analysed in Chapters 4, 5 & 6. The first failure mode covered refers to the CMAS fluxing attack resulting from sand ingestion into the engine, followed by deposition and interaction with TBCs. The analysis of the CMAS infiltration kinematics in Chapter 4 is performed using the method developed and detailed in Submission 5, and validated using the results in Submission 4.
Chapter 5 discusses the comparative assessment of the particle impact performance of the produced coatings. The link to previous experience and the morphology quantification performed in Chapter 3 is supplemented by advanced crystallographic studies of the deposited coatings.
The last failure mode covered is the cyclic oxidation-induced spallation of TBCs. This failure mode, discussed in 6, was of critical importance in the early development of TBCs, and, due to its high sensitivity to temperature, is likely to become critical as the Turbine Inlet Temperature is increased, in pursuit of aeroengines with higher efficiency.
Having detailed the results obtained in the course of the research project, the impact of the research results is discussed in Chapter 7. This covers the application of the results to the research question and the adjacent research problems being subject of research by the Thermal Barrier Coating community, and of potential interest for OEMs.
The conclusions derived from the research undertaken are presented in Chapter 8. Recommendations for and perspectives into the development of TBCs for increased engine efficiency are outlined, in the context of the need for decarbonizing air transport.

Chapter 2

Review of the literature

The operation of the air transport industry relies on the performance of one of the crowning achievements of engineering - the jet engine. Modern jet engines are highly complex gas turbines that extract the power generated in the combustion of jet fuel and use it to generate a propulsive thrust (14). The monetary and environmental cost of their operation is directly controlled by the fuel efficiency achieved, defined as specific fuel consumption (SFC). The SFC is defined as the ratio of fuel consumption to generated thrust rate. For turbo-fan[1] engines, with high pressure ratios the SFC is reduced with increased Turbine Entry Temperature (TET).

There is a constant pursuit of engine efficiency, pushed initially by commercial operators interested in economical operation of aircraft, and increasingly also through the environmental pressure imposed by the need to combat anthropogenic climate change. This has imposed constant pressure to increase the efficiency, and therefore the TET of jet engines. The components exposed to the highest temperatures within the jet engine are those located in the combustor and high pressure turbine, with the latter also being exposed to high mechanical loads as a result of rotation speeds that can reach 12,000 rpm (15, 16). Achieving the required TETs has necessitated the development of advanced cooling technology, and thermally protective materials, deposited on the turbine components. A summary of the historic development of TET and the supporting technologies is represented in Figure 2.1

The increase in the maximum temperature capability of TBCs shown in Figure 2.1 is a result of the continuous development of TBC deposition technology and an understanding of the failure modes limiting TBC life.

This review covers the following: Section 2.1 provides a succinct summary of Submission 3: Microstructure quantification, covering TBC development, deposition technologies and microstructural features of EB-PVD TBCs, while Section 2.2 provides an overview of the main modes of failure covered in great detail in Submission 1: Review of TBC failure modes.

[1] Jet engines where the bulk of the thrust is generated by a fan powered by the gas turbine.

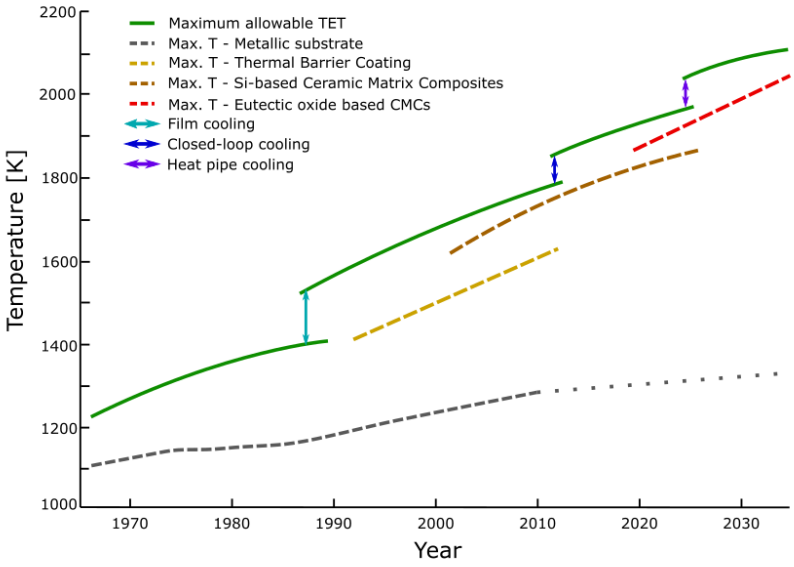


Figure 2.1: Evolution of maximum TET over the years and materials and technologies contributing to it. Adapted from (1)

2.1 TBC form and function

The fundamental function of Thermal Barrier Coatings, as stated in Chapter 1, is to protect the underlying metallic substrates from the high temperature gas stream in the high pressure turbine. State-of-the art TBCs exhibit a low thermal conductivity, between 1.0 and 1.6 $W \cdot m^{-1} \cdot K^{-1}$ (17). This low conductivity, in conjunction with internal and film cooling, results in temperature gradients of just under 1°C per coating μm, which for a typical coating thickness of 150-200 μm, results in a 100-150°C temperature drop (18, 19).

The ceramic coatings are not directly deposited onto the metallic substrates they protect. Instead, an intermediate layer, a Bond Coat (BC), is deposited first, to provide the required adhesion between the substrate and the ceramic TBC (20). This BC typically contains Aluminium, which readily reacts with oxygen, resulting in an Al_2O_3 (alumina) layer. This oxide layer growths through the exposure to oxygen containing atmosphere at high temperature during operation, and is therefore referred to as Thermally Grown Oxide (TGO). The TGO serves as an adhesive layer for the deposition of TBCs, while simultaneously protecting the underlying BC and substrate from further oxidation. The aluminium in the BC allows for the continued growth of the protective Alumina layer, minimizing the exposure of other metallic elements in the substrate to oxidation. Such an exposure would result in the growth of non-protective oxides, accelerating the degradation of the metallic component.

The resulting coating system comprises three layers, as depicted in Figure 2.2. The different layers possess dissimilar mechanical properties, the most important of which is the difference in deformation behaviour; both the TBC and TGO behave in a brittle manner, as expected from ceramic materials, while the BC and substrate exhibit significant ductility. Furthermore, a substantial difference in the Coefficient of Thermal Expansion (CTE) exists between the ceramic and metallic layers of the system.

This CTE mismatch, together with the thermal gradients resulting from the insulation capability of TBCs, results in thermally induced stresses both within the TBC and

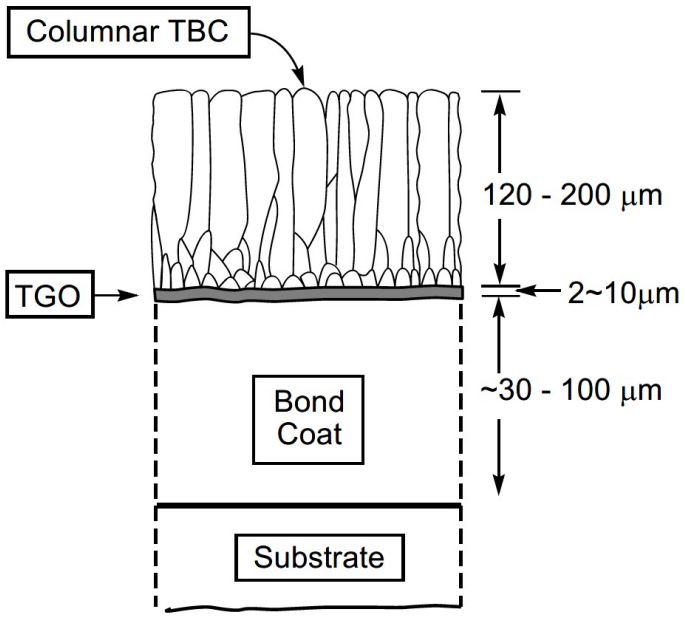


Figure 2.2: Diagram showing the layers in a TBC system, including typical thicknesses for each layer. Reproduced with permission from (2)

at the TBC-TGO-BC interface. The need to overcome the detrimental effects of these thermomechanical stresses has influenced the development of Thermal Barrier Coating technology, as detailed in section 2.1.1.

2.1.1 Brief summary of TBC development

Early research in Thermal Barrier Coating technology were spearheaded by the National Aeronautics and Space Administration (NASA), through experimental vehicles (21). NASA was also responsible for the development of 7 wt. % Y_2O_3 stabilized ZrO_2 (7YSZ) (22). This development unlocked the commercial viability of TBC technology, and 7YSZ remains the state-of-the art ceramic material despite continued efforts to find alternative material systems that would offer improved thermal capability and coating endurance.

The first TBCs were deposited by means of thermal spraying techniques (23). Atmospheric Plasma Spraying (APS) was initially established as the preferred thermal spraying method for the deposition of TBCs. APS-deposited TBCs display a characteristic lamellar microstructure as a result of the layer-wise deposition of molten and semi-molten particles (24). The porosity trapped between the lamellae, aligned with the substrate surface, confers APS with a very low thermal conductivity. However, the mechanical interlocking of contiguous "splats" results in a low in-plane mechanical compliance (25). When subjected to cyclic oxidation, the stresses caused by the CTE mismatch and thermomechanical loads resulted in the delamination of the coating and subsequent loss of thermal protection.

A significant improvement was achieved through the development of EB-PVD as a method for the manufacture of 7YSZ TBCs (26, 27). EB-PVD TBCs exhibited an increased in-plane compliance when compared to APS TBCs (25). EB-PVD TBCs show a columnar, microstructure, resulting from crystallographic grains and porosity oriented in

the direction perpendicular to the substrate surface. This microstructure confers EB-PVD TBCs with an increased mechanical compliance. As a result, lower thermomechanical loads develop in EB-PVD TBCs, increasing cyclic oxidation life. TBCs deposited via EB-PVD also showed an increased resilience against particle impact damage (28) and aerodynamic performance (27). However, EB-PVD TBCs have a higher thermal conductivity than APS TBCs due to the orientation of the porosity they exhibit (29, 30).

2.1.2 TBC deposition modes and EB-PVD microstructure

As discussed in Section 2.1.1, the microstructural dissimilarities resulting from the coating deposition mode selected, result in significant performance and durability differences. It is therefore not surprising that, since the adoption of EB-PVD, multiple alternative methods have been developed to overcome the limitations of both APS and EB-PVD. The current Section provides a brief description of the main TBC deposition methods and the characteristics of the resulting TBCs. Given that the research project is focused on EB-PVD TBCs, significant emphasis is placed on this deposition technique.

2.1.2.1 APS

Atmospheric plasma spray, as suggested by the name, consists in the spraying of the material to be deposited, by means of a plasma torch under atmospheric pressure conditions. The material, injected in the form of powder into the plasma, melts partially or totally, and solidifies in contact with the substrate being coated, resulting in frozen "splats" deposited on layers (24). The coating thickness is built up through successive passes of the plasma torch, which moves relative to the workpiece to cover the entire surface to be coated. While the typical APS microstructure exhibits, as discussed in Section 2.1.1 a low in-plane compliance, substrate temperature can be controlled during deposition to result in periodic vertical cracks in the coating microstructure. Such coatings, denominated Dense Vertically Cracked (DVC) coatings, with improved cyclic oxidation resistance. The rapid solidification process undertaken by the sprayed particles results in the crystallization of sub-micron grains within each lamella, with no preferential orientation (31).

2.1.2.2 SPS

Suspension Plasma Spray (SPS) was developed as a modification of APS, where the feedstock used was injected in the form of a suspension instead of dry powder (32). The use of suspensions modifies the interaction between the solid portion and the plasma. As a result of this modified interaction, the particles can reach the substrate in the form of molten particles, as in APS, but also agglomerated nanoparticles and partially melted suspended particles (33). The interaction can be selected through controlling the plasma characteristics and suspension medium, and, as a result, SPS coatings can exhibit a range of microstructures, ranging from those resembling APS (34) and DVC (35) to columnar morphologies (36). The crystallographic characteristics of SPS coatings consist in nano to micro-sized equiaxed crystallites with no distinct texture (37).

2.1.2.3 SPPS

Solution Precursor Plasma Spray utilizes precursors - typically nitrates and acetates - of the material to be deposited on the form of a solution. When exposed to the plasma torch, the precursors react and crystallize, solidifying. The solidification process typically occurs at the outer layer of the sprayed droplets, crating a solid shell. This shell subsequently fragments, resulting in the repeated breaking down of the droplets and melting of the fragmented solid shells (33). The material is subsequently deposited on one of three forms, as fully molten small droplets, unbroken solid shells, or agglomerated and sintered nanoparticles. The resulting coating microstructure resembles that of DVC APS TBCs. Similar to APS and SPS, the resulting crystalline structure consists in sub-micron equiaxed crystallites, with the limited evidence available suggesting random crystallographic orientation (38, 39).

2.1.2.4 PS-PVD

Plasma Sprayed-Physical Vapour Deposition, while also relying in a plasma torch for heating the material being deposited above its melting point, exhibits a significantly different deposition mechanism to APS, SPS and SPPS. As a Physical Vapour Deposition process, the majority of the material is deposited from the vapour phase (40, 41). This is achieved by spraying the material under low vacuum conditions, akin to those of Low Vacuum Plasma Spray (LVPS) (42). The resulting transition from the vapour to the solid phase results in the epitaxial growth of crystalline phases on the substrate surface. The selection of the plasma parameters and substrate temperatures can be controlled to induce the growth of large and highly textured coatings, exhibiting columnar morphologies similar to EB-PVD TBCs (43).

2.1.2.5 EB-PVD

EB-PVD, similar to PS-PVD, consists in the deposition of material from the gas to the solid phase. The main difference consists in the means used for the evaporation of the material to be deposited. As suggested by the name, EB-PVD uses a focused Electron Beam to melt and evaporate the ceramic ingots used as sources for the coating material (44). The plume of vaporized material condenses in the component surface, resulting in the nucleation and competitive growth of crystalline grains (45, 46). In the typical deposition conditions, which involve rotating and heating the substrate being coated, the growing crystals exhibit a strong crystallographic texture caused by a preferential crystalline growth direction.

The microstructure of EB-PVD TBCs exhibits the characteristic columnar morphology shown in Figure 2.3. Typically, the porosity in EB-PVD TBCs is classified into three types (47). Type I porosity refers to the large pores separating adjacent columns. Porosity is also present within the columns, as a result of voids trapped within the single crystal grain during the growth process, constituting Type II porosity. Lastly, gaps or notches are present in the column edges, resulting in features commonly referred to as feather arms in the literature (48, 49). These gaps constitute type III porosity.

The process parameters affecting the microstructure and crystallographic characteristics of the deposited TBCs are the substrate temperature, deposition pressure and rotation

speed (45, 50). Substrate temperature controls the microstructure morphology by affecting the diffusive transport of the deposited atoms. Higher temperatures promote adatom mobility and enable the deposited material to re-arrange in more energetically stable positions. Under these conditions, crystal growth is favoured over nucleation, resulting in large crystals with a clearly defined preferred growth orientation. Depositions at lower temperatures, conversely, promote nucleation, resulting in smaller crystallites without a clearly defined crystallographic texture.

Pressure affects the nucleation and growth balance by altering the chemical potential of the vapour phase. The driving force for nucleation is supersaturation, which is defined as the difference between the chemical potential of the vapour phase and the chemical potential for crystal growth (51). Increasing the deposition pressure therefore results in high supersaturation levels, which promote crystal nucleation, and are subsequently expected to result in smaller crystal sizes and reduced crystalline texture.

The effect of substrate rotation speed is in some regards analogous to deposition temperatures, as described by (50). Increased rotation speeds reduce the number of adatoms adsorbed into unstable lattice positions. This results in lower energy requirements for atoms to "jump" to stable positions, therefore having a similar effect to increased temperature.

EB-PVD is a line-of-sight deposition process, meaning that the evaporating material only deposits in surfaces directly exposed to it. Both surface asperities in the substrate being coated and grains growing in the preferential direction and protruding over the neighbouring crystallites result in self-shadowing. Self-shadowing consists in the physical blocking of the incoming vaporized material, reducing the flux to sections of the coating located in local troughs. This results in the exaggeration of substrate surface roughness and texture, especially at low homologous temperatures and high pressures (45).

Lastly, the chemical composition of the ceramic material determines the crystallographic phase being deposited, including the preferred crystallographic growth orientation, typically the lowest energy crystallographic planes (52). Note that the temperature typically referred to in Structure Zone Models - diagrams depicting the microstructure morphology as a function of manufacturing process parameters - is the homologous temperature, not the absolute deposition temperature. Homologous temperature refers to the deposition temperature (in the Kelvin scale) divided by the melting temperature of the material being deposited.

For a more detailed review of the different deposition processes, as well as the mechanisms for the EB-PVD deposition of TBCs, the reader is referred to Submission 3: microstructure quantification.

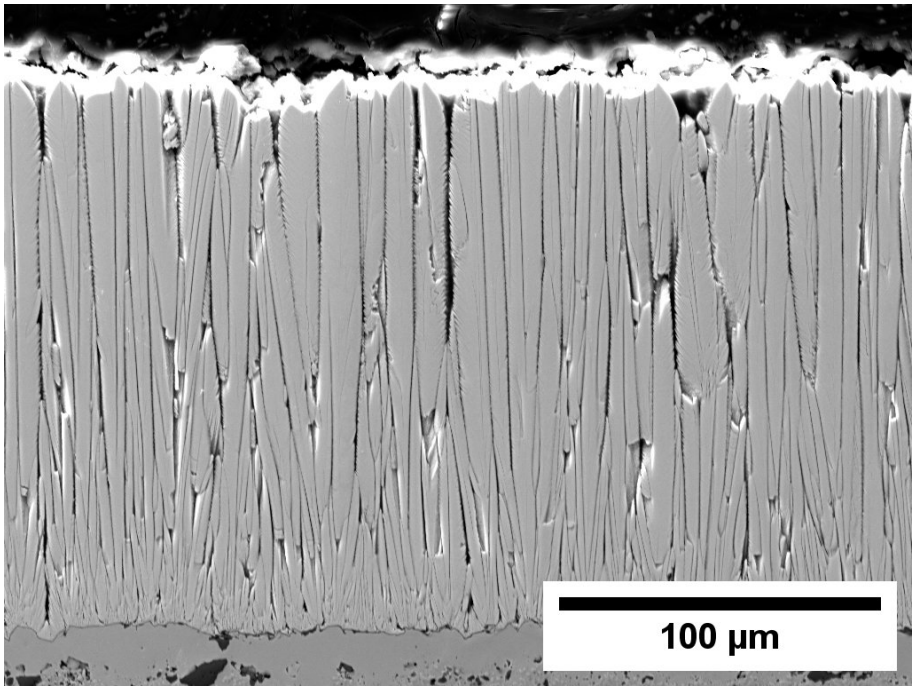


Figure 2.3: Typical EB-PVD TBC microstructure displaying ceramic columns separated by vertical pores. Work of the author.

2.1.3 Methods for the quantitative characterisation of TBC microstructures

The quantification of microstructural features of EB-PVD TBCs poses significant challenges related to the particular morphology that develops in the process of vapour deposition. The growth mechanism, under typical deposition conditions results in dendrite-like columns. The coating consisting in a collection of these columns, growing in competition with one another and filling the available space in the process. This results in coatings with a wide range of pore sizes and morphologies, ranging from nanometre sized (4), spheric or c-shaped porosities (3) to interconnected networks of intercolumnar pores, spanning the entirety of the coating thickness, circa 200 μm, but with pore throat sizes of between 0.1 to 1 μm. This multiplicity of pore morphology and dimension, depicted in Figure 2.4, imposes a requirement on the characterization techniques used of resolving nano-scale features while covering regions of interest hundreds of micrometers across.

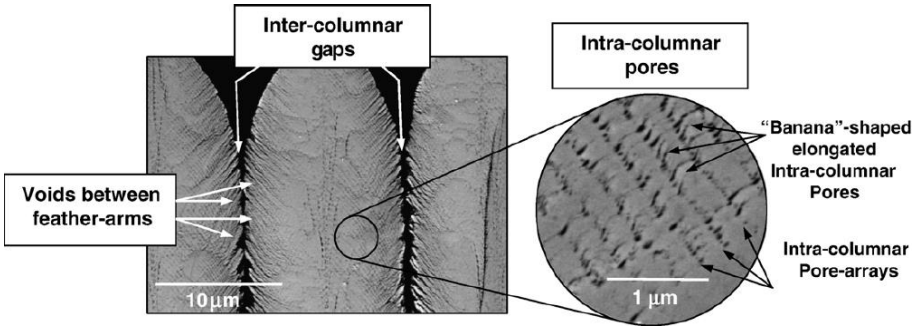


Figure 2.4: Type and distribution of porosity in typical EB-PVD columnar microstructures. Reproduced with permission from (3).

The morphology and dimension of the porosity and columnar grain morphology is also highly dependent on the through thickness position within the coating. as the mor-

phology of the crystalline grains changes according to the relative dominance of nucleation and growth mechanisms. This evolution of the microstructure in the through-thickness direction has been captured in the two-zone model proposed by Nicholls et al. (53). This evolution has been shown to have a marked effect on the thermal conductivity of TBCs, due to the changes in porosity size and morphology (54). Capturing this spatial distribution of the coating is, therefore, a key requirement for any quantification technique that aims to characterize the morphology of EB-PVD TBCs.

A focused review on techniques and methods for Environmental Barrier Coating (EBC) and TBC characterization by Scotson et al. (4) pointed out this tension between the required resolution and capturing the spatial distribution on the one hand, and the relatively large regions of interest required to capture the inherent variation of EB-PVD TBC microstructure.

Lastly, the three-dimensional nature of the porosity networks further complicates the characterization. Two types of techniques are capable of providing the spatially resolved three-dimensional data required, X-Ray Computed Tomography (XCT) and serial sectioning.

For the acquisition of 3D data, Scotson and co-workers, suggested XCT as the most practical characterization technique while acknowledging that: 'However, the limited resolution (>1 μm) and restricted penetration depth without specialized synchrotron facilities limit XCT's application in characterising ceramic coatings' (4). The particularly fine features exhibited by EB-PVD TBC porosity make this limitation all the more relevant.

Serial sectioning, which consists in alternating data capture and removal of material from the region of interest allows for reconstruction of 3D features with imaging and characterization techniques with the spatial resolution that Scanning Electron Microscopes can provide, overcoming the limitation imposed by XCT.

The limitations of serial sectioning in the SEM, explored by Echlin et al (55), as they pertain to ceramic coatings such as EB-PVD TBCs are three-fold. On the one hand, the slow removal speed of ceramic materials make milling with most common types of Focused Ion Beam (Ga FIB and Xe-PFIB) impractical, requiring instead femtosecond laser ablation for practical implementation. The non-conductive nature of ceramics can also generate issues with charging, once the conductive coatings deposited are ablated during material removal. Lastly, as illustrated in Figure 2.5, the combined dataset volume O(1 mm^3) and voxel resolution O(100 nm), results in Petabyte sized datasets, which subsequent analysis would require significant computational resources.

These challenges manifest in a lack of published methods for the systematic quantification of microstructural features of EB-PVD TBC microstructures. To the knowledge of the author, no comprehensive description of an image analysis method has been published for the characterization of EB-PVD column or porosity size morphology.

A selection of papers where image analysis for TBCs [2] is mentioned yields publications which can be categorized in one of four categories related to the details provided (or discernable) for quantitative image analysis:

1. Methods for the quantification of porosity, based on 2D data / images - No details provided

2. Methods for other morphological characterization, 2D - No details provided

[2] For the sake of completeness, APS, SPS, SPPS and PS-PVD were also considered in the search.

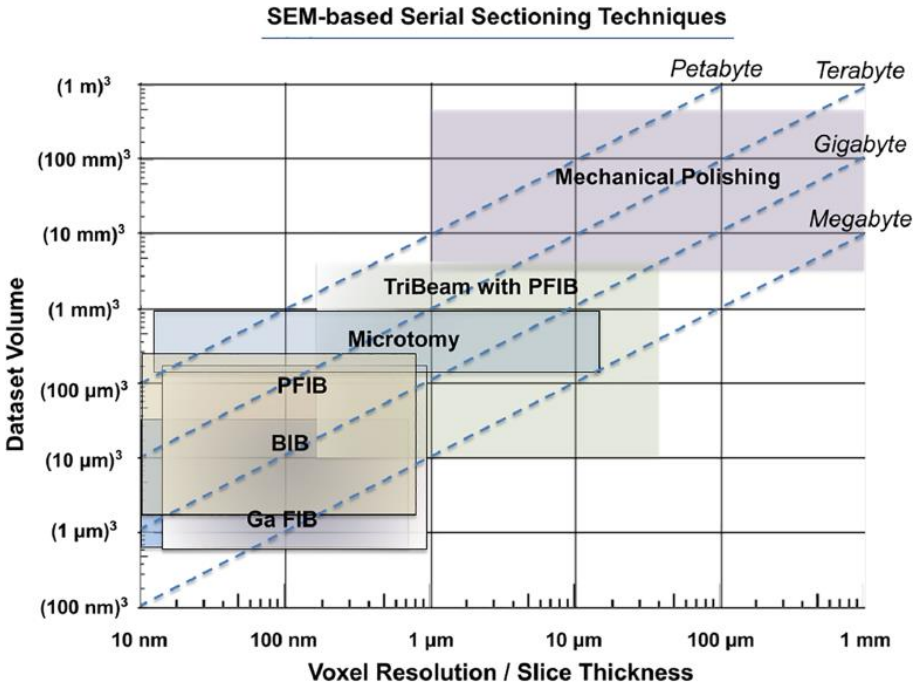


Figure 2.5: Type and distribution of porosity in typical EB-PVD columnar microstructures. Reproduced with permission from (4).

3. Methods for the quantification of microstructural features, 2D - Some details provided

4. Methods for the characterization of microstructural features, 3D

A brief discussion of the papers reviewed in each of these categories follows. The quantification of porosity, constituting the first category is the more frequent case observed for the reported use of nondescript image analysis, for TBCs deposited by different manufacturing methods: EB-PVD (56, 57, 58, 59), APS (60) and SPS and SPPS (61).

Publications in the second category also make a reference to image analysis, with no further detail as to the method used provided, but report further morphological descriptors. As way of an example, for EB-PVD coatings, column width (54), growth angle (62), pore size, morphology and aspect ratios (63), and a variety of descriptors for column morphology (64) have been reported. Similarly nondescript - often described as manual - methods have also been reported for deriving morphological descriptors of SPS coatings (65, 66).

The paper by Jiang et al (64) represents a prime example of the issues that arise from a lack of reported methodology, with two markedly different sets of figures are provided for column width, 20-36 μm in Table 1. and 1-5 μm according to the histogram in Figure 7 of the same publication. The absence of a reported method, beyond the number of grains used for the derivation of the histogram (n = 30), makes elucidating the causes for this discrepancy all but impossible.

Similarly nondescript methods were used in the quantification of pore type and size in APS coatings (67), and column morphological descriptors, almost identical to those used by Jiang et al., but for PS-PVD columns (67). Another attempt at quantifying PS-PVD microstructure was also undertaken by Zhao and coworkers (68).

The third category of publications reviewed is the most relevant for benchmarking the method described in Submission 3, as the few details provided therein point to the ca-

pabilities and issues encountered by other researchers when attempting to systematically quantify microstructural features of EB-PVD TBCs.

Unfortunately, as already mentioned, none of the papers reviewed offer a detailed methodology for the image analysis conducted on EB-PVD TBCs. Most reported methods for image analysis for quantification of microstructural morphology are instead applied to APS TBCs (69, 70, 71, 72, 73). Most of these publications either refer to or implement a variation of the method first developed by Dorvaux and coworkers (74).

Starting from a binarized image, this method consists in performing morphological operations, in particular, erosion (75) to a pixel-by pixel reduction of the size of the foreground objects - the dark pores in the image - until just the pore centroids are left. Step by step reconstruction of the total porosity [3] allows to classify the overall size, shape and connectivity of the pores present.

An alternative approach was adopted by Blanchard et al. (71, 72), using Dragonfly, an image analysis software equipped with supervised deep learning capabilities (76) to segment the solid portion, fine porosity and coarse porosity of acquired images. The obtained pore size distributions were subsequently used for modelling the optical response of the APS coatings using the finite-difference time-domain (FDTD) method.

Within the publications in this third category, APS seems to be an outlier in the complexity and sophistication of the reported methods, as only the most fundamental image analysis operations of gray value thresholding, binarizing and measuring of resulting binary images are reported for SPS (77) and PS-PVD (78) microstructures, based on electron images.

For EB-PVD microstructure characterization, an equivalent method - referred to as 'the greyscale threshold technique' was reported by Kadam et al. (79). A somewhat more elaborated method was adopted by Zotov and coworkers, adding an image sharpening filter (80). Note that, according to the ImageJ (11) documentation, (Sharpen) 'Increases contrast and accentuates detail in the image or selection, but may also accentuate noise. This filter uses ... weighting factors to replace each pixel with a weighted average of the 3x3 neighborhood.'. With this in mind, the selection of the sharpen filter may lead to exaggerated porosity, and should be carefully considered.

Zotov et al. (80) also reported a separate methodological detail for the determination of column widths - the use of 'line profiles (typically 300 μm length) [which] were taken in SEM micrographs with relatively small magnifications between 500× and 1000×', located roughly 30 μm below the surface of the ceramic top coat. No details on the determination of the number or width of the columns from the line profile were provided. However, as discussed in Submission 3 and Section 3.4.2, a modified version of this method was adopted in the present project.

Lastly, only only methods for the three-dimensional characterization of APS and EB-PVD TBC microstructure / pore morphology were found in the survey of the literature. Both the serial sectioning (81, 82) and XCT methods (83, 84, 85) were used for the characterization of APS and EB-PVD coatings. The limitations of analyzed volume (81) and resolution (82), depending on chosen sectioning technique are apparent in the serial sectioning methods applied to APS and EB-PVD techniques, respectively. As for the XCT methods, the aforementioned limit of resolved features, as well as the limited availability of the required characterization equipment are the limiting factor for capturing the full

[3] Not described in detail, but presumed to correspond to 'walking back' the erosion operations

range of porosity required for EB-PVD coatings.

The method proposed in Submission 3 aims to improve on the existing, sparsely described methods discussed here, as well as providing a repeatable and reviewable method for the quantitative analysis of EB-PVD TBC morphology, using readily available microscopic instruments.

2.2 TBC failure modes

Due to the exacting environmental conditions present in gas turbines during operation, TBCs are susceptible to a variety of failure modes. The main factors influencing TBC failure are the high gas temperature, turbine rotation speed and particles ingested into the engine. Failures caused by the high gas temperature and rotation speed, where the driving force is the accumulation of strain energy in the system from thermomechanical mismatches between the various layers, are classed as intrinsic modes of failure (86). On the other hand, failure modes that result from interaction of the TBC with ingested particles are denominated extrinsic, due to the causes of failure being external to the TBC system.

Intrinsic modes of failure comprise sintering, intrinsic delamination, sintering and low cycle fatigue delamination. These modes of failure are summarized below, with the exception of the latter, which is caused by failure originating in the substrate and therefore not considered. The extrinsic modes of failure are caused by the ingested particles either impacting the TBCs with high energy, or melting and adhering to TBCs, resulting in a complex thermo-chemo-mechanical failure mode generally referred to as CMAS attack. These extrinsic failure modes are also covered. An additional mode of failure discussed in the present Section is phase transformation, as it pertains to the state-of-the-art 7YSZ TBC material. Since phase transformation is not exhibited by all TBC material candidates, it is not considered a generalized mode of failure, unlike the intrinsic and extrinsic failure modes listed. However, it is considered relevant as a limiting factor of current TBCs, including the model materials investigated in the present research project.

2.2.1 Sintering

Sintering refers to the consolidation of material without melting (87). It is typically characterized by a reduction of overall porosity and a modification of the morphology of the pores and solid fraction in a material. The exposure to high temperature over time enables the diffusive migration of atoms. This migration is driven by the tendency of pores and grains to minimize their surface energy. It can be shown that the sphere is the geometrical shape with the lower surface area to volume ratio, and therefore minimizes surface energy for a given grain volume. Consequently, the microstructural changes result in “rounded” pore and grain boundary morphologies (47).

In the case of TBCs, sintering manifests in two stages; the first one consists in the smoothing of the column edges, during which the type II porosity becomes spherical or migrates out of the column entirely, and type III porosity rapidly coalesces into large linear pores (88) through the fusing together of the “feather arms”. The second phase consists in a narrowing of the type I pores, with columns fusing in contact points in a process called “necking” (89). This results in increased in-plain stiffness, negating the compliance

conferred to EB-PVD by its columnar microstructure. The accumulated strain energy can be released through cracking around groups of columns that are strongly bound together, in a mechanism called "mud-cracking" (90). Sintering does not result in TBC failure on its own, but through increasing strain energy in the system, and the open cracks that can result from its release, makes TBCs more susceptible to other modes of failure.

2.2.2 Phase transformation of 7YSZ

Zirconia (ZrO_2) exhibits a monoclinic crystal structure at room temperature, transforming to a tetragonal crystalline phase above 1200°C. The addition of Yttria and other Rare Earth Oxides (REOs) can modify the crystallographic phase stable at room temperature. Depending on the quantity of stabilizing oxides, either the (t') or the cubic (c) crystallographic phase are stabilized. In the case of the former, Zirconia is deemed to be metastable, and is called Partially Stabilized, whereas in the latter case, it is thermodynamically stable (91) and denominated Fully Stabilized Zirconia.

Partially Yttria Stabilized Zirconia (PYSZ) typically contains 4 to 12 wt.% Y_2O_3, with 7-8 wt. % being the most commonly used composition for TBCs (92). The metastable tetragonal phase stabilized in 7YSZ can, through exposure to temperature over 1200°C, partition into the tetragonal (t) and cubic phases (93, 94). The t phase can, subsequently undergo a transformation into the monoclinic (m) phase. This t $\leftarrow$ m phase transformation is accompanied by a large volume change and associated micro-strains. These generated strains can result in mechanical damage in the form of cracking (93).

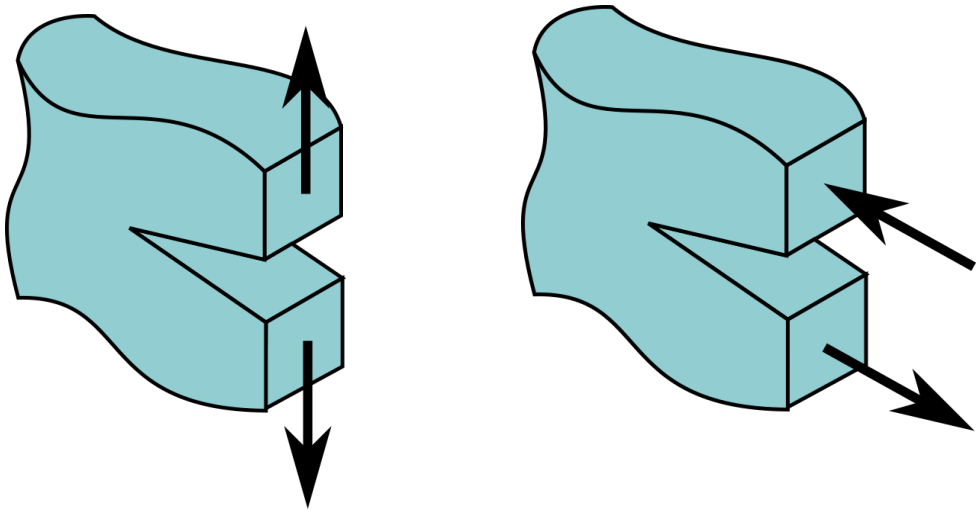
2.2.3 Intrinsic delamination

As already explained, intrinsic delamination results from the accumulation of strain energy resulting from strain mismatches between the different layers in the coating system. The driving force for the strain mismatches is the growth of the TGO when the coating system is exposed to high temperature. During the high temperature exposure, the volume of Al_2O_3 increases through reaction of the Aluminium in the BC with the oxygen present in the gas turbine environment (86). This increase in volume can be accommodated by the multilayer system due to the thermal expansion and stress relief facilitated at high temperature. However, upon cooling the additional volume gained by the TGO results in compressive stresses, which are relieved through out of plane displacements of the TGO layer in a process called ratcheting (95).

It should be noted that these out of plane displacements are interchangeably referred to as "rumpling" or "ratcheting" (96, 97). However, the distinction proposed by Evans (95) is adopted here. The distinction hinges on the direction of the out of plane displacements observed. Whereas rumpling refers to displacement occurring both towards and away from the original substrate surface, ratcheting only occurs towards the substrate. In TBC systems, the presence of the ceramic layer has been observed (98, 99) to prevent the outward displacement, resulting in ratcheting. The low compliance of the ceramic material, coupled with the tensile stresses developed as a result of the out of plane displacements of the underlying TGO layer results in the nucleation and growth of cracks in the TBC (2).

These cracks nucleate and grow throughout the lifetime of the component, until they reach a critical size, at which point spallation of the coating will occur (100). The fail-

ure typically occurs as one of two modes, depending on the location of the originating crack: Edge delamination or buckling. Edge delamination progresses as a mode II fracture from an edge, normally a film cooling hole or the edge between the coated surface to a shadow-masked area (101). Buckling, on the other hand, occurs as a mixed mode I and II fracture away from any edges (102). Figure 2.6 shows the Mode I (Opening) and Mode II (Shearing) loading cases. While the interface fracture toughness with regards to buckling is lower, the constraint imposed by the presence of the ceramic TBC inhibits buckling until the crack length exceeds ten times the coating thickness (101).



(a) Mode I (b) Mode II

Figure 2.6: Schematic diagrams for Mode I and Mode II fracture modes respectively. (c) Edge delamination mechanism, mode II. Work of the author based on (5).

2.2.3.1 Test methods for intrinsic delamination

The intrinsic delamination mechanism is tested through cyclic oxidation of TBC-coated specimens. There are two main types of cyclic oxidation test setups: Furnace tests and burner rig tests (103, 104). The tests are conducted on coupons with varying geometries, depending on the additional variables being evaluated and the test set-up being used. Cylindrical samples, discs, flat plates, bent plates and aerofoil sections (105) have been used to test the cyclic oxidation performance of TBCs. Given the influence of substrate curvature on the cyclic oxidation life of TBCs (106), especial care should be taken when comparing results obtained for equivalent TBCs using different substrate geometries.

2.2.4 Particle impact

Particles ingested into the engine can cause significant mechanical damage to the TBC upon impact, due to the high velocity they can achieve in the gas stream, and the compounding effect of the high rotational speed of some turbine components (15, 107). For small particles of 100 μm and below, impact speeds can reach 100-200 m/s (108, 109).

Using an analogous nomenclature to the one used to classify TBC failure modes, the variables affecting the erosion mechanisms and performance can be classified into extrinsic and intrinsic. Extrinsic factors refer to the characteristics of the impinging particles,

their impact angle and speed. Intrinsic variables include the mechanical properties of the TBC material and its microstructure. In the case of EB-PVD TBCs, the column width has been shown to significantly influence the erosion rate, as well as the mechanism for mass loss as a result of particle impact (6). More specifically, the ratio between the indentation (D) and column diameter (d) was proposed as a dimensionless parameter (110) to predict the damage mechanism affecting TBCs, depending on impact conditions and coating morphology. The threshold values for the different mechanisms identified are shown in equation 2.1. The contact diameter is calculated under the assumption of Hertzian contact.

$$\text{D/d: dimensionless parameter} \begin{cases} D/d \leq 2 \rightarrow \text{Mode I: Erosion} \\ 2 \leq D/d \leq 12 \rightarrow \text{Mode II: Compaction} \\ 12 \leq D/d \rightarrow \text{Mode III: Foreign Object Damage} \end{cases} \tag{2.1}$$

These values of the D/d dimensionless parameters allow to define the regions of expected damage mode based on the particle size and velocity, as depicted in Figure 2.7. Note that the values for the velocity and particle diameter presented apply specifically to Silica as an erodent, with 7YSZ TBC columns of a given width, and changes to these variables would modify the values defining the damage zones shown.

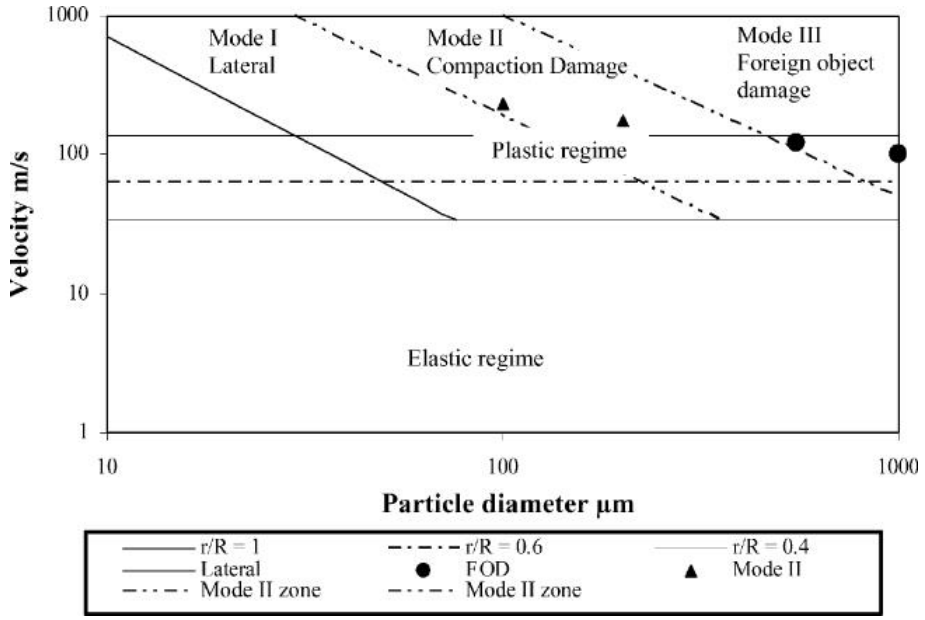


Figure 2.7: Particle impact damage mechanism zones as a function of particle size and velocity, reproduced with permission from (6).

The different mechanisms classified by the dimensionless parameter D/d are described as follows, based on the discussion provided by Wellman et al. (110): For small values of the D/d parameter, damage occurs when the impinging particle makes contact with few columns. Upon contact, stress waves propagate down the contacted columns and laterally to adjacent columns (111). The elastic response of the coating includes local bending in the area immediate to the coating surface, resulting in tensile stresses in the TBC columns (112). These tensile stresses act on the "feather arms" type III porosity, which are akin to notches in the columns. The effect of the tensile stresses is to open up these notches, resulting in the propagation of cracks through the columns.

The impact also compresses the columns, resulting in a level of plastic deformation which can lead to mechanical interlocking of adjacent columns (113). The tensile stresses can, in that way, act upon interlocked columns. This, on the one hand, promotes the propagation of damage, by allowing these stresses to "jump" from column to column. On the other hand, it slows the mass loss, by keeping material that had detached from its constituent column attached to the coating through the adjacent interlinked columns (114).

For intermediate D/d values, expressed as larger / higher kinematic energy particle impacts, compaction is the main damage mechanism. This mechanism consists in a larger scale expression of the plastic deformation linking adjacent columns together already discussed for the erosion damage mode. Compaction damage, however, exhibits a significantly thick densified layer on the coating surface. Kink cracks in the compacted layer grow with the tensile stresses generated by subsequent impacts, eventually resulting in material loss (115). Radial cracks may also develop within the densified layers if part of the impinging particles remain attached on rebound (112)

Foreign Object Damage occurs for large values of D/d, which typically correspond to impacts from very large particles, predominantly at high temperatures. For EB-PVD TBCs with a nominal columnar microstructure, such large particles are not normally ingested into the engine, but rather result from the spallation of material upstream of the TBC coated components. As such, FOD is typically a single-event damage mechanism, in contrast with the gradual degradation and failure induced by erosion and compaction (112, 116, 117). Damage caused by FOD is not confined to the ceramic layer, but rather extends into the TGO and substrate due to the substantial energy of the impact (118).However, changes to the microstructure of the TBCs, in particular, a reduction of the column width, may result in D/d values conducive to FOD-like damage even for impacts by modestly-sized particles, in which case, the damage would likely be contained to the TCB.

2.2.4.1 Methods for evaluating TBC particle impact resistance

TBCs are subjected to impact from ingested particles travelling at 100-200 m/s (108, 109). The testing of particle impact resistance therefore requires accelerating erodent particles to a significant fraction of that speed, before directing them towards the test specimen. This is generally achieved through mechanical acceleration or through the acceleration of a carrier gas. The mechanical acceleration of particles can be achieved by centrifugation. Injecting the particles into a rapidly spinning guide, the accelerator disc (119, 120) that allows to target the samples being tested. As for the carrier gas method, it generally consists in the release of pressurized gas, that accelerates aerodynamically, and drags the particles injected into the stream towards the test specimen (121, 122). Both methods allow for testing at high temperatures, by either heating the substrates in the centrifugal test rig, or the carrier gas in the aerodynamic drag based tests.

2.2.5 CMAS attack

The degradation and failure of TBCs through interaction with molten ingested particles is generally referred to as CMAS. This name refers to the oxides that constitute the bulk of the ingested material, Calcia, Magnesia, Alumina and Silica. CMAS attack is a complex thermal, mechanical and chemical degradation mode (123), that occurs in three stages, as detailed in Figure 2.8.

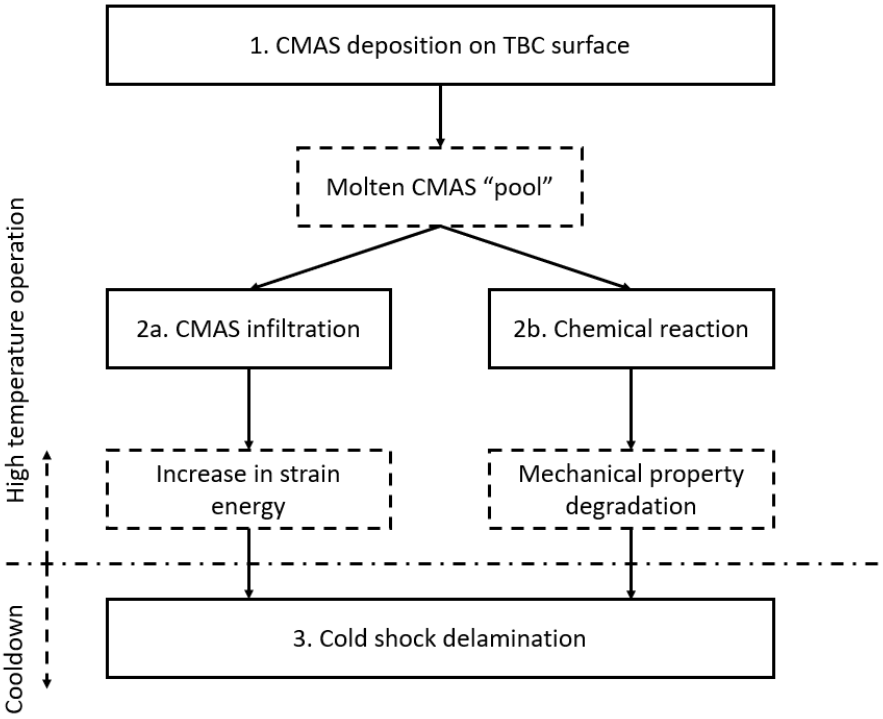


Figure 2.8: Diagram of the phases of the attack of TBC by CMAS. Work of the author.

CMAS attack starts by the accretion of molten particles onto the surface of TBC-coated components (124). Once adhered to the TBCs, molten CMAS infiltrates down the inter-columnar porosity (125, 126, 127). Simultaneously, chemical interactions between the infiltrating CMAS and the TBC can lead to the degradation of the mechanical properties of the TBC (96). This chemical interaction can, however, be used to limit the infiltration of CMAS (128, 129, 130, 131).

Upon cooling, CMAS solidifies, resulting in a loss of in-plane compliance in the infiltrated portion of the coating (102). Coupled with the thermomechanical loads induced by the CTE mismatch during the thermal transient upon cooling, this compliance loss results in the nucleation and growth of cracks, particularly at the CMAS infiltration front. The interlinking of the columns by the solidified CMAS also provides a path for crack propagation from column to column, resulting in large scale cracks, denominated "shelf cracking" (132). This mechanism for CMAS-infiltration induced mechanical damage is called "cold-shock delamination". CMAS attack results in the exfoliation of TBC thickness through this cold shock delamination mechanism, with the consequent reduction of the thermal protection afforded by the remaining TBC to the underlying substrate.

Given the complexity of the damage mechanism, a variety of analytical and computational models have been reported to predict the various aspects of CMAS attack and

underpin the design of novel TBCs with improved resistance to CMAS attack. Models for the deposition (133, 124), infiltration (134, 135, 136) & cold shock delamination (102) have been developed, complemented by a wide array of experimental and CALPHAD studies on the interaction between different TBC and CMAS compositions (128, 137, 138). These models have the potential to unlock the model-based development of CMAS-resistant TBCs, in line with IMCE principles. However, as discussed in Section 4.3 and Submissions 1 and 4, analytical tools for the validation of these models, in particular those related to CMAS infiltration, are required to establish the accuracy of the existing models.

2.2.5.1 Testing

Two fundamental methods exist for the testing of CMAS - isothermal (138, 139, 48, 127) and gradient testing (140, 141, 142). Isothermal testing consists in the exposure of CMAS-laden TBCs to a uniform high temperature field, usually in a furnace. In contrast, gradient CMAS testing consists in inducing a thermal gradient across the coating thickness, by applying a heat source and a heat sink to the opposite sides of the CMAS-loaded TBC-coated samples.

The isothermal testing method allows to evaluate the chemical interactions and, to a lesser extent infiltration kinematics of CMAS attack and is particularly useful for understanding the potential of a candidate TBC material to limit CMAS infiltration using a simple test rig (130). The cold shock delamination mechanism, however, can not be investigated by isothermal CMAS testing in a consistent manner, as it requires the establishment of a controlled thermal gradient (102). The systematic study of the cold shock delamination therefore necessitates the use of relatively more complex thermal gradient rigs (140). These rigs can also be used to study infiltration kinematics and chemical interactions between CMAS and . However, the thermal gradient infiltration studies identified correspond exclusively to APS TBCs (143)

As a consequence of these diverging capabilities and complexity of the different test methods, their use is often prioritized for interrogating different aspects of CMAS attack, or different stages in the evaluation of candidate systems. Isothermal tests are a relatively inexpensive and rapid way of screening different material systems for CMAS reactivity. Thermal gradient rigs, with the longer timescales and higher costs associated are most suitable for the CMAS testing of developed coating systems, or for comprehensive characterization of the effect of operational conditions (thermal gradient, peak temperature etc) on cyclic life of TBCs. The capabilities of either method for characterizing CMAS infiltration kinematics in EB-PVD TBCs are discussed in Chapter 4.

2.2.5.2 Methods for quantifying CMAS infiltration

The challenges in quantifying the infiltration of CMAS stem from the particular features of the columnar microstructure of EB-PVD TBCs, and thus are similar in nature to the challenges discussed in section 2.1.3, with additional challenges. The first is related to the different transport mechanisms for CMAS elements through the TBC thickness, namely surface diffusion and bulk transport in the liquid phase. This diversity of mechanisms for elemental transport is coupled with the poor spatial resolution of EDS, the most commonly available elemental characterization technique.

The interaction volume of X-rays produced by electron excitation exceeds the size of the porosity through which CMAS infiltrates. This the accurate determination of CMAS infiltration through direct observation of elemental maps produced by Energy or Wavelength Dispersive X-ray spectroscopy (EDS/WDS) challenging for EB-PVD TBC microstructures. This challenge is less pronounced in APS coatings due to the reduced pore neck dimension and the preferential pore orientation being perpendicular to the through-thickness direction. This results in slower and more uniformly distributed CMAS infiltration, with easier to determine infiltration fronts (144).

This accumulation of challenges may explain why, to date, to the knowledge of the author, no systematic method for the measurement of CMAS infiltration depth has been reported in the published literature. Even focusing on characterization techniques, one could note that few are cited by Scotson et al. (4) as capable of the required elemental concentration and spatial resolution. The widely available characterization techniques either fail to meet spatial resolution (GD-OES[4]), are limited to small areas of interest (STEM-EDS [5]/EEELS [6]/HAADF [7] (145)), requiring electron transparent lamella preparation, or require specialized equipment (Synchrotron based techniques (146)).

Notwithstanding this absence of a published method, publications concerned with the infiltration of CMAS in EB-PVD TBCs do report figures for the infiltration depth observed at different exposure conditions and for different coating microstructures and/or material systems. As mentioned previously, this challenge is especially pronounced for EB-PVD TBCs, due to the open porosity these coatings exhibit in the through thickness direction, which provide accelerated infiltration pathways for CMAS. Bearing this in mind, the following examples of reported infiltration depths will exclusively focus on EB-PVD TBCs exposed to CMAS.

Firstly, given the relatively short time required for full infiltration of EB-PVD TBCs by molten CMAS, it is unsurprising to see that published literature analysing CMAS infiltration only reports fully infiltrated TBCs (147, 148, 149, 150, 151, 152, 153, 154, 155). This full infiltration would preclude assessing the method used for the determination of CMAS infiltration depth, as the required boundary between infiltrated and un-infiltrated TBC (in the through thickness direction) is absent from the analyzed areas. Note that all of these publications used X-ray spectroscopy (EDS or WDS) to determine the spatially resolve (i.e. map) the elemental composition through the entire coating thickness.

A further group of publications do exhibit and discuss partial infiltration of the TBC thickness by CMAS, without quantifying the infiltration depth (156, 157, 158, 159, 160). The determination of infiltration depth is undertaken in these publications via a nondescript method, by determining the infiltration front in EDS maps. An exception to the use of EDS is given in Peng et al. (160), who used WDS point analysis at 5 points through the coating thickness to determine the proportion of CMAS elements present in the TBC.

Lastly, the largest group of publications discussing the infiltration of CMAS in EB-PVD TBCs is constituted by those reporting figures of CMAS infiltration depth, reportedly corresponding to partial infiltration. This group, consequently, would hold the most promise with regards to identifying a method for determining CMAS infiltration depth.

[4]Glow Discharge-Optical Emission Spectroscopy

[5]Combined Scanning Transmission Electron Microscopy with Energy Dispersive X-ray Spectroscopy

[6]Electron Energy Loss Spectroscopy

[7]High-Angle Annular Dark Field

Classifying these publications by the main analytical technique used for determining the CMAS infiltration, three subgroups can be drawn.

Firstly, publications where electron images of the TBC microstructures are the main source used in determining the infiltration depth (48, 161, 162); secondly, publications where the phase transformation induced by the interaction between CMAS and TBC is used, as determined by X-Ray radiation (163, 163) or Raman Spectroscopy (149). Lastly, publications where elemental composition, determined via EDS (126, 127, 134, 152, 153, 155, 164, 165, 166, 167, 168, 169, 170, 171, 172), and EPMA (through WDS) (150) was used to determine the infiltration front position within the coating.

It should be noted that both the first and second subgroups, those looking at microstructural and phase changes, respectively, assess some of the consequences of CMAS infiltration, rather than the infiltration itself, meaning there could be a time delay between the infiltration causing them, and the manifestation of the assessed effect.

Within the last group, different spatially resolved methods were used, from single point analysis (164), to linescans (127) and maps (126, 150, 152, 153, 155, 164, 165, 166, 167, 168, 169, 170, 171, 172). Some (134) do not report the spatial resolution of the EDS method used as the basis for infiltration depth determination.

A further difference in the apparent, if not reported, method used in determining the CMAS infiltration depth arises from the element used to track the CMAS infiltration. While the most frequent element used is Si (126, 153, 155, 166, 172), the use of Ca as a marker of infiltration (169, 171) and the maps of multiple elements (150, 164, 165, 168, 170) are also reported. Given the preferential infiltration of the different elements, apparent in publications reporting maps for multiple elements, the relatively arbitrary selection of one element may introduce bias and reduce the accuracy of the infiltration depth thus determined.

Even discounting these differences, the more fundamental issue lies, as already discussed, in the nondescript method used in the reviewed publications to determine the depth of infiltration based on the chosen characterization method and resulting data. While it is entirely possible that systematic methods were used in the determination of the reported infiltration depth values, the failure to report such a method thwart any attempt to evaluate or replicate the results independently.

In this situation, one can only treat the results as equivalent to those obtained through a ‘manual’ determination of infiltration depth, based on the perceived location of whichever marker of the infiltration front is selected. The inherent subjectivity of such methods make them unsuitable for the quantitative validation of any model aiming to predict the infiltration behaviour of CMAS in its interaction with columnar TBCs.

Chapter 3

Deposition and characterization of model TBCs

3.1 Methodology for the deposition and characterization of model TBCs

The methodology used in conducting the experiments whose results are discussed in the present innovation report are fully detailed in Submission 2: “Methodology of physical experiments”. An abridged version is provided below, to contextualize the results presented within this document.

3.1.1 Experimental Materials

The selection of substrate material and bond coat has a substantial effect on the performance and durability of EB-PVD TBCs, as shown in Submission 1. Likewise, the composition and morphology of the synthetic environmental contaminants - Erodent and CMAS - used in the testing of the degradation of the TBCs bears a significant influence on the results obtained.

3.1.1.1 Substrate materials

Three different materials have been used in the present projects as substrates for the deposition of bond coats and top coats, depending on the subsequent intended use of the samples being produced.

Al_2O_3 discs (96% purity, Pi-KEM Ltd.) were used for the isothermal CMAS testing described in Chapter 4. The discs were 12.7 mm in diameter and 0.6 mm thick.

The burner rig CMAS test specimens - discussed in Section 4.1.2 - were deposited on 30 mm diameter single crystal CMSX-4 Ni-superalloy coupons. Further details on the geometry of these burner rig coupons can be found in Submission 4: "International Research Visit - ForschungsZentrum Jülich", and in the published work of Steinke et al (141).

CMSX-4 was also the material used in the test specimens for evaluating the cyclic oxidation resistance of the TBC systems studied. Three sections were produced from

Table 3.1: CMAS powder composition

CaO	MgO	Al_2O_3	SiO_2
35.00	10.00	7.00	48.00

coated High Pressure Turbine Blade (HPTB), at 25%, 50% and 75% of the height of the blade aerofoil.

For the specimens used in the erosion testing of the model TBCs, discussed in Chapter 5, Nimonic-75 (Special Metals Corporation) Nickel-based alloy samples were used, in the shape of 25 x 25 mm squares, with an approximate thickness of 1.5 mm.

3.1.1.2 Bond coat materials

Two different bond coat systems were applied depending the metallic substrates used in the present study, to ensure TBC adhesion. For the CMSX-4 substrates, a platinum aluminide bond coat was applied. The Nimonic-75 samples were aluminised via CVD at Cranfield University. Aluminium Chromium alloy chips (40 wt.% Cr, 60 wt.% Al - Reading Alloys) were used as the aluminium source, and AlF_3 (Prince minerals) was used as the activator for the CVD process.

3.1.1.3 Top coat materials

Three top coat materials were used in the present project: 7YSZ, LowK, and GZO. LowK refers to a commercial version of partially yttria stabilized zirconia with lower thermal conductivity and a metastable tetragonal phase when deposited via EB-PVD. The ceramic ingots for the deposition of the top coat via EB-PVD were supplied by Saint-Gobain Ceramic Materials. The top coat materials and their characteristics are further discussed in section 3.3.

3.1.1.4 Consumable testing materials

Additional materials were consumed in the course of undertaking endurance testing of the produced TBCs. The tests requiring consumable materials were high velocity particle erosion testing and CMAS testing.

In the case of erosion testing, the erodent media used as a consumable was white Saftigrit™(Guyson International Ltd.) alumina, sieved to a size between 90 and 125 μm.

The synthetic CMAS used in the present project was mixed from high purity ($\leq$99.9%) CaO, MgO, Al_2O_3, and SiO_2 powders (Pi-KEM) The powders were mixed to obtain a mol% composition as per Table 3.1.

3.1.1.5 Ancillary materials

Brown alumina Saftigrit™(Guyson International Ltd.), with a 220 grit size, was used for grit blasting the bond coated samples, to remove any undesirable surface contamination (e.g. oxides other than Al_2O_3).

Ball milling was used to reduce the particle size of the CMAS component powders and homogenize the mix. ZrO_2 balls, 10 mm in diameter (Fritsch GmbH) and 250 ml

ZrO_2 bowls (Fritsch GmbH) were used to mill the powder and contain it in the process, respectively.

3.1.2 Experimental equipment

The experimental equipment used is grouped according to the role it played in the production, testing and characterization of the coatings constituting the subject of the present study. A short description of its use, supplemented by the detailed explanation given in Submission 2, is provided below.

3.1.2.1 Deposition and preparation equipment

The deposition of bond coats and ceramic top coats requires a surface free of detrimental oxides and other contaminants. Such surface was achieved in the samples to be coated by means of grit blasting with alumina grit, using a Guyson F1600 grit blasting unit. All samples were grit blasted at an incidence angle of approximately 45°to the surface normal, with the relative motion between the grit blasting gun and the work piece undertaken in two different directions to ensure the entire surface is cleaned. The air pressure on the grit blasting gun was set to 2 bar.

For samples requiring the application of an aluminium bond coat layer, the thermal Chemical Vapour Deposition rig (173) was used, with the activator and aluminium source materials detailed above. A full description of a CVD aluminising cycle and the equipment can be found in Chirivi (174). As a summary, the typical CVD cycle consists in the heating up of an argon filled where the samples, Al source and activator are placed. The thermal energy provided promotes the reaction of the activator and source, generating an vapour phase that transports aluminium to the surface of the samples being coated. The aluminising undertaken in the course of the present research was conducted at 1030°C, maintained for 5 hours.

The deposition of the ceramic TBC top coats was undertaken using the Von Ardenne EB150 multi-source evaporator in Cranfield University (175). A few details on the equipment and deposition parameters have been published elsewhere (176), and are discussed in detail in Section 3.2.2.

In addition to preparing samples for the deposition of coatings, the materials used in the endurance testing of the produced TBCs also required preparation from the as-supplied state. The alumina powder used for testing the erosion testing of the model TBCs had to be sieved to select the right size grit - 90 to 125 μm. An Endecott Octagon Digital sieve shaker, along with appropriately sized sieves, also provided by Endecot, were used for this task.

Prior to high temperature exposure, the CMAS powder used to test the resistance of produced TBCs to CMAS infiltration had to be milled, mixed to homogenize the distribution of its constituents and sprayed onto the coated samples. A Fritsch Pulverisette 5 planetary ball mill was used for the comminution of the constituent oxides. The CMAS mixture was milled at 150 RPM for 4h, at 1h intervals with 15 minute cool down periods between them.

The milled powder was subsequently mixed in a Turbula T2C 3D mixer-shaker, which uses a Schatz linkage mechanism, designed for homogeneous mixing of dissimilar materials. The CMAS powder was mixed for 15 minutes within a closed container held in the

Turbula system. A suspension was created by mixing the CMAS powders were mixed in a 1:1 volumetric ratio with deionized water. This suspension was kept in suspension by means of a magnetic stirrer, and sprayed onto samples held by a metallic holder using an airbrush, at a stand-off distance of 30 cm. The metallic substrate holders were heated to 150°C by a hot plate, to evaporate the deionized water, resulting in a dry powder deposit.

3.1.2.2 Coating endurance testing equipment

Two pieces of equipment were used as part of the present project for the endurance testing of the produced TBCs. The erosion resistance of model TBC systems, reported in Chapter 5 was undertaken in the High Velocity Erosion Rig in Cranfield University (25, 108, 177, 178). Erosion testing was conducted at room temperature, with inlet pressure set to 5.6 bar.

For CMAS and cyclic oxidation testing a calibrated Pyro-Therm box furnace, capable of temperatures up to 1400°C was used. The maximum temperature difference within the hot zone of the furnace, in the The nominal exposure times reported for CMAS and cyclic oxidation testing - Chapters 4 and 6, respectively - were calculated from the point of thermal equilibration following sample insertion on the furnace, which varied according to the combined thermal mass of the sample and holder.

3.1.2.3 Analytical equipment

The analytical equipment used in the obtention of the results presented in this report, ignoring common tabletop analytical equipment such as standard optical microscopes and precision scales, is detailed in Table 3.2.

Table 3.2: List of analytical equipment

Equipment	Manufacturer	Component/Model
Scanning Electron Microscope	Tescan	Microscope - S8000G SE detector - Everhart-Thornley BSE detector - Scintillator based In-lens ‘Multi-detector‘ In-lens axial BSE detector
	Oxford instruments	EDS detector - Ultim-max 100 EBSD detector - Symmetry S1
X-Ray Diffractometer	Bruker	D5005
Confocal microscope	Keyence	VHX-7000

3.1.3 Summary of tested samples and experimental conditions.

As a guide to aid understanding of the sytems being produced, characterized and tested throughout the present innovation report, a summary of the substrates and material systems discussed in each chapter is provided in table 3.3. All samples are referred to, in their respective chapters, by the corresponding system name (column header in Table 3.3.).

The exception to this rule is the nomenclature used in Chapter 4.2.2 to denote samples tested for CMAS under thermal gradient conditions. All tested samples correspond to 7YSZ, and the exposure time is the distinguishing factor between the main samples compared, '7YSZ' is dropped from the system name, and the exposure time, in minutes (-3' or -6') appended, to provide a unique ID for each test performed, as per Table 4.4. Additional samples discussed in Chapter 4.2.2.2, and corresponding to Submission 4, follow the naming convention laid out in said submission. All of these samples belong to the 7YSZ-Nom coating system, with differences in the CMAS loading and exposure time detailed in Table 4.5.

Table 3.3: List of material system and substrate combinations used in results presented in each chapter. † refers to historic data.

		PYSZ							GZO			
Chapter - (Characterisation / Test)	Substrates	LowK-Nom.	LowK-LT	LowK-LR	LowK-LTLR	LowK-LLT	7YSZ-Nom.	7YSZ-LT	GZO-Nom.	GZO-LT	GZO-LR	GZO-LTLR
3. Deposition - SEM	Al disc, N75 sq.	✓	✓	✓	✓	✓			✓	✓	✓	✓
3. Deposition - EBSD	Al disc, N75	✓	✓	✓	✓	✓				✓	✓	✓
4. CMAS testing - Isothermal	Al disc	✓	✓	✓	✓	✓			✓	✓	✓	✓
4. CMAS testing - Gradient	CMSX-4 button						✓	✓				
5. Erosion	N75 sq.	✓	✓	✓	✓			†	✓	✓	✓	✓
6. Cyclic oxidation	CMSX-4 blade	†	✓	✓			†		✓	✓	✓	

While the specific conditions for the testing which results are discussed in the present report are detailed in the corresponding Chapter, Portfolio Submission, or both, a summary of the experimental conditions used is provided in table 3.4. The reference to the relevant chapters and submissions is also provided in this table.

Table 3.4: Summary of test conditions for each type of test, including relevant Chapter within the present report where test results are discussed, and related Portfolio Submissions

Chapter [Submissions]	Experimental conditions
4. CMAS testing - Isothermal [2,5]	1250°C, 1300°C; 30 - 360 s exposure time, 2 samples per condition.
4. CMAS testing - Gradient [2,4]	1300°C front face, 1100°C back face. 9' pre loading, 6' or 9' exposure.
5. Erosion [2]	Room T, 5.6 bar pressure, 90°impingement angle, 0.46 g/min erodent dose.
6. Cyclic oxidation [2]	1190°C isothermal exposure, 3h cycles + 15' equilibration.

3.2 Model TBCs - materials and deposition conditions

The evaluation of the effect of the relevant process parameters on the microstructure of TBCs was undertaken. From the three primary process parameters affecting deposition discussed in Section 1.2.5 of Submission 4: "Microstructure quantification" (Pressure, Temperature, and Rotation speed), the latter two were selected.

Pressure was not considered due to the limits in operational pressure imposed by the pumping system in the EBE-150 Von Ardenne coater at Cranfield University. A narrow pressure variation window would result from this limitation. This was coupled with an expected small effect size of pressure at the conditions to be explored, according to the structure zone models discussed in Section 1.2.5.2 in Submission 4. The conclusion from this analysis of the limitations, was that the feasible deposition process window associated to the operating pressure would provide limited microstructural difference potential, at the increased cost of multiplying the dimensionality of the experimental matrix.

Additionally, the reported effects of varying rotation speed and deposition temperature on TBC microstructure morphology, namely the generation of zigzag or c-shaped columns, decreased column width and increased intercolumnar porosity tortuosity, were deemed of particular interest for the improvement of the durability of TBCs against CMAS fluxing attack and particle impact damage. The effects observed from the deposited systems with regards to these failure modes are reported in Chapters 4 and 5 respectively. The cyclic oxidation performance of the deposited TBCs is discussed in Chapter 6.

The objectives of the model TBC deposition, in the context of the research project, were as follows:

1. Evaluate the effect of deposition substrate: to understand how the limitations imposed by having to use dissimilar substrate materials for the evaluation of different failure modes - See Submission 2 - influences the relationships discovered in objectives 2 and 3 in Table 1.1.

2. Deposit TBCs with a variety of microstructures: with a multiple purpose:

    - Describe their morphological features: in both qualitative and quantitative terms, in relation to the theoretical and computational models described in Submission 4, Sections 1.2.5 & 1.4.1.
    - To provide samples for the evaluation of the effect of the dissimilar microstructures on durability and performance.

3. Deposit at least two dissimilar model materials: to extend the evaluations beyond a single material and enable a level of extrapolation/abstraction of the deposition-microstructure-performance related to the specific material properties.

3.2.1 Viable materials for deposition via EB-PVD

A number of material families have been studied as thermal barrier coating candidate materials, to try to overcome the limitations of state-of-the-art 7 wt.% Y_2O_3 stabilized ZrO_2 (179, 180, 181). However, the limitations discussed in Section 1.2.5.4 of Submission 3 restrict the commercial viability and reproducibility of many of these systems. This is in part due to the difficulty in achieving repeatable consistency for the manufacturing of the coating composition and avoid compositional segregation, which is exhibited by many of the alternative systems studied, as shown in Table 3.5.

Table 3.5: List of material candidates considered as a replacement for 7YSZ, including whether deposition via EB-PVD has been reported, and compositional segregation/banding has been observed.

Material family	Sub-Family	Material	EB-PVD	Segregation?	References
1. Modified 7YSZ	a. Other RE-stabilizers	CeSZ	YES	YES/NO	(47, 182)
		YbSZ	NO	NO	(30, 183)
		DySZ	YES	NO	(184)
		NdSZ	YES	NO	(30, 165)
		Er-Y SZ	YES	NO	(185)
	b. DC* compounds	Y+Nd+Yb+Sc	YES	NO$^{\bullet}$	(186)
	c. RC$^{\diamond}$ additions	Al_2O_3 /TiO_2	YES†	NO	(169, 187)
	d. Toughening add.	Ta_2O_5 & TiO_2	NO	NO	(188, 189, 190, 191)
2. Pyrochlores ($A_2B_2O_7$)	a. Zirconates	$Gd_2Zr_2O_7$	YES	NO	(166, 192, 193)
		$Sm_2Zr_2O_7$	YES	YES	(194, 195)
		$La_2Zr_2O_7$	YES	YES	(196, 197, 198, 199)
	b. Modif. Pyrochl.	GYbZO	YES	NO	(103)
3. Hexa-aluminates	a. Magnetoplumbites	La-Hexaaluminate	NO‡	Unknown	(200, 201)
4. Perovskites	a. Perovskites	$EuHfO_3$/$RETaO_3$	NO	Unknown	(202)
5. Lanthanide phosphates	a. LnPO4	$GdPO_4$	NO	Unknown	(203)
6. Multicomponent REOs	a. HEO	5 $RE_{0.2}M^{\odot}Al_{11}O_{19}$	NO	Unknown	(204, 205)
7. LOReM	a. Tantalates	$YbTaO_4$	YES	YES	(206)
	b. Niobates	RE_3NbO_4	NO	Unknown	(207)
	c. Mixed Zirconates	YbYZTa	YES	YES	(208)

For interpretation of Table 3.5, LOReM refers to Lanthanide Oxides mixed with Refractory Metal oxides * Defect cluster. $^{\diamond}$ Reactive crystallization. $^{\bullet}$ segregation only in the form of very small (5-20 nm) defect cluster regions. † Al_2O_3 deposited as separate layer. ‡ Claimed in a patent. $^{\odot}$ M = Mg or Zr.

In practice, two material systems, with some level of variation regarding their exact composition, have been deployed in service: PYSZ and Gadolinium Zirconate (GZO). The phase composition, properties and durability of these systems are summarized below.

3.2.1.1 Rare Earth Oxide doped PYSZ - LowK

LowK is a commercial version of PYSZ, originally developed as a low thermal conductivity[1] alternative to 7YSZ, while aiming to reproduce the t' phase. The addition of dopants has been reported to reduce the erosion resistance of EB-PVD TBCs (110, 209), which leads to an expectation that LowK will exhibit a somewhat lower erosion resistance compared to 7YSZ[2]. Other doped low thermal conductivity t' coating materials seem to exhibit erosion rates similar, if lower than 7YSZ (210). The same group also confirmed the observation of increasing erosion rate with Gd content for the version of t' LowK TBC studied when mixed with GZO (211).

PYSZ exhibits relatively sluggish crystallization kinematics with CMAS. The relative speed of dissolution, reaction and crystallization of PYSZ is not sufficiently rapid to produce crystalline products (Zircon) (128) that could block the intercolumnar porosity, which could help hinder further infiltration. Considering the limited dopant content in LowK, the interaction between LowK and CMAS is considered, in first approximation, negligible. Consequently, the effect of crystallization on viscosity and infiltration is not considered significant in LowK, since full CMAS infiltration can happen in as little as 30s (135), whereas Zircon precipitation can reportedly take up to 30 minutes (165). LowK is, consequently, a good model material to evaluate the effect of microstructure on CMAS infiltration, minimizing the effects of reactive crystallization on infiltration kinematics.

In the context of the present research, LowK is therefore selected as the model material with high erosion resistance. LowK and 7YSZ are, therefore considered as non-reactive with CMAS, with regards to CMAS infiltration and reaction kinematics.

3.2.1.2 GZO

Gadolinium Zirconate belongs to the Pyrochlore family of materials studied for TBC applications, as shown in Table 3.5 (199). The members of this family, with nominal composition $A_2B_2O_7$, strictly speaking, belong to the cubic Fluorite-related structure family. The pyrochlore structure is the structure that these materials display in their stoichiometric composition, as shown in Figure 3.1. However, various factors, including temperature, pressure, ball milling, and others (8, 212, 213) can induce disorder in the lattice, resulting in a transformation to the the defect Fluorite structure. This disorder manifests through the difference in site occupations of the A and B cations, and the presence of oxygen vacancies in the defect Fluorite structure, as shown in Figure 3.2.

In the case of $Gd_2Zr_2O_7$, a reversible transformation from the pyrochlore to the defect Fluorite structure in the range between 1773 and 1873K (214). The crystallographic group and identification of the two structures, the position and coordination of Gd, Zr, O and vacancies is provided in Table 3.6.

It should be noted that Gadolinium Zirconate exhibits limited banding when compared to other pyrochlore forming compositions. This is despite the fact that the vapour pressure of Gadolinium Oxide is over twice that of Zirconia, at the evaporation temperature (3.06 vs 1.36 atm) (176).

With regards to mechanical properties and CMAS performance, GZO defines the opposite side of the spectrum to LowK. GZO exhibits low stiffness, hardness and fracture

[1] Hence the LowK name, with K representing κ, thermal conductivity.

[2] This is confirmed by unpublished LowK erosion data collected at Cranfield University

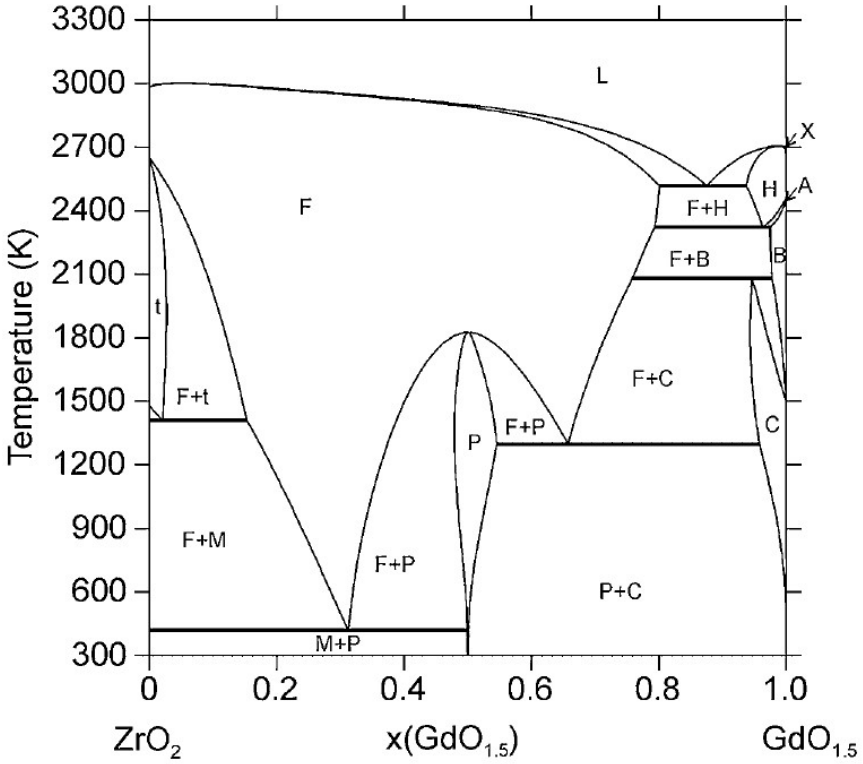


Figure 3.1: ZrO_2-$GdO_{1.5}$ diagram showing the narrow Pyrochlore field, stable at the stoichiometric composition at room temperature, reproduced with permission from (7) - L = Liquid, F = Fluorite, P = Pyrochlore, M = Monoclinic ZrO_2, C = Cubic Gd_2O_3

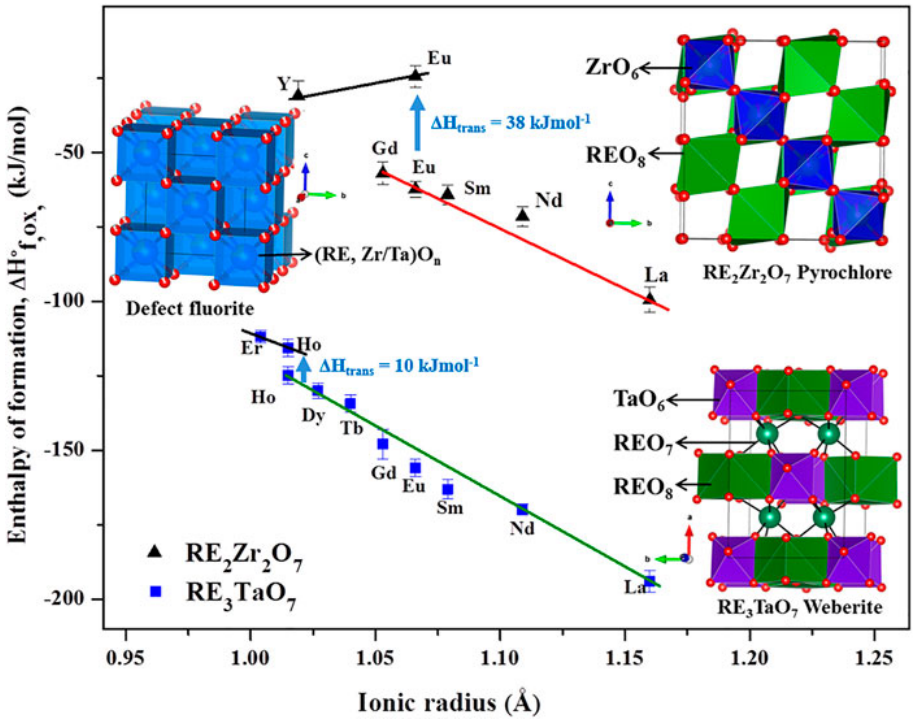


Figure 3.2: Schematic structures of Fluorite and Pyrochlore Rare Earth Zirconates, including order-disorder transition energetics, from (8), based on data from (9, 10). Also depicted the Weberite - Defect Fluorite transition of Fluorite-related structures with nominal composition A_3BO_7 (B = Ta, A = RE).

Table 3.6: Crystallographic characterization of Pyrochlore and Defect Fluorite GZO, including site occupancy and coordination of the Gd and Zr cations, based on data from (8). For interpretation of Wyckoff points, the reader is referred to (13).

Space group [No.]		Pyrochlore Fd-$\bar{3}$m [227]	Defect Fluorite Fm-$\bar{3}$m [225]
Gd	Wyckoff position	16d	4a
	Coordination [O, Vac]	8,0	7,1
Zr	Wyckoff position	16d	4a
	Coordination [O, Vac]	6,0	7,1
O	Wyckoff position	48f, 8b	8c
Vac.	Wyckoff position	8a	8c

toughness (210, 211). While CMAS-LowK and CMAS-7YSZ interactions result in sluggish reactions that are unable to limit the extent of CMAS infiltration, GZO exhibits high reactivity and the ability to seal intercolumnar gaps. It is thus selected to probe the effect of microstructure on material systems that exhibit reactive crystallization of CMAS.

3.2.1.3 GZO to LowK comparison

Compared to 7YSZ, GZO exhibits a relatively poor erosion performance, with erosion rates for GZO EB-PVD TBCs reportedly ten times those for 7YSZ (210). This relative performance was also observed by Beake et al. (215) using a randomized nano-impact test method. This difference in erosive behaviour likely stems from two sources. On the one hand, GZO does not exhibit the toughening ferroelastic transformation present in 7YSZ. On the other hand, the reduced hardness and stiffness of GZO vs. 7YSZ (E = 80 vs. 65 GPa and H = 1.6 vs. 2.4 GPa (215)), results, as discussed in Submission 1 in an increased indentation footprint, with subsequent plastic deformation and predicted material loss (110, 115, 216).

This mechanical performance handicap is compensated by the CMAS resistance exhibited by Gadolinium Zirconate. GZO has shown both in laboratory-based testing and in aircraft operation, an increased resilience against CMAS attack (96). GZO achieves this resistance through inducing reactive recrystallization in the CMAS melt. The reaction products are mostly Rare Earth Oxyapatite (Apatite) and Ca and RE-bearing ZrO_2 Fluorite (130). It has been shown that Apatite can effectively block infiltration of CMAS through the intercolumnar pores, effectively minimizing CMAS infiltration depth, and therefore limiting CMAS induced thermomechanical damage.

3.2.2 Experimental matrix

TBC systems that have shown to be easy to evaporate and deposit consistently from a single source were selected, to avoid the evaporability issues outlined in Section 3.2.1. An additional criterion used for material selection was that materials should be readily available at Cranfield University. This is justified by the fact that both the acquisition of ingots and the EB-PVD deposition of TBCs are time consuming and costly processes. Therefore, choosing other materials with poor or unproven evaporability, or long ingot manufacture lead times would have meant spending a significant portion of the time and budget of the project ensuring the reproducibility of the systems to be studied.

Using these criteria, 7YSZ, LowK, and GZO were selected as model materials for investigation, as discussed in Submission 2. The selected materials have also been extensively studied and reported in the literature (217, 218, 219, 220, 167, 193, 221), and deployed in service (96, 22). This provides a wealth of data to compare against the results of this study.

A general comparison of the thermal and mechanical properties and durability test results of 7YSZ and GZO can be seen in Table 3.7. 7YSZ is also included as a baseline material for comparison.

Table 3.7: Properties of model EB-PVD TBCs, measured at room temperature. The crystallographic phase for 7YSZ corresponds to the metastable tetragonal, and GZO to the pyrochlore. * SERR refers to Strain Energy Release Rate. † data from erosion testing at Cranfield University. § this work, for GZO-Nom - see Chapter 5. ‡ See Chapter 6 for an explanation of normalized cyclic oxidation life, 7YSZ value based on historic data from cyclic testing at Cranfield university.

Material	7YSZ	GZO
Young's modulus [GPa]	77-85 (222, 223, 224)	75 (224)
Hardness [GPa]	2.5-8.9 (114, 224)	5.4 (224)
Density [g/cm^3]	4.68 (225)	5.91 (211, 166)
Pore fraction [%]	5.70 (226)-22.3 (225)	14.6% (166)
Critical SERR* - Mode I [J·m^{-2}]	30 (102)-45 (94), 50(227)	$4.3 \pm 1.6 \cdot 10^{-3}$ (211)
Fracture toughness [MPa·$\sqrt{m}$]	1.8 - 4.5 (94)	1.0 (211)
Erosion rate [g/kg]	5-8†,20(110)	33 ± 0.5§
Characteristic cyclic oxidation life [h/h]	1.0-1.31‡	1.59-1.94

The conditions explored in the present study are detailed in Table 3.8. As mentioned in "Aims and objectives" (1.2), PID-controlled pressure (see Submission 2) was not considered as a variable, and was fixed at 5.0x10^{-3}mbar. The actual and [set] beam power for the different materials deposited is respectively - LowK ->26-28 [56] kW & GZO ->24-26 [54] kW. Note that the delivered (actual) power differs considerably from the demanded (set) power. The ingots used had a diameter of 39 mm.

Furnace set temperature refers to the temperature set in the furnace controller for the EBE-150 Coater in Cranfield University. This temperature differs from the surface temperature of the substrates being coated. The substrate temperature was determined by correcting a temperature reading for a thermocouple located next to the substrates. The correction method is discussed in section 1.3.1. in Submission 3.

Table 3.8: Test matrix for the deposition of TBCs. Each dot represents an EB-PVD run on those conditions, for either LowK (magenta) or GZO (grey). The black dot represents pre-existing data for GZO.

	Furnace set temperature [°C]		
Rotation speed [rpm]	1030	730	430
8	● ●	● ●	●
1	● ●	● ●	

3.3 Deposition of model TBCs - LowK & GZO coatings

For the deposition of the LowK and GZO coatings using the different deposition conditions outlined in Table 3.8, two types of substrate were used: Nimonic-75 (N75) squares in the polished "P" condition[3], and Al_2O_3 discs in the as produced condition. Note that, due to availability and cost of single crystal Sapphire discs, polycrystalline discs were used instead. The nomenclature for N75 and polycrystalline Alumina discs used in the present document are, respectively, N75 & AD (Alumina Discs). The nomenclature for the LowK and GZO coatings deposited as it relates to the deposition conditions is presented in Table 3.9.

Table 3.9: Nomenclature and deposition conditions explored in the deposition of LowK and GZO coatings.

System ID	Furnace set T [°C]	Rotation [rpm]
LowK-Nom	1030	8
LowK-LR	1030	1
LowK-LT	730	8
LowK-LT	730	1
LowK-LLT	430	8
GZO-Nom	1030	8
GZO-LR	1030	1
GZO-LT	730	8
GZO-LTLR	730	1

The meaning of the nomenclature used for the "System ID" column in Table 3.9 is as follows: "Nom" - nominal conditions, "LR" - low rotation speed, "LT" - low temperature, "LTLR" - low temperature and rotation, "LLT" - low low temperature.

3.4 Model TBC microstructures

Cross sectional and surface images of the model TBCs produced were captured using a Scanning Electron Microscope. A qualitative assessment of the microstructural features observed for the different deposition conditions and substrates is provided below, and compared to the PVD Structure Zone Models described in Submission 3: "Microstructure quantification". The method detailed in that same Submission is used for the quantitative assessment of the column width evolution in the model TBCs.

For ease of interpretation, a succinct interpretation of the method is provided here, as follows: The cross sectional micrographs of the TBCs to be analyzed are semantically segmented using the trainable WEKA (Waikato Environment for Knowledge Analysis) segmentation (12) algorithm in FIJI (11) (Fiji is Just ImageJ). The boundaries of the ceramic TBC portion of the image are established by analyzing the segmentation results, to confine the subsequent analysis to this area of interest. Horizontal lines are drawn at regular, user-defined intervals within the TBC thickness. A grey value profile plot is produced for each of these horizontal lines, which are subsequently analyzed to detect

[3] see Submission 3

peaks therein. These peaks (maxima or minima, depending on the image contrast) are understood to correspond to the boundaries between columns.

The identification and numbering of the peaks allows to assign column widths for each of the horizontal lines produced through the coating thickness, resulting in a through-thickness profile of the average column widths for a given coating. Different image pre-processing techniques were explored in Submission 3 to improve the identification of the intercolumnar porosity and investigate the sensitivity of the peak finding algorithm parameters to input images. The results obtained through the application of the selected parameters and image pre-processing techniques are detailed in the present Section, comparing them to results obtained manually and through crystallographic characterization of the microstructure.

3.4.1 Qualitative assessment of model TBC microstructures

3.4.1.1 LowK Systems

The corrected homologous substrate temperatures for the model LowK TBC systems deposited is presented in Figure 3.3. Note that substrate temperature is quite consistent for coating runs performed at the same temperature and different rotation speeds. The corrected temperature for the LowK-LLT coating run, however, shows an unusual behaviour in the latter stage of the deposition, with the corrected temperature exceeding that of runs with a higher furnace set temperature, such as - LowK-LT and LowK-LTLR. This may be partly attributed to the coating run parameters falling outside of the thermal survey data. The observed dip in temperature for LowK-LLT correlates with the appearance of "critters" during the evaporation run, outgrowths of ceramic on the edges of the melt pool that can partially obstruct the vapour plume when growing.

The resulting extrapolation may have led to an over-correction of the thermocouple-read temperature. The resulting microstructures, shown in Figure 3.4, however, suggest that a significant temperature increase occurred through the deposition process, resulting in the transition from the fibrous to the columnar morphology exhibited for the top 2/5- 1/3 of the deposited coating. This is particularly clear for the coating deposited on the Alumina disc substrate, where three distinct zones can be observed - see Z1-Z3 in Figure 3.4a. The ranges of homologous temperatures for the different zones are approximately: Z1 - < 0.2; $0.29 \leq$ Z2 ≤ 0.3 Note that the LLT coatings deposited on the N75 substrates displayed extensive delamination after deposition, as shown in Figure 3.4d. This circumstance prevented the testing of LowK-LLT for erosion, explaining its absence from the results presented in Chapter 5.

A difference in the size and shape of the column tips can be observed when comparing the coatings deposited at different conditions and substrates. Looking at the column tips of coatings deposited on both the Alumina and N75 substrates, (see Figures 3.5 and 3.7, respectively) the main difference observed is the rounded column tip morphology observed at lower temperatures, contrasting with the angular tips of columns deposited at high temperature. The coating deposited under nominal conditions on N75 substrates exhibits the characteristic tetragonal pyramid shaped-column tips.

An interesting observation is the apparently wider columns resulting at lower rotation speeds for coatings deposited at high temperature (Figures 3.5b vs. 3.5a and 3.7b vs. 3.7a for Alumina and N75, respectively) as well as the resulting shape anisotropy.

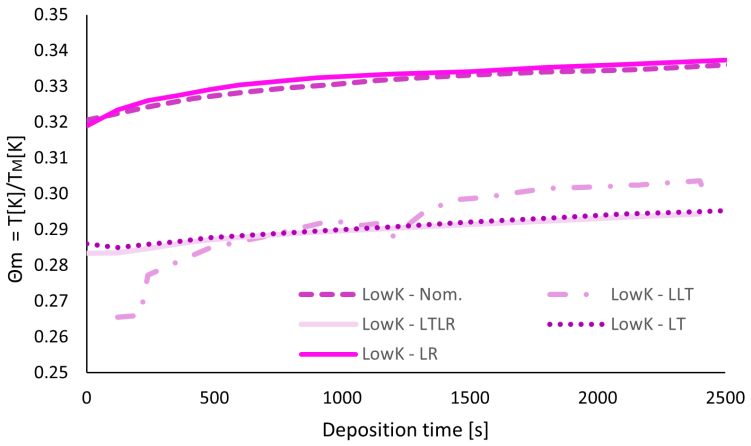
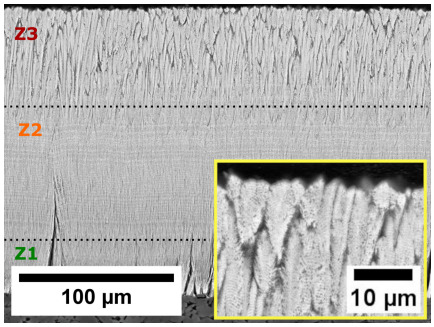
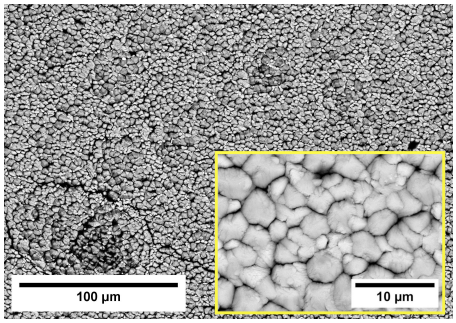


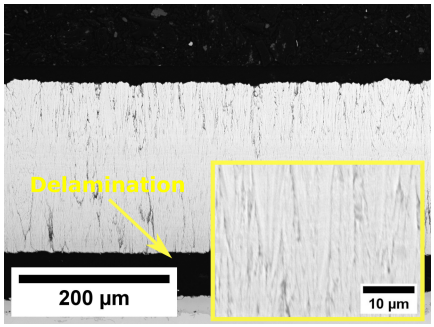
Figure 3.3: Substrate temperature, corrected according to the method detailed in Submission 3, based on thermal survey data.



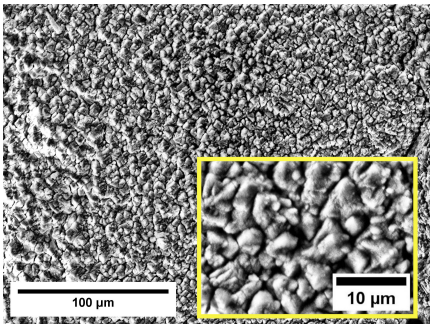
(a) AD - cross section



(b) AD - Surface SEM image



(c) N75 - cross section

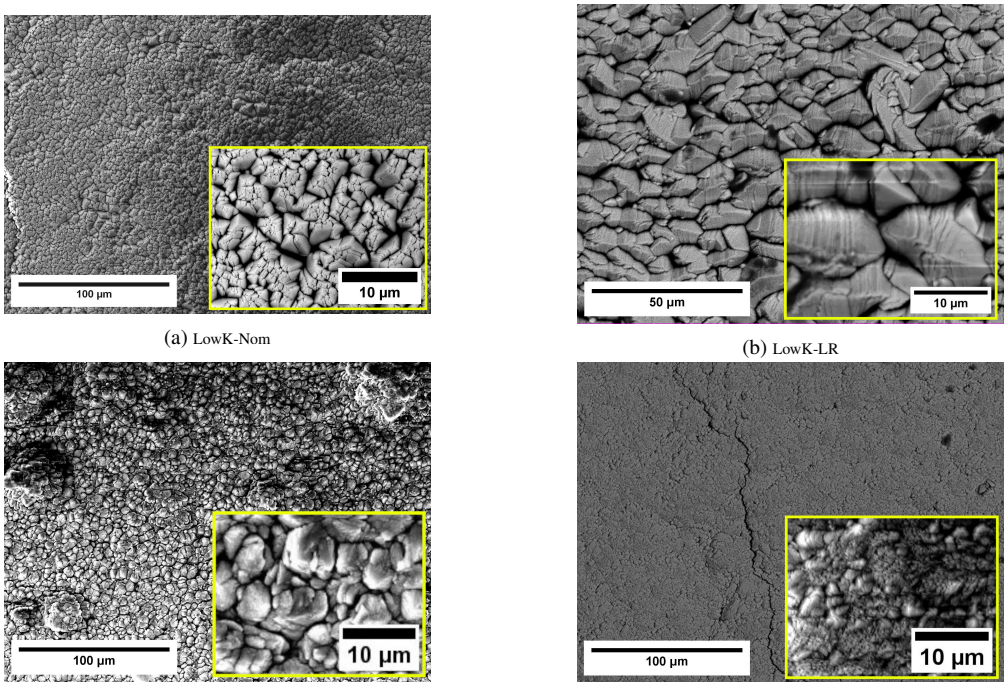


(d) N75 - Surface SEM image

Figure 3.4: Cross section and surface SEM images for the LowK-LLT systems deposited on different substrates

Whereas the LowK-Nom exhibit approximately equiaxed column tips. These tips are better defined in the N75 substrates than in the Alumina substrates, which still show approximately isotropic “sub-tip” clusters. This apparent widening of the columns contrasts with the proposed effect of rotation on the structure-zone models as proposed by Schulz et al. (50), discussed in Submission 3. Looking at the cross sections, depicted in Figures 3.6 and 3.8, wider columns are also observable for the LowK-LR samples, although with an apparently smaller difference in column width.

The effect of lower rotation speeds that is most clearly observable in the cross sectional images is the appearance of a periodic features in the microstructure (Figures 3.6b, 3.6d, 3.8b & 3.8d) . These features correspond to increased porosity zones which seem to correlate



(a) LowK-Nom (b) LowK-LR

(c) LowK-LT (d) LowK-LTLR

Figure 3.5: Coating surface SEM images for the different LowK systems deposited on Alumina discs - inset images show higher magnification details.

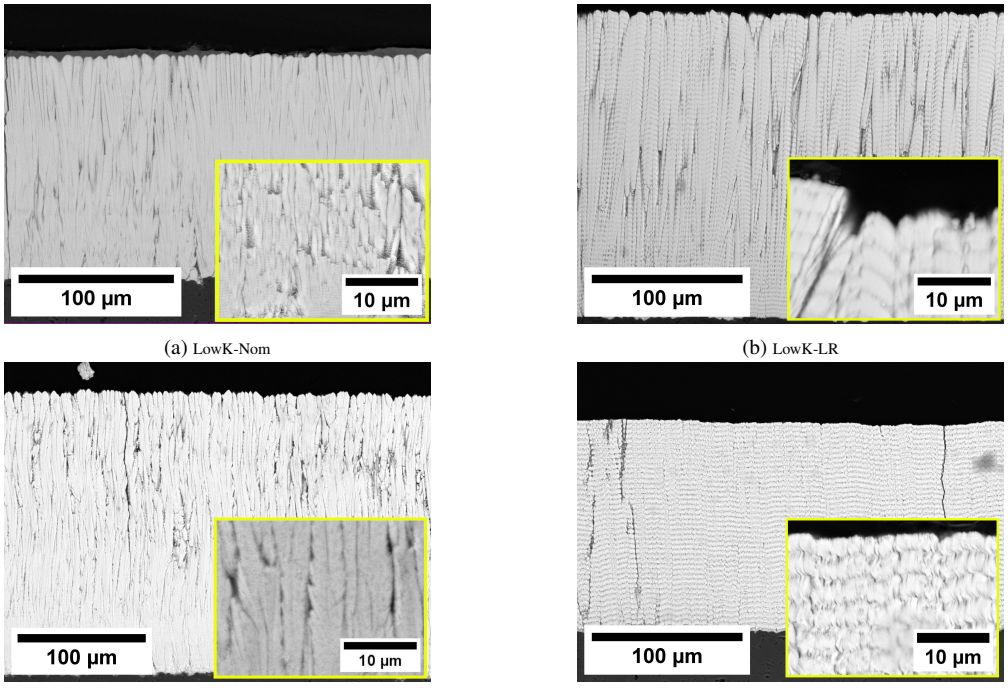
with each rotation cycle. This is confirmed by the fact that the number of these periodic features, for the coatings deposited at 1 RPM correlate with the coating deposition length in minutes. As discussed in Submission 3, the originating cause for this periodic porosity is the line-of sight nature of EB-PVD, combined with the substrate rotation during deposition. When substrates rotate out of the evaporating ceramic plume, a drop in their temperature occurs.

This temperature drop continues until substrate surfaces are again exposed to the vapour cloud, at which point deposition resumes. This resumption at a lower temperature enables less adatom mobility, causing the grains to grow in a disordered state, with embedded porosity. When looking at higher magnification cross-sectional micrographs of the coatings deposited at nominal rotation speed (8RPM) - see Figure 3.8c[4], the same features become apparent, with an increased periodicity and lower contrast. Once again, the number of features correlates with the number of rotations undertook by the samples in the course of the coating deposition, albeit with a lower contrast between the embedded porosity and the solid portion of the growing crystal.

The low rotation-deposited coatings also exhibit a c-shaped periodic morphology in the sections of the coating between adjacent porosity features. This curvature can be explained by the effect of self-shadowing. Again, for a detailed review of the effect of the different process parameters on the predicted microstructural morphology, the reader is referred to Submission 3. The self-shadowing induced by the slow rotation results in subgrains growing in the direction of the incoming vapour flux, hence resulting in a C-shape.

While the coatings deposited at lower temperature seem to exhibit thinner columns, in

[4]The reader is referred to the digital version of this document for improved resolution.



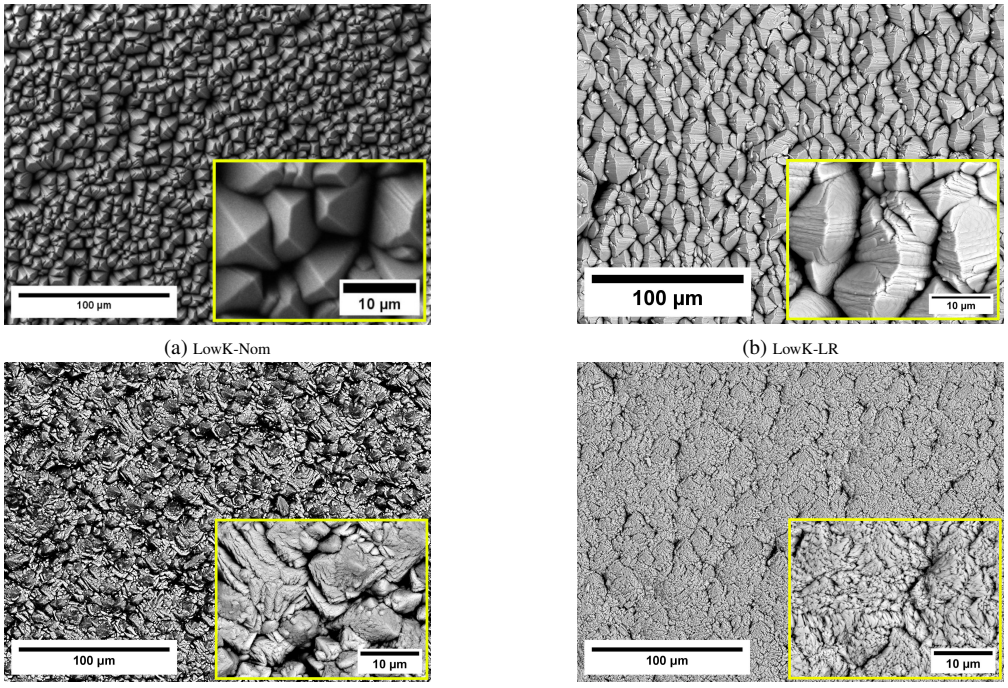
(a) LowK-Nom (b) LowK-LR

(c) LowK-LT (d) LowK-LTLR

Figure 3.6: SEM micrographs of cross sections for the different LowK systems deposited on Alumina discs.

line with the structure zone model predictions, this qualitative evaluation is complicated by the loss of features clearly identifiable as columns, especially in the LTLR coatings. These coatings display features that do not create clear clusters distinct from adjacent material. In cross section the C-shaped or fibrous grains are apparent, originating from the periodic porosity. However, establishing the lateral extent of these grains is challenging. This difficulty is shared by the surface topography images, where triangular facets or crystallites are apparent, but do not result in distinct groups that could be classed as columns. Interestingly, this does not happen for the LLT samples, that, despite the lack of a clear column-like microstructure for the bottom 3/5 to 2/3 of the coating thickness, show clearly distinct columns at the coating surface. This is true both in cross section and in the surface view, even if the column tip morphology is rounded, suggesting these columns consist in a collection of crystallites rather than a single crystal with clearly defined facets.

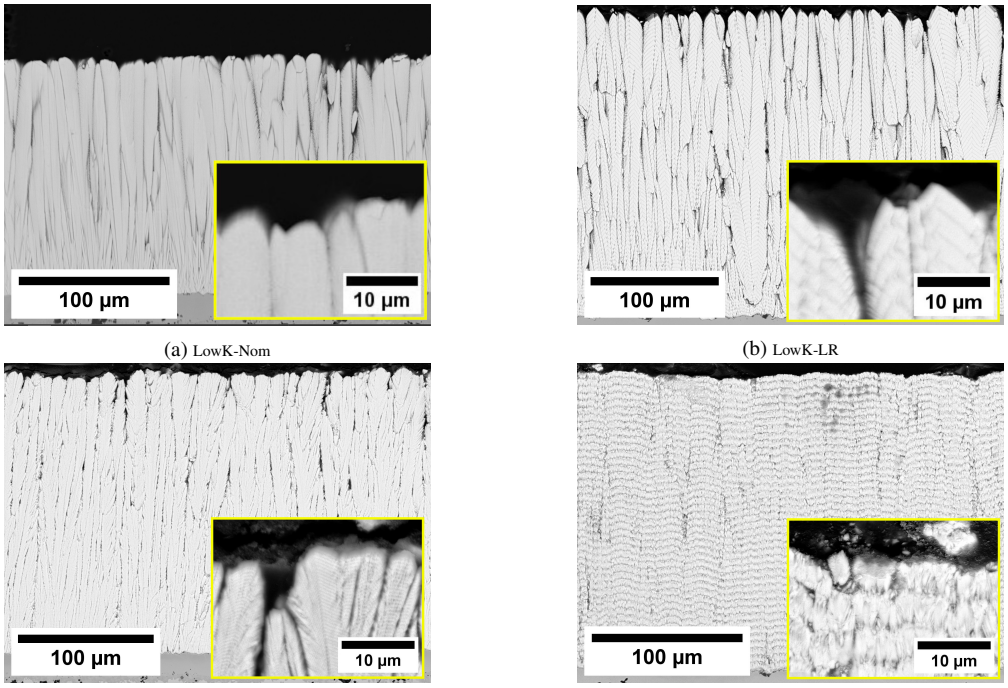
The trend for the column width of coatings deposited on different substrates observed in Submission 3 is also displayed in the model LowK coatings deposited at different conditions. Indeed, the coatings deposited on N75 substrates (e.g. Figure 3.8b) display apparently wider columns and intercolumnar gaps than Alumina discs coated under the same deposition conditions (Figure 3.6b). This has evident implications for the interpretation of test results that depend on microstructural features, when the substrate used for the test differ from the system used in engine operation. Care should therefore be taken when directly comparing test results for coatings deposited on different substrates.



(a) LowK-Nom (b) LowK-LR

(c) LowK-LT (d) LowK-LTLR

Figure 3.7: Coating surface SEM images for the different LowK systems deposited on N75 substrates.



(a) LowK-Nom (b) LowK-LR

(c) LowK-LT (d) LowK-LTLR

Figure 3.8: SEM micrographs of cross sections for the different LowK systems deposited on N75 substrates.

3.4.1.2 GZO Systems

The homologous deposition temperature, corrected to account for thermal survey results, is shown in Figure 3.9. The two-stage homologous temperature evolution exhibited in the deposition of most GZO systems corresponds to the two-layer deposition, expressed

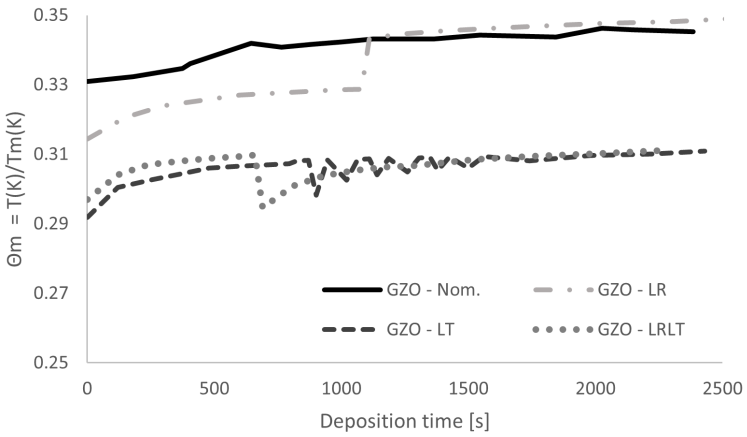
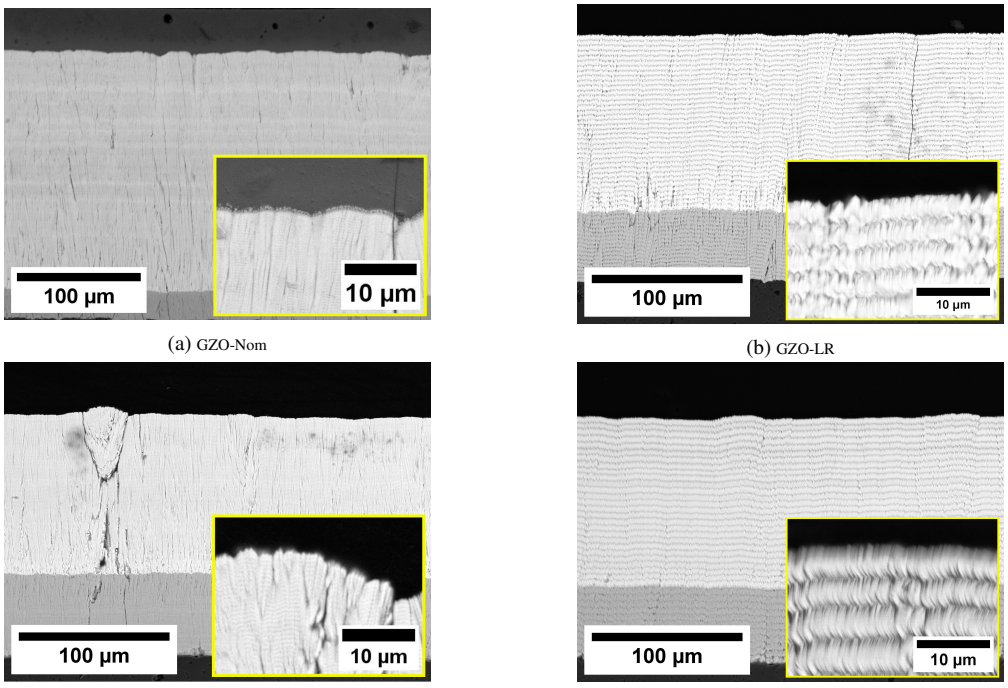


Figure 3.9: Corrected substrate temperature for the depositions of GZO coatings.

through the different melting temperature of GZO (2570°C) compared to LowK/7YSZ (2700°C) (221). The apparent exception for GZO-Nom may be explained by the thin LowK interlayer deposited in this case.



(a) GZO-Nom

(b) GZO-LR

(c) GZO-LT

(d) GZO-LTLR

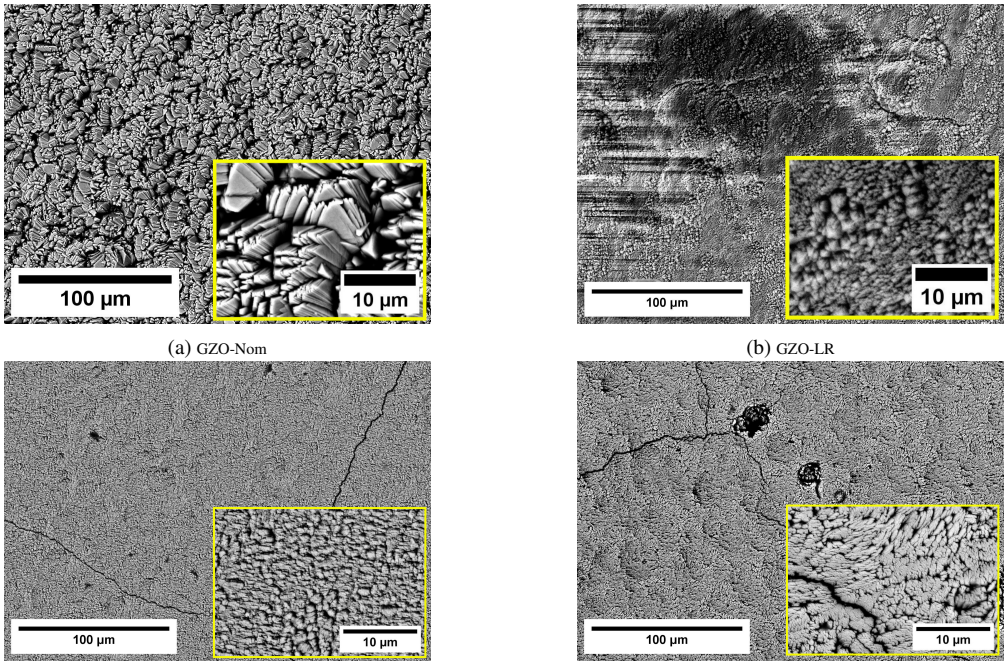
Figure 3.10: SEM micrographs of cross sections for the different GZO systems deposited on Alumina discs.

An interesting observation is the opposite effect of the transition from LowK to GZO at the low (730°C) and high (1030°C) furnace set temperatures. For the low temperature depositions, the homologous temperature shows a decline between the LowK to the GZO layer, while an increase in homologous temperature can be observed for GZO-LR, and to a lesser extent GZO-Nom While the reasons for this difference are not clear, the different thermophysical and radiative properties of GZO and LowK are hypothesized as the cause for this change in evaporation behaviour. The specific heat capacity of GZO and 7YSZ,

for example, diverge significantly at higher temperature, with the Cp of GZO exceeding that of 7YSZ by around 20% at 1000°C (228).

Regardless of these differences, the consistency of the corrected profiles on the GZO layer for equivalent deposition temperatures should be noted. This observation suggests that, the effect of temperature and rotation can separately be evaluated in the deposited systems, as intended in the experimental design.

The microstructures of the deposited model GZO systems are shown for Alumina and N75 in Figures 3.10 through 3.13. For the Alumina substrates, the systems deposited at the nominal rotation speed of 8RPM (GZO-Nom & GZO-LT - Figures 3.10a[5] & 3.10c resp.) display a fine columnar microstructure when observed in cross section, while the low rotation systems (Figures 3.10b & 3.10d) exhibit a microstructural morphology in the form of a collection of fine C-shaped grains. The surface images of the TBCs deposited on Alumina - see Figure 3.11 however, show differences between these systems.



(a) GZO-Nom (b) GZO-LR

(c) GZO-LT (d) GZO-LTLR

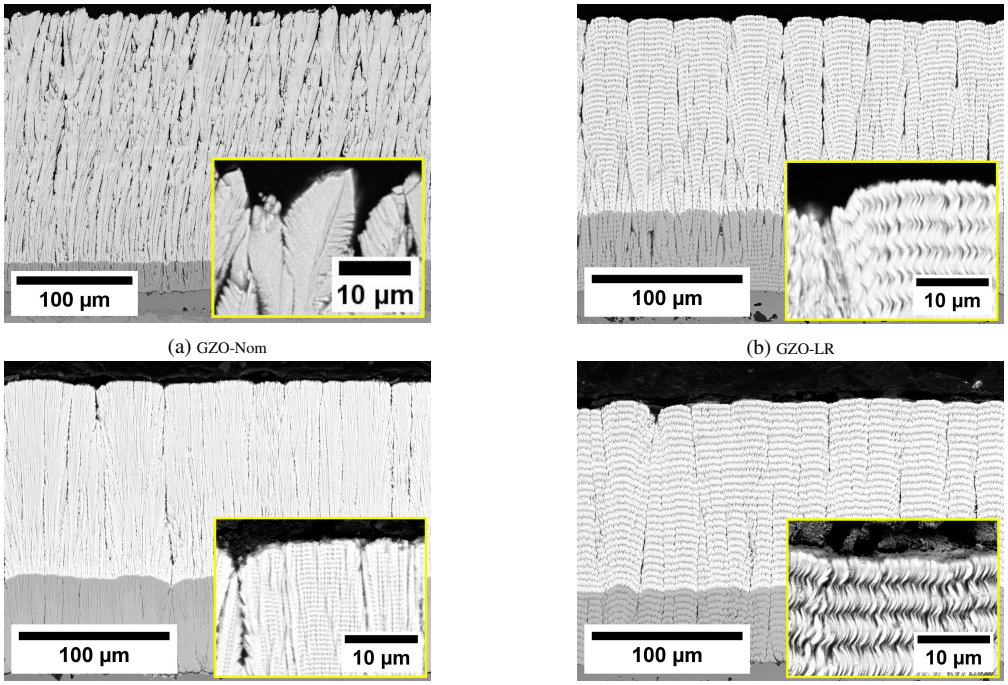
Figure 3.11: Coating surface SEM images for the different GZO systems deposited on Alumina discs. The artefacts in (b) are a consequence of SEM charging.

Among the nominal rotation systems, the surface of the GZO-Nom coating (Figure 3.11b) shows relatively large grains, which appear as a collection of triangular crystalline facets. The GZO-LT system in Figure 3.11c also displays crystals with triangular facets, albeit of a much smaller size. Both the low rotation systems show small crystallites, which seem to adopt a tetragonal pyramidal structure in the GZO-LR coating (Figure 3.11b), while the crystallites in the GZO-LTLR system (Figure 3.11d) seem to coalesce into plate-like elongated column tips.

The coatings deposited on the N75 substrates exhibit a more column-like microstructure for all the deposition conditions. The GZO-Nom coating shows the bent columnar

[5]Note that, due to few available samples for GZO-Nom, the cross section displayed corresponds to a CMAS-tested sample (1250°C, 6 min.)

morphology noted by other authors (166). A clear difference can be observed in the cross sectional micrographs between GZO-Nom and GZO-LT deposited on N75, in contrast with the observation in the systems deposited on Alumina as shown in Figure 3.12. The low rotation versions, however, are remarkably similar in cross section, despite the difference in homologous deposition temperature, with groups of C-shaped grains conforming column-like clusters. The size of these clusters is the most apparent difference, with those in GZO-LR being apparently thicker, with wider inter-cluster pores.

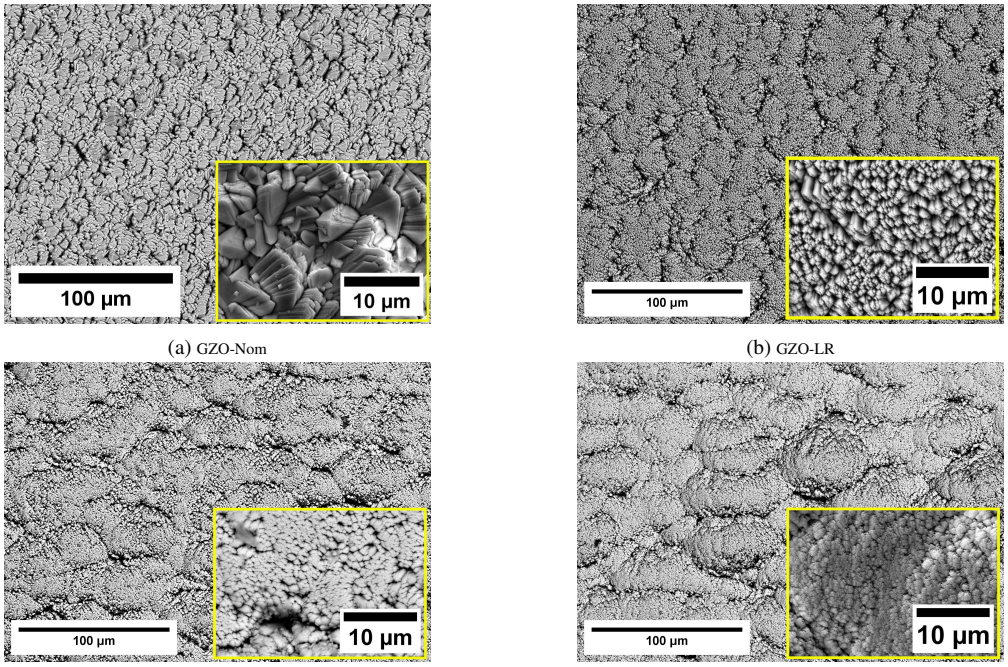


(a) GZO-Nom (b) GZO-LR

(c) GZO-LT (d) GZO-LTLR

Figure 3.12: SEM micrographs of cross sections for the different GZO systems deposited on N75 substrates.

Observing the surface micrographs of the GZO systems deposited on N75 does not yield clearly defined differences. The morphology shown by the column tips of GZO-LT, LR and LTLR consists in small tetragonal faceted crystallites arranged in groups that define the larger scale topography of the coating surface.



(a) GZO-Nom (b) GZO-LR

(c) GZO-LT (d) GZO-LTLR

Figure 3.13: Coating surface SEM images for the different GZO systems deposited on N75 substrate.

3.4.2 Quantitative analysis of model TBC microstructures

The competitive grain growth mechanism described for columnar EB-PVD coatings, at high deposition temperatures, responsible for the development of strong texture as the coating progresses is reinforced, during the practical application of the coating, by a gradual increase of the deposition temperature. This increase over time is caused by the time it takes for the substrates to achieve thermal equilibrium as they transition from the "parked" position, to the centre of the evaporation plume.

The methods detailed in Submission 3 for the quantitative evaluation of porosity and microstructural morphology, in particular, column width, was applied to the model TBCs produced. This enabled getting a numerate description of the evolution of the column width through the coating thickness, as well as the overall porosity value for each of the coatings produced. The developed method will, from this point in the document onwards, be referred as Column Counter (CoCo). A diagram succinctly showing the mechanism for CoCo is shown in Figure 3.14.

The number of columns at different sections (10%, 50% and 90%) in the coating thickness was also counted by human appraisers, to compare the results from manual counting to those obtained by the developed method. Given the time consuming nature of manual counting of columns, only a few selected images were analyzed manually. In order to minimize the bias in the manual counting, images representing the section of the coating to be appraised were produced. These sections, an example of which is shown in Figure 3.15 were assigned at random with the condition that the columns in each section were counted by two different appraisers. Given the observation that coatings deposited on Alumina discs tended to display less clearly defined columns or column-like entities, a single image of a coating deposited on an Alumina substrate (GZO-LTLR) was provided for appraisal, with the rest corresponding to coatings deposited on N75 substrates.

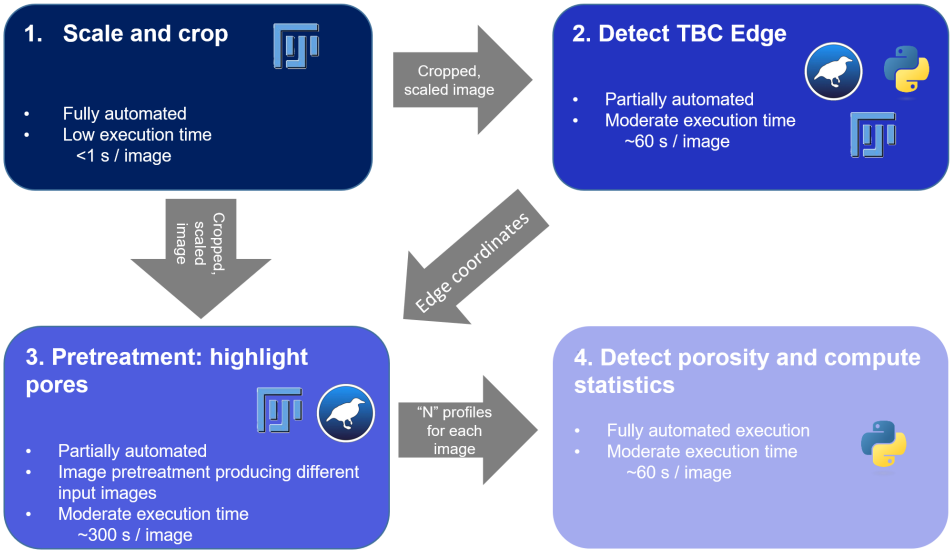


Figure 3.14: Diagram showing the steps in the quantitative evaluation of column width (CoCo). FIJI (11), WEKA (12) and Python were uses at different steps of the project, as indicated by their corresponding logos.

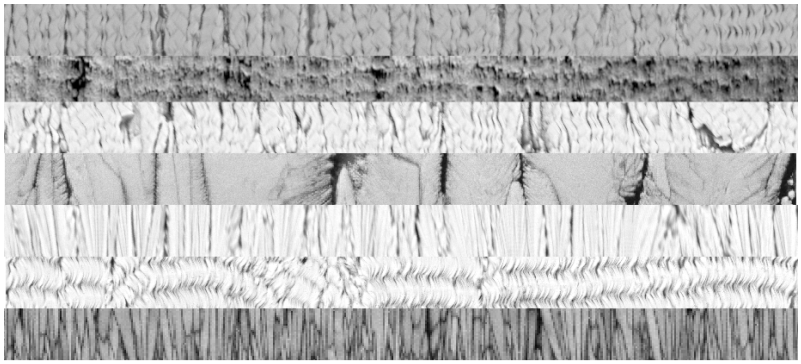


Figure 3.15: Example image sections used for manual appraisal of number of columns.

The results obtained from the quantitative evaluation are presented and discussed in the present Section. The analysis of the results obtained by the image analysis, both manual and through CoCo, is subsequently complemented by crystallographic data-based analysis of the microstructural features, as well as the crystallographic texture.

3.4.2.1 Quantitative analysis of LowK model TBCs

The overall porosity for each of the model LowK TBC systems deposited is detailed in Table 3.10. The column width figure refers to the column width range resulting from a single standard deviation from the average number of columns counted by the different appraisers.

It can be noted that, with the exception of the LowK-LT system, the porosity of the coatings in the Alumina disc is lower than the corresponding system as deposited on N75 substrates. A trend in porosity can also be observed for both substrate materials, whereby porosity increases with deposition temperature, once again with the exception of LowK-LT as deposited on the N75 substrate. These exceptions could point to an underestimation

Table 3.10: LowK coating porosity and column widths at different relative positions in the coating thickness, determined manually. NaN refers to cases where neither of the appraisers was able to resolve and count the columns in the given image. * Means that one of the appraisers could not count any columns.

Sample	Porosity [%]	Column width - 10% [μm]	Column width - 50% [μm]	Column width - 90% [μm]
LowK-Nom (AD)	21.3±4.0	-	-	-
LowK-Nom (N75)	25.8±1.9	NaN	4.02-4.81	4.91-6.70
LowK-LR (AD)	26.3±0.3	-	-	-
LowK-LR (N75)	27.8±0.9	1.98*	2.90-5.55	9.52-14.49
LowK-LT (AD)	18.2±1.5	-	-	-
LowK-LT (N75)	14.3±0.6	1.39-18.50	6.69-14.98	6.05-7.32
LowK-LTLR (AD)	17.0±3.9	-	-	-
LowK-LTLR (N75)	24.2±0.5	8.58-12.87	21.79*	2.78-20.23
LowK-LLT (AD)	14.1±1.0	-	-	-
LowK-LLT (N75)	22.3±1.2	-	-	-

of the porosity in this system, potentially due to an apparently thinner type I porosity and a low contrast between the solid portion of the columns and the type II porosity.

It also interesting to note that, at high deposition temperature, the lower rotation speed results in a higher porosity level only in the coating deposited on Alumina, while N75 apparently remains insensitive to the change in rotation speed. This could be explained by the column "thinning" effect of lower rotation speeds, coupled with the additional porosity resulting from the deposition of the C-shaped grains. In the case of the Alumina discs, which already exhibit a very thin columnar microstructure, the effect of the column thinning does not seem to significantly affect the amount of type I porosity. The additional porosity resulting from the periodic deposition of C-shaped grains, therefore, results in an increased overall porosity. In the case of the N75 deposited coatings, the lower rotation results concurrently in a decrease in the type I porosity resulting from the thinner intercolumnar gaps and the increased type III porosity through the introduction of the periodic porous features. The resulting net effect on the overall porosity seems to be only a small increase.

The broad range yielded by the manual column width measurement is a result of the intrinsic variability of subjective measurement. More specifically, the results are affected by the biases and preconceptions of the appraisers. Taking for instance the column width of LowK-LT deposited on N75 measured at 10% of the coating thickness - see Table 3.10 - the range obtained through manual appraisal of the column width (1.39 to 18.50 μm) reflects the different interpretation used in the appraisal for the concept of "column".

For the same image, appraiser 1 counted 17 columns, while appraiser 2 gave a count of 226 columns. Looking at the corresponding image, Figure 3.16, allows to establish the different conceptions used in the process of counting. Appraiser 1 seems to have used a definition of column to column boundary that required a very clear distinction of the porosity separating the columns, while Appraiser 2 seems to have understood each vertical pore completely separating apparently solid portions to correspond to a column edge. The interpretation of the results is that appraiser 1 counted as single columns what constitute column clusters. This difference in interpretation points to a fundamental difficulty at the heart of quantitative measurement of morphological features by manual means, namely the subjective interpretation of definitions, even when definitions do exist.

An advantage of having obtained column counts using the two different criteria is that an approximation of the cluster size can be made. In order to approximate the number of sub-columns per cluster, the solutions to the problem of packing n circles within a larger circle can be used (229). For the counts of 17 and 226 columns given by the two

appraisers, the average radii ratio is approx. 6.65, yielding a minimum cluster size of at least 35 (230).

For a further illustration of this definitional challenge, one of the appraisers counted the columns for the images provided to them twice, each time using a different criterion of what constituted a column. The first criterion relied in the subjective appearance of a region with "column-like" characteristics. The second criterion was similar to the one described to have likely been adopted by appraiser 2, i.e. counting any vertical pore separating solid portions as a column boundary. The results for the images analyzed by the same appraiser with these two definitions is given in Table 3.11, together with the minimum cluster size determined using the optimal packing of circles (230).

Table 3.11: Counting of columns using different criteria by the same appraiser and minimum cluster size

Image No.	1	2	3	4	5	6	7	8	9	10
Criterion 1	43	22	14	30	36	140	25	9	14	10
Criterion 2	117	98	115	372	219	360	528	9	41	NaN
Min. Cluster size	5	15	55	125	29	5	382	1	7	NaN

Note the significant variation in the cluster size estimated from the optimum packing of the fibres. This result could be interpreted as the relative position in the Zone 2 to Zone T transition, with an increasing cluster size indicating a more fibrous texture, characteristic of Zone T. These results, should, however, be confirmed by confirming cluster sizes, potentially through imaging the polished surface of the produced coatings.

Lastly, even with a consistent understanding and interpretation of the concept of "column", EB-PVD TBCs pose a singular challenge when it comes to the evaluation of their width and other morphological features. This challenge is related on the one hand to the stochastic nature of EB-PVD deposition, which yields microstructures that vary significantly within the same sample, and on the other hand, to the difficulty of characterizing the 3D features of EB-PVD microstructures with sufficient resolution. The latter challenge usually means that a compromise is made whereby the cross sections of EB-PVDs are used as a representative proxy of the entire microstructure. However, the small column sizes exhibited by EB-PVD and their growth in a direction other than the normal to the substrate surface can mean that the cross section plane does not align with the columns being examined. This can result in columns "appearing" and "disappearing" in the section plane, as oblique columns are sectioned by the metallographically prepared plane. This complicates the determination of the entities to be labelled as columns manually, even before factoring in microstructures where the columnar character of the TBC is not as clearly defined.



Figure 3.16: Image section used in the manual appraisal of the number of columns for LowK-LT deposited on N75, at 10% of the thickness.

Using CoCo for measuring the width of the TBC columns overcomes some of these issues by establishing a set of objective and replicable criteria for the identification of intercolumnar boundaries. As detailed in Submission 3, different images were used for determining the location of column boundaries in Alumina and on N75 substrates, to account for the different scale, and, consequently, contrast of the intercolumnar porosity

exhibited by the resulting coatings. The Alumina substrate coatings were analyzed using the WEKA pre-processed image, whereby the TBC portion was further segmented using the trainable WEKA segmentation algorithm to identify the pixels corresponding to porosity. As for the coatings deposited on N75, the inverted + CLAHE (Contrast Limited Adaptive Histogram Equalization) (231) route was used. The values of the peak detection parameters used are listed in Table 3.12.

Table 3.12: Values used for peak detection in the analysis of model TBC systems. *MAD refers to median average deviation. Height and prominence are calculated for each gray value profile (horizontal line) where peaks are to be detected.

Parameter	Values	Unit
Peak distance	0	pixel
Height	median + MAD*	gray value
Prominence	max/5	gray value
Distance between lines	2	[μm]

Figure 3.17 shows the results from the automated column width measurement using the image analysis method for the LowK coatings deposited on Alumina discs. As mentioned in the qualitative assessment of the deposit coating microstructure morphologies, the central area in the LowK-LLT system shows little to no columnar features in the central half of the coating thickness. This is reflected in the large spike shown by this system in the column width vs coating thickness graph.

The results for the rest of the systems analyzed yield little difference except for low values of the through-thickness coordinate. In this zone, typically identified as corresponding to the grain nucleation zone, the coatings deposited at higher temperature show smaller column width values, contrary to expectation. This is, however, likely attributed to the more clearly defined grain boundaries for these systems, that result in more column boundaries being identified as such. Systems deposited at lower temperature, show almost horizontal column thickness profiles, which indicates that the typical two zone microstructure does not develop for these systems.

While this appears to be true for the LowK-LT system, the LowK-LT coating exhibits broader grains at the coating surface when compared to the substrate adjacent area. The result is, therefore, likely due to intra-columnar porosity being counted as column boundaries by CoCo.

The differences between the coatings produced using different deposition conditions become more apparent when looking at the result analysis for N75 substrates. The column widths for the LowK systems deposited on N75, displayed in Figure 3.18 exhibit a larger degree of variation when compared to their counterparts deposited on Alumina substrates. Interestingly, all the coatings, with the exception of LowK-LT display, to a certain degree, the existence of a column width evolution, with the exception of LowK-LTLR. Most of the coatings show a two stage column width vs. thickness coordinate profile with thinner columns in the interface with the substrate and TGO which gradually grow in width with the coating thickness.

The values obtained by the manual measurement of the column width, in Table 3.10 seem to be aligned only for LowK-Nom and the lower half of LowK-LR. For most of the other areas measured, the manually determined width is in excess of the column width measured by CoCo. As already discussed both in the present document and in Submis-

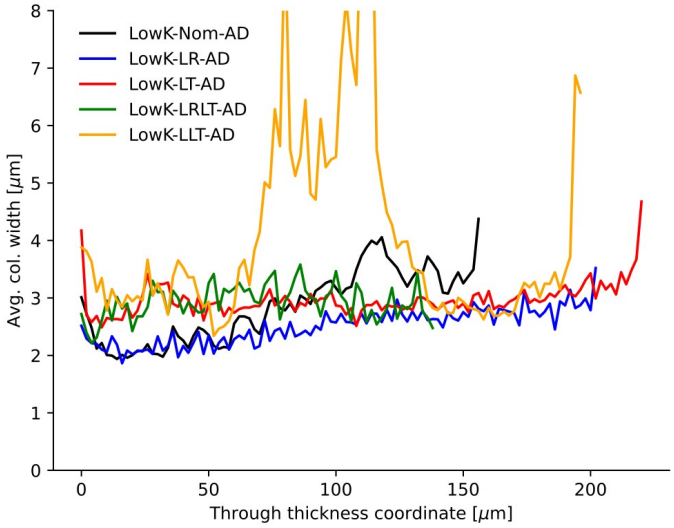


Figure 3.17: Automatic through-thickness column width measurement results for LowK TBC coatings deposited on Alumina discs.

sion 3, this is likely due to CoCo being sensitive enough to characterize intra-columnar porosity as grain boundaries, potentially leading to an underestimation of column width.

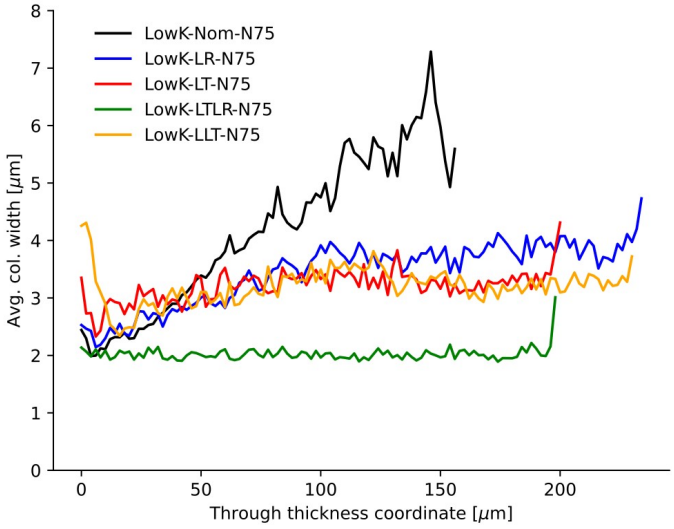


Figure 3.18: Automatic through-thickness column width measurement results for LowK TBC coatings deposited on N75 metallic substrates.

3.4.2.2 Quantitative analysis of GZO model TBCs

A quantitative analysis was also performed for characterizing the microstructures of the GZO/LowK model bilayer systems using both the automated image analysis and manual measurement of column widths. The results of this characterization are detailed below, starting from the porosity and manual appraisal of column width laid out in Table 3.13.

Note that the results presented correspond to the entire coating thickness, and are not confined to the GZO layer.

Table 3.13: Coating porosity and manually determined column widths at different relative thicknesses for GZO coatings. Interpretation as per Table 3.10

Sample	Porosity [%]	Column width - 10% [μm]	Column width - 50% [μm]	Column width - 90% [μm]
GZO-Nom (AD)	24.9±2.2	-	-	-
GZO-Nom (N75)	25.5±1.7	-	-	-
GZO-LR (AD)	20.3±1.6	-	-	-
GZO-LR (N75)	21.8±3.4	4.4-6.7	9.4-14.9	21.8-25.8
GZO-LT (AD)	14.3±2.5	4.3-6.2	4.0-6.9	1.2-13.9
GZO-LT (N75)	15.2±1.2	7.9-11.8	1.8-2.0	8.3-28.3
GZO-LTLR (AD)	16.4±0.8	-	-	-
GZO-LTLR (N75)	21.7±1.2	11.33*	15.7-16.7	14.2*

The differences observed between the coatings deposited on Alumina and N75 substrates for the LowK coatings are largely attenuated for the GZO coatings. The only exception seems to be the "LTLR" system, which conforms to the lower porosity levels for coatings deposited on Alumina discs as compared to N75 substrates observed for the LowK coatings. With regards to the results obtained from the manual measurement of column width, most conform to the expected behaviour of column growth, except for the width measured at the 50% thickness point for "GZO-LT" on N75. However, it is clear that the values obtained for the column width correspond to criterion 1 (i.e. areas showing column-like shape), which each comprise a multitude of what would be considered columns under criterion 2 - material separated from adjacent solid portions by porosity.

Looking at the results obtained through the automated width measurement method, shown in Figures 3.19 and 3.20, confirms this interpretation of the manual results. Since the automated method relies on the detection of porosity, the results yielded by it will be more closely aligned to the interpretation of column provided by criterion 2.

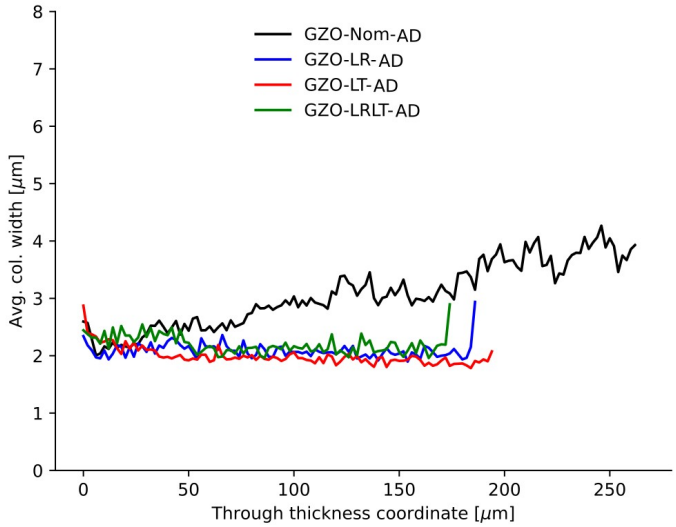


Figure 3.19: Automatic through-thickness column width measurement results for GZO TBC coatings deposited on Alumina discs.

The results obtained for "GZO-LT" deposited on N75 at the 50% coating thickness and the wide ranges obtained for certain results could, with this interpretation, be attributed

to different appraisers applying, consciously or otherwise, different criteria. This, yet again supports the requirement for a consistent method for the determination of coating thickness that can be standardized for use by different research groups, to obtain results that are comparable. At the very least, robust definitions of the criteria used for the manual determination of the morphological features reported should be undertaken.

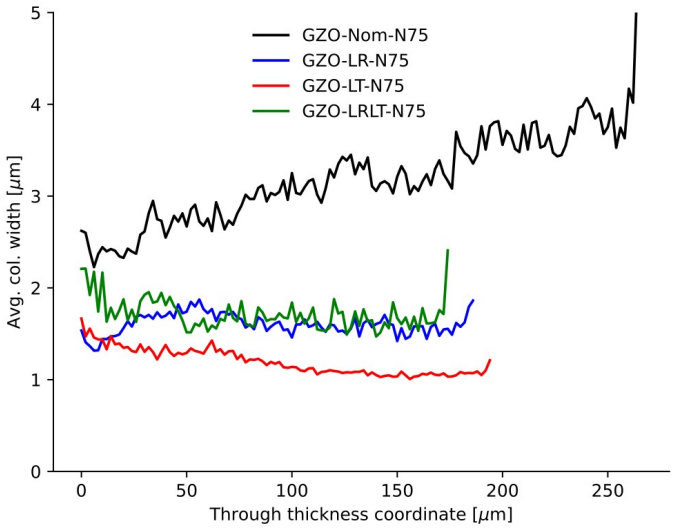


Figure 3.20: Automatic through-thickness column width measurement results for GZO TBC coatings deposited on N75 metallic substrates.

Similar to the results obtained for the LowK systems, clearer differences can be seen between deposition conditions when deposited on N75 as compared to coatings deposited on Alumina substrates. However, in the case of GZO, the two-stage growth mechanism only seems to be shown by "GZO-Nom". As already discussed, given the criterion inherent in CoCo, this does not mean that columns are not growing in width through the coating thickness. Indeed, looking at GZO systems deposited on N75 substrates, shown in 3.12, it could be stated that growth of columns, as interpreted with criterion 1 is indeed occurring throughout the thickness. However, the existence of vertical pores within these columns is detected by the developed method. The results shown suggest that the distance between contiguous pores of this kind remains nearly constant through the coating thickness for all systems except for "GZO-Nom".

These results point to a requirement for the ideal method of column detection, which revolves around not only having a robust definition of column, but also require discerning between intercolumnar porosity and intra-columnar porosity. While this may be feasible for TBCs exhibiting columnar microstructures, with clearly defined column boundaries, the development of such a method for novel materials that may not exhibit such well-defined columnar microstructures would require significant efforts.

3.4.3 Crystallographic study of model TBCs

A method for overcoming the inherent limitations outlined in the previous subsection is the addition of crystallographic data. This can provide an additional criterion to discern between the different columns, even in a situation where based on the microstructural morphology, distinguishing between intra and inter-columnar porosity may be challenging. The additional criterion that could be employed in that situation relates to the crystal orientation.

As described in detail in Submission 3, the deposition of EB-PVD TBC columns results in epitaxial nucleation and growth of crystals. As the growing crystals must capture the incoming vapour flux to grow, the crystals growing from protrusions or aligned in the preferential (i.e. lower surface free energy) crystal orientations outcompete their neighbouring grains. This typically results in the development of a strong crystalline texture. Additionally, this mechanism results in the formation of columns which can be understood as single crystals. This is particularly true for coatings exhibiting a clearly columnar microstructure. Even in cases with a more diffuse columnar microstructure, the expectation is that the growth mechanism will result in zones of grains - the "column - like" regions identified as columns using criterion 1 - with identical or very closely related crystallographic orientation.

To test this hypothesis and attempt to characterize the grain width and size for the deposited coatings, to establish the link between the process parameters and resulting microstructures, a crystallographic investigation of the deposited coatings was undertaken using both X-Ray Diffraction and Electron Back Scattered Diffraction. The crystallographic texture and grain size results, as well as the column widths are assessed and discussed in Sections 3.4.3.1 & 3.4.3.1.

The advantage of EBSD for the investigation of column and crystal size is the ability to acquire crystal orientation and phase data with a spatial resolution able to resolve sub-micron grains with the appropriate sample preparation. EBSD is based on a similar principle to X-Ray diffraction, with some differences. Both methods detect the intensity of radiation diffracted according to Bragg's law. XRD resolves the crystal parameters and phases by interrogating the intensity of X-Rays diffracted at different angles.

By contrast, EBSD captures the size and orientation of the crystalline phase in every pixel by capturing a diffracted beam of electrons as it is projected in a sensor screen. The diffraction pattern takes the form of diffraction bands with a given arrangement in space, which varies from point to point. This arrangement can be analyzed to determine the characteristics of the crystalline phase present. The diffraction bands for each pixel can also be compared to the simulated diffraction pattern for the phase of interest, allowing for faster indexing. Since EBSD can gather data equivalent to a Megapixel (MP) sized image for each pixel in the FoV analysed, the resulting image is significantly more information rich than the electron images. The analysis of EBSD data provides not only crystal orientation and phase ID data, but also pattern misfit. The data gathered can also be used for analyzing strain through different computed quantities, such as dislocation density, grain relative orientation deviation (GROD) or for parent grain reconstruction, for example in the martensitic transformation of steels.

3.4.3.1 LowK model TBCs

An example EBSD orientation map, overlaying the orientation of the tetragonal zirconia phase projected along the Y (through coating thickness) direction, and computed grain boundaries is shown in Figure 3.21. In the interest of space, this Figure is used as an illustrative example of the LowK systems, with the other EBSD orientation maps provided in Appendix B.

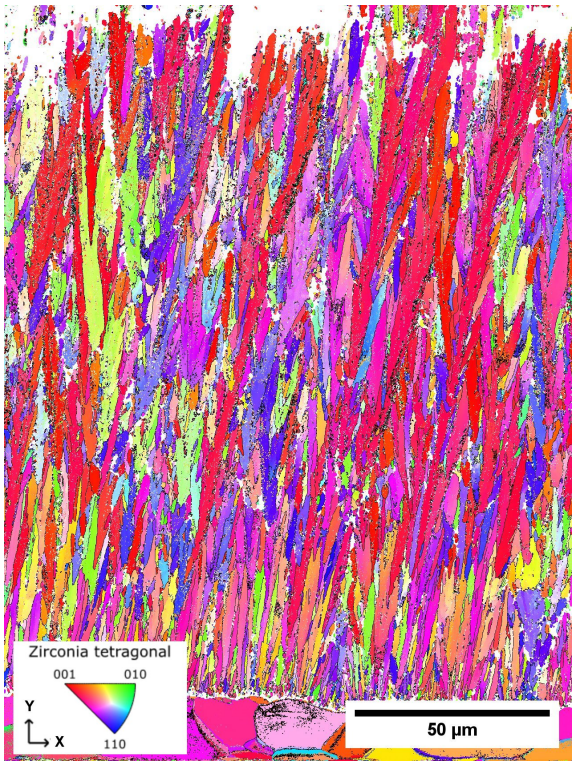


Figure 3.21: Orientation map (Y axis Inverse Pole Figure) of tetragonal zirconia for the LowK-LT system deposited on N75. The legend at the bottom left provides a guide to the crystallographic orientation colour code and sample coordinate system.

As can be seen in the orientation map, the classification of the pixels by crystal orientation allows for an easier identification of grains by grouping contiguous areas with a close orientation alignment. Note that the orientation map only displays the projection of the crystallographic orientation with regard to the Y axis. This is useful to qualitatively assess, at a glance, the level of texture of a coating[6]. However, areas aligned in a given axis could belong to different grains, misaligned with respect to each other in the other two axes.

Computing the misalignment between two grains, areas or pixels requires describing their relative orientation in three dimensional space. This is expressed through the rotation matrix R, as described in equation 3.1.

$$R = \begin{bmatrix} \omega_{11} & \omega_{12} & \omega_{13} \\ \omega_{21} & \omega_{22} & \omega_{23} \\ \omega_{31} & \omega_{32} & \omega_{33} \end{bmatrix} \tag{3.1}$$

[6]Highly textured coatings would be a close-to-monochrome

The three dimensional rotation described by the rotation matrix can be reduced to a rotation around the eigenvector $\hat{u}$ of matrix R of a given magnitude θ, representing the three dimensional misalignment, or rotation angle between the two areas being considered. For a non-symmetric rotation matrix, $\hat{u}$ and θ can be calculated using equations 3.2 and 3.3

$$\hat{u} = (\omega_{32} - \omega_{23}), (\omega_{13} - \omega_{31}), (\omega_{21} - \omega_{12}) \tag{3.2}$$

$$2 \cdot cos(\theta) = Tr(R) - 1 = (\omega_{11} + \omega_{22} + \omega_{33}) - 1 \tag{3.3}$$

Most crystallographic analysis software determines grain boundaries based on identifying areas where misalignment between pixels exceeds a user defined threshold value. A value of 5°was selected for the determination of grain boundaries and subsequent crystal size analysis. Figure 3.22 shows the grain boundaries determined based on this 5°misalignment for coating LowK-LT deposited on N75.

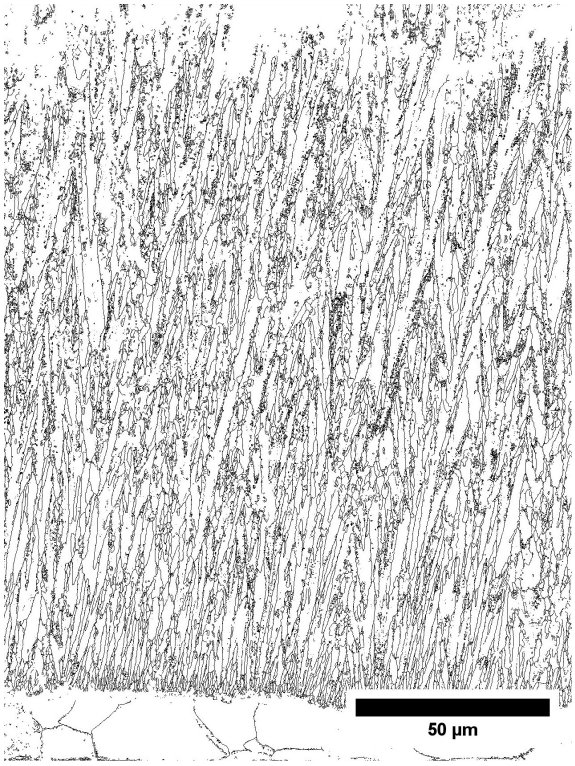


Figure 3.22: Grain boundary map for LowK-LT coating on N75, constructed using the EBSD data presented in Figure 3.21.

The well-defined grain boundaries constructed based on the crystallographic orientation data provide, in theory an ideal input for the measurement of the through thickness column width using the method for the quantitative analysis of model TBCs described in Submission 3 and discussed in the present Section. The results obtained for LowK systems deposited on N75 substrates using the grain boundary data is presented in Figure 3.23.

It is immediately evident that CoCo yields unreliable results when directly using the grain boundary data. This could be explained by the noise introduced in the grain boundary map by small crystallites or areas identified as separate small grains, apparent in

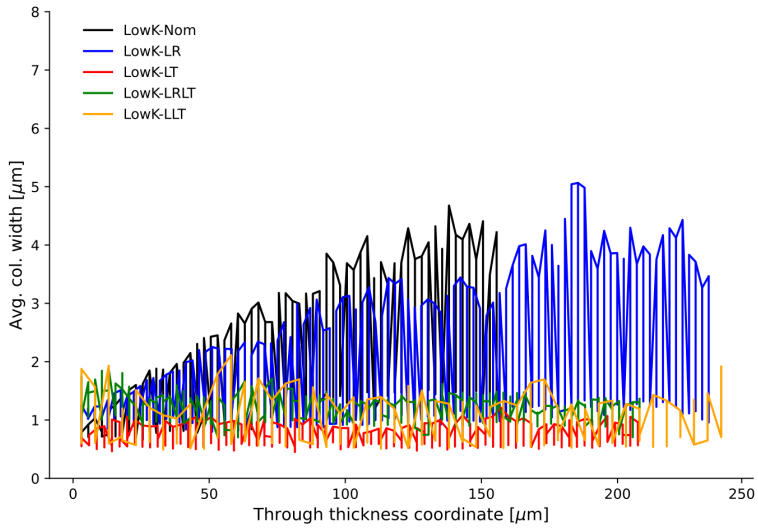


Figure 3.23: Column width result for LowK systems deposited on N75, determined using CoCo.

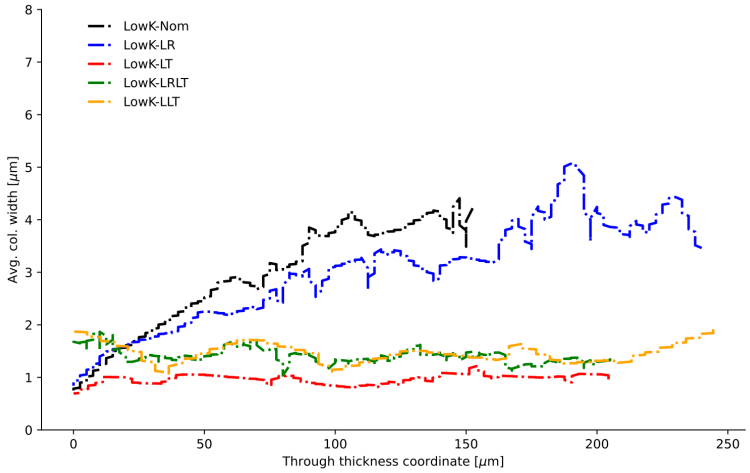
Figure 3.22. These small grains appear despite data post-processing and cleaning steps used to minimize their appearance, including correction for pseudo-symmetry, commonly occurring in tetragonal zirconia.

It should be mentioned at this point that accurate indexing and orientation rely on the quality of the surface preparation with flat surfaces being preferred for signal quality. Additionally, high beam currents increase the signal intensity and improve acquisition speed. Porous ceramic systems such as TBCs exhibit low conductivity and abundant surface imperfections, this can result in low band contrast, particularly around column edges. This low band contrast can result in misorientation of the detected crystallographic phase, which in turn can lead to the detection of grain boundaries around the misoriented datapoints. Indeed, a significant proportion of the small grains in the grain boundary map in Figure 3.22 appears to be either on the boundaries of larger grains or aligned with them.

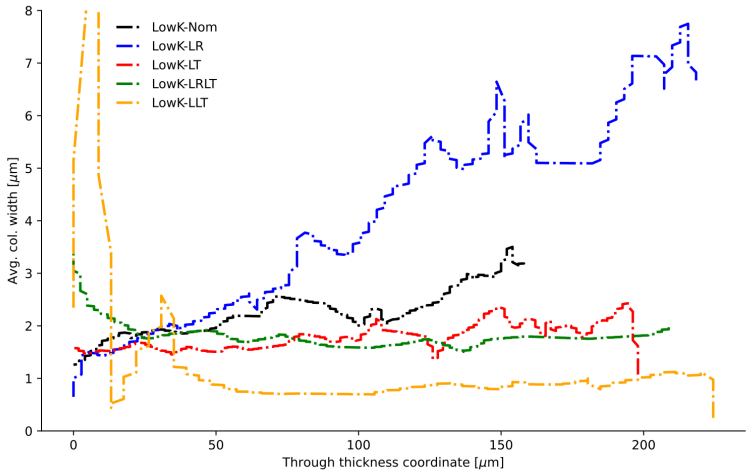
The binary (peak-trough) nature of the column width profile shown in Figure 3.22, suggests that the troughs correspond to points where the coating thickness is encountering a disproportionate amount of these small grains, leading to a significant under-measurement of the column width. It should be noted that the upper envelope in the profiles probably also correspond to an under-measurement of column width, albeit not to the same extent as that of the troughs, as a number of small grains will also be measured along with the large grains.

The method adopted for correcting the EBSD grain boundary-based column width profiles consisted in the calculation of the upper envelope of the calculated profiles This upper envelope was determined by detecting the peaks on each profile and linear interpolation of the resulting peak points. The results for the lowK system are presented in Figure 3.24.

In the case of the coatings deposited on N75, there is a significant correlation between the column width measured by CoCo as applied to the electron images and the EBSD grain boundary data. The observable differences are most apparent for the LT and LLT systems. Interestingly, the column widths measured using the EBSD data for these



(a) N75



(b) Alumina substrate

Figure 3.24: Column widths measured using the automated method developed and EBSD-grain boundary data, deposited on different substrate materials. The profile is corrected based on an interpolation of the upper envelope of the profiles shown in Figure 3.23.

systems are smaller than the ones measured in the electron images using CoCo.

As the reader may recall, this result conflicts with the expected outcome of the column width analysis based on crystallographic data. The thinner than expected results obtained from the quantitative evaluation of the microstructures based on grayscale images was attributed to the different criteria used for the definition of column. The automated method developed intrinsically uses a broader definition of column boundary that is likely to detect intracolumnar as well as intercolumnar porosity as column boundaries. The results obtained through crystallographic analysis seem to suggest that this criterion may, in part be correct, and that the more qualitative criterion, based on regions presenting "column like" morphologies may count groups of distinct crystallographic grains as single columns.

One caveat to this hypothesis is the aforementioned small crystallites, which may have caused a significant underestimation of column width, particularly for systems with

a more typical columnar morphology. While the presence of these seemingly randomly occurring small crystals, and the detection of their boundaries could indeed be diminishing the apparent column width, the author proposes that the overall trend in the column width both between systems and through the coating thickness measured are representative of the the grain width evolution. Additionally, it is hypothesized that the results obtained from the automated method represent the actual grain sizes more accurately.

This hypothesis is based on the observed variability of the un-treated EBSD data presented in Figure 3.23. It can be noted that the presence of large numbers of spurious small crystallites is displayed in the form of troughs. The number of spurious grains at a given height through the coating is expected to follow a normal distribution, since it results from randomly occurring erroneous assignation of orientation to pixels around surface defects, which are also distributed randomly.

An inverse relation exists between the number of grains and the average column width. This means that the column width would be relatively insensitive to additional grains in areas with large numbers of grains. This manifests as a relatively stable height of the lower envelope of the resulting profile. Conversely, the sensitivity of column width to changes in the number of grains would increase for lower numbers of spurious grains. However, as the proportion of spurious to actual grains is reduced, the measured width of the column would tend towards the width corresponding only to the actual width. The seemingly continuous shapes of the upper envelope of the signal suggest that a proportionally small number of spurious grains are affecting the measurement.

To probe this hypothesis, 10 grains of each of the LowK systems were manually measured using the grains apparent in the IPF maps at approximately 90% of the coating thickness, deliberately ignoring the spurious crystallites. The results of these measurements were compared to the EBSD-derived automated measurement at the equivalent relative thickness, and are presented in Table 3.14.

Table 3.14: Comparison of column measurement results, evaluated at 90% of the coating thickness for the LowK model TBCs.

Coating system	Substrate	Column width [μm] (Manually measured)	Column width [μm] (CoCo)
LowK-Nom	AD	4.8±0.6	3.0±0.3
	N75	7.2±1.0	4.1±0.2
LowK-LR	AD	6.9±1.5	7.0±0.8
	N75	6.3±1.1	4.0±0.4
LowK-LT	AD	3.9±1.3	2.1±0.3
	N75	2.9±1.1	1.0±0.0
LowK-LTLR	AD	2.2±0.8	1.8±0.1
	N75	3.5±0.7	1.3±0.1
LowK-LLT	AD	1.6±0.5	1.1±0.1
	N75	3.0±0.5	1.6±0.1

It can be noted that column widths determined by CoCo represent typically over half of the manually measured values, as shown in Figure 3.25. Two notable exceptions are LowK-LT and LowK-LTLR deposited on N75. For these systems, the automated method using EBSD grain boundary data yields about a third of the manually measured value. Even with those exceptions, the hypothesis that the relative column width across systems

and the column width evolution through the coating thickness is captured with an accuracy of an order of magnitude by CoCo, and is considered valid, based on these results.

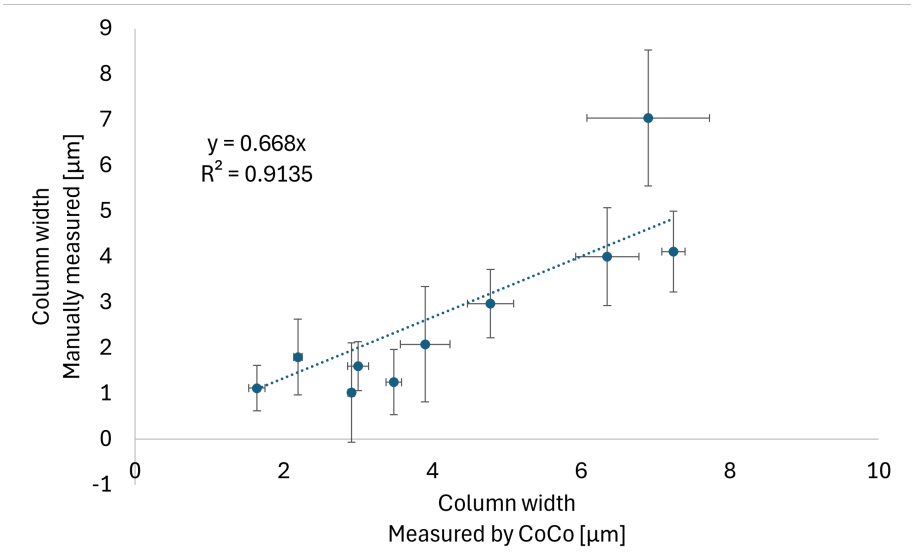
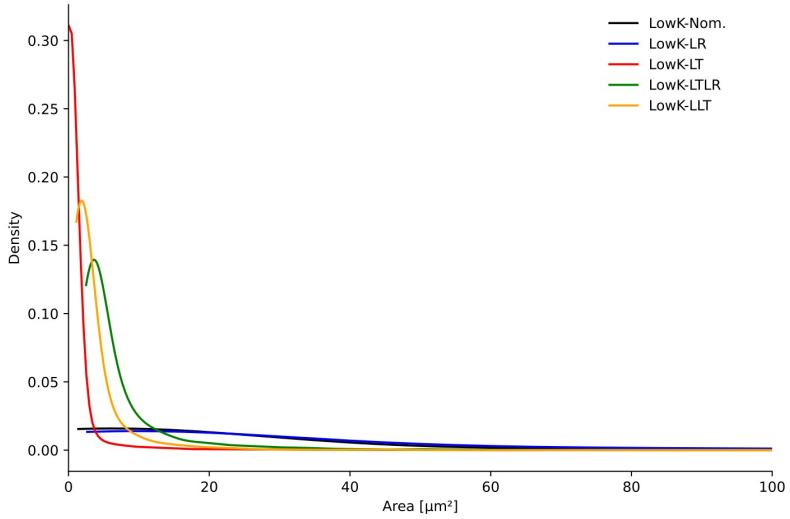


Figure 3.25: Column widths determined manually vs. using CoCo.

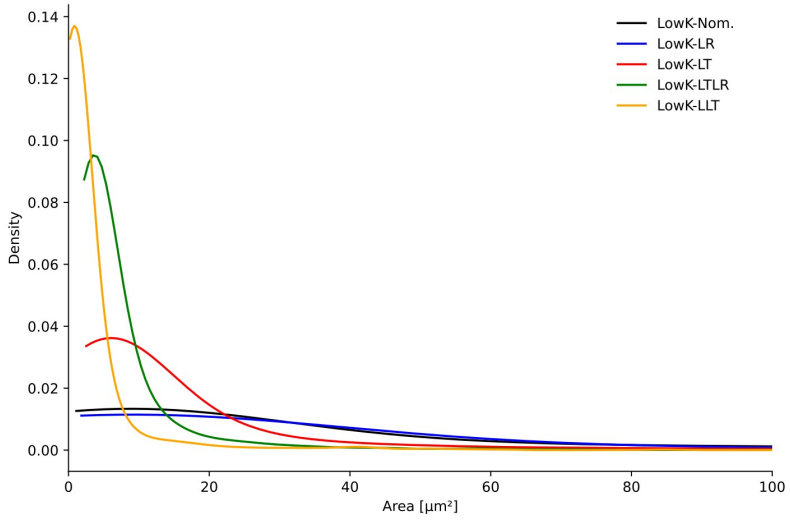
Using the EBSD-data based automated method on the model coatings deposited on Alumina discs results in cross-system differences that were not detected when analyzing the electron images. The relative ranking for the different systems seems to change, relative to the coatings deposited on N75 substrates, with the coating deposited on Low Rotation conditions exhibiting the wider columns. A common feature between both substrates is the reduced relative width of the columns for coatings deposited at lower temperature. Rotation appears to have a temperature dependent behaviour, increasing column width at high temperature, and reducing it at lower deposition temperatures. This behaviour is the inverse of the one observed for the coating systems deposited on Nimonic 75. This divergent behaviour suggests a strong effect of the deposition substrate on the dependence of the microstructural morphology on the deposition conditions.

The EBSD data gathered can also be used for other morphological and crystallographic assessments of the produced systems. An interesting variable to analyze, to complement the column width, is the size of the grains, measured by their area in cross section. In the context of TBCs deposited under different conditions, with the corresponding variation in the balance between the driving forces for crystal nucleation and growth, analyzing grain size can provide an insight into the behaviour exhibited by the model TBCs with regards to the failure modes induced by testing. The crystallographic grains detected were filtered to delete any spurious grains. A common criterion for computing grain size statistics is that grains to be included should have a minimum area of 10 pixels. Kernel Density Estimation (KDE) of the resulting particle size histogram was undertaken to compare the probability density estimation of the grain sizes for the deposited coatings. The results obtained for the LowK systems are summarized in Figure 3.26

The grain size distribution for all the systems, with the exception of LowK-LT exhibit a remarkably similar behaviour for both substrates. The systems deposited at high temperature - LowK-Nom and Lowk-LR - show an almost identical distribution in grain sizes. Lower deposition temperatures favour nucleation, resulting in smaller grain sizes. Lower



(a) N75



(b) Alumina substrate

Figure 3.26: Kernel Density Estimations for the grain size of LowK systems deposited on different substrates.

rotation speed increases the adatoms deposited on less stable lattice sites (50), which also increases the driving force for recrystallization. The grain size distributions for the coatings deposited on Alumina discs at low temperature behave as expected based on these rotation speed and deposition temperature effects, which compound for the LTLR system, curtailing grain growth. This effect is further observed for the LowK-LLT systems, which exhibit a grain size distribution on the lower end of the systems analyzed. The exception shown by LowK-LT deposited on N75 is likely explained by the oblique sectioning of the coating, which is shown by the absence of grains spanning the coating thickness in Figure 3.21. In contrast, the LowK-LT coating deposited on the Alumina disc, shown in Figure 3.27, clearly exhibits grains that span, if not the entire coating thickness, a signifi-

cant proportion of it.

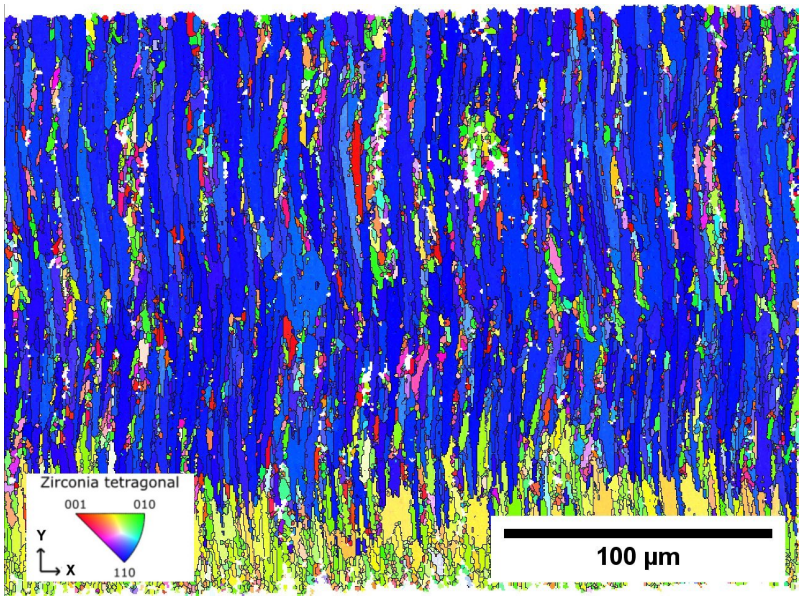


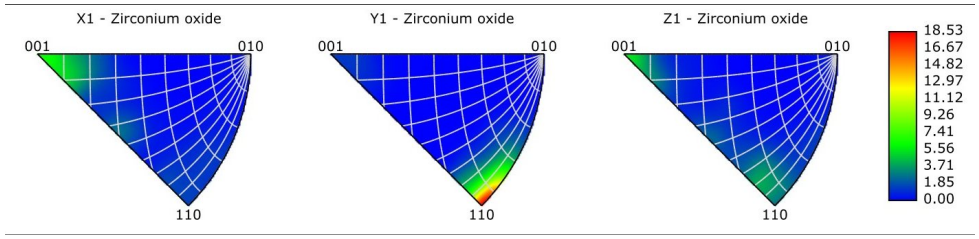
Figure 3.27: Orientation map of tetragonal zirconia for the LowK-LT system deposited on AD.

Crystallographic texture, the extent to which different grains align in a preferred spatial orientation and the preferential crystallographic orientation play an important role in defining the behaviour of polycrystalline materials, especially those with anisotropic crystal structures. TBCs deposited by EB-PVD have been shown to develop a strong crystallographic texture when deposited under "Nominal" conditions, i.e. at high temperature and rotation speed. The orientation data for each of the phases measured in a given EBSD map can be used to qualitatively and quantitatively assess the texture and preferential crystallographic orientation.

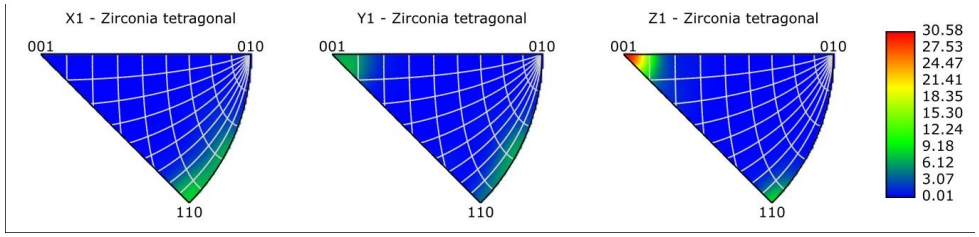
The qualitative assessment is performed through the generation of Inverse Pole Figures (IPFs). These IPFs are generated by plotting the crystallographic orientation of each pixel, projected in each of the spatial directions (X, Y, Z) defined on the sample, over the stereographic triangle projection of the crystal system (232, 233). The X and Y directions of the frame defined for the acquisition of EBSD data is shown in Figure 3.27, with Z following the right-handed convention for a Cartesian reference frame. in Figure 3.28 shows the inverse pole figures for LowK systems deposited on Alumina discs, while Figure 3.29 shows the corresponding IPFs for N75 substrate.

When observing the IPF for the projection along the Y axis as defined by the sample reference frame, it can be seen that the Nominal and LT systems in the Alumina discs, and Nominal and LR systems on N75 substrates, show a strong preference for the <110> direction. This is consistent with the strong texture detected for 7YSZ systems in nominal conditions, presented in Submission 3. The rest of the systems exhibit at least another orientation in the Y axis, with some showing a very diffuse IPF heat map, corresponding to a highly random crystallographic grain orientation.

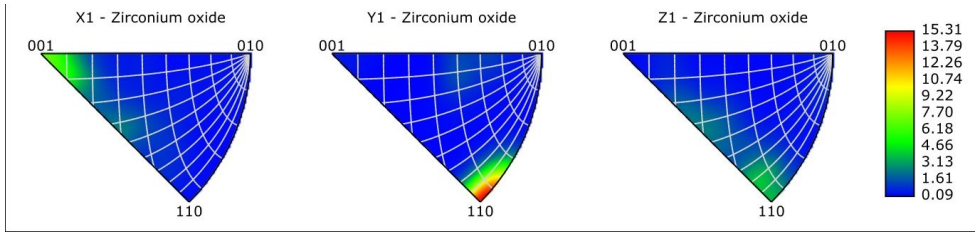
A specially interesting observation is the striking difference in the IPF for the LowK-LT system for the coating deposited on Alumina when compared to its Nimonic-75 counterpart. While the Alumina-deposited coating exhibits a strong texture, as shown by the polarized IPF, the coating deposited on N75 displays a diffuse IPF.



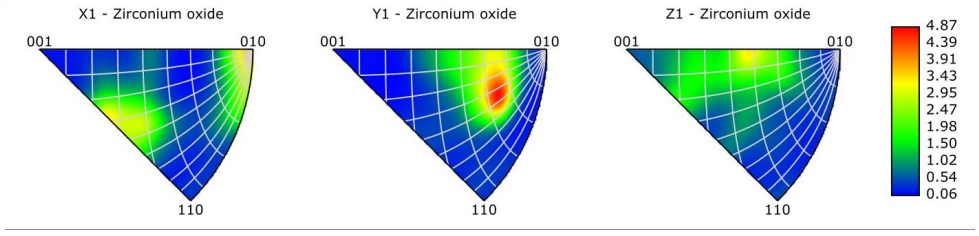
(a) LowK-Nom



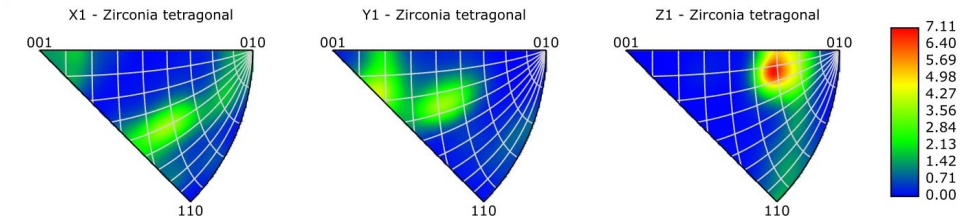
(b) LowK-LR



(c) LowK-LT



(d) LowK-LTLR

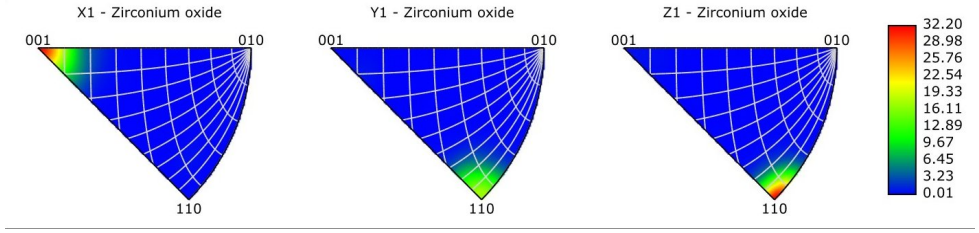


(e) LowK-LLT

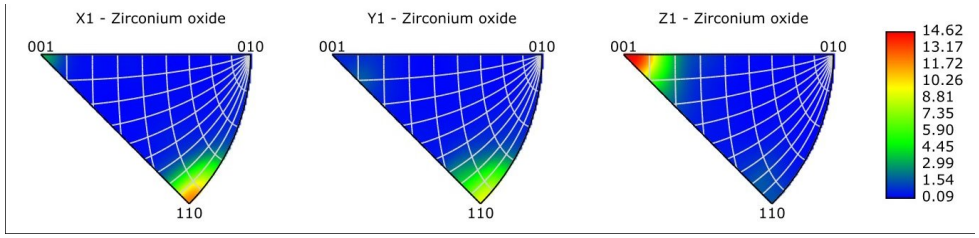
Figure 3.28: Inverse Pole Figures for LowK coatings deposited on Alumina discs.

It should be noted that this analysis is qualitative, especially considering the difference in the heat map scale bar, and the fact that the displayed values correspond to all three IPFs in the X, Y and Z orientations. A more quantitative measure of texture and preferential orientation is provided in Table 3.15. The preferential orientations and corresponding IPF intensities are recorded, and an overall measure of texture, given by the texture index J (233) is provided.

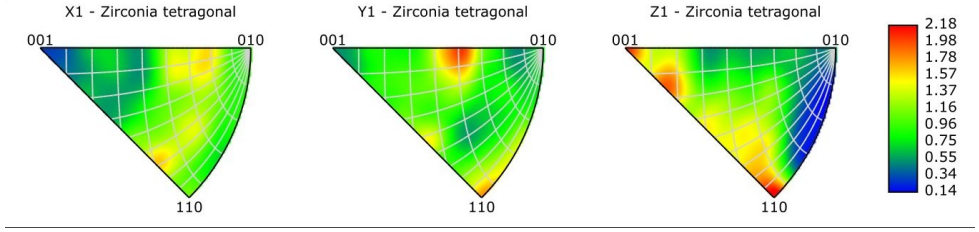
For a succinct interpretation of the meaning of the texture J-index, the Orientation Distribution Function (ODF) must first be understood. Given an orientation g in space, the ODF(g) gives the volume or area percentage of crystals that are aligned with g. The



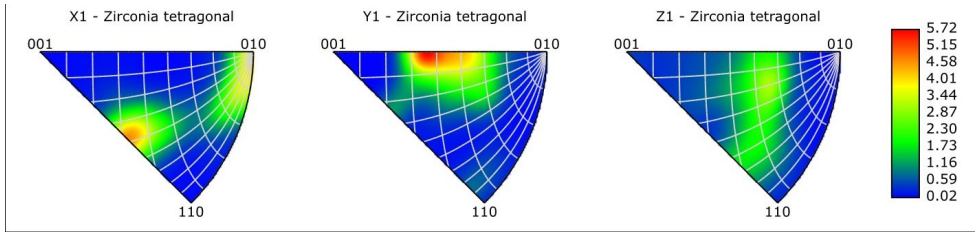
(a) LowK-Nom



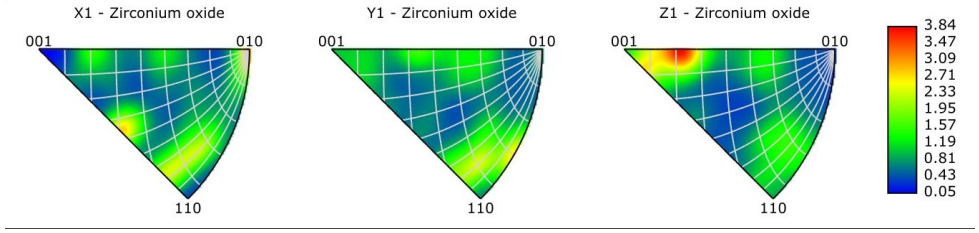
(b) LowK-LR



(c) LowK-LT



(d) LowK-LTLR



(e) LowK-LLT

Figure 3.29: Inverse Pole Figures for LowK coatings deposited on N75.

ODF of a untextured polycrystalline sample is considered as 1. The ODF for a given orientation can therefore be considered as the equivalent to the multiplier of the random distribution, meaning that the frequency of grains showing orientation g are ODF times that expected in a randomly textured sample. The texture index is obtained by integrating the ODF for all the crystal orientations present in the sample. The intensity of the IPF orientation can be interpreted as analogous to the relative XRD peak intensity for different crystalline orientations.

It is interesting to observe, once again, that significant differences in the preferred orientations and degree of texture that are exhibited by the two substrates investigated. In

Table 3.15: Preferred orientations and intensities obtained for tetragonal zirconia from IPFs for LowK coating systems and corresponding J-index for crystallographic texture.

Coating system	Substrate	IPF orientation (Corresponding intensity)	Texture J-index
LowK-Nom	AD	<110> (18.53)	13.62
	N75	<110> (17.21)	52.93
LowK-LR	AD	<001> (6.82) <120> (6.77)	36.04
	N75	<110> (9.34)	15.18
LowK-LT	AD	<110> (15.31)	14.81
	N75	<032> (2.02) <110> (1.82)	3.35
LowK-LTLR	AD	<141> (4.87)	10.89
	N75	<011> (5.72)	10.14
LowK-LLT	AD	<112> (4.28) <243> (3.58)	37.08
	N75	<020> (2.33) <120> (2.22)	11.05

the case of the Alumina substrate-deposited coatings, the maximum texture is shown by the LR and LLT systems. In the latter case, this is likely as a result of the small crystals in the nucleation zone being too small to be resolved, as shown by Figure 3.30. This unresolved area is also the likely cause for the large spike in the column width featured by Figure 3.24b, as very few boundaries will be detected.

The result obtained for the Low rotation system, however, seems to align with the results obtained for the grain size and column width, as well as the qualitative assessment of the surface appearance of the coating, which displays large column tips. The results also suggests that self shadowing promoted by the slow rotation modifies the preferred growth direction in Alumina. The rest of the systems deposited on Alumina substrates display a reasonable texture with the LTLR and LLT systems also showing a modified preferential growth direction.

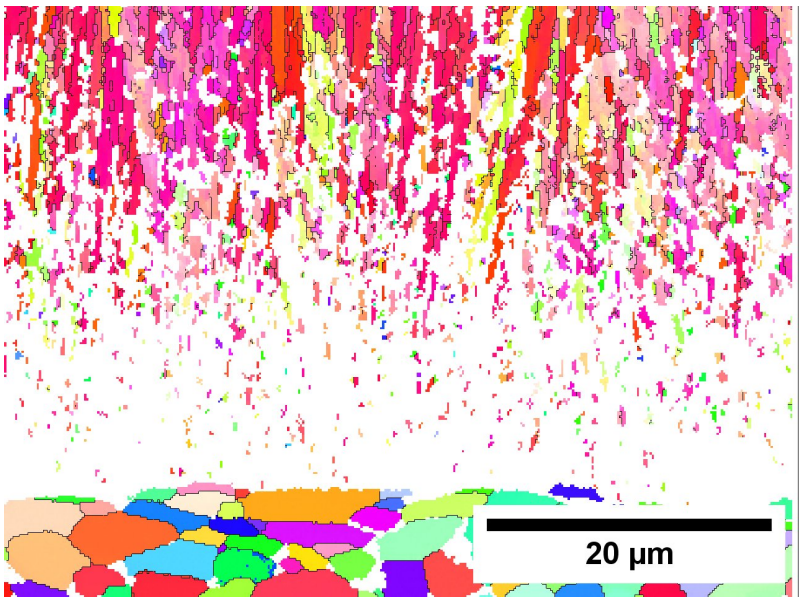


Figure 3.30: Detail of LowK-LLT map for the coating deposited on Alumina showing the large unresolved area around the nucleation zone.

For the coatings deposited on N75 substrates, the self shadowing due to the reduced rotation speed does not seem to be sufficient to promote a change in the preferential growth direction of the grains at high temperature, instead resulting in a reduced texture compared to nominal conditions. It is notable that the lower deposition temperature did, however, result in both a reduced texture and a change in the preferential growth direction. For the LLT system, a similar issue to the one observed in the Alumina disc substrates was observed, with a significant portion of the coating showing "zero solutions", i.e. areas where the crystal orientation could not be resolved. This is likely due to relatively small crystal sizes affecting the EBSD signal intensity.

A hypothesis for the very low texture displayed by the LowK-LT coating deposited on N75 could be the presence of the smaller grains discussed for this system. It should be mentioned that this system was mapped with a small pixel size (70 nm), resulting in relatively small grains (0.049 μm^2) when applying the 10 pixel filter.

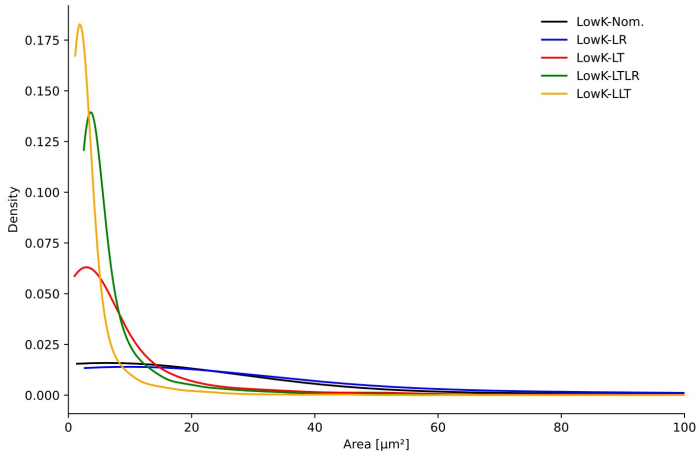


Figure 3.31: KDE of LowK systems on N75 recalculated filtering for small grains in LowK-LT

To test this hypothesis, the texture was re-calculated using a grain area filter of 0.23[7] μm^2 and 1 μm^2 filter. This resulted in a modest increase in the texture index to J = 3.48 and J = 3.57 respectively, indicating that the low texture was not a result of the spurious grains. As part of this analysis, the grain size was re-calculated for the grain list filtered for grains bigger than 0.23 μm^2, and is presented in Figure 3.31. These revised results coincide with the trend observed for the grain sizes of the different systems deposited on Alumina, confirming the effect of temperature, rotation and their combination on grain size.

3.4.3.2 GZO model TBCs

An equivalent analysis was performed for the GZO systems using EBSD maps gathered for the model TBCs produced. An example EBSD map for the GZO-LT coating system is presented in Figure 3.32. Unfortunately, EBSD maps could not be collected for the GZO-Nom coating system in either substrate. As a consequence, no meaningful evaluation of the compound effect of rotation and temperature could be performed for GZO.

[7]This value corresponds to the average area for 10 pixels for the other systems mapped.

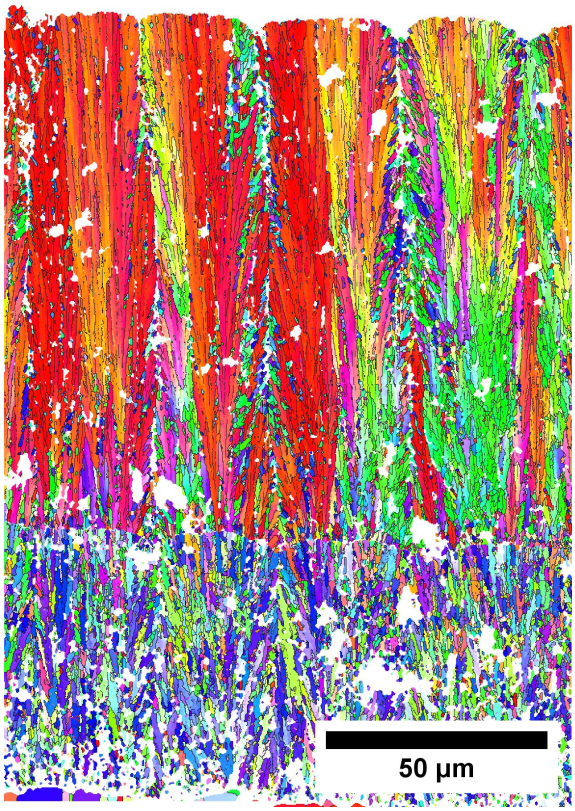
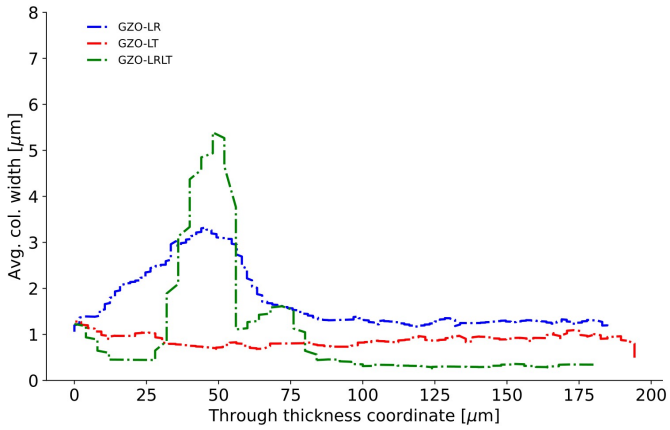


Figure 3.32: IPF (Y axis projection) map for the GZO-LT coating deposited on an N75 substrate.

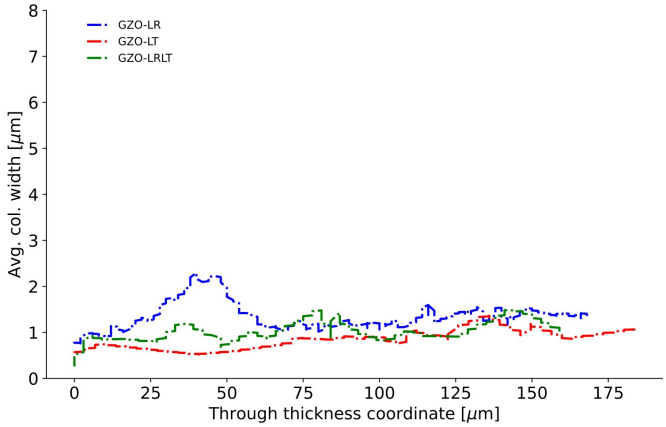
The column width profiles obtained from the EBSD-derived grain boundary data are presented in Figure 3.33. With the noted absence of GZO-Nom, the other systems broadly conform to the results obtained when applying the method to the electron images, for the GZO layer. The broader columns measured for the initial portion of the coating thickness, corresponding to the LowK layer, are the result of column broadening in the GZO-LR system. In the GZO-LTLR coating, however, they represent the presence of a large unresolved area, akin to the one displayed in Figure 3.30.

These results seem to confirm that the column width obtained by CoCo as applied to the electron images provide a more accurate quantitative measure of the column width than the manual method. The results obtained are substantially thinner than the range provided by the manual method, meaning that the notion of the "column-like" areas, described as one of the criteria used in the determination of column boundaries does not correspond to meaningful crystallographic entities.

It should be noted that, like for like, the measured column width for the Alumina substrate systems is equivalent or slightly thicker than those deposited on N75. The systems deposited on N-75 can be ranked according to their column thickness in the GZO layer as "GZO-LR" > "GZO-LT" > "GZO-LTLR". This distinction is not as clear for the coatings deposited on Alumina discs. However, when looking at the grain area size, determined by EBSD, GZO grains in GZO/LowK coatings on Alumina discs do follow that same ranking, while GZO-LTLR exhibits a distribution corresponding to larger grains than GZO-LT for coatings deposited on N75. This is due to the aforementioned issues with indexing small grains at the GZO-LowK interface, which lead to a grain size distri-



(a) N75



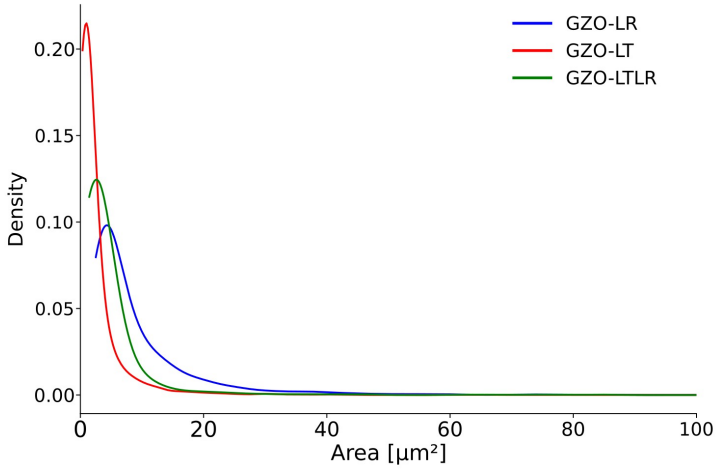
(b) Alumina substrate

Figure 3.33: Column widths measured by CoCo using EBSD grain boundary data for GZO systems.

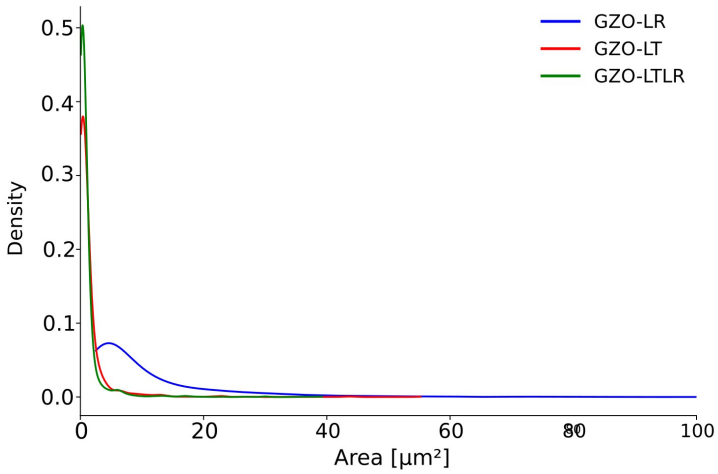
bution corresponding to the grains on the higher end of the actual distribution.

Figure 3.35 shows the IPFs for the Gadolinium Zirconate phase for the model GZO coatings. The major observable difference is the diffuse pole figures for coatings deposited on Alumina substrates at lower temperatures. The coatings deposited on N75 substrates seem to maintain a significant texture, with a preferred orientation in the <001> direction along the Y axis. This contrasts with the significant changes in preferred orientation observed between the LR, LT and LTLR LowK coatings deposited on N75 substrate.

The quantitative analysis of the IPFs for GZO, as well as the texture J-index is presented in Table 3.16. The preferred crystallographic orientation in the Y axis for all but one (GZO-LTLR AD) systems is <001>. With regards to crystallographic texture, the obtained index values seem to confirm the qualitative observations from the IPFs. For Alumina disc substrates, rotation and temperature seem to have a significant effect on the texture, with the Low Rotation high temperature system (GZO-LR) showing the highest texture index. Interestingly, the system showing the lowest texture is, as in the case of LowK, the Low temperature (LT) coating. However, in the case of GZO, it is the coating deposited on the Alumina disc instead of the one deposited on N75 the one exhibiting the least texture.



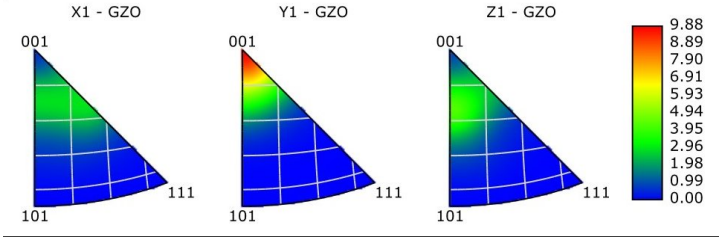
(a) N75



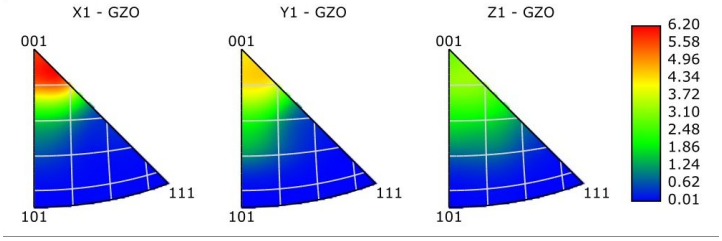
(b) Alumina substrate

Figure 3.34: Kernel Density Estimations for the grain size of GZO systems deposited on different substrates.

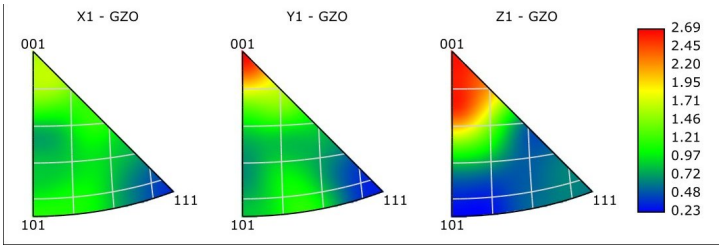
The GZO coatings deposited on N75 substrates with a LowK interlayer, on the other hand, seem to be relatively insensitive to the combined effect of rotation and temperature. Both the preferential direction, the corresponding intensity in the IPF and the texture index are remarkably similar for GZO-LR and GZO-LT. The results for LTLR are not considered accurate for the quantitative analysis due to the aforementioned large “zero solution” regions.



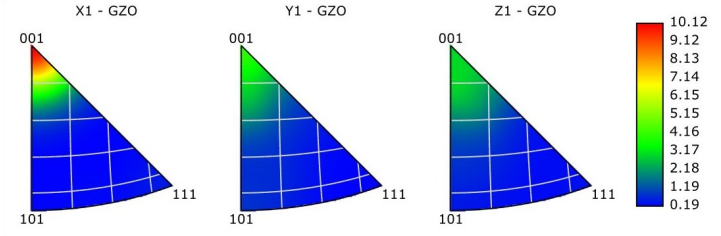
(a) GZO-LR - AD



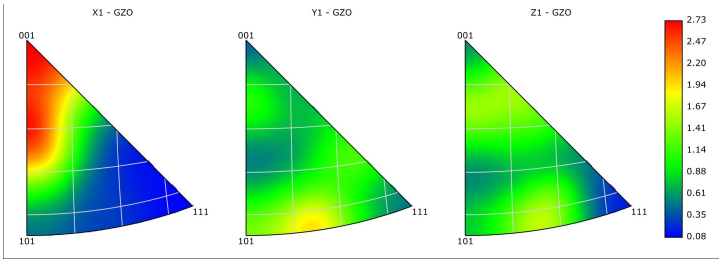
(b) GZO-LR - N75



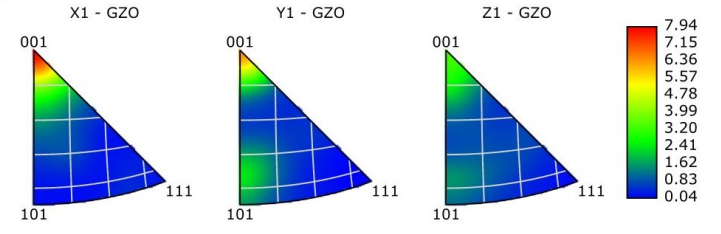
(c) GZO-LT - AD



(d) GZO-LT - N75



(e) GZO-LTLR - AD



(f) GZO-LTLR - N75

Figure 3.35: Inverse Pole Figures for GZO layer on coatings.

Table 3.16: Preferred orientations and intensities obtained for Pyrochlore Gadolinium Zirconate from IPFs for GZO coating systems and corresponding J-index for crystallographic texture.

Coating system	Substrate	IPF orientation (Corresponding intensity)	Texture J-index
GZO-LR	AD	<001> (9.88)	24.18
	N75	<001> (4.33)	12.66
GZO-LT	AD	<001> (2.63)	3.76
	N75	<001> (4.08)	13.08
GZO-LTLR	AD	<313> (1.90)	5.63
	N75	<001> (6.48)	8.33

3.5 Considerations regarding Structure Zone Models and microstructure predictions

Based on the results obtained for the column width of the coatings deposited under different conditions, a few observations can be made with regard to the Structure Zone Models for EB-PVD coatings. The first observation relates to the effect of homologous temperature on the resulting columnar microstructure. According to the Structure zone models reported in the literature, a higher homologous temperature is likely to result in a Zone 2 microstructure with more clearly defined columns. However, the results obtained for the GZO systems, deposited at equivalent temperature, and consequently, higher homologous temperature, result in thinner, less textured TBCs, with a more fibrous morphology, characteristic of Zone 1/T.

Within the same material system, the measured column widths, but especially the grain size distributions of the resulting coatings obtained by EBSD, seem to confirm the analogous effect of deposition temperature and rotation speed on grain nucleation and growth reported in the literature. This effect, observed at low temperatures, does not seem to occur for high temperature deposition, where the analyzed coatings exhibit equivalent grain size distributions. The relative column width of Nominal and Low rotation systems is equivalent, if not higher for the latter, depending on the substrate. This is an interesting observation with regards to the marked effect of the substrate material on the Structure-Zone behaviour of the deposited coating. For LowK, reducing the rotation speed at high temperature results in a marked column width increase. This increase is not apparent from the column width measurement results or the surface imaging for Gadolinium Zirconate.

Structure zone models and other computational models such as the ones described in Submission 3 do not consider the crystallinity of the coating being deposited. The results obtained in the present study corroborate other crystallographic texture studies performed using XRD (219, 62, 234). It is known that the faces of crystalline phases show different surface energies (235). The preferred crystallographic orientations exhibited by the coatings grown epitaxially depend on the energy barriers presented to the adatoms during deposition, and the thermal energy provided to overcome them. The changes observed in the crystallographic orientation and texture development are the expression of the energy balance for each deposition condition. This is reflected in the microstructure through differences in the shape of the crystalline facets comprising the column tips and sides.

One noteworthy observation is the substrate-dependent modification of the behaviour

expected based on the SZMs. The precise mechanism for this behaviour modification was not determined in the present work. However, based on the known differences for the substrates used, the relevant parameters affecting this behaviour modification can be hypothesized. Since the surface layer of both substrates used was comprised of Al_2O_3, it can be argued that the difference in composition between the different surfaces should be minimal. The main differences would thus be related to, on the one hand, the known surface roughness difference between the metallic and ceramic substrate, and on the other, the grain size of the Al_2O_3 layer on which the TBC is growing, as well as the crystallographic phase of the Alumina, which could differ between the TGO growing in aluminised N75 substrates and the Alumina discs. Efforts should be undertaken to understand the mechanism through which these differences, and any other relevant parameters, yet to be identified, act upon the epitaxial growth mechanism, resulting in the observed variation.

Based on these observations, it is proposed that both the Structure Zone Models and the Monte Carlo microstructure prediction models discussed in Submission 3 could be expanded on. In the case of the SZM, the effect of micro-texture on the grain morphology could be explored. As for the computational models leveraged in the prediction of coating microstructures, the energetics used in the determination of adatom mobility and subsequent grain nucleation and growth predictions should include the differences in surface energy of the different crystal orientations of the target phases for increased accuracy.

3.6 Conclusions

A number of conclusions can be drawn from the reported deposition and subsequent characterization of the deposited coating, as detailed below:

- EB-PVD TBC morphology:
  - The widely understood range of microstructures possible to be deposited via EB-PVD was expanded on through deposition of TBCs using a broader processing parameter window.
  - The resulting coatings exhibit markedly different microstructures, both in cross section and in the coating surface topography.
  - For each material, these differences are dependent on the deposition conditions, but also significantly on the substrate material used.
  - While broadly conforming to the behaviour predicted by Structure Zone Models, substrate-material driven deviations were identified and described:
    * For both material systems explored, reducing temperature and rotation speed, separately or jointly seemed to result in fine columnar or fibrous coatings.
    * An exception to this rule was the effect of reduced rotation speed on column width for coatings deposited at high temperature on Alumina discs, which resulted in wider columnar grains, as observed through surface topography.
- Quantitative morphology measurement

- The method for the quantitative measurement of the TBC column width, detailed in Submission 3, was used in the evaluation of the deposited model coatings.
- The main conclusion from the application and results obtained from the method is the existence of significant challenges existing for the consistent quantitative analysis of microstructural features in EB-PVD TBC systems, namely:
  - The ambiguous definition implicitly assumed for the concept of column:
    - As shown by the comparative manual to automated methods evaluated in the present work, this can lead to widely different measures of column size. The effect of the "columns", as defined by the different criteria used in their determination on the mechanical behaviour of TBCs and the infiltration kinematics of CMAS remains uncertain.
    - This uncertainty does not allow to discard the validity of the criterion based on "column-like" morphology for describing the behaviour of the systems.
    - It should be noted, however, that the results obtained from the crystallographic analysis performed suggest that this criterion is not grounded on the crystallographic grains, as measured by EBSD.
  - The two dimensional data used to describe inherently three dimensional entities:
    - The resulting evaluation is limited in the description of the system. Acquiring three dimensional data would allow for accurately describing and modelling behaviours resulting from the three dimensional character of the coatings which are not easily reducible in two dimensional space.
    - Artefacts arise from the lower dimensional evaluation, such as the oblique sectioning of columns, which leads to unreliable quantification of descriptive parameters.
  - The resolution limits of the methods used for the acquisition of the data used in the quantitative evaluation of microstructures.
    - For the secondary and backscattered electron images, this limit presents itself as a limit in the grey value contrast of the porosity to be located and quantified.
    - In the case of the crystallographic data acquired by EBSD, misindexing / misorientation of pixels due to surface condition and porosity on the one hand, and the limits to resolve very small grains result in data loss and noise. Overcoming these issues can present significant challenges for non conductive systems such as ceramic TBCs, which can exhibit charging as a result of the high beam currents used in EBSD mapping.
- The column widths measured with the developed method conformed with those determined through the crystallographic analysis:
  - For both material systems studied, the column width increased through the coating only at higher temperatures, remaining stagnant at the lower

deposition temperatures explored

* Contrary to the expected behaviour, GZO, deposited at a higher homologous temperature, showed reduced column width when compared to LowK.

- Crystallographic study of EB-PVD microstructure morphology and texture:
  - A detailed crystallographic study of tetragonal Yttria Stabilized Zirconia (LowK) and Gadolinium Zirconate (GZO) TBCs was conducted.
  - The grain area displayed by the different systems conformed with the behaviour expected based on the structure zone models.
  - The TBC materials deposited exhibited a different behaviour with regards to the effect of deposition conditions, which was dependent on substrate material. The potential explanations and implications for the Structure Zone Model and other attempts at predicting TBC microstructures are presented in 3.5

Chapter 4

CMAS testing

As discussed in Section 2.2.5, and detailed in Submission 1, fluxing attack by molten ingested particles (CMAS), is a complex mode of failure limiting the life of current TBCs. Overcoming this challenge through the design of CMAS attack resistant TBCs relies on understanding and predicting the interactions between the CMAS melt and the coating.

Current avenues being explored generally consist in attempting to limit the depth of CMAS infiltration in the coating systems, since this infiltration depth has been shown to be one of the most significant drivers of CMAS attack induced damage and coating thickness loss, through a process called cold-shock delamination. Two alternatives have been proposed to limit CMAS infiltration: hydrophobic coatings that prevent the accretion of molten sand in the first place, and coating systems that limit infiltration by inducing crystallization of the infiltrating CMAS.

Within the second avenue, this crystallization is usually induced through chemical interactions between the TBC and the infiltrating CMAS. The ability of crystallization to prevent further infiltration depends on the reaction products, but also on the relative kinematics of dissolution, reaction and crystallization which compete with the infiltration process. Different ceramic oxides, which exhibit accelerated crystallization kinematics are being investigated as candidate TBC materials. Simultaneously, the effectiveness of these systems can be increased by slowing the CMAS infiltration kinematics.

The kinematics of CMAS infiltrations are highly dependent on TBC microstructure, with open porosity playing a special role as the medium through which the infiltrating glass melt is transported. The present Section presents results of the kinematic infiltration studies performed on the model TBCs described in Chapter 3. The method developed in Submission 4 was used for the determination of the CMAS infiltration depth.

4.1 Proposed method for CMAS infiltration depth determination: Development and case studies

For a full description of the method developed, the reader is referred to Submission 5. For convenience, the method developed for the measurement of CMAS infiltration is hereafter called CMAS Infiltration Measurement Method (CIMM). A brief description of CIMM is provided as follows, and illustrated in Figure 4.1: The elemental composition of a CMAS exposed sample is determined through Energy Dispersive Spectroscopy, producing a stack of maps, which provide the elemental composition of each pixel in the analyzed area. The elemental composition data is "collapsed" in the horizontal direction of the acquired map, corresponding to the in-plane direction of the cross section being investigated. This "collapsing" of the map data is conducted for each pixel in the vertical (through thickness) direction of the acquired data, resulting in a point with an elemental composition corresponding to the average at that vertical coordinate.

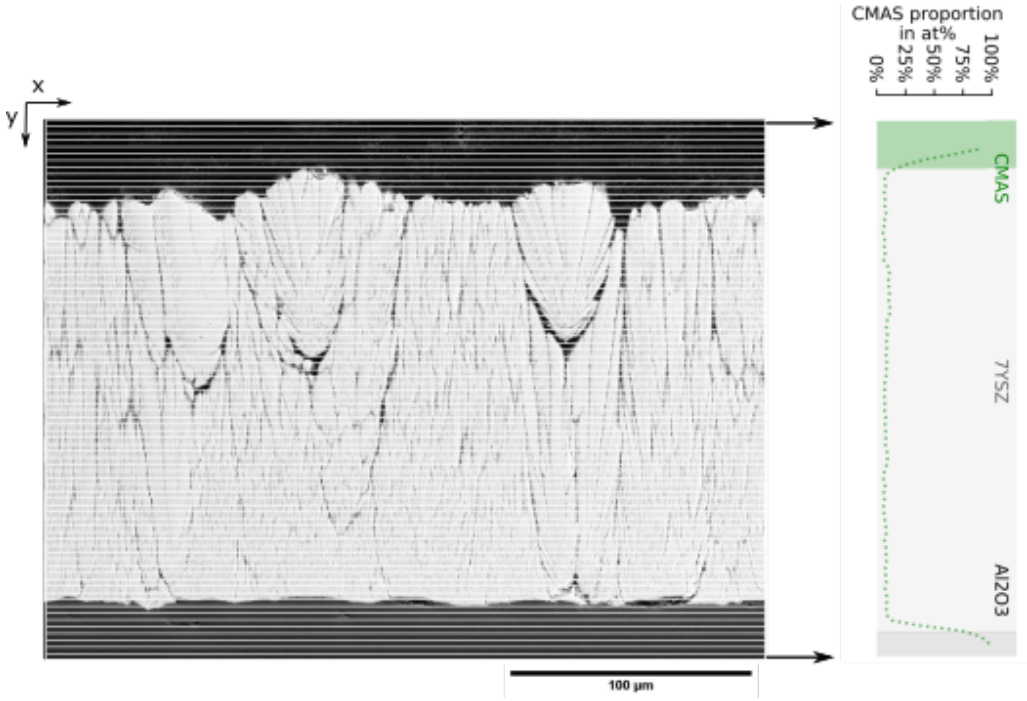


Figure 4.1: Topographic parameters used for peak detection.

Mapping the elemental composition against the through thickness composition results in a through thickness compositional profile of the CMAS-exposed TBC, efectively sinthesizing the two-dimensional compositional data from the elemental map into a 1 dimensional through-thickness compositional linescan, as depicted on the right of Figure 4.1. Tracking the metals-basis proportion of the CMAS, namely Ca, Mg, Al and Si, enables to detect the "break points", which correspond to sudden changes in CMAS composition in the through thickness direction. The most relevant points correspond to the CMAS-TBC interface at the coating surface and the infiltration front. By identifying these critical points and assigning them their corresponding vertical coordinates, the depth of infiltration can be determined for a given map. An example of the identification of these break points and their significance is provided in Figure 4.2.

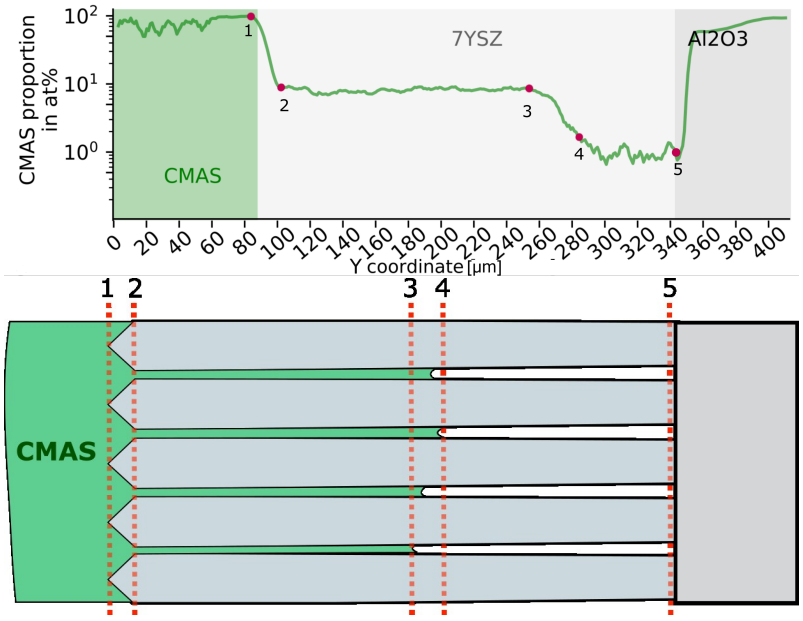


Figure 4.2: Infiltration profile of partially infiltrated sample, with break points highlighted. The diagram underneath shows the meaning of the points in an infiltrated TBC.

Multiple maps were collected at different locations of a given sample, with multiple samples being tested in equivalent conditions and subsequently analyzed. This was done to account for the microstructural variation of EB-PVD TBC coatings, which exhibit non-uniform infiltration fronts. Sections 4.1.1 and 4.1.2 summarize the results obtained from the developed method for samples tested for CMAS infiltration in isothermal and thermal gradient conditions, respectively, including the lessons learnt from these study cases for the successful application of the developed method.

4.1.1 Isothermal tests

7YSZ coatings, loaded with varying amounts of CMAS, were tested for CMAS infiltration by exposing them to isothermal conditions in a box furnace. A lower CMAS dosage threshold was identified at 4 mg/cm^2, below which full infiltration would not occur. A modified version of CIMM was tested which tracked the rate of CMAS elemental change, with the intention of aiding in the identification of break points. Application of this modified method to samples infiltrated with high CMAS loading (15 mg/cm^2) at different temperatures and exposure times yielded limited CMAS infiltration. However this was later identified as a product of the method modification yielding inaccurate results. The reanalysis of the tested samples using the original method showed full infiltration for all the high loaded samples tested. The root cause for this was attributed to the experimental practice used in the isothermal exposure, whereby the thermal inertia introduced by the sample holder delayed thermal recovery following loading of the sample onto the furnace, extending the thermal exposure significantly. The lesson learnt from this result was the need to use samples with as small a thermal mass as possible, while increasing the thermal mass within the furnace, to minimize thermal recovery time.

Despite this issue, which precluded the effective measurement of infiltration depth for

the samples tested with high CMAS loading, CIMM yielded interesting results. These were obtained when reanalysing the samples tested at the threshold dosage of 4 mg/cm^2. These samples exhibited partial infiltration, which progressed with time, especially for the samples tested at 1250°C. Additionally, an analysis of the proportion of CMAS at the infiltration front was conducted. The resulting proportion of CMAS was proposed to be equivalent to the level of saturation of the porosity by the infiltrating melt.

By evaluating this level of saturation for the tested systems, a two stage infiltration mechanism was identified for CMAS in EB-PVD columnar TBCs. The first of the two stages consisted in the rapid transport of CMAS in the through thickness direction, during which a certain level of porosity remains in the coating, even within the infiltrated depth. The initial infiltration progressed in an unsaturated manner, contrary to assumptions used in the analytical models for CMAS infiltration based on percolation theory (236). Subsequently, the level of CMAS saturation gradually increased, indicating the progressive filling of the remaining porosity. The fully detailed method, test results and recommendations are detailed in Submission 5.

4.1.2 Thermal gradient tests

A visit to ForschungsZentrum Jülich (FZJ) was undertaken in partial fulfilment of the requirements for the EngD (International). During said visit, samples coated with 7YSZ and selected model TBCs were tested for CMAS infiltration under gradient conditions, using the burner rig available at FZJ. Significant efforts, described in detail in Submission 4, were devoted to the determination of the test conditions required for inducing partial infiltration of the TBCs to be tested, a pre-requisite for the study of infiltration kinematics.

Once the appropriate exposure temperature and time was determined, three tests were conducted, exploring different loading levels and methods for applying the CMAS to the sample. The burner rig at Jülich applies the CMAS by spraying a precursor solution through a nozzle concentric to the gas burner, meaning that the CMAS is deposited in relatively hot conditions. The different methods tested consisted in pre or co-loading the sample with CMAS.

The pre-loading consisted in the deposition of CMAS at relatively low temperature (1000°C) with a subsequent increase to the test temperature (1300°C) to promote melting and infiltration. On the other hand, co-loading consisted in the deposition of the CMAS at the test condition.

The two stage infiltration mechanism was also observed for the systems tested under thermal gradient conditions. Detailed microstructural analysis revealed that the initially uninfiltrated porosity corresponded to the larger pores in the TBC, in line with observations in APS TBCs exposed to CMAS (237, 238). Full infiltration occurred for all the systems tested. However, due to the radial thermal gradient resulting from the burner rig setup, partial infiltration was induced towards the edge of the samples. Evaluating the infiltration depth at different radial positions enabled to plot the infiltration depth profile through a diametric section of the test samples. It was found that pre-loading resulted in a more consistent infiltration front, with the level of loading playing a secondary role.

The selected model TBCs were tested by the host institution following the conclusion of the international visit. Results for these additional tests conducted, as well as additional characterization performed on the samples analyzed in Submission 4 are presented in

section 4.2.2. These results complement the analysis of the isothermal CMAS testing results presented for the model TBCs in section 4.2.1

4.2 Effect of microstructure on CMAS infiltration

The produced model TBCs exhibited differences in their microstructural morphology, as characterized in section 3. The microstructural features, in particular the width and extent of porosity open to flow, as well as the tortuosity of the three dimensional porosity network are proposed to have a significant impact on the speed of CMAS infiltration through TBCs (48, 126, 134, 135, 149, 239). Thus, the model TBCs are considered to be a useful vehicle for the assessment of the effect of these microstructures in the kinematics of CMAS infiltration.

Simultaneously, the tests conducted serve the function of confirming the proposed method for determining of CMAS infiltration, and as a valid tool for the validation of CMAS infiltration models. As detailed in Submission 2: "Materials and methods", Alumina substrates were used for conducting the isothermal tests, with the resulting effect on the deposited microstructure. The use of the ceramic substrates was required because of the high exposure temperatures, which would have resulted in heavy oxidation or melting of metallic substrates, potentially compromising the coating integrity and results obtained.

4.2.1 Isothermal tests

Isothermal tests were undertaken to evaluate the kinematics of CMAS infiltration in the model TBCs deposited on Alumina substrates. As already mentioned, more than one sample was tested at each condition, to account for sample to sample microstructure variability. Coupled with the limited number of samples available for each system, this imposed a restriction on the number of conditions to be explored. Since the main aim consisted in understanding the kinematics, i.e. the time-dependent infiltrative motion of the CMAS, it was decided to vary this parameter, fixing the exposure temperature and CMAS dosage.

The selection of these fixed parameters was based on the results obtained from the isothermal test results in Submission 5. The target dosage to be applied was of at least 15 mg/cm^2, to ensure sufficient availability of CMAS for infiltration and avoid "starving" the coating. The chosen exposure temperature for LowK systems was 1250°C, which exhibited full infiltration for the longest exposures tested in the development of the method, even for lower CMAS dosages. In the case of the GZO systems, a few samples were exposed at 1300°to account for the higher resilience of GZO to infiltration through reactive crystallization. The conditions and number of samples tested are detailed in section 4.2.1.2.

Given the full infiltration identified in the isothermal testing described in Submission 5, which occurred during the 4-5 minute thermal recovery, short exposures were selected. In order to reduce the thermal recovery time, the improvement to the test method suggested in Submission 5 were implemented. The selected exposure times were 30s, 180s and 360s. It was expected that these exposure times would result in limited partial infiltration, extensive partial infiltration and full infiltration, respectively. The infiltration depth and CMAS saturation results obtained with CIMM for the model TBCs are discussed below.

4.2.1.1 Non-reactive system - LowK

The number of samples tested at each condition for the LowK model TBCs are detailed in Table 4.1.

Table 4.1: Number of samples tested for the LowK model TBCs.

Exposure Temperature°C	Exposure time [s]		
	30	180	360
1250	2	2	2

As discussed in section 3.2.1.1, LowK was considered to have sluggish reaction kinematics with CMAS, meaning that the effect of the crystallization induced by these reactions could be considered negligible in the infiltration of CMAS. In other words, as it pertains to infiltration speed, LowK was considered non-reactive with CMAS. As such, it was expected that full infiltration would proceed rapidly in the absence of infiltration-abating crystallization.

An example infiltration profile for the tested systems, confirming that partial infiltration had been induced is shown in Figure 4.3. This contrasts with the tests at 15 mg/cm^2 dosage conducted in Submission 5, where full infiltration happened even at 30 s exposures. This result confirms that the cause for this full infiltration observed in the tests reported in Submission 5 was the result of infiltration proceeding during thermal recovery due to the large thermal inertial of the sample holder.

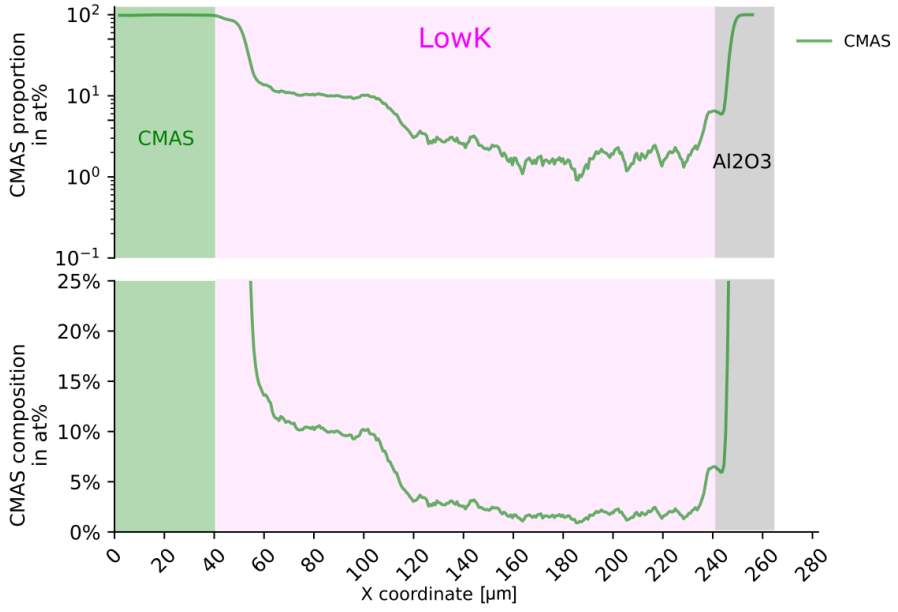
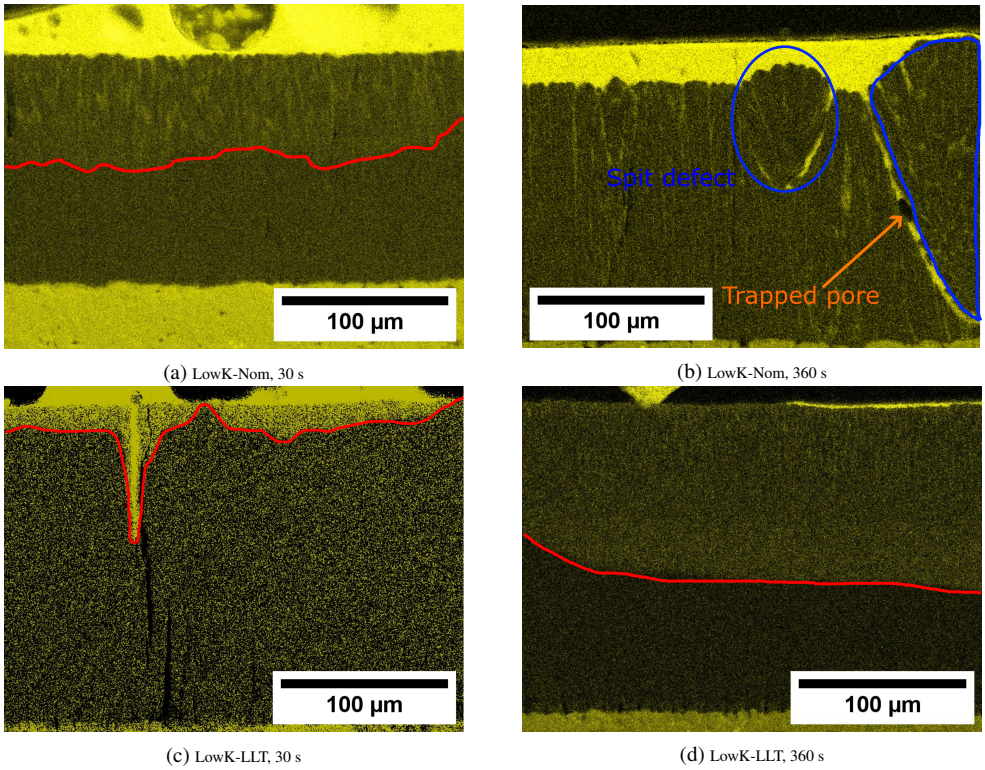


Figure 4.3: CMAS infiltration profile for LowK-Nom exposed for 30s. Note the logarithmic and linear y-axis on the top and bottom subplots, respectively.

The reduced thermal mass of the holders adopted for the testing of the model TBCs following this observation seemed to have resolved the issue of thermal recovery to a significant extent. This is supported by the infiltration depths apparent from the elemental

maps collected for the TBC systems tested, some of which are presented in Figure 4.4. These elemental maps are coloured to show the combined elemental composition of Ca, Mg, Al and Si.

On top of the partial infiltration evident, it can be seen that the LowK-LLT system exhibits a lesser extent of CMAS infiltration when compared to LowK-Nom, which shows full infiltration at 360 s of exposure. Note that even for the fully infiltrated systems, unsaturated porosity remains in areas with large intercolumnar gaps, as shown in Figure 4.4b.



(a) LowK-Nom, 30 s

(b) LowK-Nom, 360 s

(c) LowK-LLT, 30 s

(d) LowK-LLT, 360 s

Figure 4.4: Combined Ca, Mg, Al and Si elemental maps (all elements coloured yellow to show combined infiltration) for selected model LowK TBCs exposed at 1250°C for different times, showing full or partial infiltration. Red lines indicate infiltration front.

Analyzing the collected EDS data using CIMM yielded the results presented in Figure 4.5 for the LowK model systems. The partial infiltration observed in the example profile and EDS maps is clearly apparent for most of the conditions tested, with the exception of the longest exposure times. Note that the apparent stagnation of CMAS infiltration depth exhibited by the LowK-Nom coating system corresponded to a smaller coating thickness, meaning that no further infiltration could occur for this system.

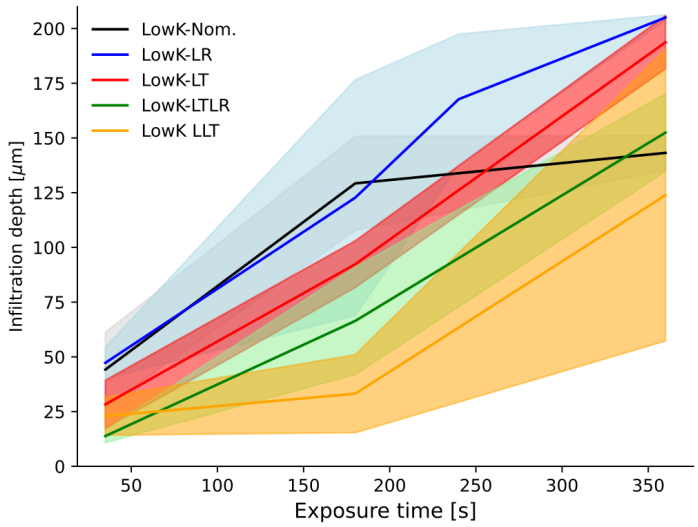


Figure 4.5: CMAS infiltration depth for LowK systems tested at 1250°C. Shaded areas correspond to 95% Confidence intervals, σ = 1.96.

The flow characteristics of a porous solid such as EB-PVD TBCs are controlled by the morphology and network characteristics of its porosity rather than the solid portion. The size of the intercolumnar pores was not measured in the present project, meaning that no such assessment can be undertaken directly.

The reason for not measuring this critical parameter is Twofold: On the one hand, the small dimension of the porosity exhibited by some of the systems would preclude undertaking such an assessment over a large enough area to capture the microstructural variability exhibited by the systems, meaning that a decision would have to be made between resolution and representativity. In addition, the difficulty in discerning between intra- and intercolumnar porosity, discussed regarding the determination of "columns" as an entity, imply a significant difficulty in distinguishing between portions of the porosity open to flow or not. Note that these difficulties also make any comparisons with the overall porosity measured for these systems less meaningful.

The EB-PVD TBC growth mechanism results in a relatively high packing of the growing columns. For a given geometrical packing, the size of the pores between the grains is reduced proportionally to the grain size. Therefore, the alternative adopted was to use column width and grain size as representative of the intercolumnar pore size.

Overall, it can be seen that, for equivalent test conditions, the infiltration depth in LowK TBCs follows an inverse relation with the column widths measured by the automated method using the EBSD data shown in Figure 3.24b, as well as with the grain size data presented in Figure 3.26b. This can be interpreted as smaller pore sizes slowing the infiltration of CMAS through the coating thickness.

While this behaviour does not correspond to the intuitive behaviour expected based on the effect of capillary forces, it is consistent with the predictions from percolation theory, as expressed by the analytical methods resulting from the modifications of the Kozeny-Carman equation proposed by Krämer (149) and Naraparaju et al. (48), and numeric models of infiltration (134).

The large variation in CMAS infiltration depth exhibited by the LowK-LLT system

can be explained by the mechanical damage exhibited by this system when exposed to the high temperature and high CMAS loading environment for 360 s. LowK-LLT coatings developed large vertical cracks spanning the thickness of the coating. The large amounts of CMAS present in these vertical cracks, shown in Figure 4.6, suggest that this damage happened during thermal exposure, rather than during cooldown. These cracks constituted a preferential infiltration path for the through-thickness infiltration of CMAS. The regular front of lateral CMAS transport results from the interconnected intercolumnar porosity.

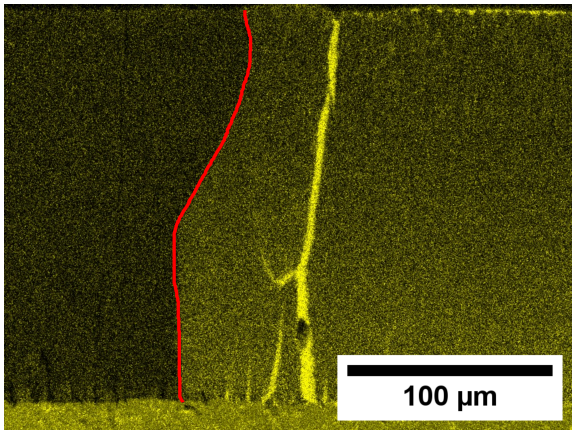


Figure 4.6: Combined Ca, Mg, Al and Si elemental map showing infiltration through large vertical crack and lateral transport of CMAS in coating LowK-LLT.

The mechanism for the occurrence of these vertical cracks is likely related to the mud-cracking defects occurring following sintering, and the strain gradient induced into the partially sintered TBCs (90). The thinner columns in LowK-LLT are assumed to exhibit stronger intercolumnar bonding, through increased column to column contact. This would result in reduced in-plane compliance, which, when subjected to the CTE mismatch-induced stresses at high temperature, could be relieved through the development of the observed vertical cracks.

The presence of these wide cracks in the coating system with the smallest column width and, consequently smallest expected intercolumnar pore size resulted in a bimodal intercolumnar pore distribution developing during testing. The consequence is the development of large differences in the local infiltration behaviour, through the uneven distribution of these crack-like defects.

This different behaviour observed for the infiltration depth is also shown for the level of CMAS saturation at the infiltration front of LowK-LLT, as shown in Figure 4.7. It can be seen that LowK-LLT exhibits a seemingly erratic behaviour with regards to the level of saturation at the infiltration front as a result of the effect of these defects

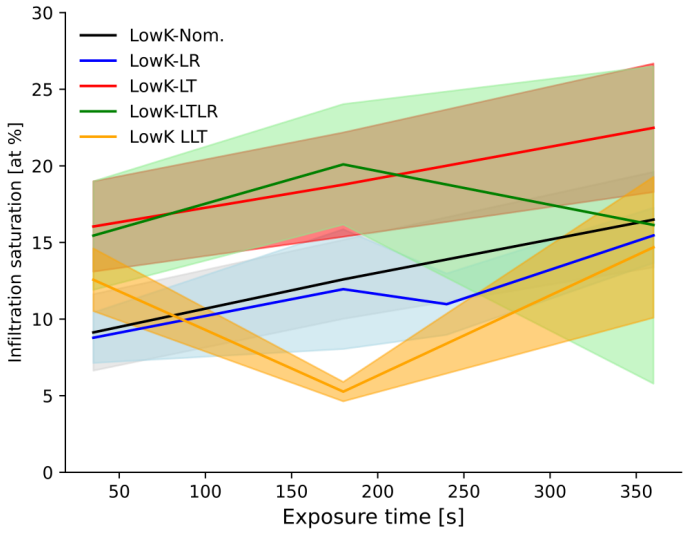


Figure 4.7: CMAS saturation for LowK systems. Shaded areas correspond to 95% Confidence intervals, $\sigma = 1.96$.

For the rest of the systems studied, the effect of column width and grain size on the saturation level seems to be the opposite of the one exhibited for infiltration depth. The coatings with thinner columns and smaller grain sizes, LowK-LT and LowK-LTLR exhibit a larger level of saturation when compared to LowK-Nom and LowK-LR. This can be explained by the relatively large interaction volume of EDS. The CMAS infiltrated porosity deep in the sample is obscured by the columns in the cross section. For coatings with wide enough columns, this infiltrated porosity will be deep enough for EDS not to detect the CMAS elements therein. In contrast, the EDS will detect the composition of the infiltrated porosity in systems with thin columns even when said porosity lies directly behind a ceramic column.

The limited thickness of the LowK-Nom system provides further evidence of the two-stage mechanism of infiltration and saturation observed in Submission 5. Indeed, despite the infiltration depth remaining constant between 180s and 360s due to the limited coating thickness, the level of saturation increased notably between these exposure times for the samples studied.

Together with the large uninfiltrated pores in Figures 4.4b & 4.6, this observation allows to outline the detailed mechanism for the two-stage infiltration in EB-PVD TBCs.

The first stage of the proposed mechanism consists in a fast transport of CMAS in the through thickness direction, occurring preferentially down large pores. The porosity is unsaturated during this first stage, with CMAS flowing around areas with trapped gas, in a manner similar to water flowing between two panels in an indoor water wall. Once infiltration has progressed through the entire coating thickness, the second stage of infiltration consists in the progressive filling of the large porosity. Note that this two stage mechanism is observed for TBCs exhibiting large pores, but whether or not uninfiltrated porosity remains in systems with thin intercolumnar pores remains an open question.

4.2.1.2 Reactive system - GZO

The number of samples tested for each condition, for the GZO model TBC systems is detailed in Table 4.2. The limited testing of GZO-Nom at 1250°C responds to the limited availability of samples for this systems. The additional testing conditions at 1300°C was intended for the evaluation of the more resilient GZO material systems, which are known to limit the infiltration depth through reactive crystallization (130)

Table 4.2: Number of samples tested for the GZO systems. *Due to the limited samples available, no GZO-Nom systems were tested at these conditions.

Exposure Temperature [°C]	Exposure time		
	30	180	360
1250	2*	2*	2
1300	-	-	2

An example of a CMAS infiltration profile for GZO model TBCs is presented in Figure 4.8. Note the relatively high level of CMAS presented for the GZO coating layer as opposed to the LowK layer. The exact cause of this difference is not known. It can be speculated that differences in the surface diffusivity of the CMAS elements between GZO and LowK could result in the observed differences.

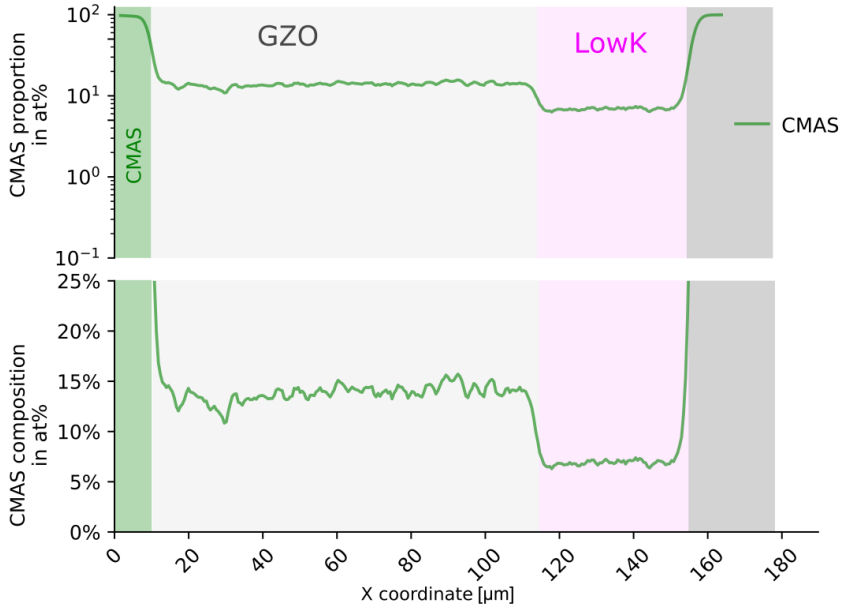


Figure 4.8: CMAS saturation profile for GZO-Nom exposed at 1300°C for 360 s.

The infiltration depth, measured by the developed method for the GZO model systems is shown in Figure 4.9. It is immediately evident that very limited infiltration occurred for all the systems tested. This shows that the ability of the GZO systems to mitigate CMAS infiltration was maintained for all the microstructures produced.

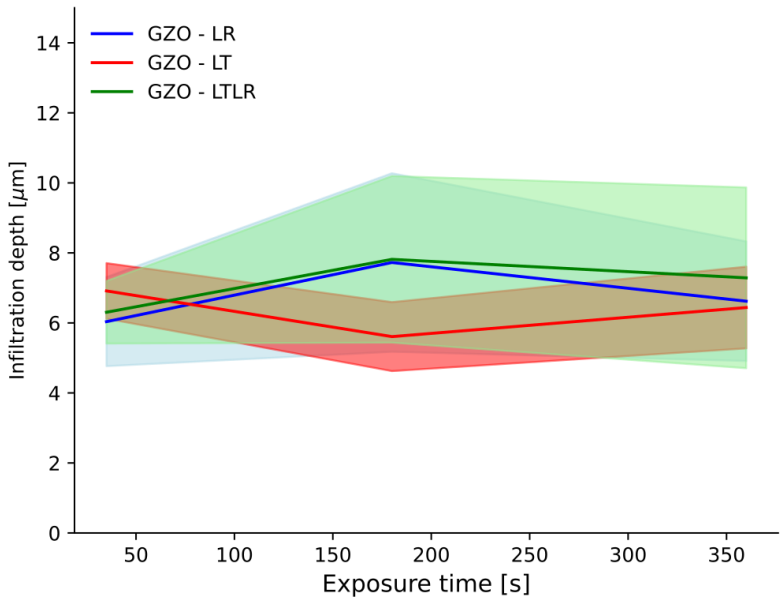


Figure 4.9: CMAS infiltration depth for GZO systems exposed at 1250°C. Shaded areas correspond to 95% Confidence intervals, σ = 1.96.

An inspection of the saturation level for the GZO TBCs deposited at the infiltration front is presented 4.10 with similar results to those obtained for the infiltration depth on these systems.

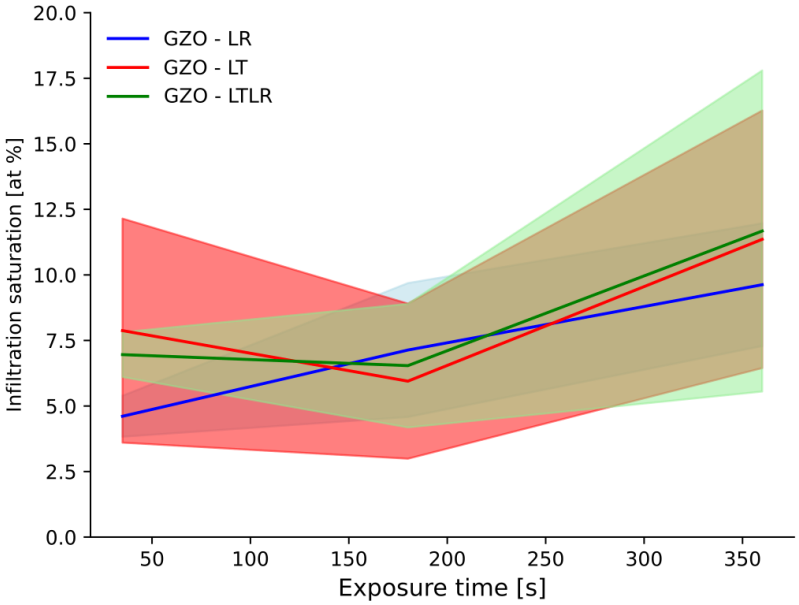
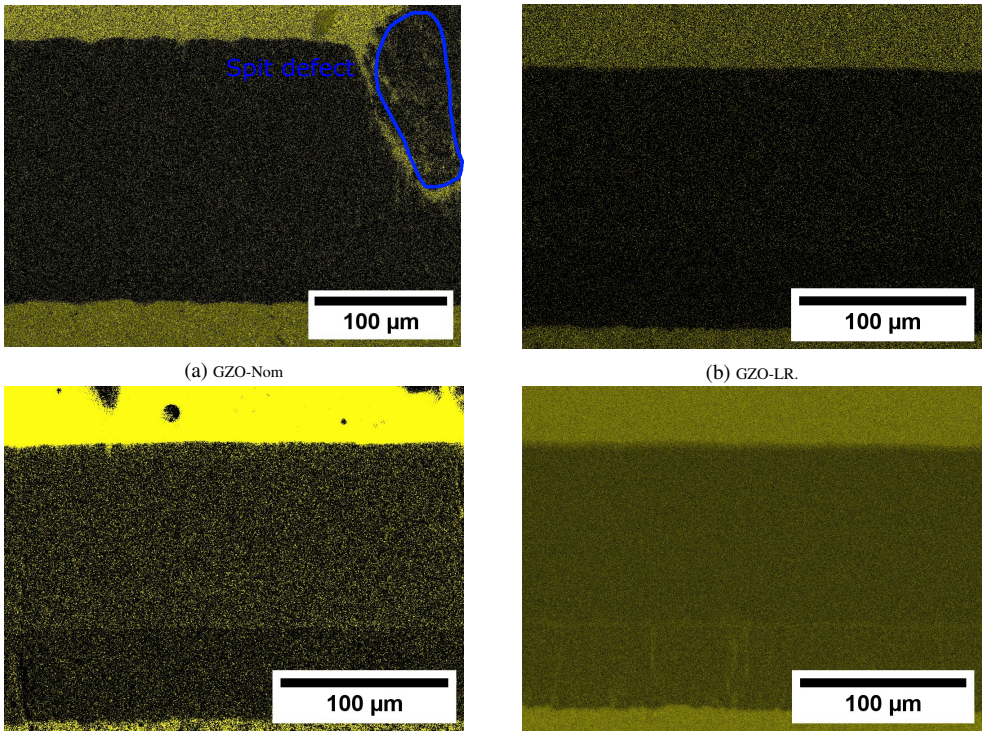


Figure 4.10: CMAS saturation level (at. % of metals basis proportion) for GZO systems exposed at 1250°C. Shaded areas correspond to 95% Confidence intervals.

The elemental maps for all the GZO TBCs tested at 1250°C for 360 s, are shown in

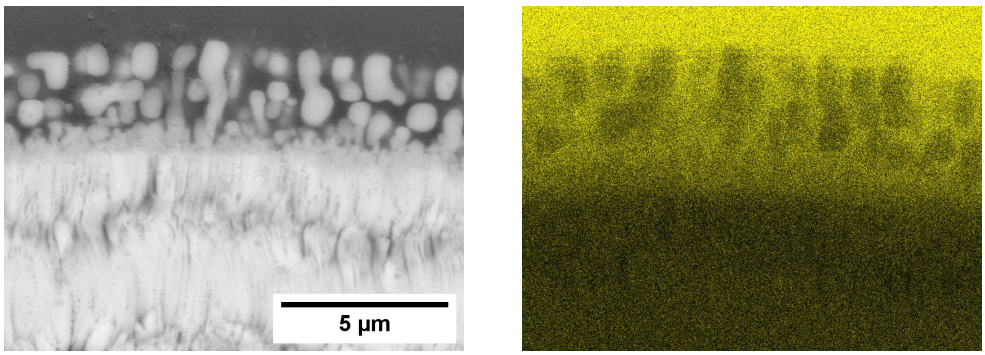
Figure 4.11. In line with the results in Figure 4.9, no infiltration is observed, with the exception of the large porosity exhibited by GZO-Nom around the "spit" defect on the right side of the EDS map. For some of the maps, the two-layer CMAS saturation level shown in Figure 4.8 can be seen as different brightness levels.



(a) GZO-Nom (b) GZO-LR. (c) GZO-LT (d) GZO-LTLR

Figure 4.11: Combined Ca, Mg, Al and Si elemental maps for model GZO TBCs exposed for 360s at 1250°C, showing no infiltration.

The lack of infiltration is evidenced when looking at the detail of the reaction zone between the GZO coating and CMAS, presented in Figure 4.12. The globular grains present correspond to reprecipitated Fluorite (130), with a dense reaction layer observable underneath. The EDS map presented in Figure 4.12b shows the rapid decay of the CMAS elements, which extends just slightly below the dense reaction layer. This is likely the result of the diffuse boundaries resulting from EDS maps due to the interaction volume limiting the horizontal resolution.



(a) (b)

Figure 4.12: Detail of reaction zones for GZO-LTLR, a) BSE image exhibiting reaction product morphology and b) EDS map for CMAS elements, showing limited infiltration beyond reaction zone.

Below the reaction layer, no obvious microstructural changes are observable, suggesting that the reaction products effectively protect the GZO from further infiltration and reaction. The time dependent thickness of this reaction layer, including the spherical Fluorite particles precipitated is shown in Figure 4.13 for the GZO model TBCs exposed at 1250°C.

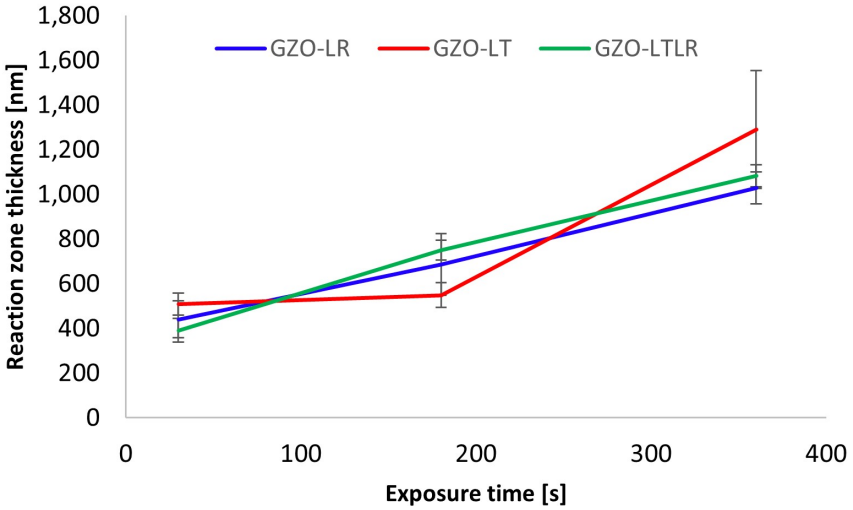


Figure 4.13: Thickness of reaction zone for the GZO model coatings exposed for different times at 1250°C. Error bars represent 95% Confidence Intervals - σ = 1.96.

Small differences can be observed between the samples exposed at 1250°C, with all exhibiting an increase in the reaction thickness. Given the effectiveness of the reaction in protecting further infiltration and reaction, the thermal exposure conditions were likely not sufficient to capture differences in behaviour between the different systems. The higher temperature exposures for 6 minutes resulted in a clearer distinction in the reaction layer systems resulting for the different GZO TBCs, as shown in Figure 4.14.

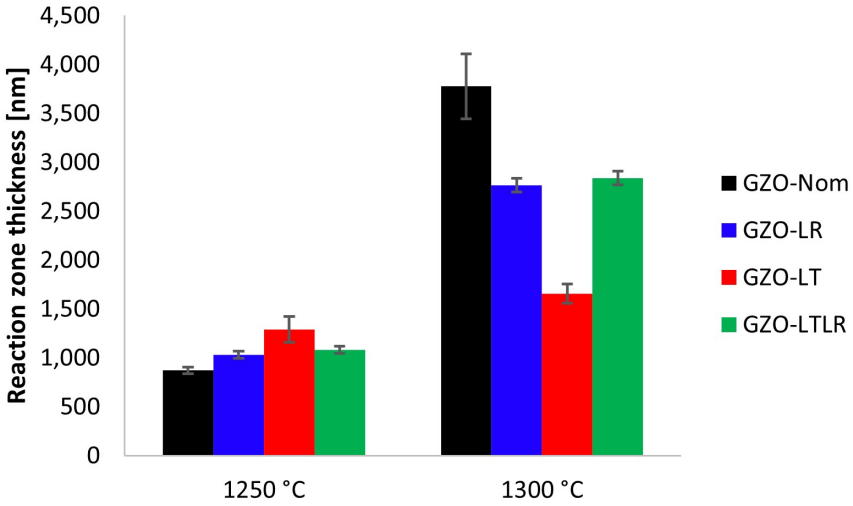


Figure 4.14: Thickness of reaction zone for the GZO model coatings exposed for 360s at different temperatures.

Replotting the data in Figure 4.14 to represent the reaction zone in a logarithmic axis and the reciprocal absolute temperature in the X axis results in an Arrhenius plot, such as the one represented in Figure 4.15. Multiplying the negative of the slope by the gas constant allows to compute the activation energy for the reaction zone growth in the different systems, summarized in Table 4.3.

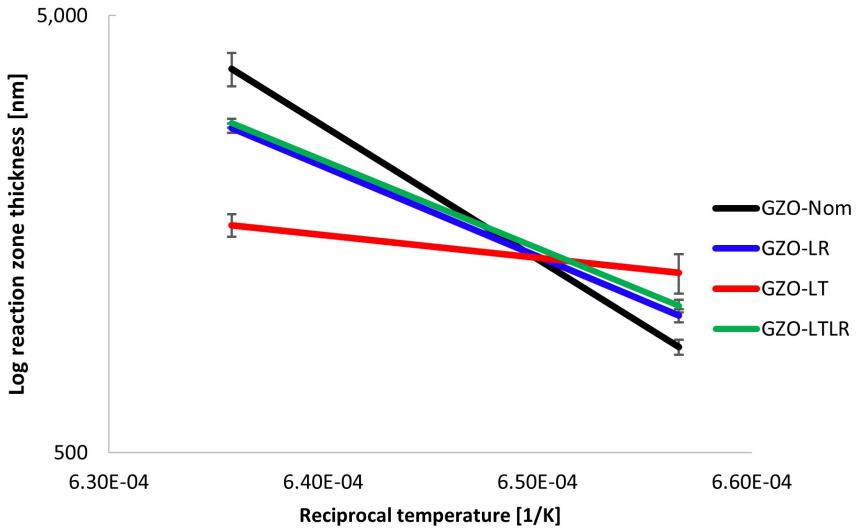


Figure 4.15: Arrhenius plot for the reaction zone thickness growth in the GZO TBC systems

Table 4.3: Activation energy for the reaction zone thickness growth of GZO systems, determined from Arrhenius plot in Figure 4.15. Note that the asymmetric confidence intervals are a result of the assumed normal distribution of reaction zone thicknesses.

TBC system	E_a [MJ/K·mol] (C.I. - α = 5%)
GZO-Nom	1157 (869 to 1239)
GZO-LR	691 (532 to 796)
GZO-LT	146 (50 to 325)
GZO-LTLR	698 (625 to 718)

It can be seen that significant differences appear between the tested systems, with GZO-LT showing the lowest activation energy, and, consequently, highest resistance to the growth of the reaction zone. A significant portion of the small (1-4 μm) reaction zone thickness comprises the column tips, which vary from system to system in the height of the crystal facets they present. As a consequence, the shape of these facets is expected to have an outsized effect on the initial reaction zone growth, implying that the results obtained are likely not representative of the overall performance of the systems studied. Longer exposures are likely to provide more accurate estimations of the resistance of the GZO systems produced to dissolution by CMAS.

4.2.2 Thermal gradient tests

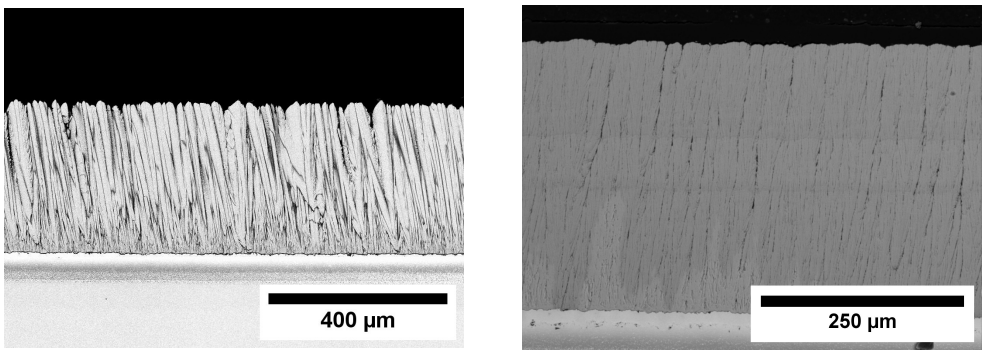
In addition to the reference nominal system, one model coating (Low Temperature) was exposed at a target front face temperature of 1300°C after a pre dosing for 9 minutes.

The metal substrate temperature was kept at circa 1100°C by cooling the rear face using a compressed air nozzle, as described in Traeger et al (140). The exposure conditions and nomenclature for the TBC systems tested is detailed in Table 4.4.

Table 4.4: Exposure times for the tests conducted in the gradient rig at FZJ.

Sample ID	Coating System	Hot time [min]
Nom-6'	7YSZ-Nom	6
Nom-3'	7YSZ-Nom	3
LT-6'	7YSZ-LT	6

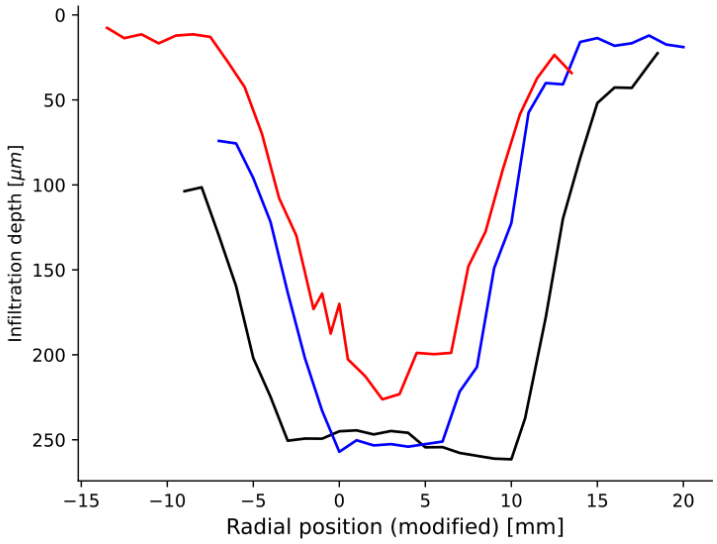
Note that 7YSZ was used as the non-reactive material system. For the purpose of infiltration and microstructure, these systems are considered close equivalents. The cross-section micrographs for the 7YSZ-Nom and 7YSZ-LT systems is shown in Figure 4.16, showing the equivalence between the tested microstructures and those analyzed in Chapter 3.



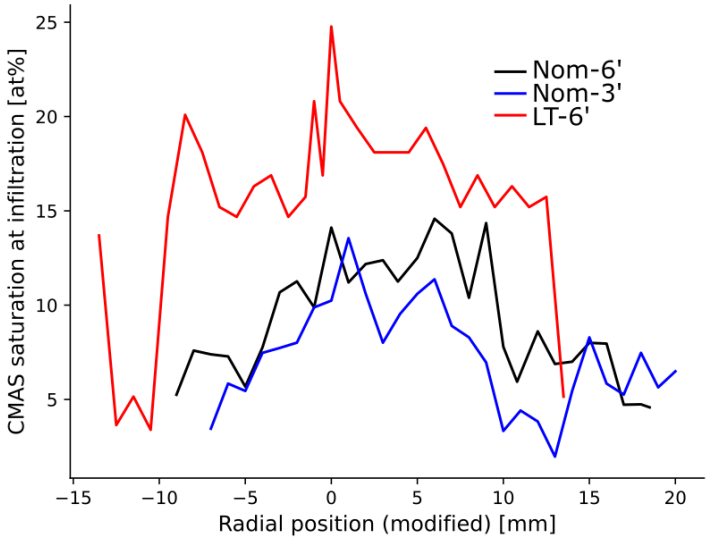
(a) (b)

Figure 4.16: Cross section images for (a) 7YSZ-Nom and (b) 7YSZ-LT coating systems tested under gradient conditions.

Following testing, the samples were cross sectioned, targetting the deposit hotspot, i.e the area with most apparent CMAS deposit. While not corresponding exactly to the thermal hotspot, the area with the thickest deposit is usually close enough to it that the metallographic section will capture the area where most infiltration occurred. For the sections obtained, EDS maps were collected at 1 mm intervals from the cross section centre and analyzed. The resulting distribution of the infiltration depth and saturation of the systems tested is shown in Figure 4.17. The (modified) qualifier used in the x axis refers to the fact that the centre of the infiltration profile is not located in the same radial position for all samples and has been adjusted for easier cross-sample comparison.



(a)



(b)

Figure 4.17: a) Infiltration depth and b) saturation radial profiles for the TBC coatings tested under gradient conditions.

Looking at the infiltration depth profiles of the tested samples in Figure 4.17b, a significant reduction in the infiltration depth for the LT-6' system can be observed. This comparison holds true even when comparing the 7YSZ-LT sample, tested for 6 minutes, to the 7YSZ - Nom coating exposed to high temperature for 3 minutes. This points to the changes in microstructure enabling a slowing down of infiltration speed by at least 50% under gradient conditions. This behaviour corroborates the comparison of CMAS infiltration kinematics observed for LowK-Nom and LowK-LT systems in the isothermal tests. Within the not fully infiltrated part of the profile.

The saturation levels observed for the gradient rig tested samples also coincide with the observations from the isothermal testing results. The LT-6' system, showing thinner

columns, exhibit a higher level of saturation, likely attributable to the relatively large interaction volume of EDS.

As for the comparative saturation levels of the 7YSZ - Nom coating tested for different times, Nom-6' displays an apparently higher level of saturation than Nom-3'. This would be in line with the two-stage infiltration and saturation mechanism described above, although the relatively small difference between both systems does not allow to conclusively confirm this.

Ideally, a quantitative comparison between the infiltration depths displayed would feature comparing the observed levels of infiltration to the depth predicted by an analytical or numerical model. The exposure conditions at the different radial positions analyzed would have to be accurately determined to support such a comparison. The efforts undertaken and challenges faced in the accurate determination of the spatially-resolved temperature at the sample substrate during testing are detailed in Section 4.2.2.1.

The 7YSZ-LT sample tested (LT-6') showed significant delamination following the single test cycle that it underwent. The extent of the delamination exhibited by this sample can be seen in Figure 4.18. As shown by the radial position either end of the delamination crack, the diameter of the delaminated area is of around 14 mm.

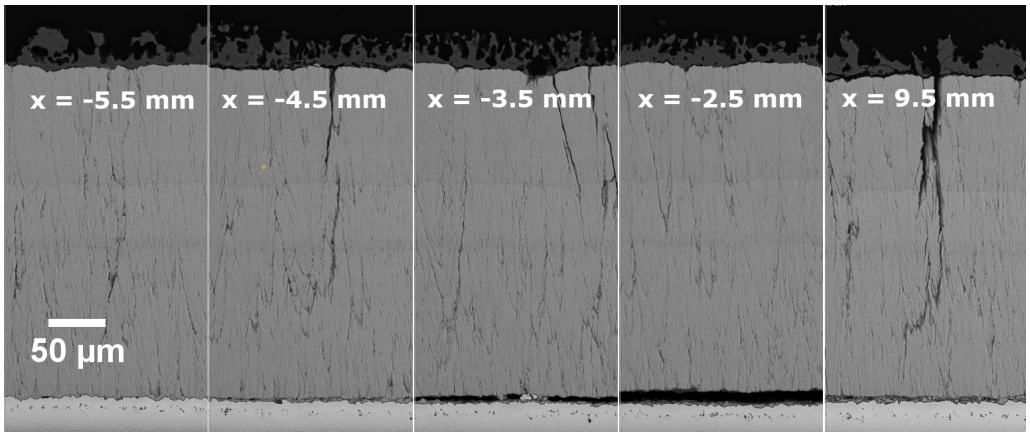


Figure 4.18: Extent of delamination across different radial positions. Positive values of X correspond to areas to the right of the cross section centre, and negative values correspond to the left.

Despite the extensive delamination, no coating spallation was observed. This points to a high intercolumnar bond strength for the LT-6' sample. This delamination likely occurred during the forced cooldown following exposure, when compressed air quenched the front and back surfaces of the substrate. The observed delamination can be explained qualitatively through the model for the mechanics of coating delamination in thin films developed by Evans and Hutchinson (102), subsequently modified by Begley et al (240, 241). This model predicts a smaller safe operation zone for cold shock delamination for coatings with higher in-plane stiffness.

Interestingly, the mechanism of delamination also departs from that predicted by the model since the delamination occurred at the TBC-TGO interface rather than within the TBC, at the depth of CMAS infiltration. This absence of shelf cracking exhibited by the coating also points to a different effect of the microstructure on the mechanical properties of the coating, namely the interfacial toughness at the TBC-TGO interface. While the fracture toughness of the CMAS-Infiltrated Nominal TBCs is smaller than the interfacial toughness, thus resulting in strain energy being released through the nucleation and

growth of cracks within the coating, strain energy release occurred at the interface between the 7YSZ-LT coating and the TGO. This could be interpreted as changes to the microstructure in the nucleation zone, not analysed separately in the current project, affecting the fracture toughness of the coating at the interface.

While it is likely that this crack developed during the cooldown period, rather than during exposure, the effect that the latter would have had on the surface temperature is worth discussing, to qualify the reliability of the results obtained for the infiltration depth of the LT-6' sample. The occurrence of delamination, from the thermal conduction perspective, is akin to the introduction of an additional layer in the substrate-coating system between the TGO and the coating. This layer is comprised of air, which at 1300 °C has a thermal conductivity of ca. 0.08-0.10 $W/m \cdot K$ (242), which is significantly smaller than that of 7YSZ TBCs at around 1 $W/m \cdot K$ (30). However, it should also be noted that this layer is relatively thin in comparison to the TBC thickness.

This additional layer between the heat source and the compressed air cooling the substrate would act as insulation between the substrate and TBC. As a result of this insulation, the temperature across the TBC thickness would likely increase. This increase would favour infiltration by reducing the viscosity of the infiltrating CMAS, meaning that the occurrence of delamination during testing would represent a more adverse case for the 7YSZ-LT coating. This further reinforces the need to accurately measure the surface temperature at the local level, to account for differences to the conductivity on the system that may occur during testing.

4.2.2.1 Accurate measurement of surface temperature

In order to correlate the surface temperature to the infiltration depth, the temperature measured for the surface temperature of the sample needs to be resolved to the metallographic section location. A method to probe the surface temperature, measured by the IR camera in a section with a specified location, orientation and shape was developed for this end. As depicted in Figure 4.19, the method consisted in drawing a virtual "probe" over the sample surface.

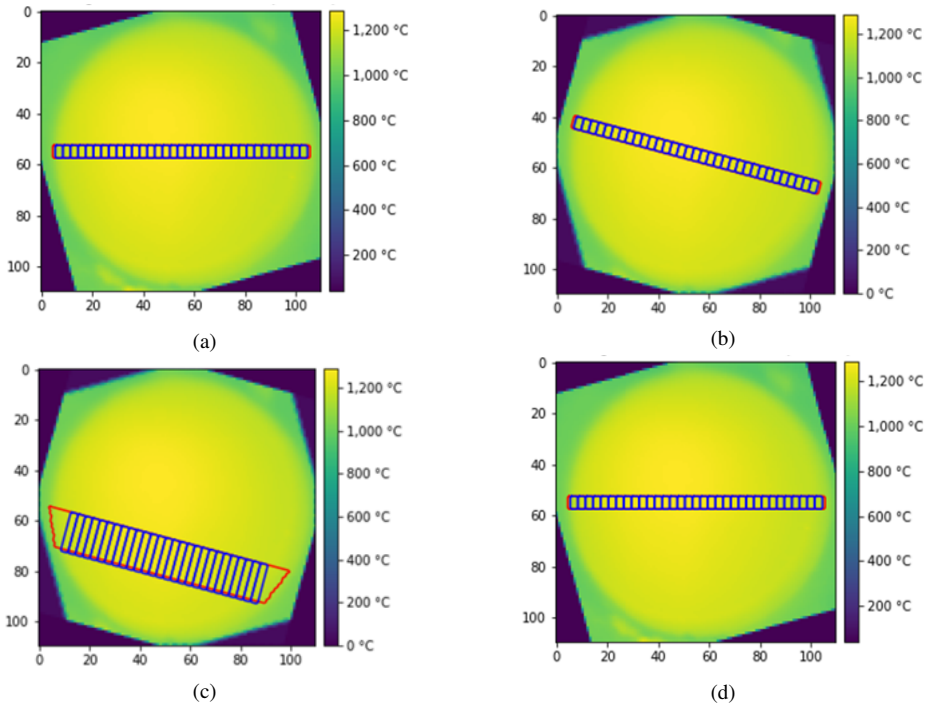


Figure 4.19: Method for probing the surface temperature at different locations in the sample surface. The blue squares correspond to an the area constrained to the inscribed rectangle, and the red trapezium shows a better fit to the circular substrate edge. X and Y axes in pixels - actual diameter of sample 30 mm.

Different positions and orientations of the probe could be drawn to match the location of the probe to that of the metallographic section. Additionally, the inscribed rectangles could be extended to cover a trapezium, to better capture the circular edge of the burner rig sample, especially relevant if a wide rectangle dimension was to be used. For each of the rectangles within the virtual section, the average temperature was calculated, based on the calibrated values of the IR camera.

Figure 4.20 shows the radial temperature distribution measured by the method developed for the location depicted in Figure 4.19a. This profile shows the asymmetric distribution of the surface temperature over the sample surface.

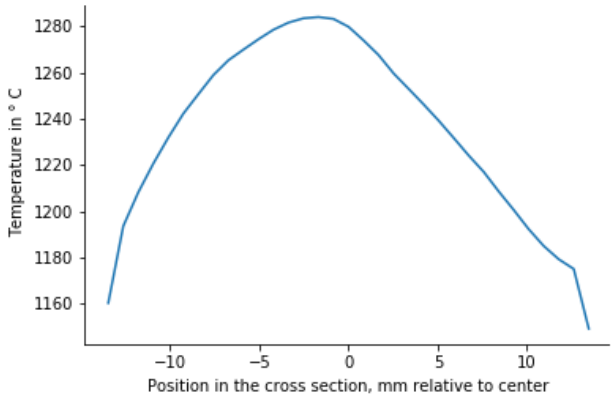
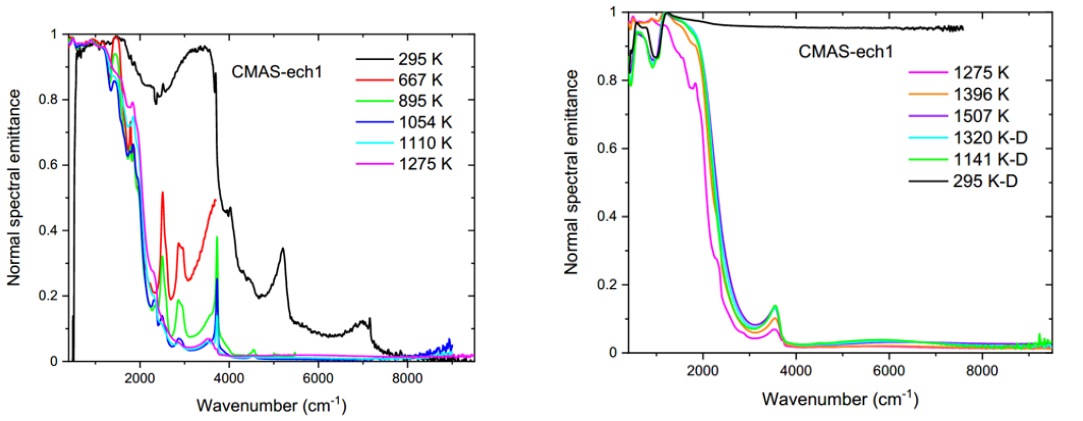


Figure 4.20: Radial temperature distribution for a virtual “probe”.

This distribution could be used to calculate the thermal profile throughout the test

duration for any given point in the sample surface. However, as discussed in Submission 4, the determination of TBCs with thick CMAS deposits relies on accurate information about the thermoscopic properties of the CMAS glass at the relevant temperatures. The IR camera used was calibrated for the emissivity of 7YSZ at the range of temperatures of interest, taken as $\varepsilon = 1$. However, at the time of testing, the emissivity of CMAS was not known.

High temperature emissivity measurement was undertaken at CEMHTI-New Orleans following the international visit using the apparatus described in De Sousa et al. (243). C33 CMAS (See Submission 2) sprayed over a polycrystalline Alumina disc was heated up from room temperature up to around 1300°C, to induce melting. The emissivity of CMAS at different temperature intervals during heating up and subsequent cool-down was measured. C33 CMAS showed a lower emissivity than the calibration value ($\varepsilon = 0.95$-0.98 over 1000 °C) for CMAS undergoing melting from powder form. The temperature dependent emissivity spectra for CMAS is shown in Figure 4.21.



(a) Measurements taken during heating up from room temperature to 1275K

(b) Measurements taken during heating up from 1275K to 1507 and subsequent cool-down

Figure 4.21: Emissivity spectra for CMAS recorded at different temperatures during the heating up and cool down cycle performed. Temperatures in K. K-D indicates measurements during cool-down.

The collected temperature-dependent emissivity data can be used for the calibration of the Infrared cameras, improving the accuracy of the substrate surface temperature measurement for future tests. Unfortunately, for the tests already conducted, it is not possible to obtain an accurate temperature reading that would enable a model based comparison such as the one described.

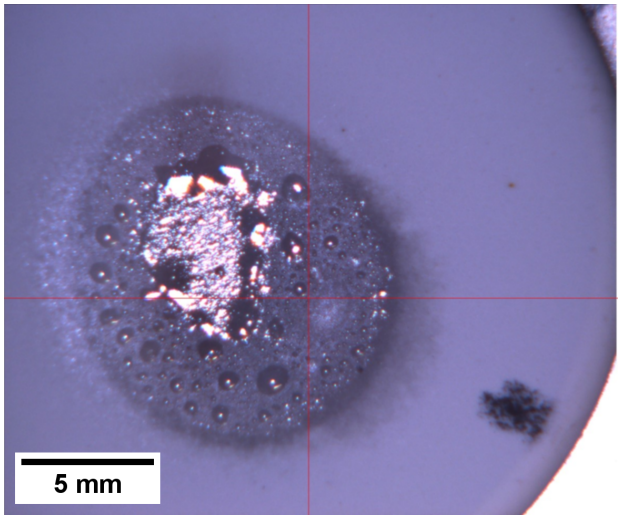
4.2.2.2 Segregation and crystallization behaviour of CMAS under thermal gradients

The samples tested during the visit to FZJ, reported in Submission 4, were analysed in Cranfield after concluding the international visit. For readability, the sample names and corresponding test conditions are reproduced in Table 4.5.

Table 4.5: Experimental conditions for the exploration of shorter high temperature exposure times to induce partial infiltration, and resulting dosage

Sample ID (Submission 4)	Coating System	Pre-loading time [min]	Hot time [min]
MT-1	7YSZ-Nom.	20	15
MT-2	7YSZ-Nom.	N/A	15
PTC-1	7YSZ-Nom.	N/A	6
PTC-2	7YSZ-Nom.	6	6

Elemental segregation was observed for MT-1 and MT-2. It was also expected to have happened in the rest of the experiments in Tables 4.4 & 4.5, based on the presence of Åkermanite within the deposit in sample Nom-6 detected via XRD. Therefore, the EDS maps gathered for the tested conditions were also analysed to assess the level of segregation. Additionally, EBSD maps were gathered for selected samples to detect the presence of crystallographic phases and locate their presence within the TBC-deposit system.



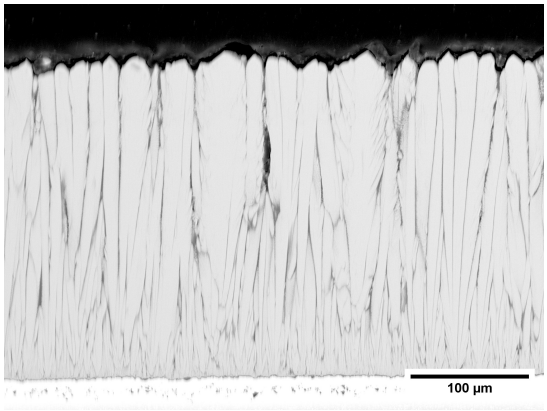
(a)

Figure 4.22: Surface image for sample Nom-6', showing a 'glassy' deposit.

4.2.2.2.1 Elemental mapping The cross sectional imaging and elemental mapping revealed deposits in the samples in line with the visual appearance in Figure 4.22. Sample PTC-2, showing a matte surface with little trace of a glassy deposit, had no homogeneous layer of deposited CMAS, even at the infiltration centre positions, as shown by Figure 4.23.

The presence of isolated deposit areas further from the center, and their absence in the sample centre, suggest that a complete infiltration of the deposited CMAS in the sample hotspot occurred. As the deposit temperature increased, its viscosity will have decreased, allowing for the deposited CMAS to more effectively wet the TBC columns and infiltrate down the intercolumnar porosity.

In contrast, fully developed deposit layers could be observed in both PTC-1 and Nom-6'. In the case of PTC-1, the presence of the homogeneous deposit, in contrast with the similarly loaded PTC-2 sample, suggests a speed of infiltration and saturation that lags

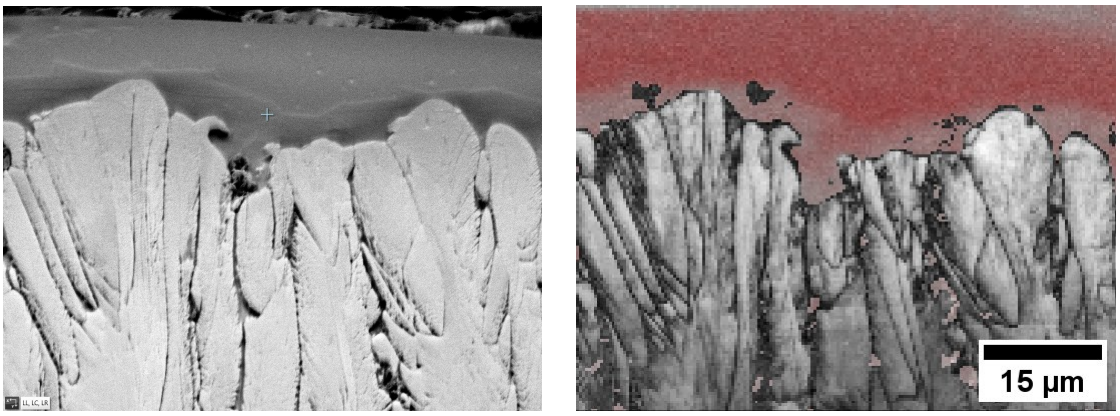


(a)

(b)

Figure 4.23: BSE micrograph of sample PTC-2 in radial positions a) x = 0.5mm and b) x = 7.5mm.

behind the rate of CMAS deposition. This is also consistent with the lower level of CMAS saturation exhibited by PTC-1.

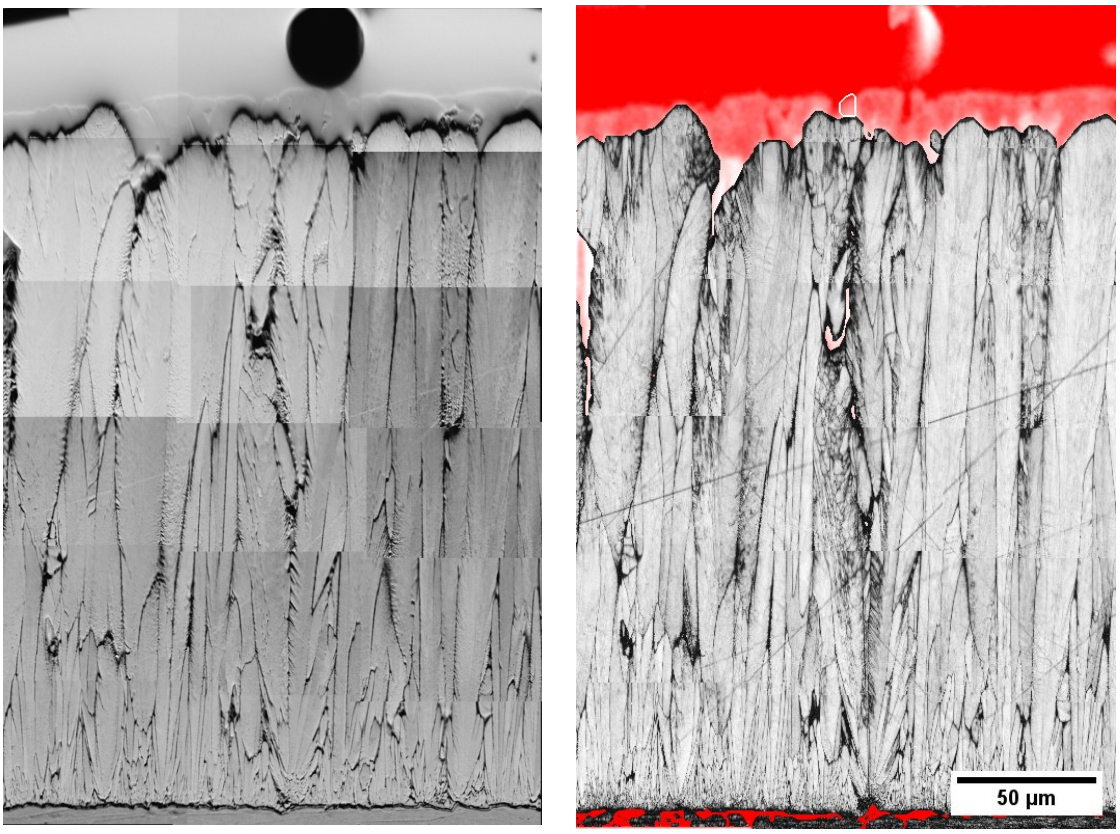


(a) (b)

Figure 4.24: Micrographs of sample PTC-1 showing a) Forward Scattered Diode image, b) Aluminium EDS map for deposit overlaid on band contrast image - captured by EBSD camera.

Regarding the elemental segregation for samples PTC-1 and Nom-6', the corresponding EDS maps - Figures 4.24b & 4.25b, confirm that the previously observed elemental segregation also occurred during these experiments. Furthermore, the deposit areas with

lower Al content seem to exhibit granular and angular morphologies, suggesting the presence of a crystalline phase within them.



(a) (b)

Figure 4.25: Large area map montages of sample Nom-6' showing a) Forward Scattered Diode image, b) Aluminium EDS map for deposit overlaid on band contrast image for TBC.

4.2.2.2.2 EBSD mapping of crystalline nature of Deposits. The crystalline nature of the lower aluminium areas, and the presence of Melilite and Åkermanite were investigated by EBSD mapping of the observed areas that exhibited elemental segregation.

This allowed to confirm the crystalline nature of the segregated area in Nom-6', wherein the Mg-rich, low-Al phase was indexed as Åkermanite, confirming the XRD results. Figure 4.26 shows the large area EBSD map of Nom-6', highlighting the Åkermanite grains. The colour code corresponds to the IPF projected on the X direction.

The Åkermanite detected in the EBSD map seems to not have a strong texture, based on the spread of the IPF colouring. This becomes even clearer when looking at the Inverse Pole Figure for Åkermanite, comparing its apparent texture to that of Tetragonal zirconia, as shown in Figure 4.27

The development of texture in Thermal Barrier Coatings, has already been discussed in 3. At nominal deposition conditions, crystals whose <110> direction aligns with the through-thickness direction outcompete crystals growing with different orientations, resulting in the development of crystallographic texture.

Despite the apparently crystalline morphology observed in the deposit in sample PTC-1, Figure 4.24a, none of the Melilite group crystals were indexed in the corresponding



Figure 4.26: EBSD map of Åkermanite mapped over band contrast image for sample Nom-6'. Interpretation of the colour scheme as per Figure 4.27.

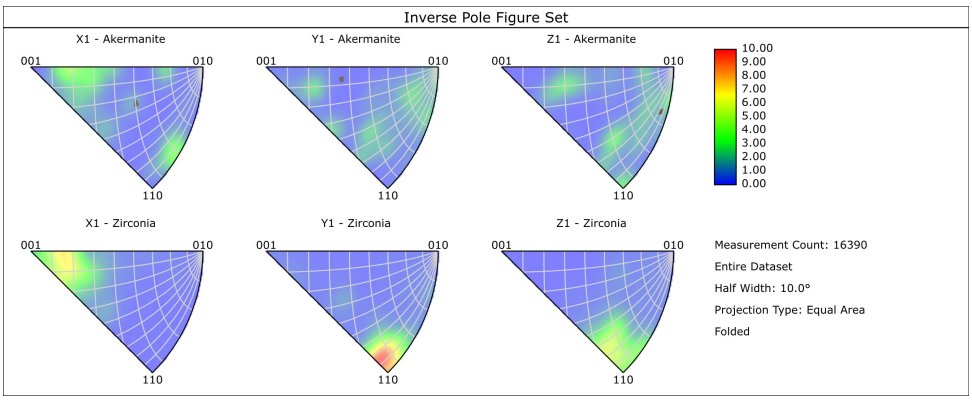


Figure 4.27: IPF sets for Åkermanite and tetragonal Zirconia for the EBSD map in Figure 4.26. The multiple of uniform density values demonstrate a stronger texture in Zirconia relative to Åkermanite, particularly in the Y1/<110> direction.

area. Furthermore, the band contrast image, Figure 4.28 shows a very low contrast for the area expected to be crystalline, suggesting an amorphous nature instead, with the exception of two potential grains (highlighted). The sections of the EBSD map within the TBC indexed as Åkermanite are the result of misindexing, as they clearly overlap with the ceramic columns.

4.2.2.3 Phase diagrams and Equilibrium calculations

Thermochemical simulations were performed with CALPHAD software FactSAGE (244, 245) in order to understand the effect of the observed elemental segregation on the stable phases and solidification of the melt. Figure 4.29 shows the effect of the Al_2O_3 content on the liquidus field of CMAS at 1300°C. It can be seen that a reduction on the Alumina

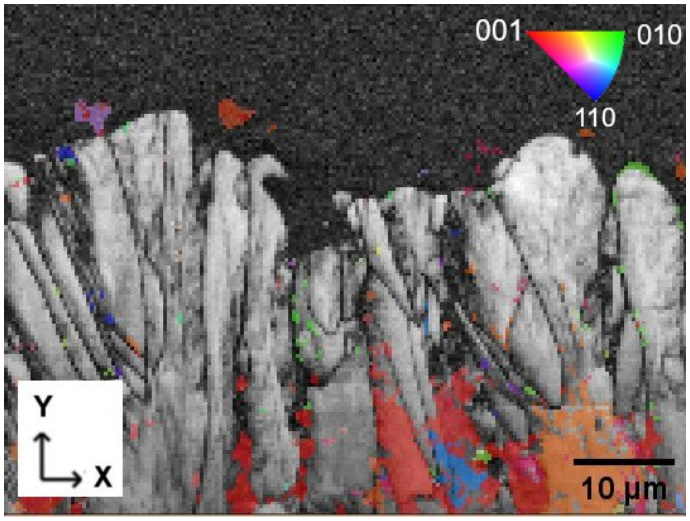
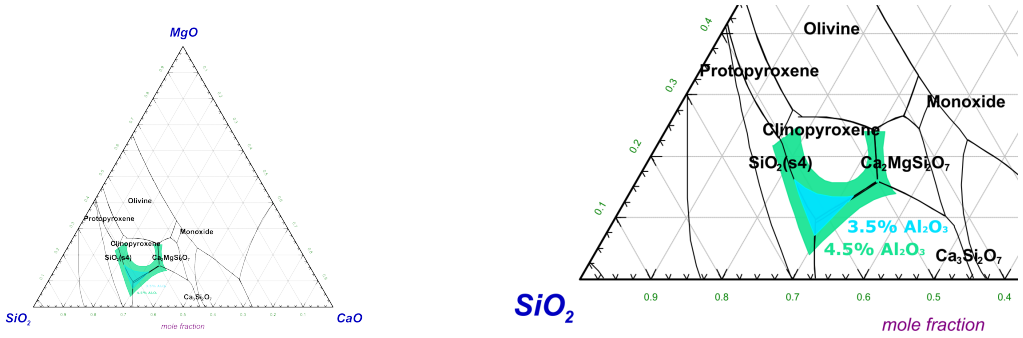


Figure 4.28: EBSD map of Åkermanite mapped over band contrast image for sample PTC-1. Inverse Pole Figure (IPF) colour code for projection on Y coordinate are inset.

content results in a shrinking of the molten field. This would be consistent with the observed segregation and crystallization behaviour.



(a) (b)

Figure 4.29: 1300°C Liquidus fields for different Alumina content isopleths projected in CaO-MgO-SiO2 ternary diagram.

A Scheil-Gulliver equilibrium simulation was performed to understand the phase evolution during cooldown of the CMAS melt. The Scheil-Gulliver calculation, as opposed to the equilibrium cooling, assumes no diffusion between the liquid and solid phases. The solidifying phases predicted by the simulation for the cooling route are presented in Figure 4.30.

The simulation predicts initially the preferential solidification of Åkermanite at 1300°C followed by Wollastonite, which becomes the predominant solidifying phase at ca. 1250°C. It should be noted that the thermochemical simulations predict the likely phase to solidify, but do not calculate the likelihood of crystallization. This means that the equilib module in FactSAGE (244) can not predict the solidification of glass, as shown by the fact that the simulation predicts the entire molten slag solidifying into crystalline phases.

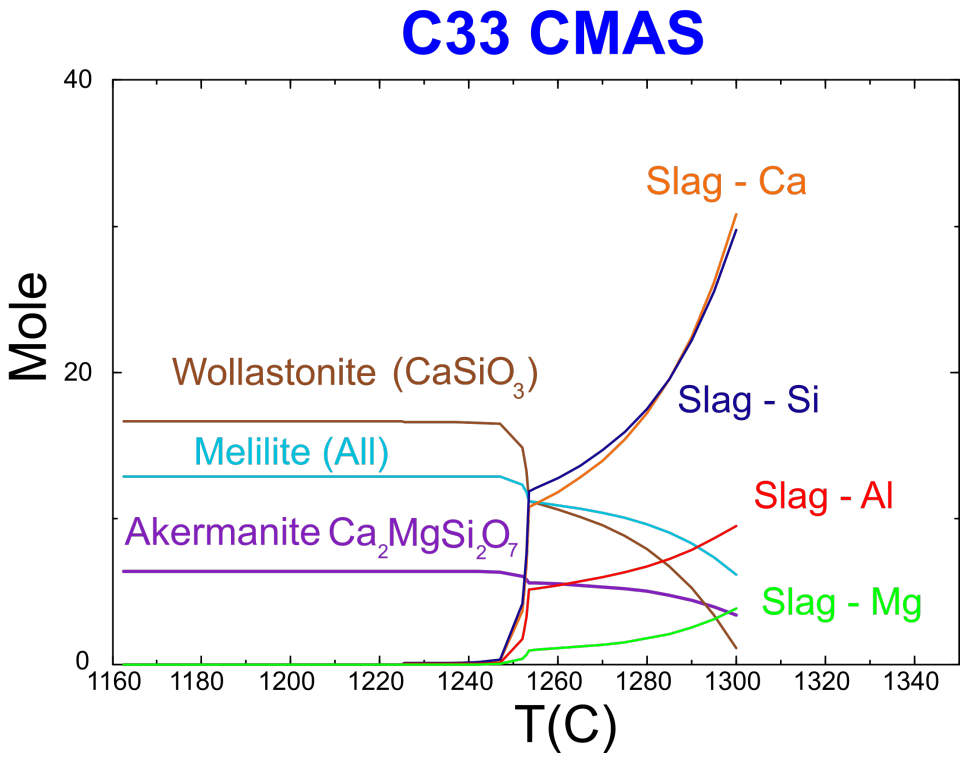


Figure 4.30: Phase evolution of the C33 composition melt under Scheil-Gulliver cooling conditions, calculated between 1300°C and 1100°C.

4.3 Summary of findings and conclusions

1. CMAS infiltration depth was effectively measured by CIMM.
2. Partial infiltration was induced in model TBCs both in isothermal and thermal gradient conditions.
3. A marked influence of the microstructural features on the CMAS infiltration kinematics was observed for LowK systems.
   (a) Coatings with smaller crystallographic grains and column widths showed an increased resistance to CMAS infiltration, both in isothermal and gradient conditions.
      i. The difference between the average infiltration of systems tested in isothermal conditions was of up to 100 μm (between LowK-Nom and LowK-LLT tested for 270 s).
      ii. The infiltration depth spread does not show statistically significant differences between the tested systems for all conditions tested.
      iii. Under gradient conditions, 7YSZ-LT showed a ca. 100 μm reduction in infiltration depth when compared to 7YSZ-Nom tested for an equivalent time, and approximately 50 μm reduction against 7YSZ-Nom exposed for half the time (3 minutes).

(b) For equivalent infiltration depths, the saturation level at the infiltration front was approximately 50% higher for coatings with smaller grains and thinner columns under gradient and isothermal conditions.

i. The spread in saturation level complicates determining consistent statistically significant differences between the model TBCs, even when the average trend supports this difference.

ii. For systems tested under thermal gradient, the level of saturation of the system with thinner columns reached 3 times that of the nominal coating system in the outer edges of the area being infiltrated.

4. The microstructure was also found to have a significant effect on the thermomechanical behaviour of CMAS-exposed TBCs.

(a) Coatings with thinner columns, which have a reduced intercolumnar porosity width, exhibited vertical cracking in isothermal tests and delamination under gradient conditions.

(b) This was hypothesized to be due to reduced in-plane compliance and reduced fracture toughness at the TBC-TGO interface.

5. The two step infiltration mechanism observed in the initial tests reported in Submissions 4 and 5 was confirmed for the LowK model TBCs.

(a) The first stage consisted in an unsaturated transport of CMAS through the coating thickness, predominantly in large pores.

(b) The level of saturation was not found to be affected by CMAS loading.

(c) During this first stage of infiltration, saturation does seem to increase with infiltration depth, only in isothermally tested samples suggesting that infiltration rates are faster than saturation rates under isothermal conditions.

(d) The second stage occurs once full infiltration has occurred, and consists in the progressive increase in saturation of the porosity open to flow.

(e) The dimension of the intercolumnar pores was found to affect the infiltration speed both in levels of through thickness transport and saturation.

i. Wide intercolumnar pores resulted in relatively fast through thickness infiltration, while exhibiting relatively sluggish saturation.

ii. On the contrary, small sized pores resisted CMAS transport, while being quickly saturated by CMAS.

(f) While this two step mechanism is not predicted by any analytical or numerical infiltration model published, the effect of microstructure on infiltration speed coincides with model predictions.

6. Elemental segregation was observed, exclusively in thermal gradient content. While the exact mechanism for the segregation remain unknown, three hypothesis are proposed:

(a) Spinoidal decomposition of the liquid phase resulting in local composition changes inducing crystallization.

(b) Preferential infiltration of Aluminium locally starving the surface level melt and inducing crystallization of Åkermanite. This is unlikely to be the case, given the absence of Åkermanite detected in isothermal exposures.

(c) Crystallization of Åkermanite, with a limited Aluminium solubility driving segregation of Al in the melt.

7. Åkermanite does not seem to be able to block CMAS infiltration. However, understanding how the interaction between TBO and CMAS affects the solidification kinematics is critical.

   (a) In the case of Åkermanite, Ca additions to the TBC may accelerate crystallization kinetics.

   (b) Even with accelerated crystallization, the ability of Åkermanite in blocking further CMAS infiltration is uncertain.

   (c) However, understanding how thermal gradients affect the interaction between the TBCs and CMAS slags may provide viable routes for the abatement of CMAS infiltration and damage.

8. Gadolinium Zirconate coatings have proved effective in preventing CMAS infiltration for all the microstructures produced.

   (a) For all systems tested, the measured depth of infiltration was limited to the topmost few microns.

   (b) A small difference in the reaction layer thickness was identified for tests conducted at 1300°C, however, longer exposures should be undertaken to confirm the effect of microstructure on the evolution of reaction thickness.

Chapter 5

Erosion resistance of model TBCs

The model TBC systems deposited on Nimonic-75 substrates analyzed in Chapter 3 were tested using the high velocity particle erosion rig at Cranfield University. The test consisted in the injection of controlled dose of Al_2O_3 erodent particles into a compressed air jet aimed at the sample being eroded. The samples being tested were weighed and photographed after being impacted by each erodent dose.

The mass loss of the sample exhibits a linear correlation to the mass of erodent used. The slope of this linear relation represents the erosion rate of the systems being tested. This erosion rate is the inverse of the erosion resistance of a TBC, therefore, high values of the erosion rate correspond to low erosion resistance and vice versa.

The mechanism proposed by Wellman (177) for the mass loss in columnar TBCs is as follows: The tensile and flexural stresses resulting from the column displacement and elastic wave propagating through the coating upon impact results in the opening of feather arm porosity, which acts as crack initiating notches in each individual columns. When sufficient stress is applied, the crack grows until it spans the width of the column, as observed in LowK-Nom and LowK-LR. Fully cracked columns are held in place by the neighbouring uncracked columns. When sufficient columns are cracked in a given location, the interconnected cluster of cracked columns spalls off.

With this proposed mechanism, the higher erosion resistance of coatings with thinner columns is explained through the assumption that impact events result in the cracking of a given column. For thinner columns, the amount of volume and mass lost per impact is reduced, by confining it to a single column with a reduced mass. In other words, the mass loss increases more rapidly with column width than the energy required to crack individual columns, especially if the assumed critical size (in number of contiguous columns) for mass loss is constant.

5.1 LowK TBC systems

Figure 5.1 shows the steady state erosion rates of the tested LowK systems, comparing it to the 7YSZ coatings tested at Cranfield University. Note that, the nominal LowK system shows a higher erosion rate than 7YSZ, as predicted due to its higher dopant content (110). LowK-LT, however, exhibits a lower erosion rate than 7YSZ-Nom

Within the LowK TBC systems, LowK-Nom, LowK-LR and LowK-LT exhibit the expected erosion resistance based on the the column width, according to the findings of

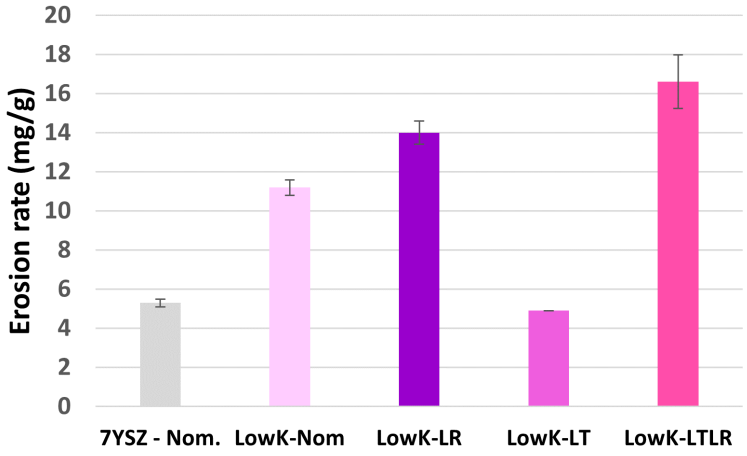


Figure 5.1: Erosion rates of LowK systems. The erosion rate of nominal 7YSZ EB-PVD TBCs is included as a benchmark. Error bars represent 95% Confidence Interval, σ = 1.96.

Wellman et al (6). However, LowK-LTLR, despite having thinner TBC columns than LowK-Nom and LowK-LR, exhibits a significantly higher erosion rate in comparison. When compared to LowK-LT, LowK-LTLR shows slightly wider columns but smaller crystallographic grains, and an erosion rate approximately 2.5 times higher.

To analyze how the changes in microstructural morphology and grain size affects the mechanism for mass loss, cross sectional micrographs of the eroded TBCs were acquired. The details of the eroded microstructures of the model LowK TBCs are shown in Figure 5.2.

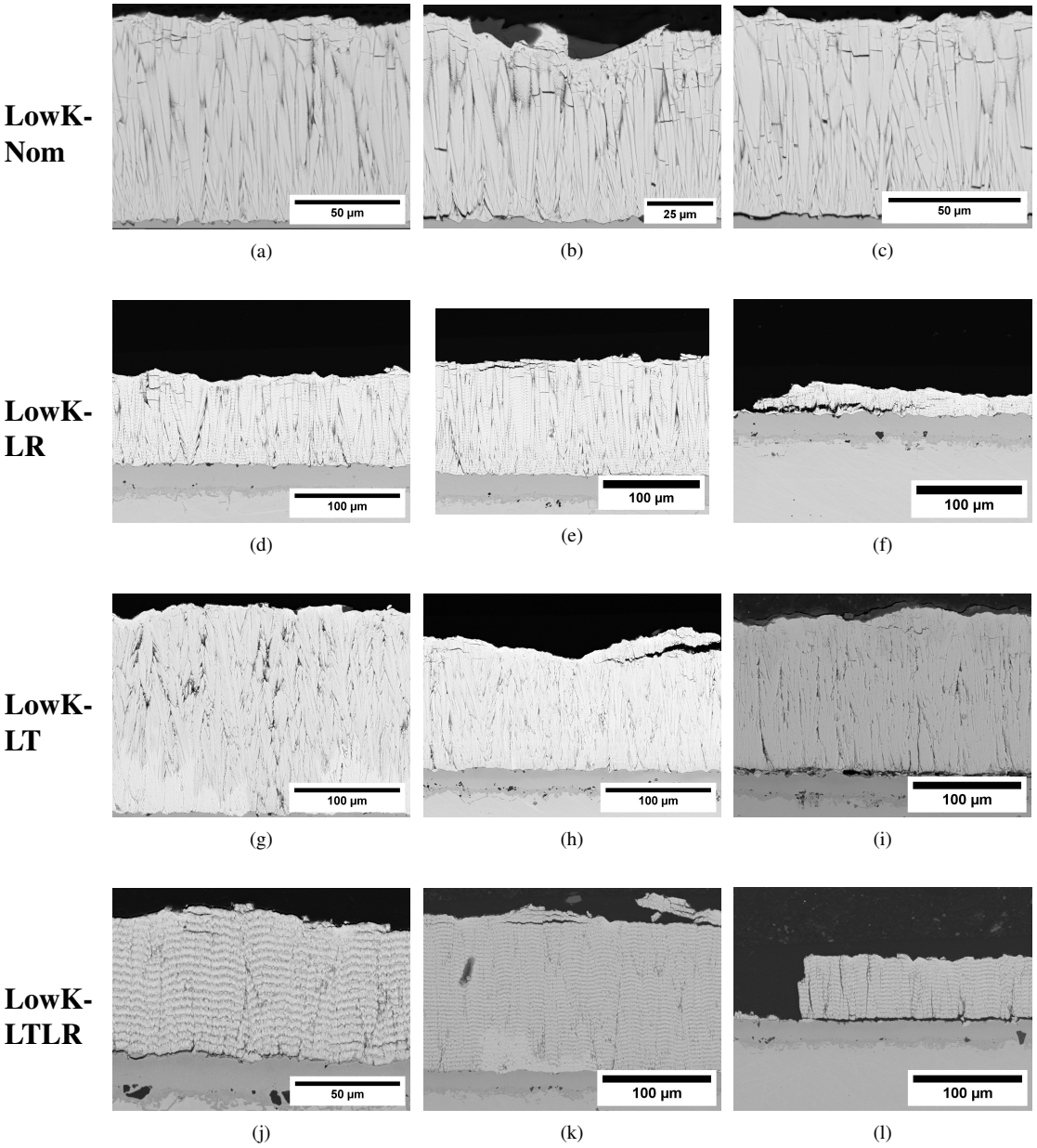


Figure 5.2: Selected micrographs of model LowK TBCs, (a)-(c) correspond to LowK-Nom, (d)-(f) LowK-LR, (g)-(i) LowK-LT & (j)-(l) LowK-LTLR. Micrographs correspond to representative damage morphologies at different magnifications and are not arranged by radial position.

LowK-Nom coatings exhibit the typical damage morphology for columnar microstructures. The TBC surface exhibits a limited amount of consolidation, displayed as the loss of apparent porosity, especially visible in the areas around the embedded particles in Figure 5.2b. A high density of unconnected cracks, each spanning a few columns are present in the eroded coating. The cracks, while concentrated in the area immediately below the densified surface layer are also present deep within the coating, around 70 μm from the coating surface in Figure 5.2c. Delamination damage is also present in areas with significant TBC thickness remaining.

Densification is also visible in the micrographs of eroded LowK-LR coatings, which also show a high density of sub-surface cracks within the coating thickness. However, the length of the cracks that developed in these systems is significantly larger than in LowK-

Nom systems, spanning ca. 100 μm, as compared to the 5-20 μm in the latter. The cracks developed do not follow the layered porosity exhibited by the LowK-LT coating. No delamination damage was observed in the eroded LowK-LR coatings, beyond the thin (20 μm) coating remnants in the area immediately next to the scar edge, as shown in Figure 5.2f.

The system exhibiting the lowest erosion rate, LowK-LT, shows relatively smaller cracks, which are confined to the top 40 μm of the eroded coatings. The few cracks that are most clearly visible seem to have coalesced and grown. The longer cracks present in this coating exceed 100 μm in length. This coating system exhibits both densification - Figure 5.2g - and incipient delamination - Figure 5.2i.

Lastly, fewer cracks are apparent within the remaining thickness of eroded LowK-LTLR coatings. These cracks consist in long delaminations along the periodic porosity present, reaching a length under 100 μm. Parallel cracks seem to be co-located at different heights in the same region of the coating, resulting in crack "stacks". In regions where significant thickness remains, the cracks seem to be confined to the topmost 3-5 "layers", with deeper cracks developing for regions with a remaining thickness of 50-80 μm. These deeper cracks eventually occur at the interface between the TGO and TBC, leading to delamination. The delaminated coating, however remains attached even with delamination cracks with a length of over 2500 μm.

It is interesting to see that the cracks in LowK-LR seem to comprise individual columns and then coalesce across neighbouring grains, in the same way as LowK-Nom However, cracks in LowK-LR grow until they run through a large number (> 10) of adjacent columns, whereas no cracks in LowK-Nom span more than 4-5 columns. This indicates a stronger intercolumnar bond for the low rotation system when compared to LowK-Nom.

Given the similar column and grain size, this should, according to the mass loss model proposed by Wellman (6), result in a reduced erosion rate for LowK-LR, relative to LowK-Nom, as impacts within the already-cracked cluster of columns would not necessarily result in further cracking of the neighbouring columns. This assumption is more likely met with an increasing size of the interconnected cluster, as this would reduce the stress on the distant, yet-uncracked columns.

The results obtained, however, run contrary to this prediction, with LowK-LR showing a higher erosion rate than LowK-Nom The increased intracolumnar porosity exhibited by LowK-LR could be the cause for this reduction in erosion resistance, by reducing the fracture toughness. However, if the embedded porosity was the cause of the reduced resistance to crack growth, it would be expected for cracks to propagate through the layered porosity exhibited by the system, which is not the case. The cause for this difference is, therefore not explained.

System LowK-LT does conform with the expected erosion resistance based on the thinner column and smaller grain size of this system. The strong intercolumnar bond results in a large number of columns being interconnected into clusters, resulting in the aforementioned increase in erosion resistance. It is proposed that this increase results from the relatively large cluster acting as a shock absorber. In the event of a particle impacting these cracked clusters, at a significant distance from the uncracked columns bound to the cluster, the damage to both the uncracked columns at the cluster edge and those under the cracked cluster would be reduced, relative to the damage caused by impacts in regions with no substantial cracking. This shock absorbing mechanism is proposed to

work through dissipation of the impact energy both in the form of elastic deformation of the cluster and increased cracking within the already delaminated portion of the cluster. The resulting erosion rate would be reduced, through the increased damage accumulation required for equivalent mass loss.

Lastly, as already discussed, LowK-LTLR exhibits an abnormally high erosion rate for a coating with thin columns. Observing the damage mechanism, this increased erosion rate can be explained both through a reduced fracture toughness of the periodic porosity layers and a departure from the assumptions of the model proposed by Wellman (110). The former is evidenced by the alignment of the cracks with the porous layers in the coating.

The departure from the model consists in the violation of the assumption that columns act as independent entities, with individual impact events resulting in cracks that can only extend through a single column. In the case of LowK-LTLR, the strong in-plane bonding of adjacent "columns" results in the coating behaving as a continuous layer. This results in a more efficient use of the available strain energy for crack growth, since cracks are not arrested at the column boundaries.

When combining these two effects, the observed behaviour, where the coating seems to exfoliate through the porous layers, gives a significant increase in erosion rate which is observed.

5.2 GZO TBC systems

The relative erosion resistance of the GZO systems, shown in Figure 5.3 corresponds to the one already discussed for LowK systems, suggesting that the effects observed in the microstructure transfer between the model materials studied, even if the effect size varies. In general, it can be seen that all GZO systems have a significantly reduced resistance to particle erosion when compared to t' PYSZ coatings, in line with results reported in the literature.

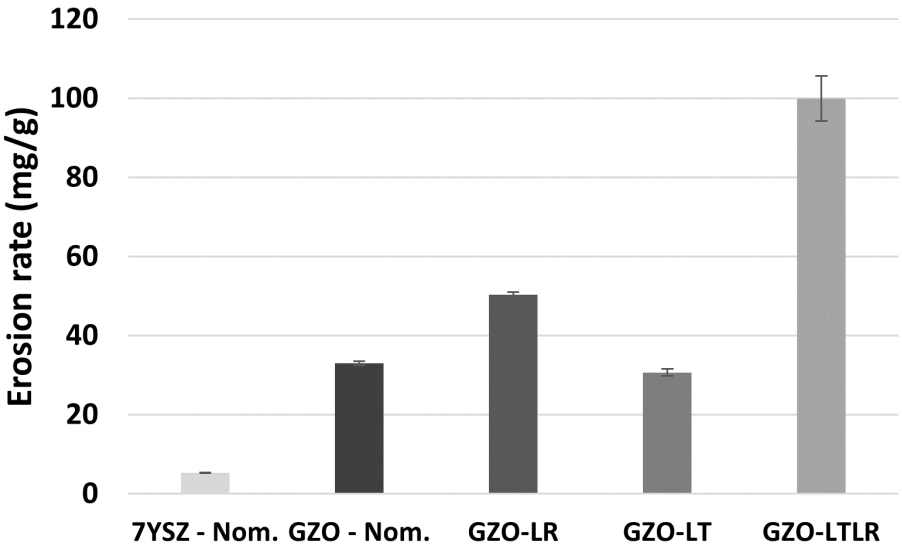


Figure 5.3: Erosion rates of GZO systems. The erosion rate of nominal 7YSZ EB-PVD TBCs is included as a benchmark.

The microstructural aspects of the eroded GZO model TBCs following erosion testing were investigated, with some representative examples of the damage observed shown in Figure 5.4. As expected from the lower toughness GZO material, the cracking exhibited by the TBCs is significantly more extensive than the one observed in the LowK systems. Bearing this difference in mind, some similarities exist between the damage mechanisms observed in LowK and in GZO.

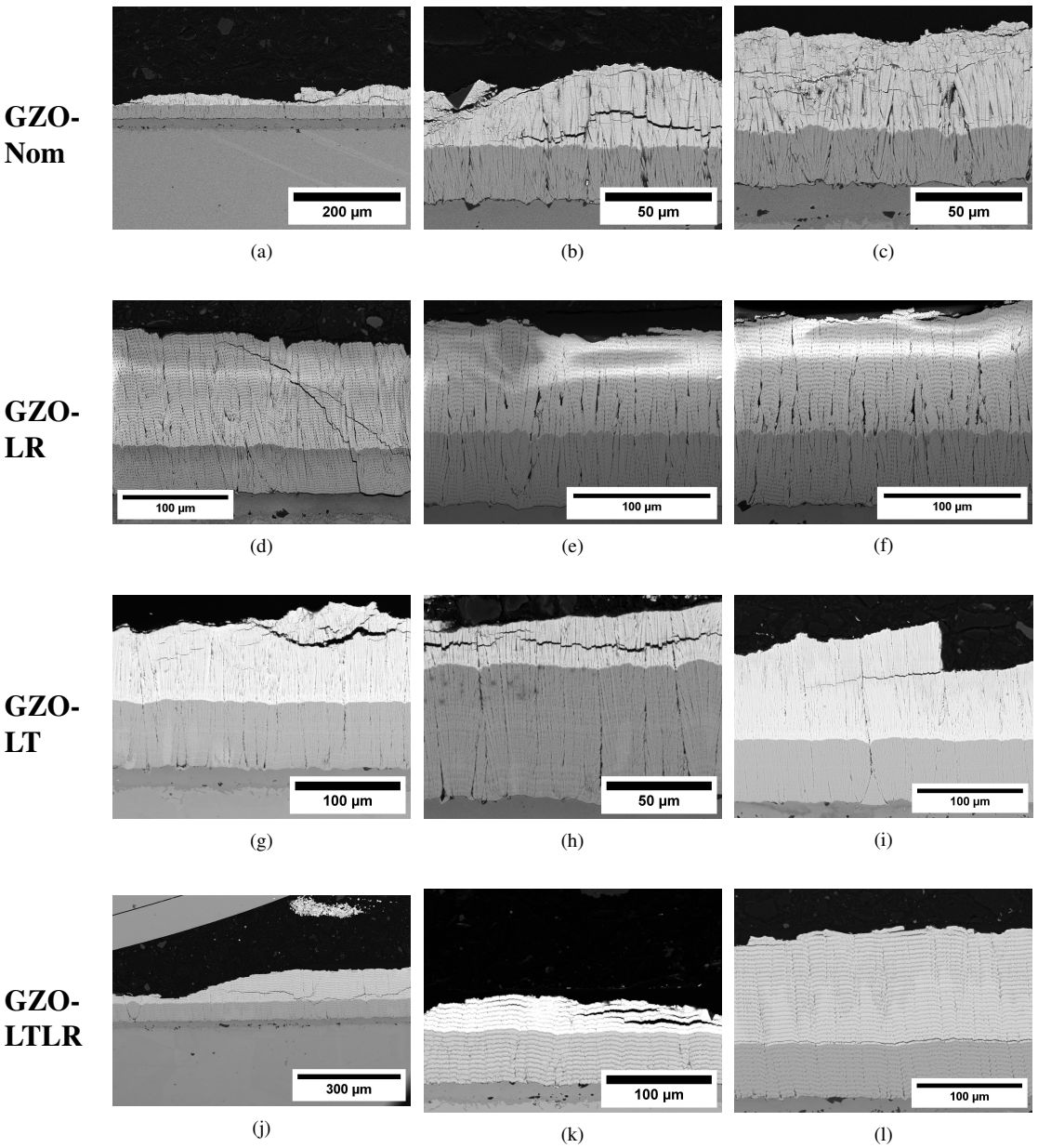


Figure 5.4: Micrographs of model GZO TBCs, (a)-(c) correspond to GZO-Nom, (d)-(f) GZO-LR, (g)-(i) GZO-LT & (j)-(l) GZO-LTLR. Criteria for selection of images and their position as per 5.2.

GZO-Nom exhibits a high density of cracks, distributed across the coating thickness (Figure 5.4c), as was the case for LowK-Nom, but with the mentioned difference of the scale of the cracks present. The surface layer of the GZO layer also shows significant signs of densification, which can be more difficult to identify given the preponderance of cracks, which obscure the loss of porosity. In contrast with the LowK-Nom system,

no delamination was observed on the GZO-Nom coatings subjected to erosion. This could be due to the dissipation of the impact energy through the nucleation and growth of cracks within the GZO layer. Indeed, it can be seen that even in cases when limited GZO thickness remains (Figure 5.4a), the LowK interlayer remains free of cracks, in contrast with the single layer coating.

The erosive damage of the GZO coating deposited under low rotation conditions, GZO-LR, shows characteristics identified for LowK-LTLR. The main differences relate to the extent of plastic deformation and crack opening, as well as the delamination behaviour. GZO-LR exhibits larger densification zones near the coating surface (Figure 5.4f), which are largely absent from LowK-LTLR.

The location of the cracks in GZO-LR coincides with the periodic porosity (Figure 5.4e), but the extent of crack opening is reduced when compared to the one exhibited by the exfoliation mechanism identified in LowK-LTLR(Figure 5.2k), with the crack 'stacks' being largely absent from the identified damage morphology. Delamination also occurred for the GZO-LR systems (Figures 5.4e & 5.4f), but in contrast with LowK-LTLR, and thanks to the relatively large intercolumnar gaps in the LowK interface, the delamination cracks are deflected, limiting the length of coating that is delaminated. The subsequent evolution of the delamination tends towards the exfoliating mechanism identified for the overall material loss in this system.

These differences are largely lost for GZO-LTLR, which behaves in a very similar manner to LowK-LTLR. The only remarkable difference lies in the location of the delamination damage shown by the TBC, which is within the GZO layer, rather than in the TBC-TGO interlayer. This is aligned with the observations regarding crack location in GZO-Nom, whereby the damage is contained within the layer with the lower fracture toughness - GZO. It is also interesting to observe that the crack does not actually occur at the interface between GZO and LowK, but rather at the pore layer (Figure 5.4l).

Lastly, GZO-LT shows a similar damage mechanism to LowK-LT with large cracks progressing through multiple columns (Figure 5.4g). However, the higher compliance and reduced hardness and toughness result for GZO-LT is a phenomena absent from LowK-LT. As in the other bilayer GZO coatings, the large cracks are confined to the GZO layer, with the underlying layer remaining largely undamaged. This difference is likely explained by the difference in intrinsic mechanical properties, but also due to the change that the different layer stiffness imposes on the propagation speed of the elastic wave resulting from the impact. The thin columns of GZO-LT, combined with its mechanical properties also give raise to FOD-like damage, as shown by the Kink band formation visible in Figure 5.4g.

GZO-LR and GZO-LTLR show a higher erosion rate, than LowK-LR and LTLR relative to the comparable nominal coating system for each material system, i.e. GZO-Nom and LowK-Nom, respectively. Part of the difference may be explained by the modification of the propagation of the elastic waves introduced by the bilayer system when compared to the single layer coating. The intrinsic material property difference, combined with the reduction in the fracture toughness introduced by the porosity is also likely contributing to this difference. For the GZO-LR coating, the mixed damage mechanism observed indicates that the coating can be considered an edge case with regards to the assumption for the erosion model proposed by Wellman et al (6). The columns, while cracking preferentially along the layered porosity, do not exhibit the layer-wise bonding shown by

LowK-LTLR and GZO-LTLR, instead behaving as a mix between a single column and a solid layer.

5.3 Summary of findings

The effect of the microstructural features identified in the model Coatings in the erosion resistance of TBCs was evaluated through comparison of the steady state erosion rate obtained through high velocity particle impact testing. This quantitative comparison was complemented by the evaluation of the damage mechanisms observed for each of the systems, in the context of the microstructural quantification introduced in Chapter 3. The main findings with regards to the behaviour of the system and their implication for one of the key analytical-parametric models proposed for the erosive behaviour of TBCs as a function of their microstructure and mechanical properties (6) are discussed below:

1. For the low rotation systems, the introduction of the layered porosity seemed to alter the mechanical properties of the columns with regards to crack growth, resulting in a reduction of erosion resistance. From the crack propagation perspective, this is equivalent to introducing an increase in the critical defect size, leading to a reduction in fracture toughness.

    (a) For LowK-LR and GZO-LR, this resulted in a moderate increase in the erosion rate when compared to the nominal systems, of 0.7 mg/g (+5%) and 17.4 mg/g (+52%) respectively.

    (b) For LowK-LTLR and GZO-LTLR, the resulting increase in erosion rate was more significant, of 3.3 mg/g (+25%) and 66.9 mg/g (+203%) respectively

    (c) The biggest increases in erosion rate were associated with a change in behaviour of the coating with regards to crack propagation.

        - The difference consisted in a gradual transition of the columns behaving as separate entities to a situation where adjacent neighbours behaved as a coherent layer, separated from the underlying coating by the periodic porosity.
        - This transition departed from the assumption of independent columns implicit in the Monte Carlo model developed by Wellman and coworkers (6).
        - This departure explains the higher than expected erosion rates shown by the systems behaving mechanically as layers.

2. For the coating systems not exhibiting the layered porosity - Nom and LT, the reduction in column thickness and grain size resulted in an increased erosion resistance, for both materials.

    - LowK-LT, showed an erosion resistance 2.7 times that of LowK-Nom, with the lowest erosion rate on record for tests performed at Cranfield University.
    - The erosion resistance increase exhibited by GZO-LT was more moderate, with an erosion rate reduction of 2.3 mg/g, corresponding to a 7% improvement in erosion resistance.

3. Bilayer systems - GZO coatings - showed damage that was mostly contained within the GZO layer. This behaviour could be exploited to design coatings with controlled damage propagation paths, spreading the damage to the coating across a large area and reducing the thickness loss, therefore reducing the loss of thermal protection at preferentially damaged locations in the turbine components.

Chapter 6

Cyclic oxidation performance of model TBCs

Cyclic oxidation was the life-limiting failure mechanism affecting Thermal Barrier Coatings during their early adoption for the protection of aeroengine turbine components. The increased substrate durability enabled by Air-plasma sprayed TBCs could even be negated by TBC spallation in critical areas (246).

A substantial research programme was undertaken by the National Aeronautics and Space Administration in conjunction with the Pratt & Whitney Aircraft Group to develop strain tolerant TBC systems that would overcome the cyclic life shortcomings of APS TBCs (247). Within the evaluated systems, the performance of EB-PVD TBCs was "outstanding in all tests except cycling hot corrosion" (247), but were not taken forward for subsequent testing due to the yet-unsurmounted challenge of coating turbine components reproducibly.

Further developments in processing and TBC chemistry - namely the selection of partially (6-8 wt.% Y_2O_3) stabilized zirconia over fully (20 wt.% Y_2O_3) stabilized zirconia - allowed EB-PVD coatings to overcome the reproducibility issues (248). The cyclic performance of these optimized EB-PVD coatings significantly outperformed their APS counterparts (249) which has ultimately resulted in their preferential adoption on turbine component surfaces subjected to highly cyclic, high temperature conditions, such as High Pressure Nozzle Guide Vane and Turbine Blade aerofoils.

As discussed in Submission 1, the cyclic oxidation performance of EB-PVD TBCs depends on the BC strength, surface roughness, exposure temperature, cycle time and in-plane compliance of TBCs. In order to assess specifically the effect of top coat morphology on cyclic oxidation, all other parameters were kept constant. This was achieved through the use of turbine blades to which an equivalent BC (PtAl) was applied. The substrates were prepared for EB-PVD coating by being grit blasted in a similar manner for the same time as described in Submission 2, in order to achieve as homogeneous a surface texture across samples as possible.

All of the systems being evaluated for cyclic oxidation performance, see Table 6.1, were exposed simultaneously to reduce testing condition variability. Note that cyclic oxidation data acquired separately from the current research project, but included for benchmarking reasons, is presented.

As detailed in Submission 2, the cyclic oxidation tests consisted in 3 hour cycles,

Table 6.1: Systems whose cyclic oxidation performance is presented and clarification of systems tested as part of the research project and pre-existing data.

System ID	Explanation	Tested in current project
7YSZ-Nom	Nominal 7YSZ coating	No - Legacy data
LowK-Nom	Nominal LowK coating	No - Legacy data
LowK-LR	Low rotation LowK coating	Yes
LowK-LT	Low Temperature LowK coating	Yes
GZO-Nom	Nominal GZO coating	Yes
GZO-LR	Low rotation GZO coating	Yes
GZO-LT	Low Temperature GZO coating	Yes

during which the samples were exposed to 1190°C. 15 additional minutes were allowed for thermal recovery of the furnace used for undertaking the thermal exposure.

Before discussing the cyclic oxidation results, however, a common framework for the evaluation of the performance and a definition for failure with regards to cyclic oxidation must be provided. Section 6.1 reviews two models for analysing failure of TBCs subjected to cyclic oxidation: Descriptive statistics and lifetime statistical distribution analysis. The failure criteria typically used for each of these models is discussed, and an argument is made for the preferential use of lifetime statistical distribution over descriptive statistics, presenting the results obtained with the former.

6.1 Failure analysis models and criteria setting

The stochastic nature of the growth of EB-PVD TBC columns during deposition results in the production of samples with varying cyclic oxidation lives. Furthermore turbine blades have a varying curvature radii along the blade span, but especially along the aerodynamic profile. The local substrate curvature radii affect growth morphology and strain energy (105, 250), as shown by Figure 6.1. This sample to sample and within sample variability needed to be quantified, if any meaningful comparison between different samples and coating systems was to be made.

The sectioning of the coated turbine blades into three slices and subsequent subdivision into different areas as depicted in 6.2 was used to account for the changing column morphology. Figure 6.2 displays the areas in a section, indicating, through similar colours, those belonging to the Zones of Interest: Pressure side, Leading edge and Suction Side.

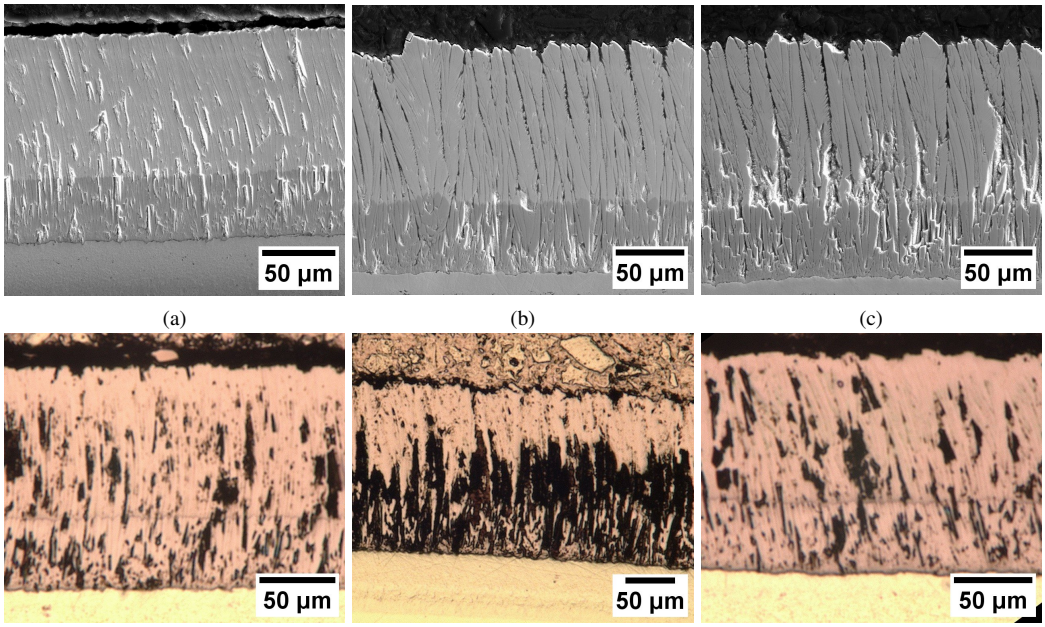


Figure 6.1: SEM (a-c) and optical microscope (d-e) micrographs showing: (a,d) Pressure Side, (b,e) Suction side, and (e,f) Leading edge.

Logging the extent of failure for each of the zones allows to have 3 datapoints for each group, per blade section, while the grouping was used to take into account that areas within each of these groups tend to show a similar coating morphology and cyclic oxidation performance.

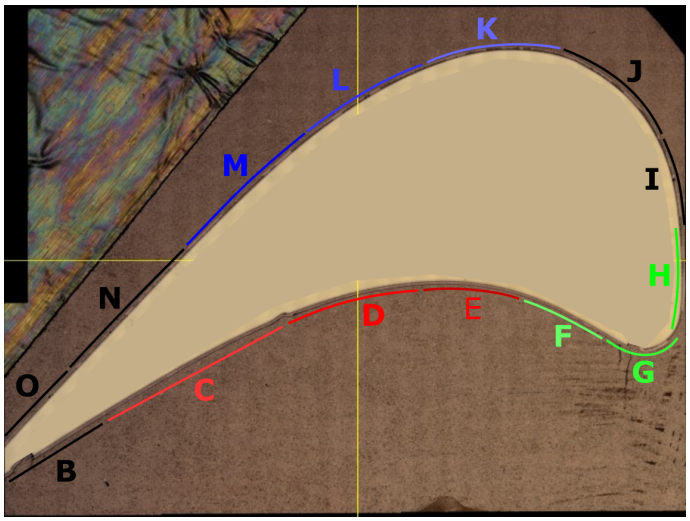


Figure 6.2: Optical microscope micrograph of a turbine blade section with areas B-O overlaid. The colour coding refers to the areas used to assess the Pressure Side (red), Leading Edge (green) and suction side (blue). Note area A is absent from the picture.

Two failure analysis models can be used for comparative assessment of the systems tested: The first is the use of summary statistics to describe the location and spread of the oxidation life data, presented through box plots. The second is the use of statistical distribution, especially the Weibull distribution (251), to represent the failure behaviour. Each of the models used employs a different criterion to define the failure of the different

areas of the blade sections tested. The criterion selected depends on the predicted effect of the coating loss on substrate life and ability to accurately determine when the threshold value has been met. Previous work performed by Rolls-Royce plc (105, 252, 253) on reference systems, is used in the present work as a reference for the analysis.

6.1.1 Descriptive statistics

The first, and simplest model for describing the observations obtained from test results from the oxidation test consists in computing summary statistics to represent the central tendency, dispersion and shape of the distribution. Box plots, showing the quantities corresponding to either the five or seven-number summary are a common way to convey these summary statistics. While this type of statistical analysis can be very useful in providing an easy to digest summary of the characteristics for the life data distribution, the metrics usually depicted, as well as the calculation of the outliers presented implicitly assumes the normality of the underlying data (254, 252).

Failure life data does not usually conform to the normal distribution, instead being better fit by the extreme value distribution. Furthermore, the aforementioned prior work by Chirivi et al. (250) and Morrell et al. (105) used the Weibull distribution as a way to analyse the oxidation life of TBC systems deposited on High Pressure Turbine Blade (HPTB) sections. For that reason, this analysis is selected over the descriptive statistics to present the results obtained in this project.

6.1.2 Lifetime distributions

Using statistical distributions that represent certain behaviour of the system being studied, in this particular case, the failure of the system. A distribution commonly used for describing failure, especially in the context of reliability engineering, is the Weibull distribution, which provides a useful description of the distribution of the smallest value of the quantity of interest. Borrowing an analogy from Hansen (255) - "When [a] chain is loaded, it will be the link with the smallest failure threshold that will break first... the strength distribution of an ensemble of chains is an extreme value distribution, but with respect to the smallest rather than the largest value."

The Weibull distribution is defined by its Probability Density Function (pdf), given by equation 6.1. The interpretation of the pdf, in the context of failure analysis, is the function providing the relative likelihood of a failure occurring for a given value of the life-limiting variable. In the case of the cyclic oxidation testing, the variable considered is time (t).

$$f(t) = \frac{\beta}{\alpha}\left(\frac{t}{\alpha}\right)^{\beta-1} e^{-\left(\frac{t}{\alpha}\right)^{\beta}} \tag{6.1}$$

The pdf presented for the Weibull in equation 6.1 is known as the 2-parameter Weibull, where the two parameters are the characteristic life (α) and the shape parameter (β). The characteristic life figures presented in this Innovation Report are given relative to the characteristic life of 7YSZ-Nom coatings on the Leading Edge, and are hitherto referred to as 'Normalized characteristic life'. To compare the failure life distributions of the different zones for each of the systems, the progress of the area failed for each of the

regions defined in Figure 6.2 are monitored, and logged as a failure once the criterion is met. To conform to the threshold value used by Morrell et al, a region (A-O) was considered failed when 20% of the area in that region had spalled off.

The time of failure for each of the areas was logged, and arranged in order, assigning it a numerical rank, 'n' out of the N failures logged for the equivalent system and area. This numerical rank was subsequently used to approximate the cumulative distribution function (cdf), which corresponds to the cumulative value of the pdf for a given value of the life-limiting variable. For the Weibull distribution, the CDF takes the form given in equation 6.2.

$$F(t) = 1 - e^{-\left(\frac{t}{\alpha}\right)^{\beta}} \tag{6.2}$$

The approximation of the cdf using the rank values is performed using Bernard's equation for the median ranked approximation, following equation 6.3

$$y = (n - 0.3)/(N + 0.4) \approx F(t) \tag{6.3}$$

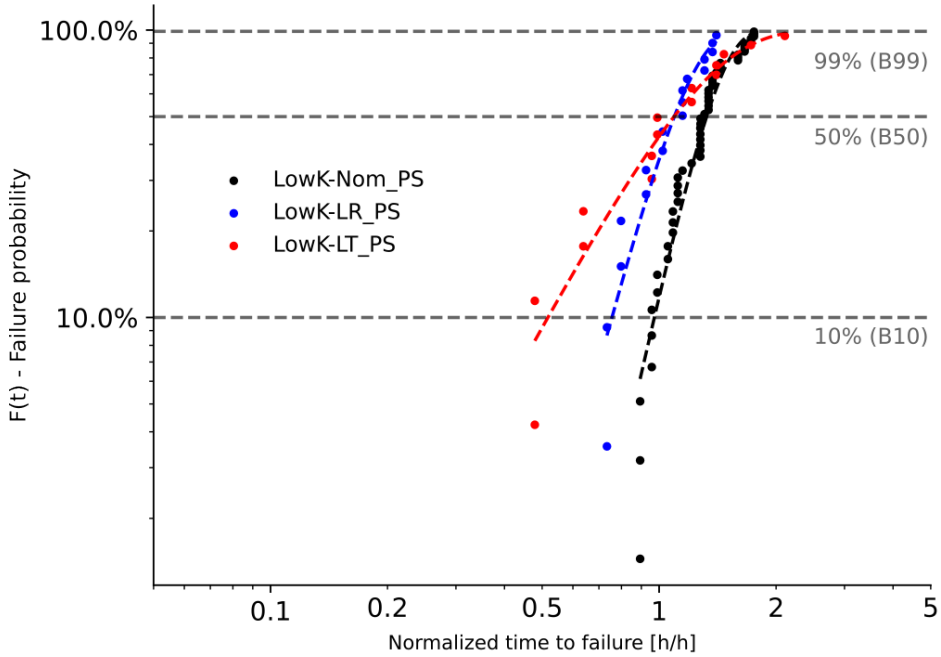
Lastly, ln(ln(1/(1-y))) is plotted against the ln(t), where t corresponds to the times to failure for each sample. Fitting a linear regression against this data allows to obtain the characteristic life and shape parameter, corresponding to the intercept and slope of the linear regression, respectively. For comparing different systems or designs, a direct evaluation of the Weibull plots may prove sufficient to spot differences, if these are sufficiently large. An alternative approach consists in calculating the confidence bounds for the linear fit of the life data, and plotting the contours of the confidence intervals around the α (characteristic life) and β (scale) parameters. The confidence intervals were represented using the likelihood plot functionality of the Reliability library in python (256)

The results from the Weibull distribution analysis provide the most value when accompanied by forensic investigation of the coating microstructure in the failed and interrupted state. Unfortunately it was not possible to conduct such an assessment during the present project due to time constraints. Therefore, the results of the life distribution analysis are presented, to provide a view of the comparative performance of the systems tested with regards to cyclic oxidation. The reported figures for the characteristic life are relative to the characteristic life of 7YSZ coatings in the leading edge.

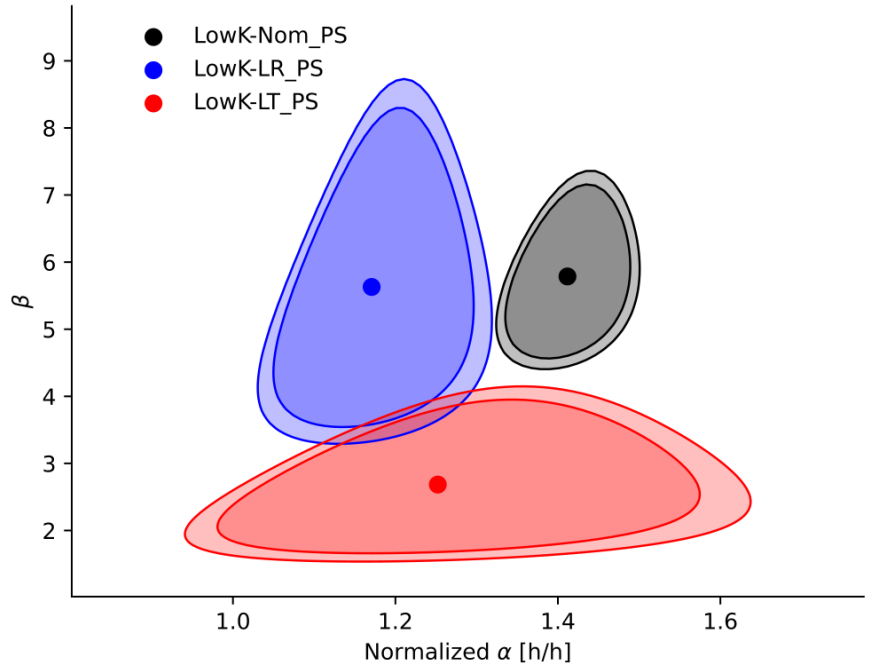
6.1.2.1 LowK systems

The comparison of the Weibull plots for the LowK systems tested is presented in the present Section, along with the confidence intervals, aggregated for the pressure side, suction side and leading edge of the sections tested. Starting from the pressure side, the results of the Weibull analysis performed are shown in Figure 6.3. As previously mentioned, a linear fit of ln(ln(1/(1-F(t)))) to ln (t) is undertaken. However, the y axes on Figure 6.3a and subsequent Weibull plots (Figures are logarithmic, yielding the visual representation of this linear fit, visually non-linear.

The horizontal lines in (a) correspond to the CDF set levels, that is to say, the cumulative probability of failure, set to a 10%, 50% and 99%, respectively. The intercepts between the probability levels and the Weibull trend lines, yield the B10, B50 and B90 lives, respectively. These lives can be understood as the percentage of coatings or components expected to fail by or before the corresponding time at condition.



(a) Weibull plot

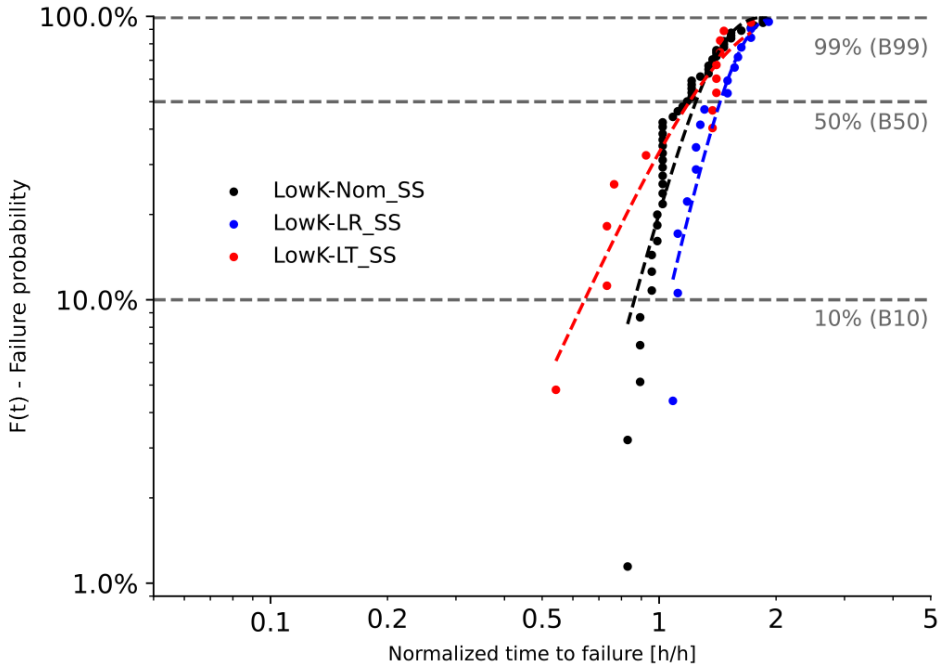


(b) Likelihood plot

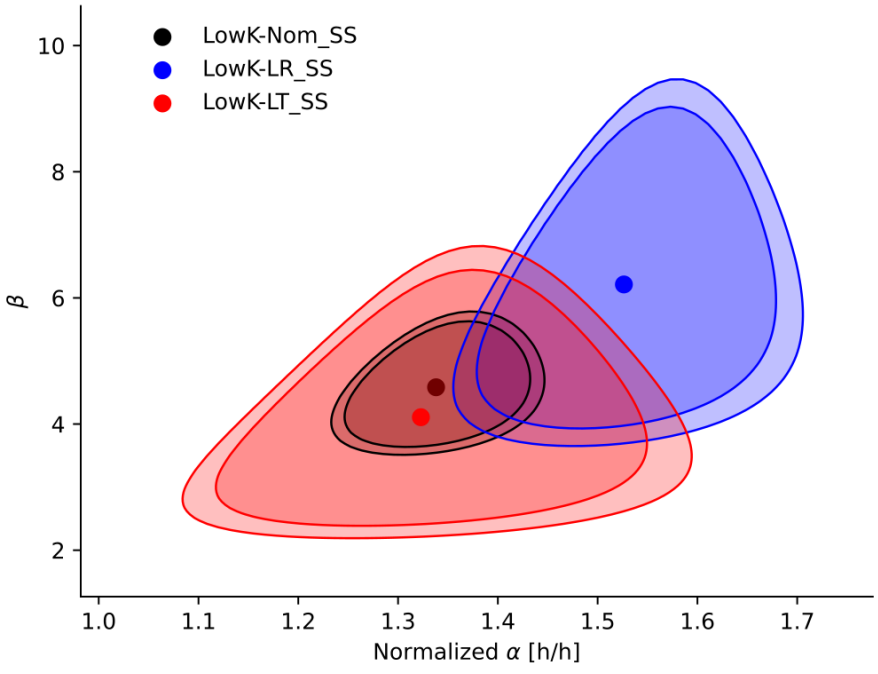
Figure 6.3: Weibull (a) and likelihood (b) plots for the cyclic life LowK coatings exposed to 1190°C in 3 h cycles, corresponding to the pressure side. The inner contour in the reliability plot corresponds to a 90% level of confidence, and the outer to a 95%.

On the pressure side, the nominal LowK coating exhibits a larger characteristic life and slope, meaning a tighter distribution of the life to failure under cyclic oxidation con-

ditions with a confidence of 95%. In the case of the Low Rotation and Low Temperature coatings, they are different with a level of confidence of 90%, given the overlap between the contours at the 95% level.



(a) Weibull plot

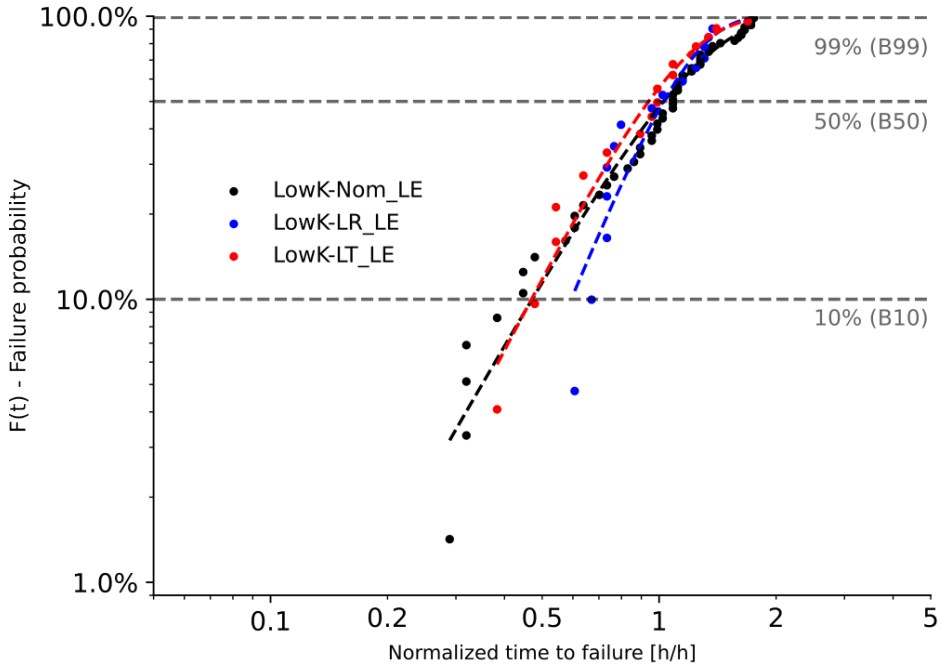


(b) Likelihood plot

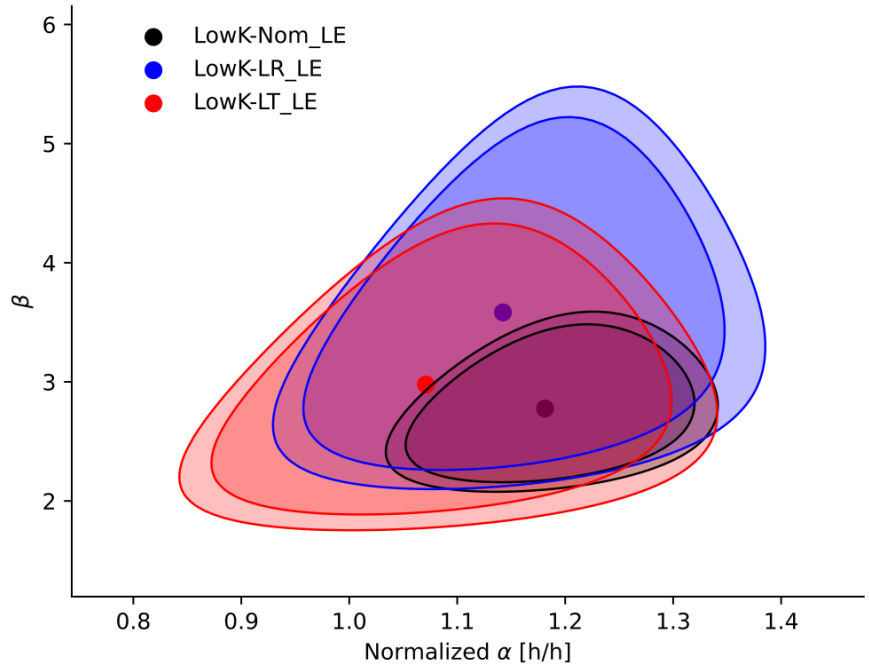
Figure 6.4: Weibull and likelihood plots corresponding to the suction side for LowK systems exposed to 1190°C in 3 h cycles.

Note that LowK-Nom and LowK-LR seem to exhibit vertical clusters of points at the lower life end of the distribution in Figures 6.3 & 6.4. This indicates that a 3 parameter Weibull may have been appropriate to use to better fit the failure data. The third parameter, γ, called the location parameter, represents the failure free life for a distribution. However, not all the systems being compared exhibit

For the suction side, no statistically significant differences can be inferred for the data, as shown by the large overlap between all systems in Figure 6.4. The same assertion can be made about the life of the LowK systems deposited on the leading edge, as shown in Figure 6.5.



(a) Weibull plot



(b) Likelihood plot

Figure 6.5: Weibull and likelihood plot for LowK systems exposed to 1190°C in 3 h cycles, corresponding to the leading edge

Despite the relatively large microstructural differences in grain size, column width and texture observed for the LowK systems tested for cyclic oxidation life, the only clear difference occurs in the pressure side, with the nominal LowK coating outperforming

LowK-LR and LowK-LT in terms of characteristic life and shape parameter. The normalized characteristic life and β parameter values obtained through the maximum likelihood estimation method are displayed for the systems tested discriminated by zone of interest in Table 6.2.

Table 6.2: Characteristic life and beta values for LowK systems. 7YSZ-Nom included as a reference. Numbers **in bold** correspond to highest values for the corresponding zone of interest.

	Normalized characteristic life [h/h]			β (shape parameter)		
	L.E.	P.S.	S.S	L.E.	P.S.	S.S.
7YSZ-Nom (Ref.)	1.00	1.31	1.16	2.6	**9.2**	**12.2**
LowK-Nom	**1.18**	**1.41**	1.34	2.8	5.8	4.6
LowK-LR	1.14	1.17	**1.52**	**3.6**	5.6	6.2
LowK-LT	1.06	1.24	1.32	3.0	2.7	4.1

6.1.2.2 GZO coatings

An equivalent analysis was performed for the GZO coatings tested with the results for the pressure side shown in Figure 6.6. The GZO-LR system exhibits a clearly worse performance when compared to the GZO-LT and GZO-Nom coatings, which do not show statistically significant differences. Despite the ability of the Weibull distribution to accommodate relative outliers relatively robustly, it does seem like a a single early failure in the GZO-LR system may have affected the results, especially with regards to the estimated slope of the Weibull plot.

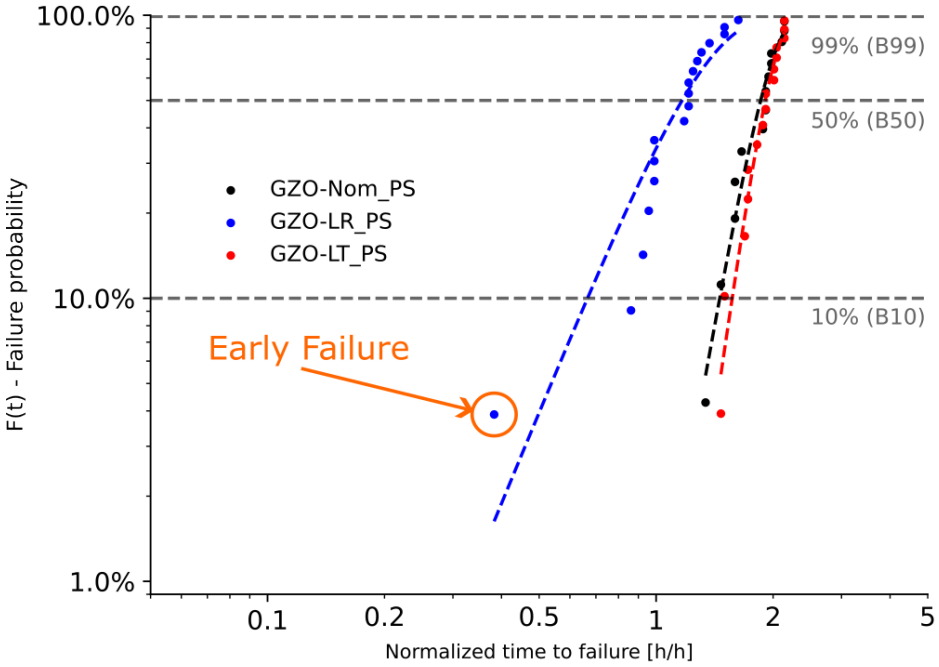
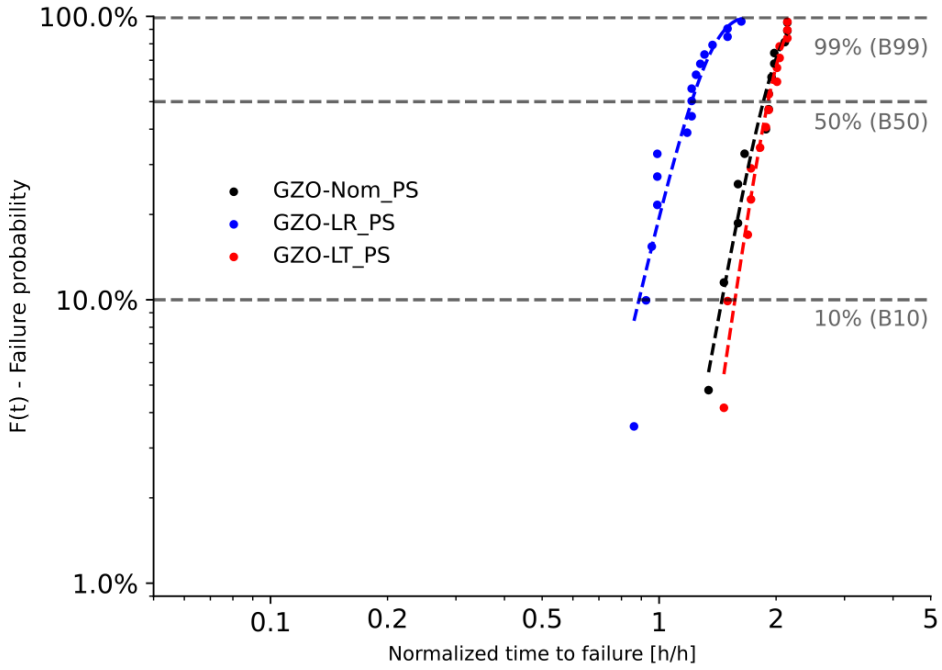
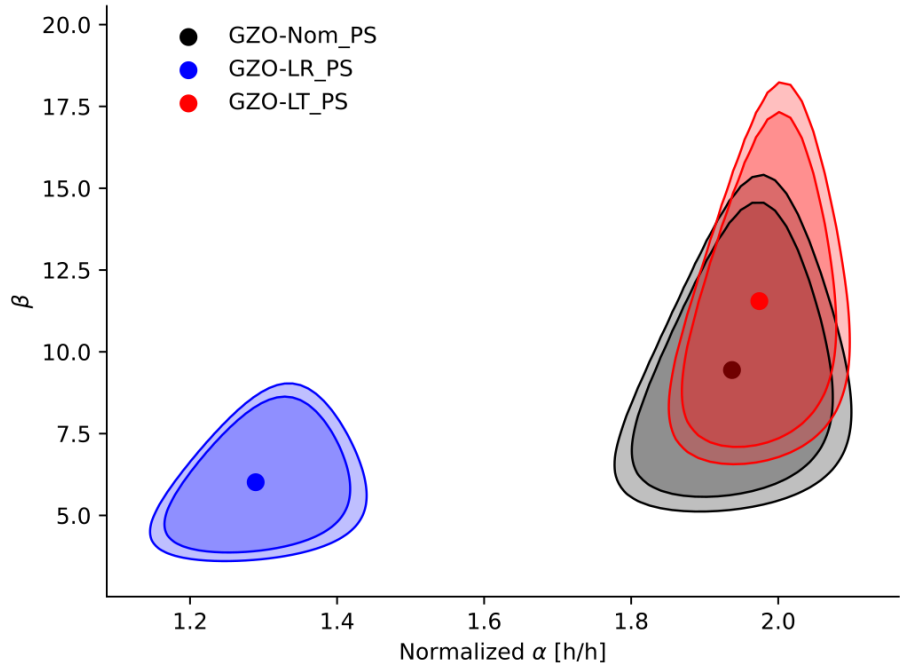


Figure 6.6: Weibull plot for the GZO coatings, corresponding to the pressure side. Note the infant failure for GZO-LR

The re-analysis of the failure data removing the early failure was conducted. The results from the re-analysis are presented in Figure 6.7. Despite the removal of the early failure, the cyclic oxidation life distribution of GZO-LR exhibits a significantly lower characteristic life and shape parameter when compared to GZO-Nom and GZO-LT.



(a) Weibull plot

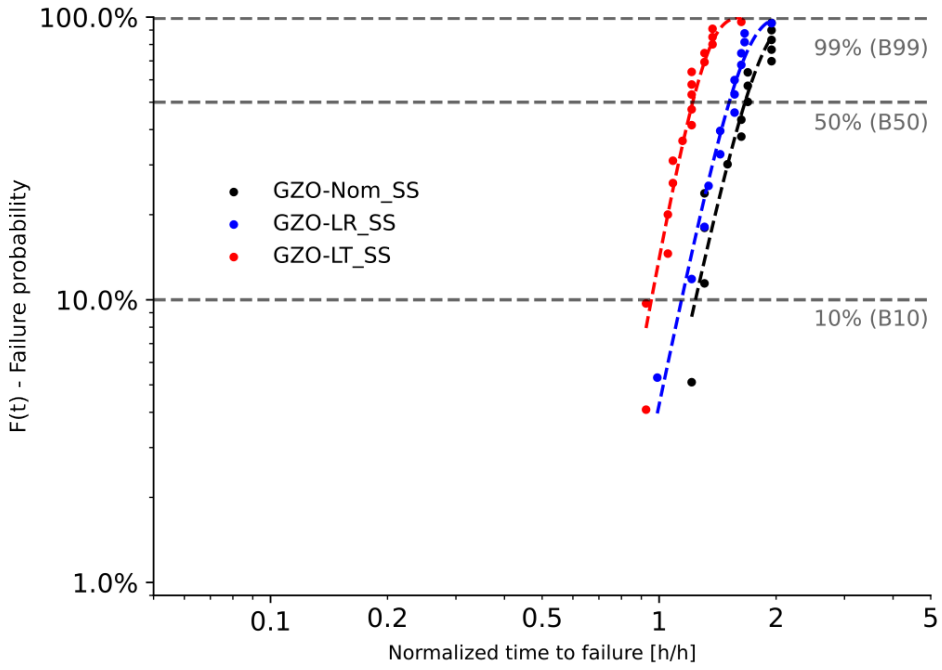


(b) Likelihood plot

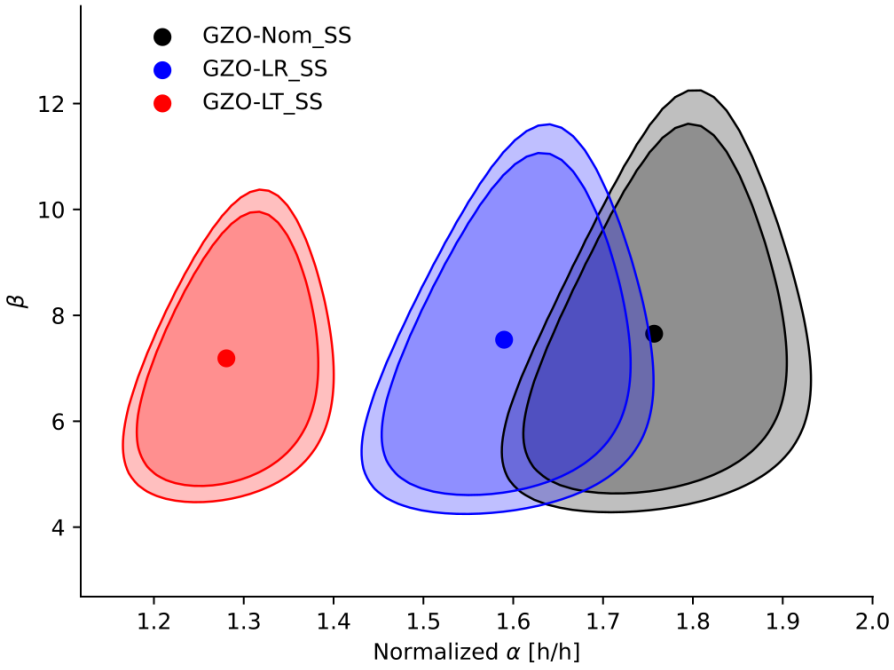
Figure 6.7: Weibull and confidence interval plots for the GZO coatings exposed to 1190°C in 3 h cycles, corresponding to the pressure side. The inner contour in the reliability plot corresponds to a 90% level of confidence, and the outer to a 95%.

For the suction side, the situation is reversed, with GZO-LT being outperformed by GZO-LR and GZO-Nom, as shown in Figure 6.8. Despite the GZO-Nom having a higher

characteristic value according to the linear fit, the overlap in the likelihood plot discards any statistically significant differences between both systems in this zone of interest.



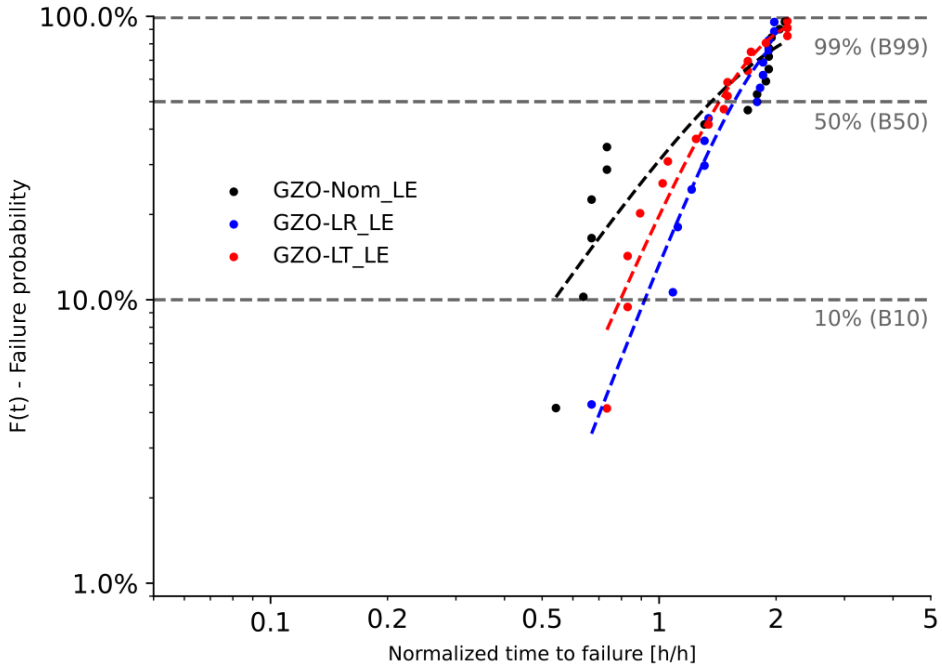
(a) Weibull plot



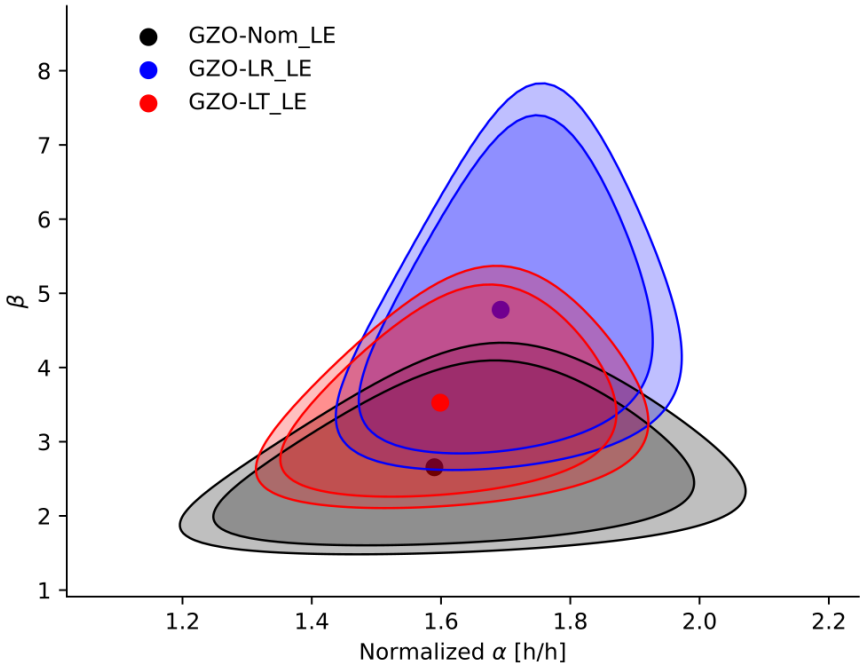
(b) Likelihood plot

Figure 6.8: Weibull and likelihood plots corresponding to the suction side for GZO systems exposed to 1190°C in 3 h cycles

Lastly, a similar situation to that seen for the LowK systems in the leading edge is also observed for the GZO coatings. All of the GZO coatings tested overlap in the likelihood plot.



(a) Weibull plot



(b) Likelihood plot

Figure 6.9: Weibull and likelihood plot for GZO systems exposed to 1190°C in 3 h cycles, corresponding to the leading edge

The normalized characteristic life and β parameter values for GZO are summarized in Table 6.3.

Table 6.3: Characteristic life and beta values for GZO coatings. 7YSZ-Nom included as a reference.

	Normalized characteristic life [h/h]			β (shape parameter)		
	L.E.	P.S.	S.S	L.E.	P.S.	S.S.
7YSZ-Nom (Ref.)	1.00	1.31	1.16	2.6	**9.2**	**12.2**
GZO-Nom	1.59	1.94	**1.76**	2.6	9.2	7.7
GZO-LR	**1.69**	1.29	1.59	**4.8**	6.0	7.6
GZO-LT	1.60	**1.97**	1.28	3.5	**11.4**	7.2

6.1.2.3 Comparison of the coating systems to 7YSZ

The cyclic lives of LowK and GZO coatings deposited in nominal conditions, are compared to the values obtained for the nominal 7YSZ coatings tested at Cranfield, for benchmarking the results obtained using relatively similar microstructures. This comparison is performed for the suction side of the turbine blade profile. The results are presented in Figure 6.10.

It is immediately evident that a clear difference exists between the different coating materials. An inverse relation between the intrinsic material stiffness and the parameter α seems to be apparent for the suction surface results, with GZO exhibiting a characteristic life $\approx$ 32% higher than LowK, and 50% higher than 7YSZ.

6.2 Conclusions

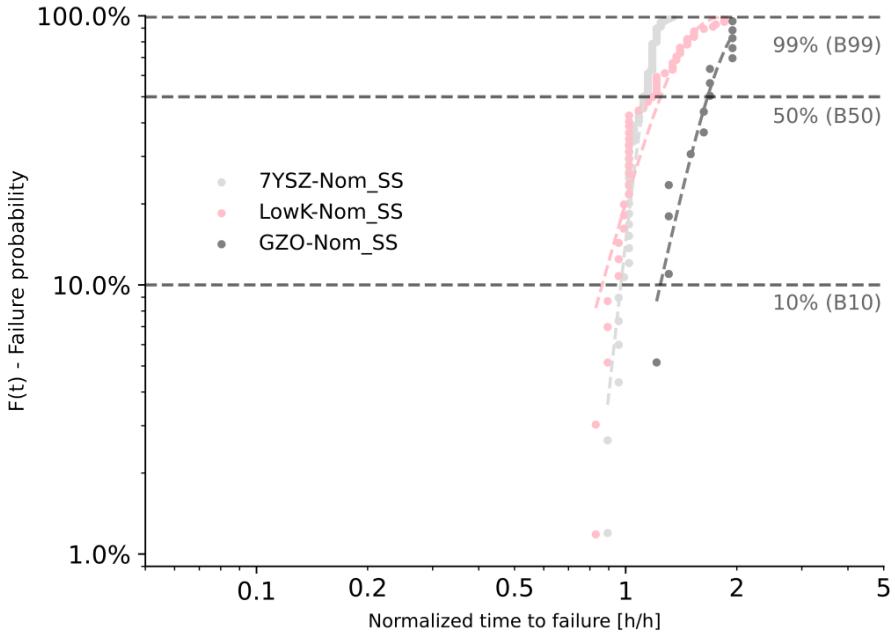
The life distribution of the model TBC systems tested for cyclic oxidation were investigated, evaluating the effect of the microstructural differences in the life expectancies for each zone of interest around a turbine blade aerofoil profile. The differences were most clear in the pressure side, with the Low Rotation system exhibiting the lowest characteristic life for both materials tested. A more moderate difference was observed for the GZO coatings in the suction side, with GZO-LT showing the lowest characteristic life. No such difference was observed in the suction side for the LowK systems.

For both material systems, statistically significant differences were observed in the leading edge area. This was also shown when comparing the different material systems, suggests that cyclic oxidation failure in this area may be dominated by the substrate, potentially due to the small radii of curvature of the blade in this region.

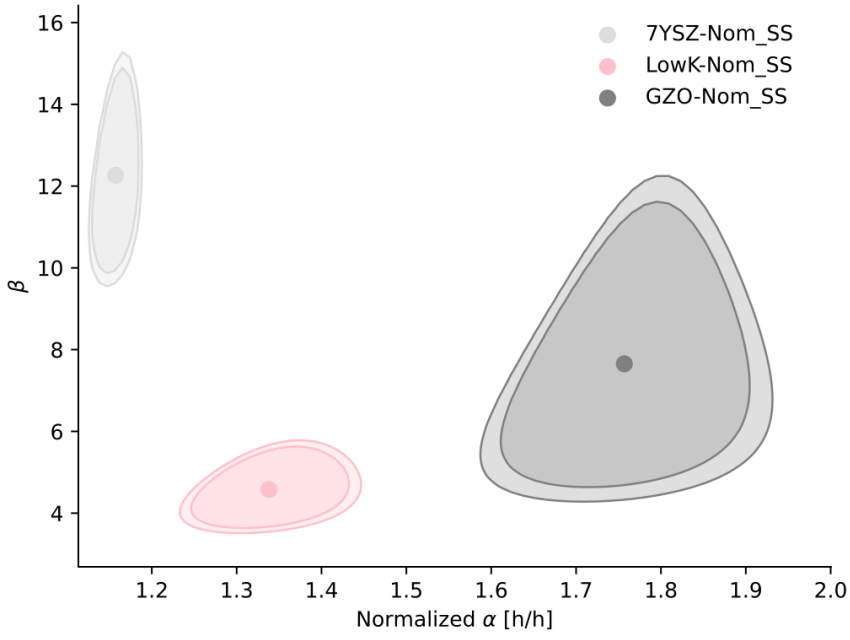
Comparing the nominal LowK and GZO to 7YSZ as the benchmarking material, significant differences were observed, with the more compliant systems (LowK and GZO) exhibiting higher characteristic lives when compared to 7YSZ.

Despite the overlap in the parameter estimation exhibited by most systems, a summary of the systems exhibiting the highest characteristic life and smaller life spread, as per the maximum likelihood estimation are as follows:

In the Leading Edge, GZO-LR showed both the highest characteristic life, at 1.69, and slope, with a value of β of 4.8. Another modified GZO system, GZO-LT exhibited the highest relative life in the Pressure Side - 1.97 - and β - 11.4. This characteristic life



(a) Weibull plot



(b) Likelihood plot

Figure 6.10: a) Weibull plot and b) likelihood plot for Weibull parameters for the cyclic life of 7YSZ, LowK and GZO nominal coatings exposed to 1190°C in 3 h cycles, evaluated for the suction surface.

was the highest of any systems tested, in any zone. As for the Suction Side, GZO-Nom showed the highest characteristic life, at 1.76, while 7YSZ-Nom displayed the highest value of β, at 12.2.

Chapter 7

Review of research impact

The results presented in this Innovation Report and companion Submissions have been developed through discussion with Rolls-Royce plc as the sponsoring organization, Forschungs Zentrum Jülich and the Surface Engineering and Precision Centre in Cranfield University. The research project was eminently method-oriented and used extensively studied coating materials as models for the validation of the methods developed. Due to this focus, as well as the notoriously long development and industrialization cycles of the aerospace industry, the results presented in this portfolio have not yet been implemented in production. However, the motivation for the methods presented is to contribute to the development of the next generation of TBCs. The potential use, in pursuing such endeavour, of the methods developed and the relevance of the results obtained is discussed below.

7.1 Methodology for the determination of CMAS infiltration

One of the major hurdles in the development of TBCs capable of enduring higher temperatures, a requirement for the accelerated development of aeroengines with increased efficiency is the degradation of turbine components due to fluxing attack by CMAS. Overcoming this hurdle requires developing an intimate understanding of the damage mechanisms which affects EB-PVD TBCs, with the ultimate aim of accurately modelling the degradation method.

The method developed for the quantitative determination of CMAS infiltration depth can be simultaneously used to evaluate the performance of candidate TBC systems, and to validate CMAS infiltration kinematics predicted by computational models, enabling model-led development of CMAS resistant TBC. Understanding the kinematics of CMAS infiltration is critical not only to understand the performance of EB-PVD TBCs, but also TBCs produced by other manufacturing routes, and could be extended to include Environmental Barrier Coatings (EBCs). The method developed is anticipated to contribute to reducing the time and cost of development of CMAS resistant coatings.

7.2 CoCo: An algorithm for the measurement of column width

Predicting the performance and durability of most material systems, especially those that are as susceptible to changes in the microstructure as TBCs, requires understanding the links between the microstructure, the performance, and failure modes being studied. This understanding necessitates invariably the identification of the material characteristics significantly affecting TBC performance and durability, and their quantification. The latter is also necessary for establishing links between the process parameters used and the resulting performance.

The method developed for the measurement of the width of EB-PVD columns constitutes a significant first step towards a systematic quantification of the microstructural features relevant to the durability of EB-PVD TBCs. The further development of the method, coupled with the automated quantification of other relevant microstructural quantities (intercolumnar pore width, pore network tortuosity...) represent a promising avenue for establishing these critical links.

7.3 CMAS testing methodology

The experimental programme undertaken with the aim of developing and validating the method for CMAS infiltration has provided valuable insight into the different CMAS testing methods. In particular, their potential advantages and limitations with regards to their use for investigating the kinematics of CMAS infiltration have been interrogated

7.3.1 Isothermal testing

It has been shown that isothermal testing can be used to effectively induce partial CMAS infiltration, even in coating systems that do not resist penetration through reactive crystallization. The disadvantages of the method have also been discussed, with special focus in the complication introduced by the thermal recovery period and the potential microstructural changes induced by the substrate material.

This knowledge is useful for the design of the experimental plans to be performed in coating development programmes, as isothermal testing represents a relatively low cost alternative to gradient rig testing for the down selection of candidate materials. In addition to the reduced cost, isothermal testing typically is less time consuming due to the simplicity of the setup and sample geometry. The resulting trade off is therefore between the reduced cost and test time required on the one hand and the reduced accuracy in the test conditions logged and representativeness of the microstructure being tested. This allows to suggest that isothermal CMAS testing can be used for the screening phase of any investigation into the interactions of candidate systems and CMAS.

7.3.2 Gradient rig testing

The testing conducted at ForschungsZentrum Jülich has also highlighted the requirements for a test rig with advanced capabilities. The investigations into the manner of delivery

of the high CMAS loading required have exposed the limits of CMAS injection of the spraying nozzle, highlighting the criticality of the nozzle design if high CMAS delivery rates are desired. The successful testing of pre-dosed samples, however, suggest that such high rates are not required for CMAS infiltration kinematic studies.

Another effect uncovered through the testing of TBC samples with high CMAS loading is the effect of molten CMAS in the accuracy of the surface temperature measurement. Appropriate calibration to the thermoscopic properties of the sample being tested is therefore critical for recording the test conditions accurately. It has been shown that such a calibration is complicated by the evolution of the emissivity with temperature and the changes in the state of the surface-deposited CMAS layer. While not tested in the current project, it can be anticipated that the thickness and extent of the CMAS deposit will also affect the surface temperature measured by the infrared camera.

These factors should be considered to understand the design requirements of improving the capabilities of a burner rig. The successful implementation of such capabilities would simultaneously provide more flexibility to the delivery of CMAS, and the accuracy required for modelling the actual conditions experienced by the coupons during test.

7.3.2.1 Script for probing the surface temperature

A script was developed and provided to the host institution of the international visit that enables the automated probing of the surface temperature based on infrared camera data. Together with ongoing efforts at FZJ to accurately determine the location of the metallographic section in relation to the surface temperature data, the provided script will enable Jülich to obtain chronologically and spatially resolved temperature data for the metallographic sections taken. This will provide the thermal history of any given point in the section, allowing for a more comprehensive understanding of the causes of the features observed following testing. The typical testing conducted by FZJ consists in cyclic testing under low CMAS dosage. This means that the aforementioned challenges with emissivity calibration do not apply to most of the test conducted, making the script immediately useful to FZJ.

7.4 TBC durability data

Extensive data was collected for the different modes of failure investigated in the present project. This data has been summarized and collected in a self-contained folder structure, which allows for future re-evaluation of the data, as well as the addition of the results obtained to historic data collected at Cranfield University.

Efforts are ongoing at Cranfield University related to the further development of the methods introduced in the current work. In this context, the availability of this data can be an invaluable resource for the validation of the future iterations of the developed methods or new methods being proposed.

Provided the gathered data meets the quality criteria for Rolls-Royce, the experimental data can be incorporated into the relevant material databases used in the evaluation of engineering data. Likewise, the method developed for evaluating the infiltration depth of CMAS in EB-PVD TBCs could be incorporated to the corpus of material test methodology standards used by Rolls-Royce plc.

7.5 Crystallographic evaluation of EB-PVD TBCs

The evaluation of the crystallographic characteristics of the model TBCs produced in this work has resulted in the identification of microstructural features whose effect on TBC performance has so far seldom been investigated, in particular grain size, and crystallographic texture. It is anticipated that the systematic study of these features will result in an increased understanding of the quantitative links between processing parameters, microstructural features and performance.

Chapter 8

Conclusions and future perspectives

The aim of this research project is establishing links between the EB-PVD process parameters, resulting microstructure, and degradation of TBCs. The objectives set to accomplish said aim, and their links to the Chapters addressing them are as follows:

1. Explore the boundaries of EB-PVD TBC microstructures depositing TBCs under a broad array of EB-PVD process parameters, both to expand the reported variety of EB-PVD TBC microstructures and to provide sufficiently dissimilar systems for subsequent testing - addressed in Chapters 2 and 3.

2. Establish links between process parameters and microstructure studying the salient microstructural features of TBC produced under different coating conditions, linking the observed changes to the existing mechanistic understanding of the deposition process - discussed in Chapters 2 and 3.

3. Evaluate the effect of microstructure on durability testing the produced TBCs for a variety of failure modes, drawing links between the observed differences in endurance and the microstructural features - Chapters 3, 4, 5 and 6.

The project has resulted in the following outcomes: A method for the quantification of a key microstructural parameter of EB-PVD TBCs, the column width, a method for the determination of CMAS infiltration depth and advanced characterization and durability data for the model TBCs studied.

The method developed for the determination of CMAS infiltration was validated against isothermal and thermal gradient test results. The latter, through the collaboration with ForschungsZentrum Jülich as part of the international visit. These validation efforts have expanded the understanding of the capabilities and limitations of both test methods with regards to CMAS infiltration investigation.

The results presented in this project are anticipated to reduce development time and cost for novel TBCs, through underpinning the validation of models that can predict their form and function based on the EB-PVD parameters used and the material selected for their deposition. This diminished cost and time is critical to tackle the decarbonization efforts required from the aerospace industry in a timely fashion.

The results, interpretation and conclusions from the areas researched are summarized in the next section.

8.1 Conclusions

8.1.1 Deposition methods and failure modes of TBCs

The review conducted on the main methods used in the deposition of TBCs, and failure modes limiting component life are summarized in Chapter 2. This chapter draws on Submissions 1 and 3. The review of the literature yielded the following areas as promising topics to be researched:

- The effect of the different microstructural parameters on CMAS attack mechanisms. Infiltration was identified as a key mechanism driving the damage to TBCs resulting from CMAS attack.
- A gap in knowledge was identified in the available methods for determining the depth of CMAS penetration in columnar TBCs
- The erosion resistance of EB-PVD TBCs was affected by coating microstructural features, and material properties. Among the microstructural features, column width showed a marked effect on erosion rate.
- Coatings produced by different manufacturing methods show significant variability in their cyclic oxidation life. However, limited studies on the effect of microstructural differences of EB-PVD TBCs on cyclic life were available.
- Based on the mechanism for coating deposition via EB-PVD, structure zone models and computational models that aim to predict the microstructure of TBCs based on the deposition conditions were identified. Areas for improvement of existing models were identified, to account for crystal nucleation, growth and texture development. The ultimate aim is to quantitatively predicting microstructure morphology.
- The validation of the existing and future models would require quantitative evaluation of experimentally produced coatings. No methods for such quantitative assessment were identified in the literature.

Two methods were developed as part the research project, to address the identified gaps. The first, CoCo, consisted in an image analysis method for the quantification of column width, an important microstructural feature. While quantification of this feature was reported in the literature, especially in connection to the different failure modes affecting EB-PVD TBCs, no method for automated and repeatable measurement had been published.

The second method, CIMM, was developed to quantify the depth of infiltration for EB-PVD TBCs exposed to CMAS at high temperature. Methods to analyse CMAS attack under Isothermal and thermal gradient conditions already existed, but no method focused on the measurement of the infiltration depth was identified.

8.1.2 Deposition and characterization of model TBCs

The deposition of model TBCs and their characterization was covered in Chapter 3. Results for the LowK and GZO coatings deposited using different EB-PVD process parameters were presented. A quantitative assessment of the microstructures produced was

undertaken, using the developed algorithm CoCo. The development of CoCo is detailed in Submission 3: Microstructure quantification. This evaluation was complemented by a crystallographic study of the model TBCs using EBSD.

A summary of the findings from this evaluation is presented as follows:

- The model TBCs deposited showed significantly different microstructures, some of which have not previously been reported in the literature for EB-PVD coatings
- TBC microstructures produced broadly conformed to the Structure-Zone-Models for EB-PVD, while showing coating and substrate material-specific differences. GZO in particular, seemed to exhibit features attributed to zones corresponding to homologous temperatures lower than those used in their deposition.
- The method developed for the quantitative evaluation of TBCs was validated against manual measurement results, showing significant differences between the results obtained for both methods.
  - These differences were attributed to an ambiguity in the definition of the concept of "column", and its different interpretation by the human appraisers and the automated method.
- A crystallographic evaluation of the coatings produced was undertaken via EBSD to couple the observed morphology to crystallographic grains.
  - The results obtained for column width from the grain boundary data were closer to those obtained by the automated system than to those measured manually.
  - The crystallographic analysis also showed substantial changes in the grain area, preferred crystallographic growth direction and texture. These changes were also dependent on coating and substrate material.

These findings and the novelty of the developed method and analysis performed have implications for the understanding of TBC microstructures and their behaviour. The challenges presented by the quantification of the TBC microstructure stem in part from the lack of a formal definition of a column in EB-PVD TBCs.

The use of EBSD has shown promise in overcoming this lack of formal definition, through the use of well established definitions for the identification of crystalline grains. Depending on the deposition conditions, the informally defined columns have been shown to be comprised of one or multiple grains. The determination of crystalline grains, their orientation and the overall texture of the coating could be used to produce a formal definition of a TBC column grounded in the effect that grain boundaries and orientation have in the micromechanical behaviour of polycrystalline materials. This definition could also be extended to coatings produced by other manufacturing methods resulting in columnar or column-like TBC morphologies. It should be noted, however, that EBSD requires specialist equipment and knowledge, as well as careful sample preparation.

8.1.3 Functional testing

Chapters 4 to 6 covered the functional testing undertaken for evaluating the durability of the model TBCs with regards to three failure modes: CMAS attack, High velocity particle impact erosion and Spallation due to cyclic oxidation.

8.1.3.1 CMAS infiltration

Chapter 4 covered the CMAS testing of the model TBCs, focused on CMAS infiltration. The method developed for measuring the depth of infiltration of CMAS, detailed in Submission 5 was used for determining the changes in depth of infiltration with time and temperature for the different model TBCs. The observations and conclusions from the tests conducted under isothermal and thermal gradient conditions are presented below.

- A two-stage mechanism for CMAS infiltration, not reported previously on EB-PVD TBCs, was identified both in the isothermal and thermal gradient exposures.
  - The first stage consisted in the through thickness transport of CMAS, during which thin columns were filled with CMAS, but thicker columns remained unsaturated, exhibiting large trapped pores.
    - The level of saturation increased with infiltration depth for isothermal exposures, while remaining constant for thermal gradient tests.
  - The second stage resulted in the gradual increase in saturation of the pores that remained unsaturated at that stage.
- Model TBCs with thin column sizes and small crystalline grains showed an increased resistance to CMAS infiltration, exhibiting a reduced infiltration depth for equivalent thermal exposures.
- Coatings with thinner columns did, however, show increased susceptibility to thermomechanical damage when compared to coatings with wider columns.
- Samples tested under gradient conditions exhibited elemental segregation and the nucleation of a crystalline phase in the CMAS deposit. This crystalline phase was identified through XRD and EBSD as Åkermanite.
  - While the mechanism driving the segregation and crystallization of Åkermanite remains unclear, the effect of the Al content of the melt in the stability of the liquid phase was demonstrated to be a factor, as analyzed through CALPHAD.
  - It is proposed that crystallization of the melt could be promoted through additions of Ca to the TBC for the given CMAS composition. However, Åkermanite did not seem to prevent further infiltration of the TBC and is, therefore, not a complete solution to the issue of CMAS attack of TBCs.
- Gadolinium Zirconate effectively blocked CMAS infiltration for all the model microstructures studied, exposed at 1250°C and 1300°C for 6 minutes.

These findings are found to be of high relevance for the validation of CMAS infiltration models, both from a quantitative and a mechanistic perspective. The ability to accurately measure CMAS infiltration, coupled with appropriate monitoring of test conditions, is a requisite for the validation of infiltration depth predictions. The results obtained conform with the qualitative results obtained for CMAS infiltration based on existing models, if not quantitatively.

From the mechanism perspective, the two-stage infiltration observed allows to criticise the hypotheses underlying some of the existing analytical models. Indeed, most of the analytical models for CMAS infiltration assume CMAS transport and saturation to occur simultaneously, so that the infiltrated depth is fully saturated at any given time. This is also the premise for the cold-shock delamination models. The observed mechanism invalidates this assumption for the conditions studied, while opening the door to the validation of analytical and computational models based on this revised premise.

8.1.3.2 Erosion resistance

The resistance of the model TBCs to damage by high velocity particle impact are discussed in Chapter 5. The results obtained are discussed against the background of the microstructural characterization performed in Chapter 3. The conclusions of this discussion and observed mechanisms for erosive damage are:

- The presence of periodic porosity in the coating systems deposited at low rotation speeds resulted in a modification of the damage mechanism observed
  - While TBCs with no periodic porosity behaved as individual or closely connected clusters of individual columns, coatings deposited at low rotation speeds behaved mechanically as layered structures. As a result, material loss happened through exfoliation.
- Coatings deposited at low temperature and nominal rotation speed (8 RPM) showed an increased resistance to erosion damage, attributed to thinner columns which retained cracked material in place beyond their immediate neighbouring columns. The cracked material held in place is proposed to dissipate the impact energy, reducing impact to the undamaged material.
- In the bilayer coatings, the damage was contained to the GZO layer, which shows reduced fracture toughness when compared to LowK and 7YSZ.

These findings could be implemented in the design of layered coatings with controlled erosion damage mechanisms. Exploiting both the change in behaviour due to the microstructural changes and layers with different mechanical properties could be used to produce coatings which would dissipate impact energy within the layers. This could conceptually result in a spreading of the erosive damage over a larger area, while reducing the thickness loss in a specific point, thus diffusing hotspots resulting from erosion.

8.1.3.3 Cyclic oxidation

The spallation testing results for the model TBCs are discussed in Chapter 6. The lack of metallographic assessment data for interrupted testing hardware precluded the evaluation

of the damage mechanisms resulting from the microstructural differences. However, the use of lifetime distribution analysis allowed to derive statistically significant differences (and their absence) from the test results, as follows:

- No statistically significant differences could be inferred within each coating material in the leading edge lives of the different systems tested. The proposed reason for this observation is the dominant role of the high and variable curvature of the substrate in this section of the airfoil. This substrate curvature could potentially be acting over the cyclic life of the coatings in two ways:
  1. By modifying the local microstructure: an increased substrate curvature provides a larger flux of vapour per unit area, affecting crystal nucleation and growth.
  2. By altering the strain energy accumulated in the coating as a result of the TGO growth.
- In the Suction Side, these differences were attenuated for GZO and completely absent for LowK. For each material system, the coatings exhibiting a longer characteristic life were LowK-LR (1.52) and GZO-Nom (1.76).
- No statistically significant differences were observed for either material in the Pressure Side, however, the maximum likelihood estimation result was highest for LowK-Nom was the highest among the LowK systems, at 1.43. GZO-LT and GZO-LR showed the highest characteristic life values among all the systems and zones of interest, at 1.97 and 1.94, respectively.
- LowK systems exhibited a similar characteristic life when compared to 7YSZ-Nom. for L.E. and P.S, and somewhat higher on the Suction Side (1.32-1.52 vs. 1.16). LowK-LR showed the highest difference in characteristic life to 7YSZ-Nom. in the suction side with a 31.5 % increase.
- GZO systems exhibit an increase in cyclic oxidation life when compared to 7YSZ-Nom. For the best performing GZO coating on each zone of interest, this increase is of at least 50 %.
- With the exception of the low rotation systems, all coatings deposited on the Pressure Side exhibit a longer characteristic life when compared to coatings deposited on the Leading Edge.
- For different materials, a marked difference was observed for the suction side, with higher compliance materials showing a significantly greater cyclic life, as expected based on the literature.

Few definite conclusions could be drawn regarding the relative performance of the coating systems tested across the different zones of interest. However, the observed differences could still be interesting for component life if one of the modified TBC model coating systems exhibits a marked improvement relative to the nominal in the areas most prone to delamination. An interesting observation is that the increased thermomechanical damage sustained by the coatings deposited at low temperature under gradient testing

conditions does not directly translate to the cyclic oxidation test results. This suggests that the differences in thermomechanical loads due to the thermal gradient have a marked influence in the microstructure dependent thermomechanical behaviour of TBCs.

8.1.3.4 Summary of the performance of the coating systems tested

The study correlations between single microstructural features and performance indicators could be undertaken, as explained throughout the present report. However, this would, at this moment, yield limited value for multiple reasons. As already discussed, the reliability and accuracy of the developed methods should be improved, to increase confidence on the obtained quantified features (microstructure and CMAS infiltration in particular). This is notwithstanding the promise that the presented methods hold in the author's opinion, to eventually underpin such a correlation, and more sophisticated models with statistical confidence.

The second hurdle for establishing such correlations comes from the more granular and multivariate nature of the characterization undertaken in the current project, both for microstructural features (column widths vs thickness, grain size) and performance (CMAS infiltration depth and saturation, oxidation life by zone in airfoil). Establishing meaningful correlations between the microstructural features and performance would require, as a minimum, the establishment of robust criteria for the selection of the key variables to be correlated, and possibly the undertaking of multivariate analysis.

While such an exercise would be worthwhile, it would likely require more time than it is currently available, and given the contentions expressed regarding the reliability of the quantification methods developed, in their current state of development, the author considers this to be part of future work.

In the absence of such a correlation, the relative rank, presented through colour coding of the results obtained by coating system is presented in Table 8.1. The criteria used in the determination of the performance indicators used for the comparison are laid out in Table 8.2.

It can be noted that, despite no system outperforming all others across the degradation mechanisms investigated, the coatings deposited at low temperature seem to exhibit the best average ranking, especially when comparing their 'within material' performance. Additional investigation of the performance of these systems following sintering would be beneficial to understand the possibility of exploiting the apparent advantage they exhibit in actual engine operation conditions.

8.2 Perspectives on the development of Future TBCs

What follows is a discussion of the perspective of the author on the research that could be conducted to fulfil the aspirational aim stated for the present project. This is accompanied by the concrete further work required for overcoming the limitations of the research presented in this Innovation Report, in each of the areas outlined in the present section.

Table 8.1: Relative performance ranking of tested systems.

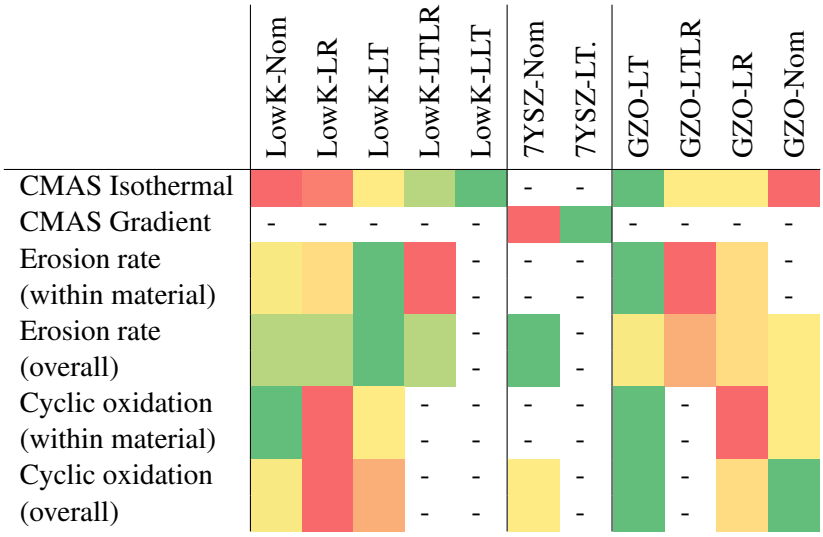


Table 8.2: Criteria used in the determination of performance ranking presented in Table 8.1. †Profile drop refers to the sharp infiltration depth transition from the uninfiltrated to the fully infiltrated/plateaued infiltration in the radial distribution profiles - see Figure 4.17a.

	LowK	7YSZ	GZO
CMAS Isothermal	Infiltration depth at 170 s	-	Activation energy
CMAS Gradient	-	Midpoint of depth profile drop†	-
Erosion (within material) Erosion (overall)	Erosion rate [mg/g]		
Cyclic oxidation (within material) Cyclic oxidation (overall)	Characteristic life in Pressure Side		

8.2.1 TBC systems and materials

The results obtained indicated that designed layering could help control the damage and mass loss in EB-PVD TBCs. Given that erosion resistance is one of the limiting factors for the adoption of existing CMAS resistant materials, such as GZO, the effect of different layering parameters in the distribution of erosive damage should be investigated.

The results obtained for LowK deposited at low temperature suggest an overall improvement in component life could be achieved by its implementation, provided the detrimental effects observed to the cyclic life and its variability do not become life limiting. Given the influence of the substrate in cyclic life, this issue could be overcome through layering or graded deposition, by reducing the temperature between the initial layer and the outer layer.

In the broader context of the novel TBC material candidates being developed and researched, the aforementioned effect of layering should be considered, for those materials where impact damage appears to be the limiting mechanism. The development of mechanistic understanding for impact and cold shock delamination damage based on mechanical behaviour incorporating crystal size, orientation and texture are expected to improve the predictive ability of damage models, and aid with the down selection of the candidate materials.

8.2.2 Quantitative coating characterization

A wide array of analytical techniques are employed in the characterization of TBCs, resulting in both quantitative and qualitative data. It is the author's view that data typically considered qualitative, such as electron images, can be post-processed to yield quantitative results. The method developed for the measurement of column width is an example of such quantification of nominally qualitative data.

In order to do that, the author proposes that scientific computing techniques and the associated understanding of data types and structures could benefit the materials scientists currently working to tackle the challenges posed by the development of TBC systems with higher temperature capability and durability.

In parallel, a physics based understanding of the characterization techniques, their capabilities and limitations is considered of paramount importance, for appropriate selection of the method to be used and interpretation of results obtained by each method.

8.2.2.1 Analytical techniques

The use of alternative analytical techniques could help overcome some of the limitations of the present project that derive from the use of a sub-optimal analytical technique based on the existing constraints for the project.

The method developed for the measurement of CMAS infiltration depth could be improved by the use of elemental characterization techniques with improved spatial resolution, such as Electron Probe Micro Analysis (EMPA). This technique could yield better defined depths of infiltration, reducing the variation in the obtained results.

Both of the methods developed - for microstructure and infiltration quantification - would benefit greatly from the use of three dimensional characterization. A candidate method for the three dimensional reconstruction of microstructures, crystallinity and porosity would be X-ray tomography, particularly, X-ray Diffraction Contrast Tomography, which has been used for the non destructive 3D characterization of the crystalline structures and the porosity therein.

An alternative method would consist in the reconstruction of the 3D structure based on FIB assisted EBSD, by collating EBSD maps taken for different sections in the area of interest. This method, however, presents significant challenges for signal stability, based on the high beam currents required for EBSD mapping, the non-conductive nature of TBC ceramics and the difficulty of re-depositing the thin conductive coatings of carbon, platinum or gold typically used to prevent these charging issues.

8.2.2.2 Data analysis

Even with improved resolution, the method developed for the measurement of CMAS infiltration would still potentially rely on the manual determination of the break points, as discussed in Chapter 4 and Submission 5. Overcoming the need for manual and subjective assessments of the infiltration profile requires the evaluation of different methods for the determination of change points. Algorithms for signal processing and time series data analysis could be leveraged to determine the critical points and automate the accurate measurement of the depth of infiltration.

With regards to the quantification of TBC microstructural features, the combination of different data sources could be used to improve the accuracy of the measured column widths. As an example, virtual stacks could be created using the orientation maps collected, the corresponding electron images and, if required, elemental composition maps. The author expects that these stacks would result in an increased accuracy in column boundary detection, since the combined criteria of material continuity and close orientation could be used to train the classification algorithm, overcoming the artefacts present in either of the sources of data separately.

8.2.3 Reproducibility and Replicability

The author believes that the publication of the materials, methods and parameters used in researching a given problem are necessary for the advancement of the collective knowledge through scientific enquiry. While the publication of certain material data may be sensitive and therefore, reasonably withheld, sharing the detailed methods used for processing the data acquired would significantly improve the confidence in the results presented, the ability to reproduce them and the opportunities for methods to be improved and disseminated. This aspect has long been a tenet of the field of scientific computing, with some journals mandating publication of data and code used in the generation of the presented results.

In this vein, the author intends to publish the code used for the algorithms CoCo and CIMM, developed in this project. While not all of the data used in the generation of the results can be shared, the open evaluation of the method will necessitate the use of model data. These collections of model data, commonly referred to as benchmarks, are also common for scientific computing applications. The development of such benchmarks for non-restricted materials data, for the validation and evaluation of methods for the quantitative assessment of TBCs, produced via EB-PVD or otherwise, would be a boon for advancing the understanding of TBCs.

8.2.4 Integrated Computational Materials Engineering

Both the stated aims and the developed methods were inspired by the Integrated Computational Materials Engineering (ICME) approach to materials design. At its most fundamental, the aim of ICME is to establish reliable predictive links between materials processing, structure and properties, using computational models integrated at multiple scales. The quantification of the produced microstructures and their behaviour, as well as standard formats for data sharing constitute a core requirement for the validation of such models. The reliability of the models would benefit greatly if experimental data could be used in the construction of the models and their validation.

A step in that direction would be to use the EBSD data acquired to directly build computational models of the TBCs studied. These models could be used for the finite element analysis of the mechanical response of TBCs to high velocity particle impact. It should be noted that a range of open-source workflows already exist to generate meshes from EBSD data.

As a further improvement, the three dimensional characterization through X-ray Diffraction Computed Tomography of microstructural features mentioned in section 8.2.2.1 could

be used to build more representative models. Given sufficiently high resolution, these models could even be used for simulating the pore network and associated behaviour with regards to CMAS infiltration. Naturally, this would require the commitment of significant skills in computational analysis and modelling, as well as computing power, given the scale differences between the resolution required and the size of the system needed to capture a representative enough volume.

References

1. University of Virginia. High Temperature Coatings - Wadley Research Group; 2013. Available at: https://www2.virginia.edu/ms/research/wadley/high-temp.html. available online at https://www2.virginia.edu/ms/research/wadley/high-temp.html, date accessed 24/02/2022.

2. Karlsson AM, Hutchinson JW, Evans AG. A fundamental model of cyclic instabilities in thermal barrier systems. Journal of the Mechanics and Physics of Solids. 2002;50(8):1565-89.

3. Renteria AF, Saruhan B, Schulz U, Raetzer-Scheibe HJ, Haug J, Wiedenmann A. Effect of morphology on thermal conductivity of EB-PVD PYSZ TBCs. Surface and Coatings Technology. 2006;201:2611-20. Available at: http://dx.doi.org/10.1016/j.surfcoat.2006.05.003.

4. Scotson D, Paksoy AH, Xiao P. Characterisation techniques for investigating TBC and EBC failure: a review. Frontiers in Ceramics. 2024 1;1.

5. McGinty R. Loading Modes I, II, III; 2014. Available at: https://www.fracturemechanics.org/modes123.htmlhttps://web.archive.org/web/20240624124104/https://www.fracturemechanics.org/modes123.html. available online at https://www.fracturemechanics.org/modes123.html, accessed 2024 Jun 22, archived at https://web.archive.org/web/20240624124104/https://www.fracturemechanics.org/modes123.html.

6. Wellman RG, Nicholls JR. A Monte Carlo model for predicting the erosion rate of EB PVD TBCs. Wear. 2004;256(9-10):889-99.

7. Fabrichnaya O, Wang C, Zinkevich M, Levi CG, Aldinger F. Phase Equilibria and Thermodynamic Properties of the ZrO_2-$GdO_{1.5}$-$YO_{1.5}$ System. Journal of Phase Equilibria and Diffusion. 2005 12;26:591-604.

8. Subramani T, Voskanyan A, Jayanthi K, Abramchuk M, Navrotsky A. A Comparison of Order-Disorder in Several Families of Cubic Oxides. Frontiers in Chemistry. 2021 9;9.

9. Saradhi MP, Ushakov SV, Navrotsky A. Fluorite-pyrochlore transformation in Eu2Zr2O_7—direct calorimetric measurement of phase transition, formation and surface enthalpies. RSC Adv. 2012;2:3328-34. Available at: http://dx.doi.org/10.1039/C2RA00727D.

10. Subramani T, Navrotsky A. Energetics of Formation and Disordering in Rare Earth Weberite RE3TaO$_7$ Materials. Inorganic Chemistry. 2019 12;58:16126-33.

11. Schindelin J, Arganda-Carreras I, Frise E, Kaynig V, Longair M, Pietzsch T, et al. Fiji: An open-source platform for biological-image analysis. Nature Methods. 2012 7;9:676-82.

12. Azuaje F, Witten I, E F. Witten IH, Frank E: Data Mining: Practical Machine Learning Tools and Techniques. Biomedical Engineering Online. 2006 01;5:1-2.

13. Aroyo MI, Wondratschek H. Crystallographic viewpoints in the classification of space-group representations. International Tables for Crystallography. 2006. Available at: `https://api.semanticscholar.org/CorpusID:94892204`.

14. Rolls-Royce plc . The Jet Engine. 2015th edn. Chichester, UK: John Wiley & Sons; 2015.

15. European Aviation Safety Agency. E.111. Type Certificate Data Sheet - No. E.111. European Union Aviation Safety Agency; 2019.

16. Katranidis V. Employment of the operational centrifugal forces of the turbine to resist the Calcium-Magnesium-Alumninosilicates infiltration in the thermal barrier coating. A numerical simulation.. MSc Thesis; 2013.

17. Song JB, Wang LS, Dong H, Yao JT. Long lifespan thermal barrier coatings overview: Materials, manufacturing, failure mechanisms, and multiscale structural design. Ceramics International. 2023 1;49:1-23. Available at: `https://linkinghub.elsevier.com/retrieve/pii/S0272884222038032`.

18. Schulz U, Leyens C, Fritscher K, Peters M, Saruhan-Brings B, Lavigne O, et al. Some recent trends in research and technology of advanced TBCs. Aerospace Science and Technology. 2003;7:73-80.

19. Lu Z, Myoung SW, Kim EH, Lee JH, Jung YG. Microstructure Evolution and Thermal Durability with Coating Thickness in APS Thermal Barrier Coatings. Materials Today: Proceedings. 2014;1:35-43.

20. Karlsson AM, Hutchinson JW, Evans AG. The displacement of the thermally grown oxide in thermal barrier systems upon temperature cycling. Materials Science and Engineering A. 2003;351(1-2):244-57.

21. Miller RA. History of Thermal Barrier Coatings for Gas Turbine Engines: Emphasizing NASA's Role From 1942 to 1990. Nasa Tm —2009-215459. 2009;215459(March):29 pages. Available at: `http://www.sti.nasa.gov`.

22. Smialek JL, Miller RA. Revisiting the birth of 7YSZ thermal barrier coatings: Stephan Stecura. Coatings. 2018;8(7):7-12.

23. Goward GW. Seventeen Years of Thermal Barrier Coatings. Fairbanks J, (ed.). Coatings for advanced heat engines workshop. Maine, Maine; 1987. p. 114-23.

24. Sampath S, Jiang XY, Matejicek J, Leger AC, Vardelle A. Substrate temperature effects on splat formation, microstructure development and properties of plasma sprayed coatings Part I: Case study for partially stabilized zirconia. Materials Science and Engineering. 1999;272:181-8. Available at: www.elsevier.com/locate/msea.

25. Jaslier Y. Development of EB-PVD TBCs: The role of deposition temperature and plasma assistance. PhD Thesis. Cranfield University; 1995.

26. Meier SM, Gupta DK, Sheffler KD. Ceramic thermal barrier coatings for gas turbine engines. Proceedings of the ASME Turbo Expo. 1991;5(March):50-3.

27. Rigney DV, Viguie R, Wortman DJ, Skelly DW. PVD thermal barrier coating applications and process development for aircraft engines. Journal of Thermal Spray Technology. 1997 6;6:167-75. Available at: http://link.springer.com/10.1007/s11666-997-0008-6.

28. Nicholls JR, Jaslier Y, Rickerby DS. Erosion of EB-PVD thermal barrier coatings. Materials at High Temperatures. 1998;15(1):15-22.

29. Jordan EH, Jiang C, Gell M, Roth J. Low Thermal conductivity YSZ thermal barrier coatings made by the solution precursor plasma spray process; 2014. Available at: http://asmedigitalcollection.asme.org/GT/proceedings-pdf/GT2014/45752/V006T02A005/4234383/v006t02a005-gt2014-26244.pdf. In: ASME Turbo Expo 2014: Turbine Technical Conference and Exposition [Internet]; 2014 June 16-20; Dusseldorf, Germany: ASTM; 2014 [cited 2024 Jun 21]. Available from: http://asmedigitalcollection.asme.org/GT/proceedings-pdf/GT2014/45752/V006T02A005/4234383/v006t02a005-gt2014-26244.pdf.

30. Nicholls JR, Lawson KJ, Johnstone A, Rickerby DS. Methods to reduce the thermal conductivity of EB-PVD TBCs. Surface and Coatings Technology. 2002;151-152:383-91.

31. Morelli S, Testa V, Bolelli G, Ligabue O, Molinari E, Antolotti N, et al. CMAS corrosion of YSZ thermal barrier coatings obtained by different thermal spray processes. Journal of the European Ceramic Society. 2020 9;40:4084-100.

32. Fauchais P, Vardelle M, Vardelle A, Goutier S. What Do We Know, What are the Current Limitations of Suspension Plasma Spraying?. Springer New York LLC; 2015.

33. Mittal G, Paul S. Suspension and Solution Precursor Plasma and HVOF Spray: A Review. Journal of Thermal Spray Technology. 2022 6;31:1443-75.

34. Vardelle A, Moreau C, Themelis NJ, Chazelas C. A Perspective on Plasma Spray Technology. Plasma Chemistry and Plasma Processing. 2015 4;35:491-509.

35. Stuke A, Kassner H, Marqués JL, Vassen R, Stöver D, Carius R. Suspension and air plasma-sprayed ceramic thermal barrier coatings with high infrared reflectance. International Journal of Applied Ceramic Technology. 2012 5;9:561-74.

36. Curry N, Tang Z, Markocsan N, Nylén P. Influence of bond coat surface roughness on the structure of axial suspension plasma spray thermal barrier coatings - Thermal and lifetime performance. Surface and Coatings Technology. 2015 4;268:15-23.

37. Klement U, Ekberg J, Ganvir A. EBSD analysis and assessment of porosity in thermal barrier coatings produced by axial suspension plasma spraying (ASPS). Materials Science Forum. vol. 879. Trans Tech Publications Ltd; 2017. p. 972-7.

38. Khan M, Zeng Y, Hu N, Lan Z, Wang Y. Optimizing the structure and properties of Y_2O_3 stabilized zirconia: An atmospheric plasma spray (APS) and solution precursor plasma spray (SPPS) based comparative study. Ceramics International. 2018;44(15):18135-42.

39. Khan M, Hu N, Zhenhua L, Wang Y, Yi Z. Influence of solution-precursor plasma spray (SPPS) processing parameters on the mechanical and thermodynamic properties of 8 YSZ. Ceramics International. 2018 5;44:7794-8. Available at: https://linkinghub.elsevier.com/retrieve/pii/S0272884218302219.

40. Niessen KV, Gindrat M. Plasma spray-PVD: A new thermal spray process to deposit out of the vapor phase. Journal of Thermal Spray Technology. 2011 6;20:736-43.

41. Mauer G. Plasma characteristics and plasma-feedstock interaction under PS-PVD process conditions. Plasma Chemistry and Plasma Processing. 2014;34:1171-86.

42. Von Niessen K, Gindrat M, Refke A. Vapor phase deposition using plasma spray-PVD™. Journal of Thermal Spray Technology. 2010;19(1-2):502-9.

43. He W, Mauer G, Schwedt A, Guillon O, Vaßen R. Advanced crystallographic study of the columnar growth of YZS coatings produced by PS-PVD. Journal of the European Ceramic Society. 2018 5;38:2449-53. Available at: https://linkinghub.elsevier.com/retrieve/pii/S0955221917308622.

44. Yamaguchi N, Wada K, Kimura K, Matsubara H. Microstructure Modification of Yttria Stabilized Zirconia Layers Prepared by EB-PVD. Journal of the Ceramic Society of Japan. 2003;111:883-9.

45. Thornton JA. High Rate Thick Film Growth. Annual Review of Materials Science. 1977;7:239-60.

46. Movchan BA, Demchishin AV. Study of the structure and properties of thick vacuum condensates of Nickel, Titanium, Tungsten, Aluminium oxide and Zirconium dioxide. Fiz Metallov i Metalloved. 1969;28(4):653-60.

47. Schulz U, Saruhan B, Fritscher K, Leyens C. Review on Advanced EB-PVD Ceramic Topcoats for TBC Applications. Applied Ceramic Technology. 2004;1(4):302-15.

48. Naraparaju R, Hüttermann M, Schulz U, Mechnich P. Tailoring the EB-PVD columnar microstructure to mitigate the infiltration of CMAS in 7YSZ thermal barrier coatings. Journal of the European Ceramic Society. 2017;37(1):261-70. Available at: http://dx.doi.org/10.1016/j.jeurceramsoc.2016.07.027.

49. Liu D, Mu R, He L, Li S, Yang W. Failure behaviour of EB-PVD YSZ thermal barrier coatings under simulated aero-engine operating conditions. Surface and Coatings Technology. 2023 12;474.

50. Schulz U, Fritscher K, Rätzer-Scheibe HJ, Kaysser WA, Peters M. Thermocyclic behaviour of microstructurally modified EB-PVD thermal barrier coatings. Materials Science Forum. 1997;251-254(PART 2):957-64.

51. Suemitsu M, Filimonov SN. Understanding crystal growth mechanisms in silicon-germanium (SiGe) nanostructures; 2011. p. 45-71.

52. Moon J, Kwon S, Alahbakhshi M, Lee Y, Cho K, Zakhidov A, et al. Surface Energy-Driven Preferential Grain Growth of Metal Halide Perovskites: Effects of Nanoimprint Lithography beyond Direct Patterning. ACS Applied Materials and Interfaces. 2021 2;13:5368-78.

53. for Aerospace Research AG, Development. Thermal Barrier Coatings - Agard-R-823; 1997.

54. Rätzer-Scheibe HJ, Schulz U, Krell T. The effect of coating thickness on the thermal conductivity of EB-PVD PYSZ thermal barrier coatings. Surface and Coatings Technology. 2006 5;200:5636-44. Available at: `https://linkinghub.elsevier.com/retrieve/pii/S0257897205010066`.

55. Echlin MP, Burnett TL, Polonsky AT, Pollock TM, Withers PJ. Serial sectioning in the SEM for three dimensional materials science. Current Opinion in Solid State and Materials Science. 2020 4;24.

56. Doleker KM, Ozgurluk Y, Kahraman Y, Karaoglanli AC. Oxidation and hot corrosion resistance of HVOF/EB-PVD thermal barrier coating system. Surface and Coatings Technology. 2021 3;409:126862.

57. Ostadi A, Hosseini SH, Fordoei ME. The effect of temperature and roughness of the substrate surface on the microstructure and adhesion strength of EB-PVD ZrO_2-coating. Ceramics International. 2020 2;46:2287-93.

58. Pfeiffer C, Affeldt E, Göken M. Miniaturized bend tests on partially stabilized EB-PVD ZrO_2 thermal barrier coatings. Surface and Coatings Technology. 2011 2;205:3245-50.

59. Lee KS, Jung KI, Heo YS, Kim TW, Jung YG, Paik U. Thermal and mechanical properties of sintered bodies and EB-PVD layers of Y_2O_3 added $Gd_2Zr_2O_7$ ceramics for thermal barrier coatings. Journal of Alloys and Compounds. 2010 10;507:448-55.

60. Tahir M, Qasim M, Ahmed N, Satti AN, Malik AE, Khan ZS, et al. Impact of atmospheric plasma spraying parameters on microstructure, mechanical properties and thermal cycling performance of YSZ coatings. Ceramics International. 2024 10.

61. Rosado E, Cañas E, Recio P, Sánchez E, Moreno R. $ZrSiO_4/ZrO_2$ thermal barrier coatings produced by suspension plasma spraying. Journal of the European Ceramic Society. 2024 Jan;44(1):460–470. Available at: http://dx.doi.org/10.1016/j.jeurceramsoc.2023.09.024.

62. Wada K, Yoshiya M, Yamaguchi N, Matsubara H. Texture and microstructure of ZrO_2-4molobliquely deposited by EB-PVD. Surface and Coatings Technology. 2006 1;200:2725-30. Available at: https://linkinghub.elsevier.com/retrieve/pii/S0257897205003191.

63. Yang G, Zhao CY. Infrared radiative properties of EB-PVD thermal barrier coatings. International Journal of Heat and Mass Transfer. 2016 Mar;94:199–210. Available at: http://dx.doi.org/10.1016/j.ijheatmasstransfer.2015.11.063.

64. Jiang C, Hao W, Liu C, Shi D, Song W. Thermal cycling performance of GYbZ/YSZ thermal barrier coatings with different microstructures based on finite element simulation. Journal of Alloys and Compounds. 2025 Jan;1010:177185. Available at: http://dx.doi.org/10.1016/j.jallcom.2024.177185.

65. Bernard B, Bianchi L, Malié A, Joulia A, Rémy B. Columnar suspension plasma sprayed coating microstructural control for thermal barrier coating application. Journal of the European Ceramic Society. 2016 Mar;36(4):1081–1089. Available at: http://dx.doi.org/10.1016/j.jeurceramsoc.2015.11.018.

66. Bernard B, Quet A, Bianchi L, Joulia A, Malié A, Schick V, et al. Thermal insulation properties of YSZ coatings: Suspension Plasma Spraying (SPS) versus Electron Beam Physical Vapor Deposition (EB-PVD) and Atmospheric Plasma Spraying (APS). Surface and Coatings Technology. 2017 5;318:122-8.

67. Liu Y, Zhang W, Wang W, Liu W, Yang T, Li K, et al. Structural optimization for the thermal conductivity and thermal cycling behavior in thermal barrier coatings and analysis of thermomechanical properties by computational investigation. Surface and Coatings Technology. 2024 Jul;488:130923. Available at: http://dx.doi.org/10.1016/j.surfcoat.2024.130923.

68. Zhao H, Zeng Z, Zhang X, Lv B, Deng Z, Mao J, et al. Towards enhanced corrosion resistance of PS-PVD TBCs in marine environments by structural design. Surface and Coatings Technology. 2024 Oct;494:131391. Available at: http://dx.doi.org/10.1016/j.surfcoat.2024.131391.

69. Deshpande S, Kulkarni A, Sampath S, Herman H. Application of image analysis for characterization of porosity in thermal spray coatings and correlation with small angle neutron scattering. Surface and Coatings Technology. 2004 Oct;187(1):6–16. Available at: http://dx.doi.org/10.1016/j.surfcoat.2004.01.032.

70. Ghai RS, Chen K, Baddour N. Modelling Thermal Conductivity of Porous Thermal Barrier Coatings. Coatings. 2019 Feb;9(2):101. Available at: http://dx.doi.org/10.3390/coatings9020101.

71. Blanchard F, Kadi MJ, Bousser E, Baloukas B, Azzi M, Klemberg-Sapieha JE, et al. Effect of CMAS infiltration on the optical properties of thermal barrier coatings: Study of the mechanisms supported by FDTD simulations and ALD. Acta Materialia. 2023 May;249:118830. Available at: http://dx.doi.org/10.1016/j.actamat.2023.118830.

72. Blanchard F, Kadi MJ, Bousser E, Baloukas B, Azzi M, Klemberg-Sapieha JE, et al. Effect of thermal ageing on the optical properties and pore structure of thermal barrier coatings. Surface and Coatings Technology. 2023 1;452:129080.

73. Ghai RS. Modelling thermal conductivity of porous thermal barrier coatings for high-temperature aero engines. 2017 9. Available at: https://ruor.uottawa.ca/server/api/core/bitstreams/e9bd2447-38f0-4dc0-a4b0-de49cf94fb13/content. available online at https://ruor.uottawa.ca/server/api/core/bitstreams/e9bd2447-38f0-4dc0-a4b0-de49cf94fb13/content, date accessed: 2024 Nov 26, archived online at https://web.archive.org/web/20201103140659/http://www.theobjects.com/dragonfly/.

74. Dorvaux JM, Lavigne O, Mevrel R, Poulain M, Renollet Y, Rio C. Modelling the Thermal Conductivity of Thermal Barrier Coatings. NATO - AGARD SMP - R823. Aalborg: Canada Communication Group, Inc.; 1998. p. 13.1-13.10.

75. Lehmann G, Arganda-Carreras I, Legland D, Rueden C, Burri O. MorphoLibJ; 2024. Available at: https://imagej.net/plugins/morpholibj#opening-and-closinghttps://web.archive.org/web/20241126114147/https://imagej.net/plugins/morpholibj#opening-and-closing. available online at https://imagej.net/plugins/morpholibj#opening-and-closing, date accessed: 2024 Nov 26, archived online at https://web.archive.org/web/20241126114147/https://imagej.net/plugins/morpholibj#opening-and-closing.

76. Inc ORSO. Dragonfly; 2020. Available at: Available:http://www.theobjects.com/dragonfly.https://web.archive.org/web/20201103140659/http://www.theobjects.com/dragonfly/. available online at http://www.theobjects.com/dragonfly, date accessed: 2024 Nov 26, archived online at https://web.archive.org/web/20201103140659/http://www.theobjects.com/dragonfly/.

77. Guo L, Zhang B, He Q, Liu M, Liang L. Fabrication and characterization of thermal barrier coatings for internal combustion engines via suspension plasma spray with high solid loading. Surface and Coatings Technology. 2024 Mar;479:130523. Available at: http://dx.doi.org/10.1016/j.surfcoat.2024.130523.

78. Schmitt MP, Harder BJ, Wolfe DE. Process-structure-property relations for the erosion durability of plasma spray-physical vapor deposition (PS-PVD) thermal barrier coatings. Surface and Coatings Technology. 2016 Jul;297:11–18. Available at: http://dx.doi.org/10.1016/j.surfcoat.2016.04.029.

79. Kadam NR, Karthikeyan G, Kulkarni DM. Effect of substrate rotation on the microstructure of 8YSZ thermal barrier coatings by EB-PVD. Materials Today: Proceedings. 2020;28:678–683. Available at: http://dx.doi.org/10.1016/j.matpr.2019.12.276.

80. Zotov N, Bartsch M, Chernova L, Schmidt DA, Havenith M, Eggeler G. Effects of annealing on the microstructure and the mechanical properties of EB-PVD thermal barrier coatings. Surface and Coatings Technology. 2010 Oct;205(2):452–464. Available at: http://dx.doi.org/10.1016/j.surfcoat.2010.07.008.

81. Longchamp V, Girardot J, André D, Malaise F, Quet A, Carles P, et al. Discrete 3D modeling of porous-cracked ceramic at the microstructure scale. Journal of the European Ceramic Society. 2024 Apr;44(4):2522–2536. Available at: http://dx.doi.org/10.1016/j.jeurceramsoc.2023.11.026.

82. Kelly M, Singh J, Todd J, Copley S, Wolfe D. Metallographic techniques for evaluation of Thermal Barrier Coatings produced by Electron Beam Physical Vapor Deposition. Materials Characterization. 2008 Jul;59(7):863–870. Available at: http://dx.doi.org/10.1016/j.matchar.2007.07.010.

83. Zhu W, Cai XN, Yang L, Xia J, Zhou YC, Pi ZP. The evolution of pores in thermal barrier coatings under volcanic ash corrosion using X-ray computed tomography. Surface and Coatings Technology. 2019;357(September 2018):372-8.

84. Zhang X, Kulczyk-Malecka J, Carr J, Xiao P, Withers PJ. 3D characterization of porosity in an air plasma-sprayed thermal barrier coating and its effect on thermal conductivity. Journal of the American Ceramic Society. 2018;101(6):2482-92.

85. Kulkarni A, Goland A, Herman H, Allen AJ, Dobbins T, DeCarlo F, et al. Advanced neutron and X-ray techniques for insights into the microstructure of EB-PVD thermal barrier coatings. Materials Science and Engineering: A. 2006 Jun;426(1–2):43–52. Available at: http://dx.doi.org/10.1016/j.msea.2006.03.070.

86. Evans AG, Clarke DR, Levi CG. The influence of oxides on the performance of advanced gas turbines. Journal of the European Ceramic Society. 2008;28(7):1405-19.

87. Ou H, Sahli M, Gelin JC, Barrière T. Experimental analysis and finite element simulation of the co-sintering of bi-material components. Powder Technology. 2014 12;268:269-78.

88. Azzopardi A, Mévrel R, Saint-Ramond B, Olson E, Stiller K. Influence of aging on structure and thermal conductivity of Y-PSZ and Y-FSZ EB-PVD coatings. Surface and Coatings Technology. 2004 1;177-178:131-9.

89. Lughi V, Tolpygo VK, Clarke DR. Microstructural aspects of the sintering of thermal barrier coatings. Materials Science and Engineering A. 2004;368(1-2):212-21.

90. Hutchinson RG, Fleck NA, Cocks ACF. A sintering model for thermal barrier coatings. Acta Materialia. 2006;54(5):1297-306.

91. Yang GJ, Chen ZL, Li CX, Li CJ. Microstructural and mechanical property evolutions of plasma-sprayed YSZ coating during high-temperature exposure: Comparison study between 8YSZ and 20YSZ. Journal of Thermal Spray Technology. vol. 22; 2013. p. 1294-302.

92. Huang R, Yang W, Fan X, Lai C, Mao J, Liu M, et al. Insights into the primitives and sequence deposition mechanism of 7YSZ TBCs respectively by EB-PVD and PS-PVD. Surface and Coatings Technology. 2023 9;468.

93. Chevalier J, Gremillard L, Virkar AV, Clarke DR. The tetragonal-monoclinic transformation in zirconia: Lessons learned and future trends. Journal of the American Ceramic Society. 2009;92(9):1901-20.

94. Mercer C, Williams JR, Clarke DR, Evans AG. On a ferroelastic mechanism governing the toughness of metastable tetragonal-prime (t') yttria-stabilized zirconia. Proceedings of the Royal Society A: Mathematical, Physical and Engineering Sciences. 2007;463(2081):1393-408. Available at: `https://royalsocietypublishing.org/doi/abs/10.1098/rspa.2007.1829`.

95. Evans HE. Oxidation failure of TBC systems: An assessment of mechanisms. Surface and Coatings Technology. 2011;206(7):1512-21.

96. Levi CG, Hutchinson JW, Vidal-Sétif MH, Johnson CA. Environmental degradation of thermal-barrier coatings by molten deposits. MRS Bulletin. 2012;37(10):932-41.

97. Chirivi L, Nicholls JR. Influence of surface finish on the cyclic oxidation lifetime of an eb-pvd tbc, deposited on PtAl and Pt-diffused bondcoats. Oxidation of Metals. 2014;81(1-2):17-31.

98. Yanar NM, Pettit FS, Meier GH. Failure characteristics during cyclic oxidation of yttria stabilized zirconia thermal barrier coatings deposited via electron beam physical vapor deposition on platinum aluminide and on NiCoCrAlY bond coats with processing modifications for improved performances. Metallurgical and Materials Transactions A. 2006 5;37:1563-80. Available at: `https://link.springer.com/10.1007/s11661-006-0100-4`.

99. Pint BA, Haynes JA, Zhang Y. Effect of superalloy substrate and bond coating on TBC lifetime. Surface and Coatings Technology. 2010 11;205:1236-40.

100. Evans AG, Mumm DR, Hutchinson JW, Meier GH, Pettit FS. Mechanisms controlling the performance and durability of thermal barrier coatings. Key Engineering Materials. 2001;197:199-230.

101. Choi SR, Hutchinson JW, Evans AG. Delamination of multilayer thermal barrier coatings. Mechanics of Materials. 1999;31(7):431-47.

102. Evans AG, Hutchinson JW. The mechanics of coating delamination in thermal gradients. Surface and Coatings Technology. 2007;201(18):7905-16.

103. Zhang H, Guo L, Ma Y, Peng H, Guo H, Gong S. Thermal cycling behavior of (Gd0.9Yb0.1)2Zr2O$_7$/8YSZ gradient thermal barrier coatings deposited on Hf-doped NiAl bond coat by EB-PVD. Surface and Coatings Technology. 2014 11;258:950-5. Available at: https://linkinghub.elsevier.com/retrieve/pii/S0257897214006525.

104. Tolpygo VK, Clarke DR, Murphy KS. Evaluation of interface degradation during cyclic oxidation of EB-PVD thermal barrier coatings and correlation with TGO luminescence. Surface and Coatings Technology. 2004 11;188-189:62-70.

105. Morrell P, Rickerby DS, Brewster G, Lee K, Nicholls JR. High-temperature coatings in turbines in extreme military environments. NATO, RTO-MP-AVT-187. 2010;10(1):10-28.

106. Lance MJ, Haynes JA, Pint BA. The effects of temperature and substrate curvature on TBC lifetime and residual stress in alumina scales beneath APS YSZ. Surface and Coatings Technology. 2016 12;308:19-23.

107. Ghenaiet A. Study of particle ingestion through two-stage gas turbine. Proceedings of the ASME Turbo Expo. vol. 2C; 2014. p. 1-12.

108. Wellman RG, Nicholls JR, Murphy K. Effect of microstructure and temperature on the erosion rates and mechanisms of modified EB PVD TBCs. Wear. 2009;267(11):1927-34.

109. Ghoshal A, Murugan M, Walock MJ, Nieto A, Barnett BD, Pepi MS, et al. Molten particulate impact on tailored thermal barrier coatings for gas turbine engine. Journal of Engineering for Gas Turbines and Power. 2018;140(2):1-10.

110. Wellman RG, Nicholls JR. A review of the erosion of thermal barrier coatings. Journal of Physics D: Applied Physics. 2007;40(16).

111. Evans AG, Fleck NA, Faulhaber S, Vermaak N, Maloney M, Darolia R. Scaling laws governing the erosion and impact resistance of thermal barrier coatings. Wear. 2006;260(7-8):886-94.

112. Chen X, Wang R, Yao N, Evans AG, Hutchinson JW, Bruce RW. Foreign object damage in a thermal barrier system: Mechanisms and simulations. Materials Science and Engineering A. 2003;352(1-2):221-31.

113. Zisis A, Fleck NA. Mechanisms of elastodynamic erosion of electron-beam thermal barrier coatings. Zeitschrift fuer Metallkunde/Materials Research and Advanced Techniques. 2007;98(12):1196-202.

114. Wellman RG, Tourmente H, Impey S, Nicholls JR. Nano and microhardness testing of aged EB PVD TBCs. Surface and Coatings Technology. 2004;188-189(1-3 SPEC.ISS.):79-84.

115. Chen X, He MY, Spitsberg I, Fleck NA, Hutchinson JW, Evans AG. Mechanisms governing the high temperature erosion of thermal barrier coatings. Wear. 2004;256(7-8):735-46.

116. Nicholls JR, Wellman RG. Erosion and foreign object damage of thermal barrier coatings. RTO AVT Specialists' Meeting on "The Control and Reduction of Wear in Military Platforms". vol. 251-254. Williamsburg: RTO; 2003. p. 935-48.

117. Nicholls JR, Jaslier Y, Rickerby DS. Erosion and foreign object damage of thermal barrier coatings. Materials Science Forum. 1997;251-254(PART 2):935-48.

118. Geng X, Wellman R, Arrom LI, Chalk C, Castelluccio GM. Estimation of thermal barrier coating fracture toughness using integrated computational materials engineering. Ceramics International. 2023 8;49:25788-94.

119. Söderberg S, Hogmark S, Engman U, Swahn H. Erosion classification of materials using a centrifugal erosion tester. Tribology International. 1981 12;14:333-43. Available at: https://linkinghub.elsevier.com/retrieve/pii/0301679X81901018.

120. Noon AA, Jabbar AU, Koten H, Kim MH, Ahmed HW, Mueed U, et al. Strive to reduce slurry erosion and cavitation in pumps through flow modifications, design optimization and some other techniques: Long term impact on process industry. Materials. 2021 2;14:1-33.

121. Tabakoff W. Investigation of coatings at high temperature for use in turbomachinery. Surface and Coatings Technology. 1989;39-40(C):97-115.

122. Wellman RG, Nicholls JR. High temperature erosion-oxidation mechanisms, maps and models. Wear. 2004;256(9-10):907-17.

123. Nieto A, Agrawal R, Bravo L, Hofmeister-Mock C, Pepi M, Ghoshal A. Calcia–magnesia–alumina–silicate (CMAS) attack mechanisms and roadmap towards Sandphobic thermal and environmental barrier coatings. International Materials Reviews. 2020;0(0):1-42. Available at: https://doi.org/10.1080/09506608.2020.1824414.

124. Song W, Lavallee Y, Hess KU, Kueppers U, Cimarelli C, Dingwell DB. Volcanic ash melting under conditions relevant to ash turbine interactions. Nature Communications. 2016;7:1-10.

125. Chavez Gomez JJ. Cmas / volcanic Ash Infiltration Performance Of Yttria Rich-Zirconia Thermal Barrier Coatings Produced By Electron Beam Physical Vapor Deposition Doctoral Program in Mechanical Engineering. PhD. University of Texas at El Paso; 2019.

126. Naraparaju R, Gomez Chavez JJ, Niemeyer P, Hess KU, Song W, Dingwell DB, et al. Estimation of CMAS infiltration depth in EB-PVD TBCs: A new constraint model supported with experimental approach. Journal of the European Ceramic Society. 2019;39(9):2936-45. Available at: https://doi.org/10.1016/j.jeurceramsoc.2019.02.040.

127. Zhao H, Levi CG, Wadley HNG. Molten silicate interactions with thermal barrier coatings. Surface and Coatings Technology. 2014;251:74-86. Available at: http://dx.doi.org/10.1016/j.surfcoat.2014.04.007.

128. Poerschke DL, Barth TL, Levi CG. Equilibrium relationships between thermal barrier oxides and silicate melts. Acta Materialia. 2016;120:302-14. Available at: http://dx.doi.org/10.1016/j.actamat.2016.08.077.

129. Krämer S, Yang J, Levi CG. Infiltration-inhibiting reaction of gadolinium zirconate thermal barrier coatings with CMAS melts. Journal of the American Ceramic Society. 2008;91(2):576-83.

130. Ball JAJ, Martins JF, Brewster G, Chen Y, Xiao P. An investigation into RESZ (RE = Yb, Er, Gd, Sm) materials for CMAS resistance in thermal barrier coatings. Journal of the European Ceramic Society. 2024 6;44:3734-46. Available at: https://linkinghub.elsevier.com/retrieve/pii/S0955221924000554.

131. Rai AK, Bhattacharya RS, Wolfe DE, Eden TJ. CMAS-resistant thermal barrier coatings (TBC). International Journal of Applied Ceramic Technology. 2010;7(5):662-74.

132. Zaleski EM. Mechanisms and Mitigation of CMAS Attack on Thermal Barrier Coatings. PhD. University of California Santa Barbara; 2013.

133. Pearson D, Brooker R. The accumulation of molten volcanic ash in jet engines; simulating the role of magma composition, ash particle size and thermal barrier coatings. Journal of Volcanology and Geothermal Research. 2020;389.

134. Kabir MR, Sirigiri AK, Naraparaju R, Schulz U. Flow kinetics of molten silicates through thermal barrier coating: A numerical study. Coatings. 2019;9(5).

135. Cavainolo B, Kinzel MP, Naraparaju R, Kabir MR. Simulating CMAS Infiltration of an EB-PVD Thermal Barrier Coating Using the Volume-of-Fluid Method. American Institute of Aeronautics and Astronautics; 2023. Available at: https://doi.org/10.2514/6.2023-4427. doi:10.2514/6.2023-4427.

136. Munuhe TW, Chen RH, Zhu L, Ma R. Modeling molten droplet spreading and infiltration into non-isothermal thermal barrier coatings. International Journal of Heat and Mass Transfer. 2022 1;182.

137. Poerschke DL, Levi CG. Effects of cation substitution and temperature on the interaction between thermal barrier oxides and molten CMAS. Journal of the European Ceramic Society. 2015;35(2):681-91. Available at: http://dx.doi.org/10.1016/j.jeurceramsoc.2014.09.006.

138. Ndamka NL, Wellman RG, Nicholls JR. The degradation of thermal barrier coatings by molten deposits: Introducing the concept of basicity. Materials at High Temperatures. 2016;33(1):44-50. Available at: http://dx.doi.org/10.1179/1878641315Y.0000000017.

139. Boissonnet G, Chalk C, Nicholls JR, Bonnet G, Pedraza F. Thermal insulation of CMAS (Calcium-Magnesium-Alumino-Silicates)- attacked plasma-sprayed thermal barrier coatings. Journal of the European Ceramic Society. 2020;40(5):2042-9.

140. Traeger F, Vaßen R, Rauwald KH, Stöver D. Thermal cycling setup for testing thermal barrier coatings. Advanced Engineering Materials. 2003;5(6):429-32.

141. Steinke T, Sebold D, Mack DE. A novel test approach for plasma-sprayed coatings tested simultaneously under CMAS and thermal gradient cycling conditions. Surface and Coatings Technology. 2010;205:2287-95.

142. Jackson RW, Zaleski EM, Poerschke DL, Hazel BT, Begley MR, Levi CG. Interaction of molten silicates with thermal barrier coatings under temperature gradients. Acta Materialia. 2015;89:396-407. Available at: http://dx.doi.org/10.1016/j.actamat.2015.01.038.

143. Yang T, Wang W, Tang Z, Liu Y, Li K, Liu W, et al. CMAS infiltration behavior of atmospheric plasma-sprayed thermal barrier coating with tailored pore structures. Ceramics International. 2024 3;50:7218-29.

144. Krause AR, Senturk BS, Garces HF, Dwivedi G, Ortiz AL, Sampath S, et al. $2ZrO_2Y_2O_3$ Thermal Barrier Coatings Resistant to Degradation by Molten CMAS: Part I, Optical Basicity Considerations and Processing. Journal of the American Ceramic Society. 2014;97(12):3943-9.

145. Sternlicht H, McComb DW, Padture NP. Interaction of ytterbium pyrosilicate environmental-barrier-coating ceramics with molten calcia-magnesia-aluminosilicate glass: Part I, Microstructures. Acta Materialia. 2022 Dec;241:118360. Available at: http://dx.doi.org/10.1016/j.actamat.2022.118360.

146. Zhou R, Zhang H, Gao X, Sun B, Li C, Wu P, et al. Applications of synchrotron-based X-ray diffraction in investigating thermal barrier coatings. Journal of Materials Research and Technology. 2024 Jan;28:2831–2844. Available at: http://dx.doi.org/10.1016/j.jmrt.2023.12.196.

147. Wang Y, Fu Q, Dong H, Zhuo X, Liang X, Liu G, et al. CMAS corrosion behavior of interface for EB-PVD $Gd_2Zr_2O_7$/YSZ thermal barrier coatings. Materials Today Communications. 2024 Dec;41:110756. Available at: http://dx.doi.org/10.1016/j.mtcomm.2024.110756.

148. Zhou P, Ogle K. The corrosion of copper and copper alloys. Encyclopedia of Interfacial Chemistry: Surface Science and Electrochemistry. 2018;(May):478-89.

149. Krämer S, Yang J, Levi CG, Johnson CA. Thermochemical interaction of thermal barrier coatings with molten CaO-MgO-Al 2O 3-SiO 2 (CMAS) deposits. Journal of the American Ceramic Society. 2006;89(10):3167-75.

150. Montero X, Naraparaju R, Galetz MC, Schulz U. Study of CMAS infiltration and evaporation behaviour under water vapour/sulphur oxide conditions in EB-PVD 7YSZ. Corrosion Science. 2022 Apr;198:110123. Available at: http://dx.doi.org/10.1016/j.corsci.2022.110123.

151. Lei X, Wang Y, Wang Q, Li L, Ning X. A case study on CMAS corrosion of an in-situ microstructure modification YSZ TBCs fabricated by EB-PVD. Surface and Coatings Technology. 2021 Nov;425:127738. Available at: http://dx.doi.org/10.1016/j.surfcoat.2021.127738.

152. Steinberg L, Mikulla C, Naraparaju R, Toma FL, Großmann H, Schulz U, et al. Erosion resistance of CMAS infiltrated sacrificial suspension sprayed alumina top layer on EB-PVD 7YSZ coatings. Wear. 2019 Nov;438–439:203064. Available at: http://dx.doi.org/10.1016/j.wear.2019.203064.

153. Xia J, Zhang L, Matsushita Y, Wu RT. Evolution of the microstructure and mechanisms of performance degradation in EB-PVD YSZ thermal barrier coatings corroded by volcanic ash at 1150 °C. Corrosion Science. 2022 Nov;208:110626. Available at: http://dx.doi.org/10.1016/j.corsci.2022.110626.

154. Sun Y, Nie X, Cai C, Yang L, Zhou Y. Phase transformation failure in YSZ TBCs induced by component-dependent CMAS corrosion. Surface and Coatings Technology. 2023 Jul;464:129547. Available at: http://dx.doi.org/10.1016/j.surfcoat.2023.129547.

155. Cui JJ, Ouyang JH, Liu ZG. Hot corrosion behavior of $LaMgAl_11O_19$ ceramic coated with molten CMAS deposits at temperature of 1250 °C in air. Journal of Alloys and Compounds. 2016;685:316-21. Available at: http://dx.doi.org/10.1016/j.jallcom.2016.05.272.

156. Yan G, Liu W, Sun Y, Li C, Yang L, Zhou YC. Failure behavior of $RE_2M_2O_7$/YSZ TBCs prepared by EB-PVD in gas thermal shock-CMAS corrosion environment. Journal of the European Ceramic Society. 2025 Mar;45(3):117027. Available at: http://dx.doi.org/10.1016/j.jeurceramsoc.2024.117027.

157. Weiwei Q, Zehao C, Shusuo L, Mengmeng W, Yanling P, Shengkai G. Failure mechanism of YSZ coatings prepared by EB-PVD under partial penetration of CMAS attacking. Corrosion Science. 2022 Jul;203:110339. Available at: http://dx.doi.org/10.1016/j.corsci.2022.110339.

158. Huo K, Zhao Y, Hua Y, Cai J, Ye Y, Dai F. Study of CMAS wettability, penetration, and degradation behaviors on EB-PVD 8YSZ coatings laser micro-glazed (LMGed) by an ultraviolet picosecond ultrashort pulsed laser. Surface and Coatings Technology. 2024 Aug;489:131136. Available at: http://dx.doi.org/10.1016/j.surfcoat.2024.131136.

159. Dong H, Liang X, Wang Z, Luo N, Zhang J, Zhan Y, et al. Enhancing the performances of EB-PVD TBCs via overlayer Al-modification. Surface and Coatings Technology. 2023 Nov;473:130001. Available at: http://dx.doi.org/10.1016/j.surfcoat.2023.130001.

160. Peng H, Wang L, Guo L, Miao W, Guo H, Gong S. Degradation of EB-PVD thermal barrier coatings caused by CMAS deposits. Progress in Natural Science: Materials International. 2012 Oct;22(5):461–467. Available at: http://dx.doi.org/10.1016/j.pnsc.2012.06.007.

161. Mechnich P, Braue W, Schulz U. High-temperature corrosion of EB-PVD yttria partially stabilized zirconia thermal barrier coatings with an artificial volcanic ash overlay. Journal of the American Ceramic Society. 2011;94(3):925-31.

162. Schulz U, Braue W. Degradation of La_2Zr2O_7 and other novel EB-PVD thermal barrier coatings by CMAS (CaO-MgO-$Al2O_3$-SiO_2) and volcanic ash deposits. Surface and Coatings Technology. 2013;235:165-73. Available at: http://dx.doi.org/10.1016/j.surfcoat.2013.07.029.

163. Stein Z, Kenesei P, Park JS, Almer J, Naraparaju R, Schulz U, et al. High-energy X-ray phase analysis of CMAS-infiltrated 7YSZ thermal barrier coatings: Effect of time and temperature. Journal of Materials Research. 2020;35(17):2300-10.

164. Gomez Chavez JJ, Naraparaju R, Mechnich P, Kelm K, Schulz U, Ramana CV. Effects of yttria content on the CMAS infiltration resistance of yttria stabilized thermal barrier coatings system. Journal of Materials Science &; Technology. 2020 Apr;43:74–83. Available at: http://dx.doi.org/10.1016/j.jmst.2019.09.039.

165. Vidal-Sétif MH, Panteix PJ, Rapin C, Vilasi M. Calcium-Magnesium-Alumino-Silicate (CMAS) degradation of thermal barrier coatings: solubility of different oxides from ZrO_2-Nd_2O_3 system in a model CMAS. Surface and Coatings Technology. 2012;208:39-45. Available at: https://www.researchgate.net/publication/281555892.

166. Mikulla C, Steinberg L, Niemeyer P, Schulz U, Naraparaju R. Microstructure Refinement of EB-PVD Gadolinium Zirconate Thermal Barrier Coatings to Improve Their CMAS Resistance. Coatings. 2023;13(5):1-23.

167. Chavez JJG, Naraparaju R, Mikulla C, Mechnich P, Kelm K, Ramana CV, et al. Comparative study of EB-PVD gadolinium-zirconate and yttria-rich zirconia coatings performance against Fe-containing calcium-magnesium-aluminosilicate (CMAS) infiltration. Corrosion Science. 2021 9;190:109660. Available at: https://linkinghub.elsevier.com/retrieve/pii/S0010938X21004261.

168. Wang B, Jiang C, Wu Y, Pan L, Chen Y, Lang X, et al. Effect of microstructure on CMAS corrosion behavior of (Gd0.8Yb0.2)2Zr2O7/YSZ thermal barrier coatings prepared by EB-PVD. Corrosion Science. 2023 Oct;223:111477. Available at: http://dx.doi.org/10.1016/j.corsci.2023.111477.

169. Naraparaju R, Pubbysetty RP, Mechnich P, Schulz U. EB-PVD alumina ($Al2O_3$) as a top coat on 7YSZ TBCs against CMAS/VA infiltration: Deposition and reaction mechanisms. Journal of the European Ceramic Society. 2018 8;38:3333-46.

170. Naraparaju R, Gomez Chavez JJ, Schulz U, Ramana CV. Interaction and infiltration behavior of Eyjafjallajökull, Sakurajima volcanic ashes and a synthetic CMAS containing FeO with/in EB-PVD ZrO 2 -65 wtActa Materialia. 2017 Sep;136:164–180. Available at: http://dx.doi.org/10.1016/j.actamat.2017.06.055.

171. Wang L, Guo L, Li Z, Peng H, Ma Y, Gong S, et al. Protectiveness of Pt and Gd2Zr2O7 layers on EB-PVD YSZ thermal barrier coatings against calcium–magnesium–alumina–silicate (CMAS) attack. Ceramics International. 2015 Nov;41(9):11662–11669. Available at: http://dx.doi.org/10.1016/j.ceramint.2015.05.128.

172. Vidal-Sétif MH, Rio C, Boivin D, Lavigne O. Microstructural characterization of the interaction between 8YPSZ (EB-PVD) thermal barrier coatings and a synthetic CAS. Surface and Coatings Technology. 2014;239:41-8. Available at: http://dx.doi.org/10.1016/j.surfcoat.2013.11.014.

173. Chemical Vapour Deposition - Bespoke 'in house' CVD rig; 2024. Available at: https://www.royce.ac.uk/equipment-and-facilities/chemical-vapour-deposition/https://web.archive.org/web/20240529191015/https://www.royce.ac.uk/equipment-and-facilities/chemical-vapour-deposition/. available online at https://www.royce.ac.uk/equipment-and-facilities/chemical-vapour-deposition/, accessed 2024 Nov 18, archived at https://web.archive.org/web/20240529191015/https://www.royce.ac.uk/equipment-and-facilities/chemical-vapour-deposition/.

174. Chiriví L. Effect of Manufacturing Parameters on TBC Systems Cyclic Oxidation Lifetime. PhD Dissertation. Cranfield University; 2011. available online at https://dspace.lib.cranfield.ac.uk/handle/1826/7893, date accessed 24/02/2022.

175. Multi-Source Electron Beam Physical Vapour Deposition - Von Ardenne EB-150; 2024. Available at: https://www.royce.ac.uk/equipment-and-facilities/multi-source-electron-beam-physical-vapour-deposition/. available online at https://www.royce.ac.uk/equipment-and-facilities/multi-source-electron-beam-physical-vapour-deposition/, accessed 2024 Nov 18, archived at https://web.archive.org/web/20240529185853/https://www.royce.ac.uk/equipment-and-facilities/multi-source-electron-beam-physical-vapour-deposition/.

176. Chevallier J, Isern L, Almandoz Forcen K, Chalk C, Nicholls JR. Modelling evaporation in electron-beam physical vapour deposition of thermal barrier coatings. Emergent Materials. 2021;4(6):1499-513. Available at: https://doi.org/10.1007/s42247-021-00284-5.

177. Wellman RG. Modelling the erosion of electron beam physical vapour deposited thermal barrier coatings. PhD Dissertation. Cranfield University; 2001.

178. Wellman RG, Deakin MJ, Nicholls JR. The effect of TBC morphology and aging on the erosion rate of EB-PVD TBCs. Tribology International. 2005;38(9 SPEC. ISS.):798-804.

179. Vaßen R, Mack DE, Tandler M, Sohn YJ, Sebold D, Guillon O. Unique performance of thermal barrier coatings made of yttria-stabilized zirconia at extreme temperatures (>1500°C). Journal of the American Ceramic Society. 2021;104(1):463-71.

180. Karaoglanli AC, Doleker KM, Ozgurluk Y. Interface failure behavior of yttria stabilized zirconia (YSZ), La_2Zr2O_7, $Gd_2Zr_2O_7$, YSZ/La_2Zr2O_7 and YSZ/$Gd_2Zr_2O_7$ thermal barrier coatings (TBCs) in thermal cyclic exposure. Materials Characterization. 2020 1;159:110072.

181. Abuchenari A, Ghazanfari H, Siavashi M, Sabetzadeh M, Talebi S, Chemeh ZK, et al. A review on development and application of self-healing thermal barrier composite coatings. Journal of Composites and Compounds. 2020 5;2:147-54.

182. Schulz U, Fritscher K, Peters M. EB-PVD Y_2O_3- and -stabilized zirconia thermal barrier coatings — crystal habit and phase composition. Surface and Coatings Technology. 1996 8;82:259-69. Available at: https://linkinghub.elsevier.com/retrieve/pii/0257897295027270.

183. Zhang J, Wang ZG, Song X, Xie M, Zhang Y, Mu R, et al. Tailoring the thermal conductivity of Sc_2O_3–Yb_2O_3 Co-stabilized ZrO_2 thermal barrier materials and mechanism insight. Ceramics International. 2023 5;49:13601-9. Available at: https://linkinghub.elsevier.com/retrieve/pii/S0272884222046685.

184. Munawar AU, Schulz U, Cerri G, Lau H. Microstructure and cyclic lifetime of Gd and Dy-containing EB-PVD TBCs deposited as single and double-layer on various bond coats. Surface and Coatings Technology. 2014 4;245:92-101.

185. Boissonnet G, Chalk C, Nicholls JR, Bonnet G, Pedraza F. Phase stability and thermal insulation of YSZ and erbia-yttria co-doped zirconia EB-PVD thermal barrier coating systems. Surface and Coatings Technology. 2020 5;389.

186. Zhu D, Chen YL, Miller RA. Defect Clustering and Nanophase Structure Characterization of Multicomponent Rare Earth-Oxide-Doped Zirconia-Yttria Thermal Barrier Coatings; 2004. Available at: http://www.sti.nasa.gov.

187. Schaedler TA, Fabrichnaya O, Levi CG. Phase equilibria in the TiO_2-$YO_{1.5}$-ZrO_2 system. Journal of the European Ceramic Society. 2008 9;28:2509-20.

188. Pitek FM, Levi CG. Opportunities for TBCs in the ZrO_2-$YO_{1.5}$-TaO_2.5 system. Surface and Coatings Technology. 2007 3;201:6044-50.

189. Limarga AM, Shian S, Leckie RM, Levi CG, Clarke DR. Thermal conductivity of single- and multi-phase compositions in the ZrO_2-Y_2O_3-Ta_2O_5 system. Journal of the European Ceramic Society. 2014;34:3085-94.

190. Sun Y, Wu X, Tan Z, Yang L, Zhou Y. Boosting the strain tolerance of Ta_2O_5 stabilized ZrO_2 TBCs through prefabricated cracks by in-situ reaction. Journal of Alloys and Compounds. 2023 2;935.

191. Tan ZY, Yan G, Cao K, Cheng CY, Yang L, Zhou YC. Effect of microstructure on the performance of Zr6Ta_2O17 ceramics as thermal barrier coatings. Ceramics International. 2023 9;49:29449-58.

192. Schulz U, Nowotnik A, Kunkel S, Reiter G. Effect of processing and interface on the durability of single and bilayer 7YSZ / gadolinium zirconate EB-PVD thermal barrier coatings. Surface and Coatings Technology. 2020 1;381.

193. Gok MG, Goller G. State of the Art of Gadolinium Zirconate Based Thermal Barrier Coatings: Design, Processing and Characterization. Nánai L, Samantara A, Fábián L, Ratha S, (eds.). Methods for Film Synthesis and Coating Procedures. Rijeka: IntechOpen; 2019. Available at: https://doi.org/10.5772/intechopen.85451.

194. Kember T. Compositional Variations in Vapor Deposited Samarium Zirconate Coatings. PhD Thesis. University of Virginia; 2011.

195. Zhao H, Levi CG, Wadley HNG. Vapor deposited samarium zirconate thermal barrier coatings. Surface and Coatings Technology. 2009 7;203:3157-67.

196. Ozgurluk Y, Doleker KM, Ahlatci H, Karaoglanli AC. Investigation of calcium–magnesium-alumino-silicate (CMAS) resistance and hot corrosion behavior of YSZ and La_2Zr2O_7/YSZ thermal barrier coatings (TBCs) produced with CGDS method. Surface and Coatings Technology. 2021 4;411.

197. Bobzin K, Brögelmann T, Kalscheuer C, Yildirim B, Welters M. Thermoschock- und isothermes Oxidationsverhalten von vierlagigen EB-PVD Wärmedämmschichten. Materialwissenschaft und Werkstofftechnik. 2017 6;48:502-18.

198. Liu G, Shen Z, He L, Mu R, Huang G. LaYZrO/YSZ double ceramic layer thermal barrier coatings by EB-PVD: Thermal performance, morphology and failure behavior. Materialia. 2023 3;27.

199. Saruhan B, Francois P, Fritscher K, Schulz U. EB-PVD processing of pyrochlore-structured La_2Zr2O_7-based TBCs. Surface and Coatings Technology. 2004 4;182:175-83.

200. B SB;. Schulz U., Kroder, C. J., inventors; Deutsches Zentrum fur Luft und Raumfahrt eV, asignee. Thermal-insulating material having an essentially magnetoplumbitic crystal structure [Internet]. United States patent US8986792B2. 2002 May 09 [cited 2024 Jun 28]. Available online at https://patents.google.com/patent/US7048836B2/en.

201. Zhang J, Zhong X, Cheng Y, Wang Y, Xu Z, Chen X, et al. Thermal-shock resistance of $LnMgAl_11O_19$ (Ln = La, Nd, Sm, Gd) with magnetoplumbite structure. Journal of Alloys and Compounds. 2009 8;482:376-81.

202. Liu Y, Cooper VR, Wang B, Xiang H, Li Q, Gao Y, et al. Discovery of ABO 3 perovskites as thermal barrier coatings through high-throughput first principles calculations. Materials Research Letters. 2019 4;7:145-51.

203. Guo L, Li M, Cheng Y, Zhang C, He S, Zhang Y, et al. Plasma sprayed nanostructured GdPO4 thermal barrier coatings: Preparation microstructure and CMAS corrosion resistance. Journal of the American Ceramic Society. 2017 9;100:4209-18.

204. Luo X, Huang S, Huang R, Hong J, Yuan S, Shu Z, et al. Rare-earth high-entropy magnetoplumbite structure hexaluminates (La1/5Nd1/5Sm1/5Eu1/5Gd1/5)$MAl_1$1O19 (M = Mg, Zn) for thermal barrier coating applications with enhanced mechanical and thermal properties. Ceramics International. 2024 6;50:21281-8. Available at: https://linkinghub.elsevier.com/retrieve/pii/S0272884224011891.

205. Zhao Z, Ruan Z, Li R, Yan S, Sun X, Liu C, et al. High entropy pyrochlore (La0.3Gd0.3Ca0.4)2(Ti0.2Zr0.2Hf0.2Nb0.2Ta0.2)2O_7 ceramic with amorphous-like thermal conductivity for environmental/thermal barrier coating applications. Journal of Materials Science & Technology. 2024 1.

206. Sluytman JSV, Krämer S, Tolpygo VK, Levi CG. Microstructure evolution of ZrO_2-YbTaO4 thermal barrier coatings. Acta Materialia. 2015 6;96:133-42.

207. Yang J, Pan W, Han Y, Zhao M, Huang M, Wan C. Mechanical properties, oxygen barrier property, and chemical stability of RE3NbO_7 for thermal barrier coating. Journal of the American Ceramic Society. 2020;103(4):2302-8.

208. Heinze SG, Sluytman JSV, Levi CG. Microstructure evolution and physical properties of ZrO_2-(Y+Yb)$O_{1.5}$-TaO_2.5 thermal barrier coatings. Surface and Coatings Technology. 2020 5;389.

209. Steenbakker RJL, Wellman RG, Nicholls JR. Erosion of gadolinia doped EB-PVD TBCs. Surface and Coatings Technology. 2006;201(6):2140-6. Available at: http://dx.doi.org/10.1016/j.surfcoat.2006.03.022.

210. Schmitt MP, Rai AK, Bhattacharya R, Zhu D, Wolfe DE. "Multilayer thermal barrier coating (TBC) architectures utilizing rare earth doped YSZ and rare earth pyrochlores". Surface and Coatings Technology. 2014 7;251:56-63.

211. Schmitt MP, Stokes JL, Gorin BL, Rai AK, Zhu D, Eden TJ, et al. Effect of Gd content on mechanical properties and erosion durability of sub-stoichiometric $Gd_2Zr_2O_7$. Surface and Coatings Technology. 2017;313:177-83.

212. Zhang FX, Saxena SK. Structural changes and pressure-induced amorphization in rare earth titanates RE2Ti2O_7 (RE: Gd, Sm) with pyrochlore structure. Chemical Physics Letters. 2005 9;413:248-51.

213. Moreno KJ, Fuentes AF, Maczka M, Hanuza J, Amador U. Structural manipulation of pyrochlores: Thermal evolution of metastable Gd2(Ti1-yZry)2O_7 powders prepared by mechanical milling. Journal of Solid State Chemistry. 2006 12;179:3805-13.

214. Maram PS, Ushakov SV, Weber RJK, Benmore CJ, Navrotsky A. Probing disorder in pyrochlore oxides using in situ synchrotron diffraction from levitated solids-A thermodynamic perspective. Scientific Reports. 2018 12;8.

215. Beake BD, Goodes SR, Zhang H, Isern L, Chalk C, Nicholls JR, et al. Randomised nano-/micro- impact testing – A novel experimental test method to simulate erosive damage caused by solid particle impacts. Tribology International. 2024 7;195:109647. Available at: https://linkinghub.elsevier.com/retrieve/pii/S0301679X24003992.

216. Slikkerveer P. Mechanical etching of glass by powder blasting. Phd Thesis 2 (Research NOT TU/e / Graduation TU/e). Chemical Engineering and Chemistry; 1999. Proefschrift.

217. Steinberg L, Naraparaju R, Heckert M, Mikulla C, Schulz U, Leyens C. Erosion behavior of EB-PVD 7YSZ coatings under corrosion/erosion regime: Effect of TBC microstructure and the CMAS chemistry. Journal of the European Ceramic Society. 2018;38(15):5101-12. Available at: https://doi.org/10.1016/j.jeurceramsoc.2018.06.039.

218. Witz G, Shklover V, Steurer W, Bachegowda S, Bossmann HP. Phase evolution in yttria-stabilized zirconia thermal barrier coatings studied by rietveld refinement of X-ray powder diffraction patterns. Journal of the American Ceramic Society. 2007;90(9):2935-40.

219. Teng X, Peng H, Li L, Guo H. Investigation on crystal orientations in EB-PVD YSZ coatings under different substrate rotation mode. Journal of the European Ceramic Society. 2023;43(12):5373-80. Available at: https://doi.org/10.1016/j.jeurceramsoc.2023.05.010.

220. Mechnich P, Braue W. Volcanic ash-induced decomposition of EB-PVD Gd 2 Zr 2 O 7 thermal barrier coatings to Gd-oxyapatite, zircon, and Gd, Fe-zirconolite. Journal of the American Ceramic Society. 2013 jun;96(6):1958-65. Available at: https://onlinelibrary.wiley.com/doi/10.1111/jace.12251.

221. Mahade S, Curry N, Björklund S, Markocsan N, Joshi S. Durability of gadolinium zirconate/YSZ double-layered thermal barrier coatings under different thermal cyclic test conditions. Materials. 2019 7;12.

222. Johnson CA, Ruud JA, Bruce RW, Wortman D. Relationships between residual stress, microstructure and mechanical properties of electron beam-physical vapor deposition thermal barrier coatings. Surface and Coatings Technology. 1998;108-109:80-5.

223. Gregori G, Lì L, Nychka JA, Clarke DR. Vibration damping of superalloys and thermal barrier coatings at high-temperatures. Materials Science and Engineering A. 2007;466:256-64.

224. Steinberg L, Mikulla C, Naraparaju R, Pavlov P, Löffler M, Schulz U, et al. Erosion behavior of CMAS/VA infiltrated EB-PVD $Gd_2Zr_2O_7$ TBCs: Special emphasis on the effect of mechanical properties of the reaction products. Wear. 2022 10;506-507.

225. Feuerstein A, Knapp J, Taylor T, Ashary A, Bolcavage A, Hitchman N. Technical and economical aspects of current thermal barrier coating systems for gas turbine engines by thermal spray and EBPVD: A review. Journal of Thermal Spray Technology. 2008;17:199-213.

226. An K, Ravichandran KS, Dutton RE, Semiatin SL. Microstructure, Texture, and Thermal Conductivity of Single-Layer and Multilayer Thermal Barrier Coatings of Y_2O_3-Stabilized ZrO_2 and Al2O_3 Made by Physical Vapor Deposition. Journal of the American Ceramic Society. 1999;82:399-406.

227. Watanabe M, Mercer C, Levi CG, Evans AG. A probe for the high temperature deformation of thermal barrier oxides. Acta Materialia. 2004;52(6):1479-87.

228. Pędrak P, Dychtoń K, Drajewicz M, Góral M. Synthesis of $Gd_2Zr_2O_7$ Coatings Using the Novel Reactive PS-PVD Process. Coatings. 2021 oct;11(10):1208. Available at: https://www.mdpi.com/2079-6412/11/10/1208.

229. Pfoertner H. A084644 - Best packings of m>1 equal circles into a larger circle setting a new density record.; 2003. available online at https://oeis.org/A084644, date accessed: 27 Jun 2024, archived at https://web.archive.org/web/20240324172922/https://oeis.org/A084644.

230. Pfoertner H. Minimum area of circle needed to cover n circles of area 1; 2003. available online at https://www.randomwalk.de/sequences/a084618.pdf, date accessed: 27 Jun 2024, archived at https://web.archive.org/web/20041113041855/http://www.randomwalk.de/sequences/a084618.pdf.

231. Zuiderveld K. Heckbert PS, (ed.). VIII.5. - Contrast Limited Adaptive Histogram Equalization. Academic Press; 1994. p. 474-85. Available at: https://www.sciencedirect.com/science/article/pii/B9780123361561500616.

232. Britton TB, Jiang J, Guo Y, Vilalta-Clemente A, Wallis D, Hansen LN, et al. Tutorial: Crystal orientations and EBSD - Or which way is up? Materials Characterization. 2016 7;117:113-26.

233. Engler O, Randle V. Introduction to texture analysis. 2nd edn. Boca Raton, FL: CRC Press; 2010.

234. Das DK, Lakshmi SG, Rao DS, Banumathy S, Singh AK. Microstructure, texture and thermal cycling performance of EB-PVD TBCs deposited under different processing conditions. High Temperature Materials and Processes. 2012 1;30:539-48.

235. Tran R, Xu Z, Radhakrishnan B, Winston D, Sun W, Persson KA, et al. Data Descriptor: Surface energies of elemental crystals. Cancer Gene Therapy. 2016;23(9):321-5.

236. Paterson MS. The equivalent channel model for permeability and resistivity in fluid-saturated rock—A re-appraisal. Mechanics of Materials. 1983 12;2:345-52. Available at: https://linkinghub.elsevier.com/retrieve/pii/016766368390025X.

237. Shan X, Luo L, Chen W, Zou Z, Guo F, He L, et al. Pore filling behavior of YSZ under CMAS attack: Implications for designing corrosion-resistant thermal barrier coatings. Journal of the American Ceramic Society. 2018;101(12):5756-70.

238. Shan X, Chen W, Yang L, Guo F, Zhao X, Xiao P. Pore filling behavior of air plasma spray thermal barrier coatings under CMAS attack. Corrosion Science. 2020;167(September 2019):108478. Available at: https://doi.org/10.1016/j.corsci.2020.108478.

239. Investigation of Volume-of-Fluid Method to Simulate Melting-Solidification of CMAS Particles. vol. Volume 2: Multiphase Flow (MFTC); Computational Fluid Dynamics (CFDTC); Micro and Nano Fluid Dynamics (MNFDTC) of Fluids Engineering Division Summer Meeting; 2022. Available at: https://doi.org/10.1115/FEDSM2022-85863.

240. Begley MR, Hutchinson JW. The Mechanics and Reliability of Films , Multilayers and Coatings. Cambridge, UK: Cambridge University Press; 2017.

241. Begley MR. LayerSlayer - Multilayer Analysis Suite; 2020. Available at: https://sites.engineering.ucsb.edu/~begley/LayerSlayer.html. date accessed 27/02/2022.

242. Stephan K, Laesecke A. The Thermal Conductivity of Fluid Air. Journal of Physical and Chemical Reference Data. 1985 1;14:227-34.

243. Meneses DDS, Melin P, Campo LD, Cosson L, Echegut P. Apparatus for measuring the emittance of materials from far infrared to visible wavelengths in extreme conditions of temperature. Infrared Physics and Technology. 2015;69:96-101.

244. Bale CW, Bélisle E, Chartrand P, Decterov SA, Eriksson G, Gheribi AE, et al. FactSage thermochemical software and databases, 2010-2016. Calphad: Computer Coupling of Phase Diagrams and Thermochemistry. 2016 9;54:35-53.

245. GTT-Technologies. FactSage-Databases; 2022. Available at: https://gtt-technologies.de/data/. available online at https://gtt-technologies.de/data/, date accessed: 2022 Feb 09. Archived at https://web.archive.org/web/20240628122428/https://gtt-technologies.de/data/.

246. Siemers PA, Hillig WB. SRD-81-083 - Thermal barrier coated turbine blade study. National Aeronautics and Space Administration; 1981.

247. Anderson NP, Sheffler KD. NAS 1.26:168251 - Development of Strain Tolerant Thermal Barrier Coating Systems Tasks I-III. National Aeronautics and Space Administration; 1984.

248. Miller RA. Thermal barrier coatings for aircraft engines: History and directions. Journal of Thermal Spray Technology. 1997;6(1):35-42.

249. Meier SM, Gupta DK. The Evolution of Thermal Barrier Coatings in Gas Turbine Engine Applications. ASME 1992 International Gas Turbine and Aeroengine Congress and Exposition, GT 1992. 1992;5.

250. Nicholls J, Chirivi L, Long K. A Probabilistic Life Model for EB-PVD Thermal Barrier Coatings on Diffusion Bondcoats. The 22nd Advanced Aerospace Materials and Processes (AeroMat) Conference and Exposition. American Society of Materials; 2011. .

251. Kızılersü A, Kreer M, Thomas AW. The Weibull Distribution. Significance. 2018 04;15(2):10-1. Available at: https://doi.org/10.1111/j.1740-9713.2018.01123.x.

252. Nicholls JR, Hancock P. Analysis of oxidation and hot corrosion data - A statistical approach.; 1983. p. 198 – 210. Available at: https://www.scopus.com/inward/record.uri?eid=2-s2.0-0020887583&partnerID=40&md5=b7074c6bb3a19f29224430cda0f164ee.

253. Nicholls JR, Stephenson DJ. A life prediction model for coatings based on the statistical analysis of hot salt corrosion performance. Corrosion Science. 1992;33(8):1313-25. Available at: https://www.sciencedirect.com/science/article/pii/0010938X9290138S.

254. Kendall MG, Stuart AL, Ord JK. Kendall's advanced theory of statistics. Journal of the American Statistical Association. 1995;90:398. Available at: https://api.semanticscholar.org/CorpusID:121544407.

255. Hansen A. The Three Extreme Value Distributions: An Introductory Review. Frontiers in Physics. 2020;8(December):1-8.

256. Reid M. MatthewReid854/reliability: v0.5.7. Zenodo; 2021. Available at: https://doi.org/10.5281/zenodo.5030847.

Appendix A

Ethical Approval Letter

This appendix includes the ethical approval letter:



20 November 2019

Dear Mr Almandoz Forcen ,

Reference: CURES/9423/2019
Title: Multi-layer thermal barrier coating systems optimised for manufacturability and performance in demanding gas turbine environments

Thank you for your application to the Cranfield University Research Ethics System (CURES).

We are pleased to inform you your CURES application, reference CURES/9423/2019 **has been reviewed. You may now proceed with the research activities you have sought approval for.**

If you have any queries, please contact CURES Support.

We wish you every success with your project.

Regards,

CURES Team

Appendix B

EBSD maps of model TBC systems.

The EBSD maps of the model TBC systems are presented in this appendix in the order given in Table 3.9. Note that the IPF given corresponds to the Y (Through thickness) direction. IPF color keys given in LowK coatings are consistent across all LowK coatings and LowK layers in GZO/LowK coatings. The IPF color key for the GZO layer is consistent and given in Figure B.11.

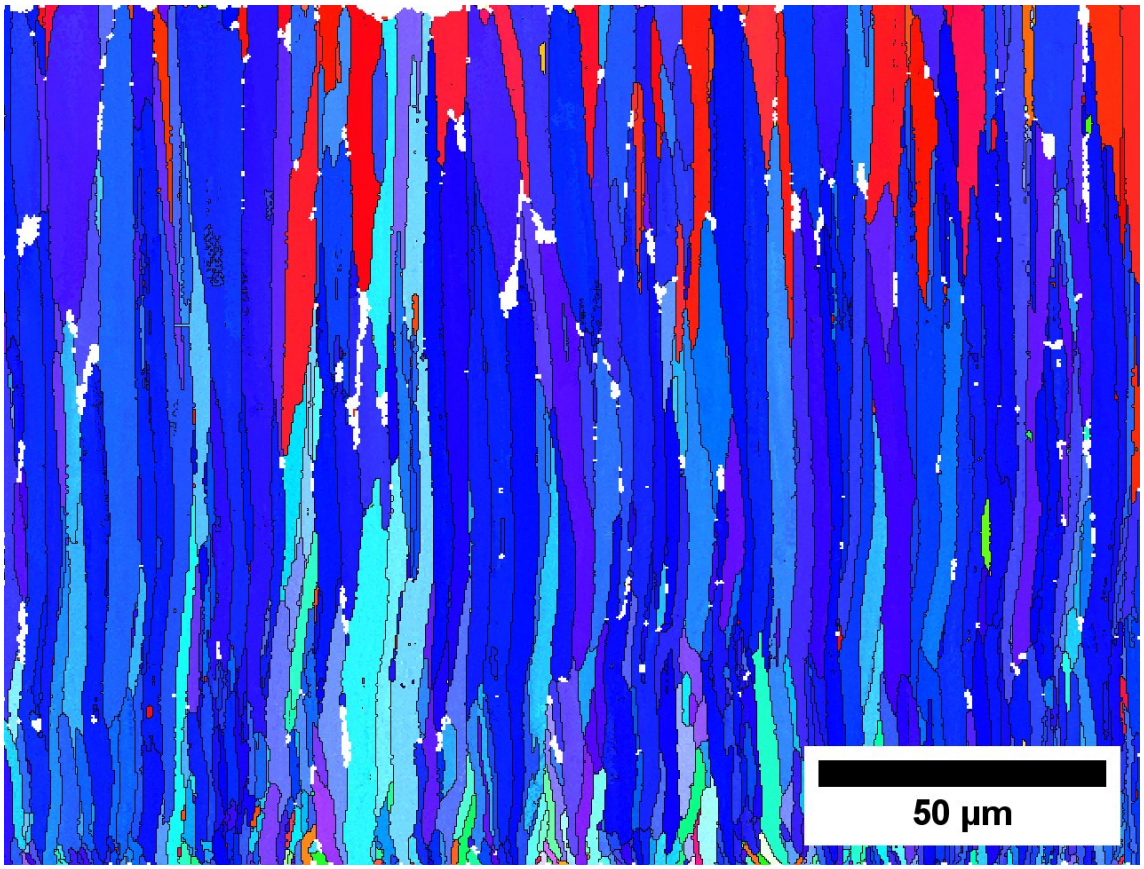


Figure B.1: LowK-Nom AD

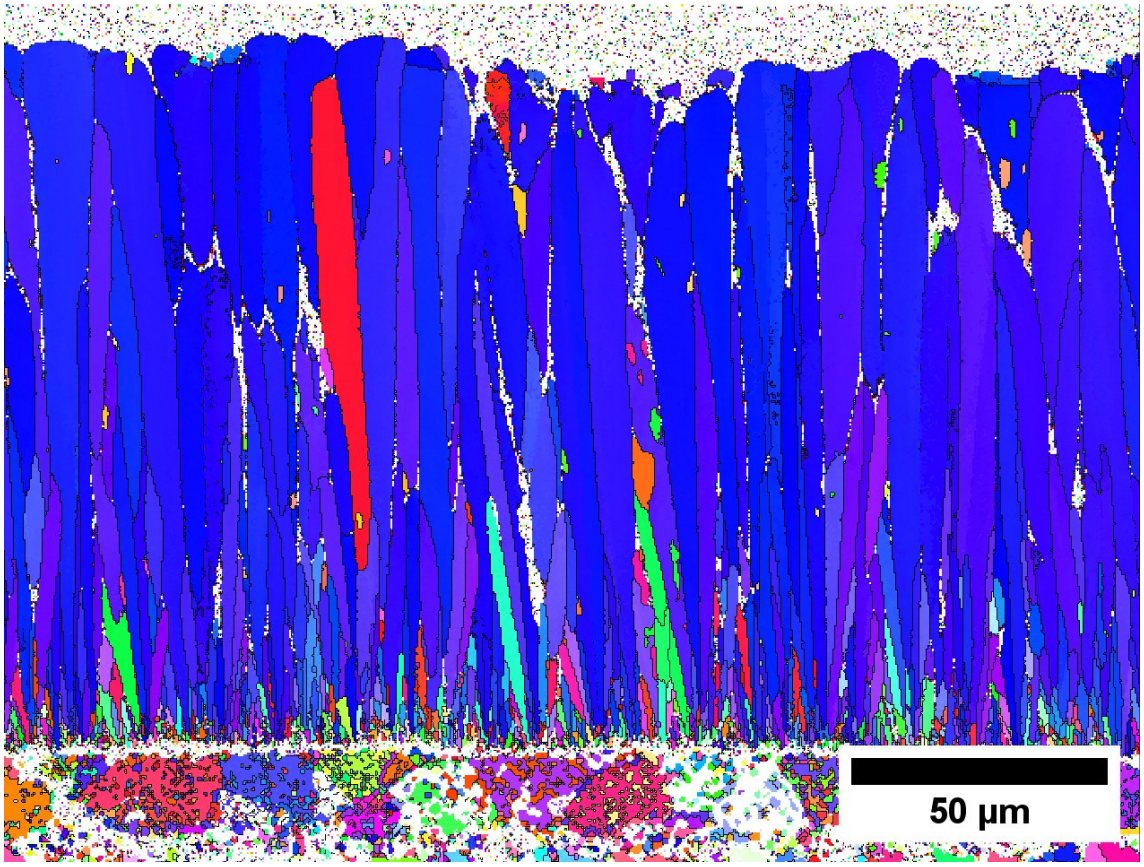


Figure B.2: LowK-Nom N75

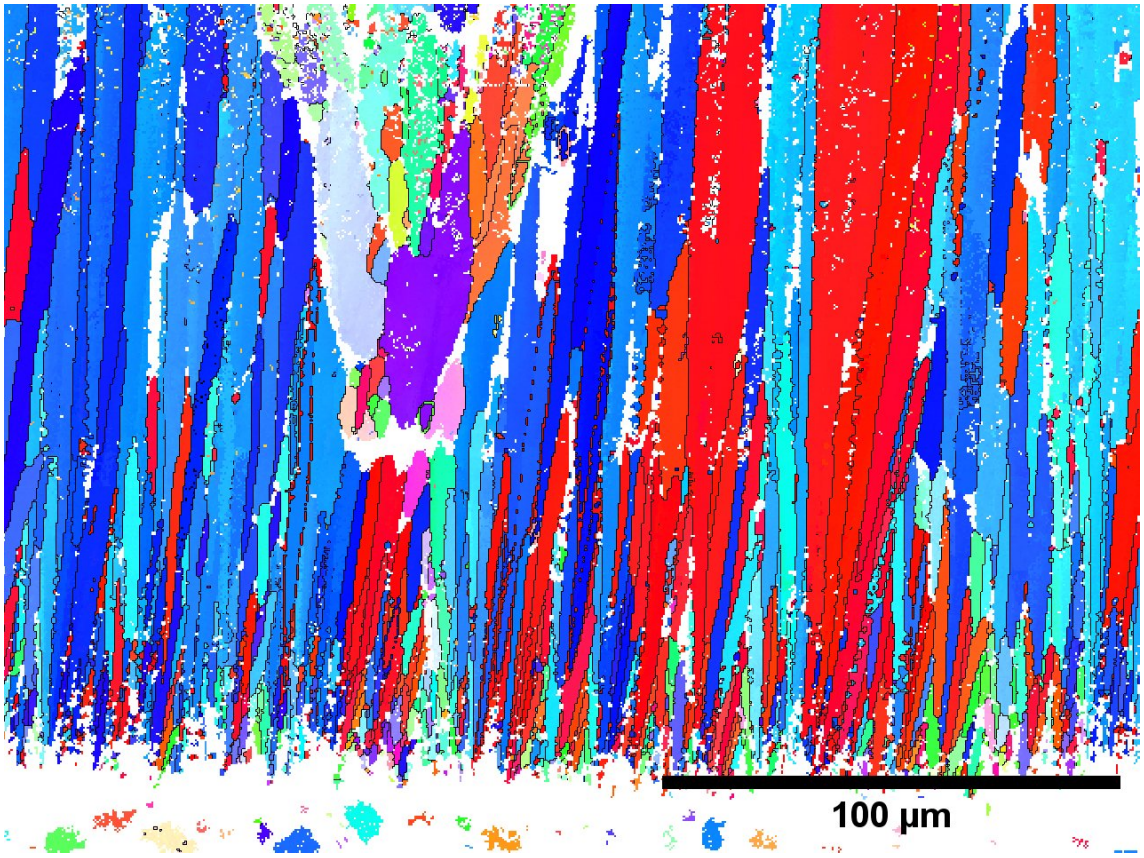


Figure B.3: LowK-LR AD

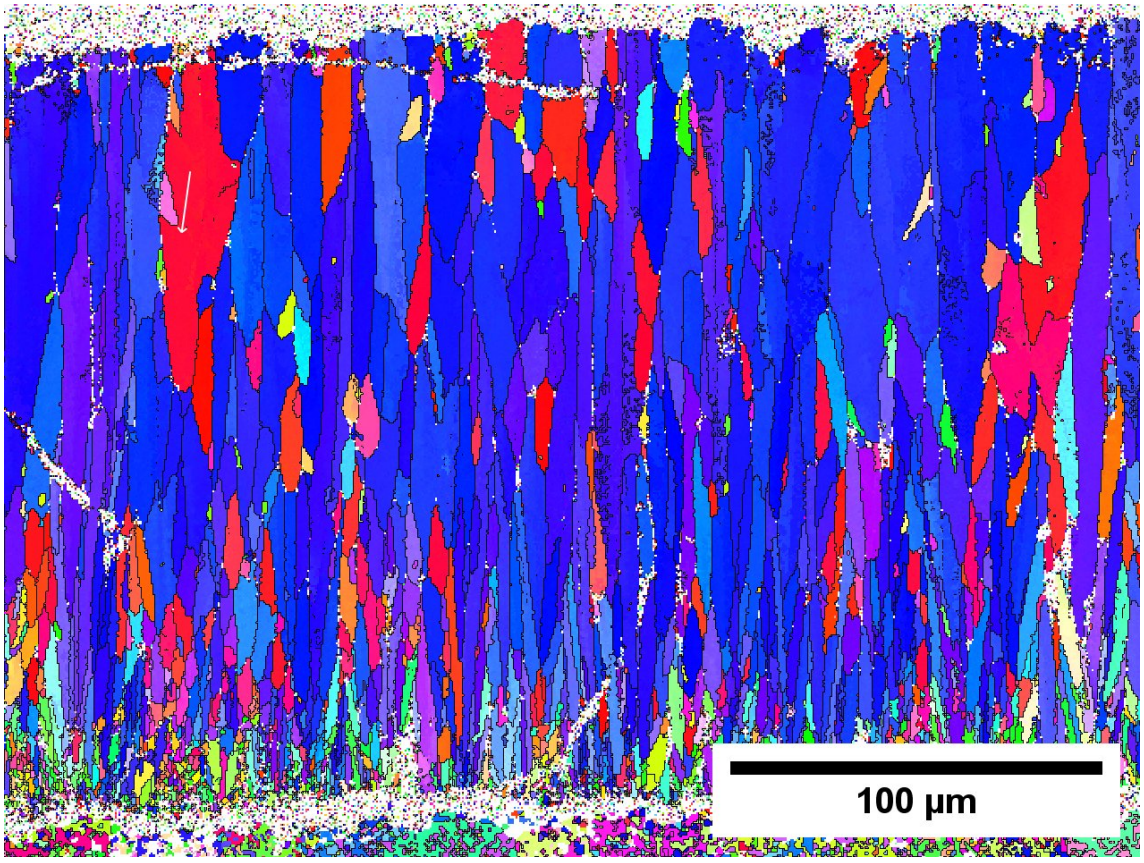


Figure B.4: LowK-LR N75

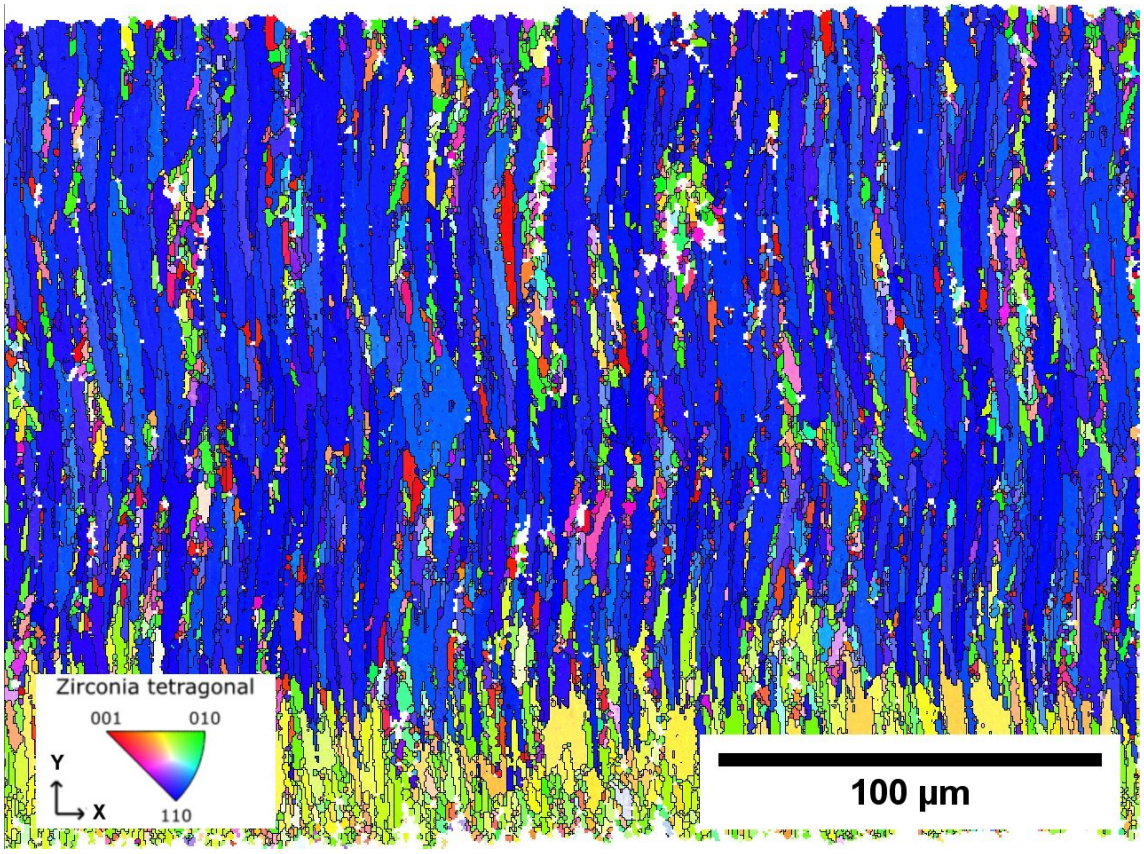


Figure B.5: LowK-LT AD

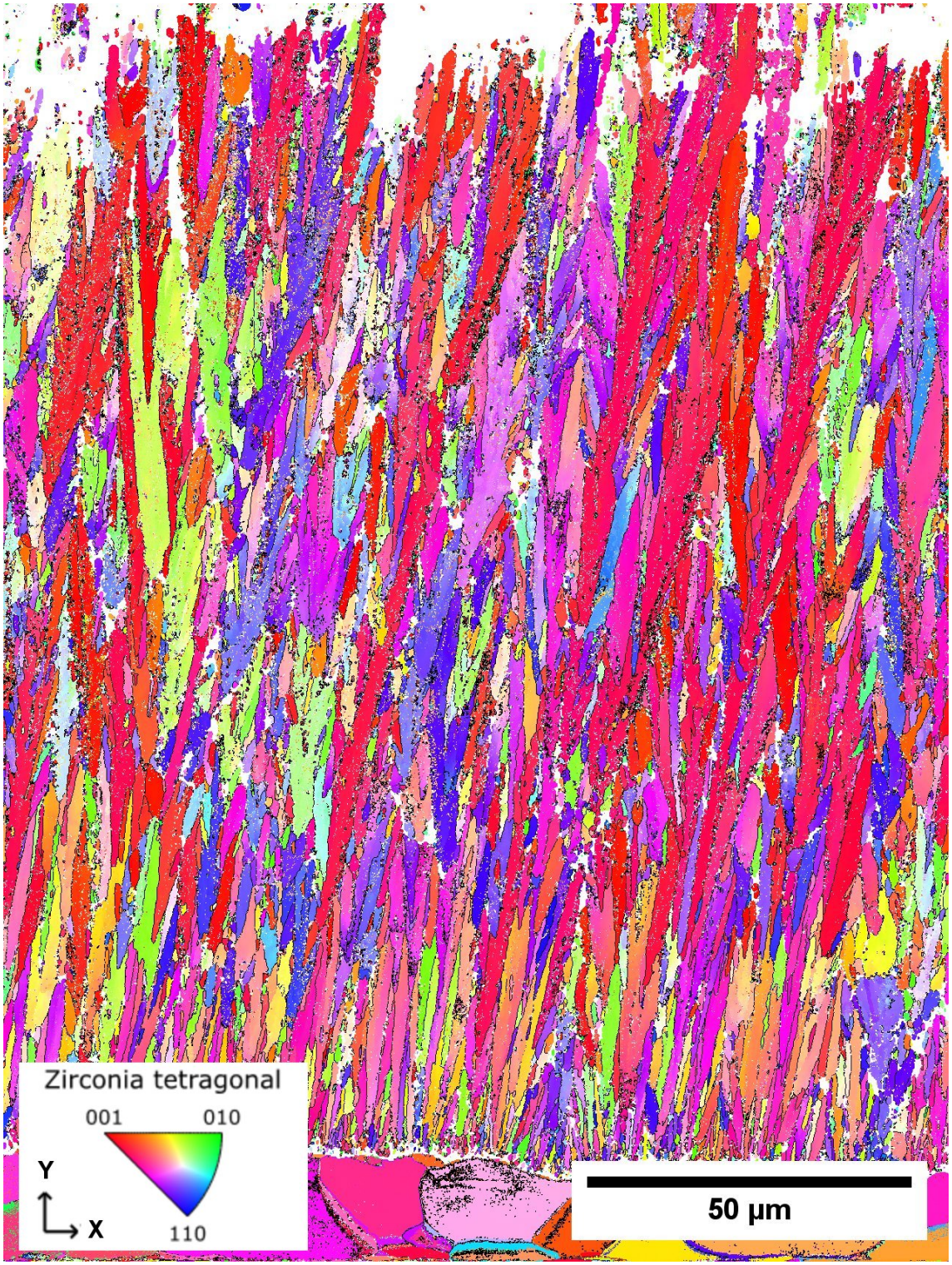


Figure B.6: LowK-LT N75

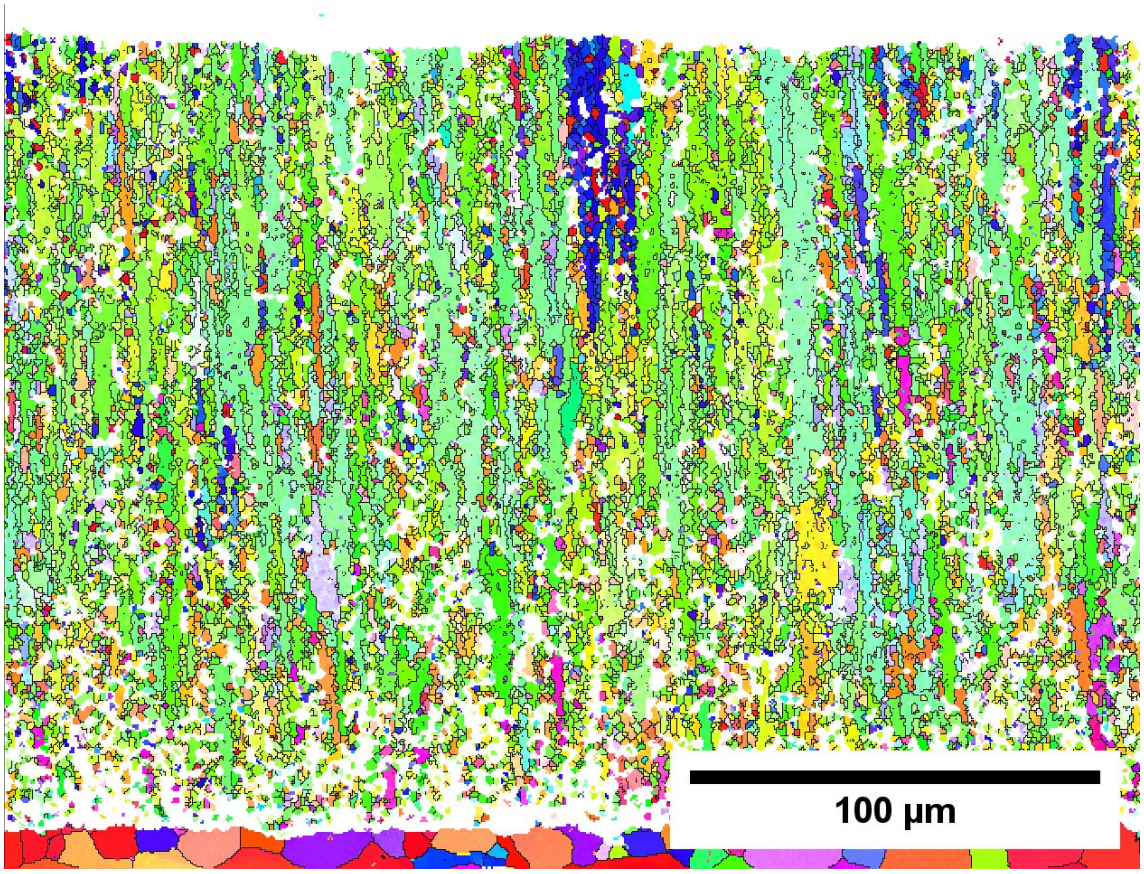


Figure B.7: LowK-LTLR AD

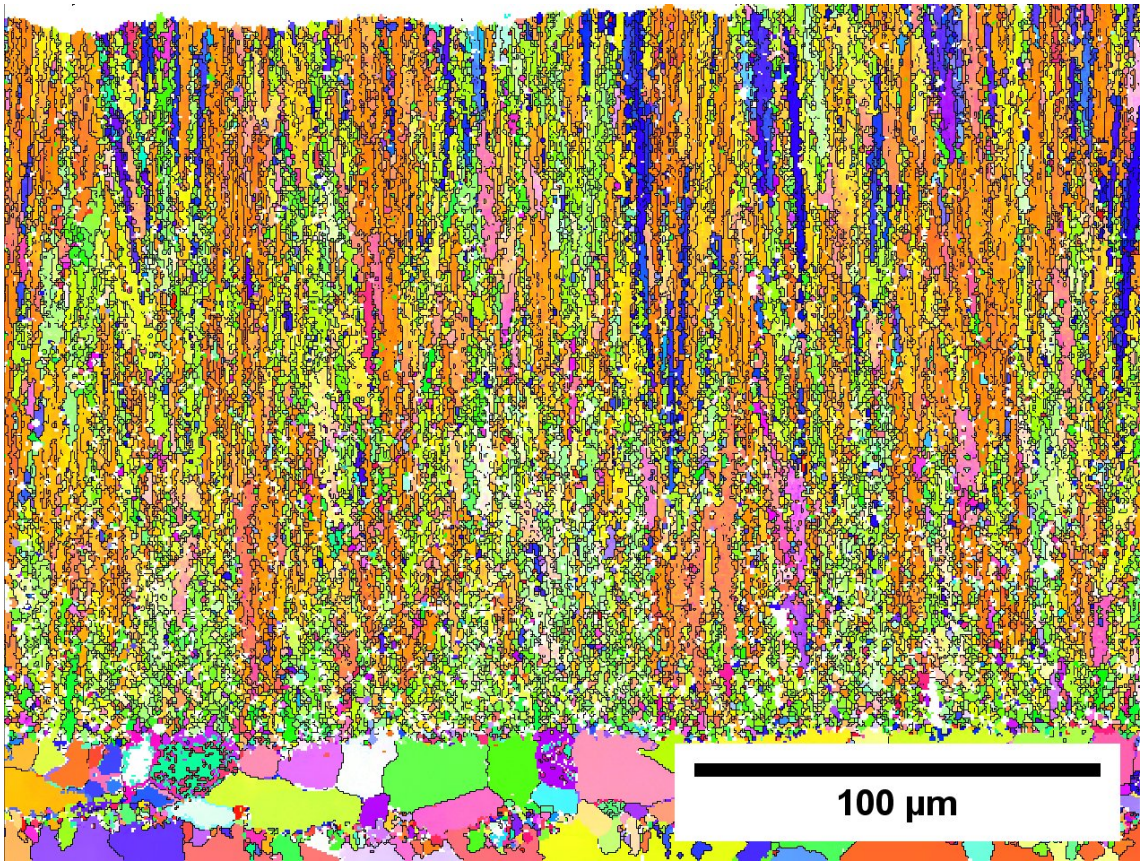


Figure B.8: LowK-LTLR N75



Figure B.9: LowK-LLT AD

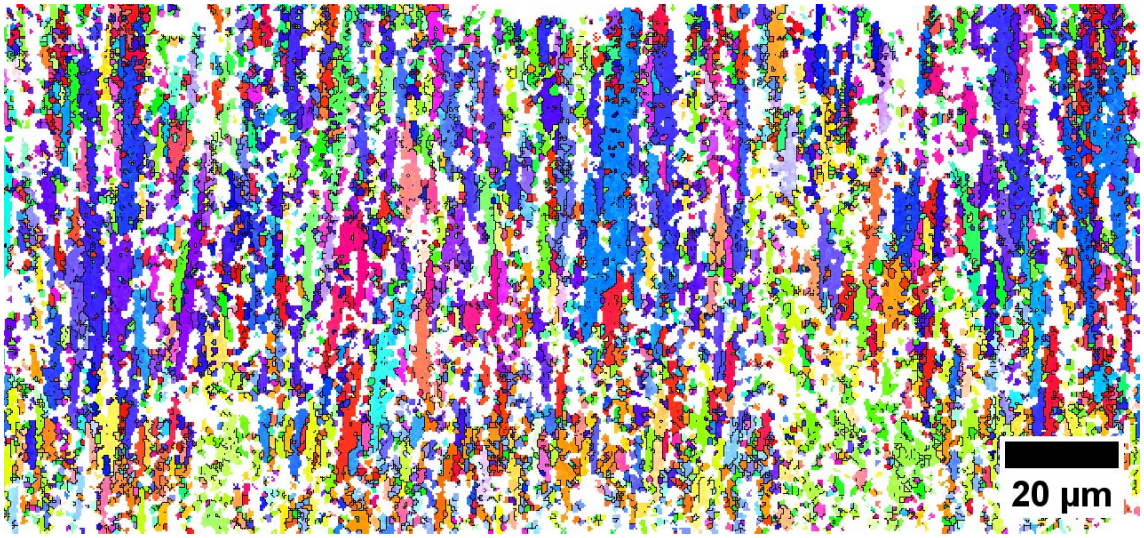


Figure B.10: LowK-LLT N75

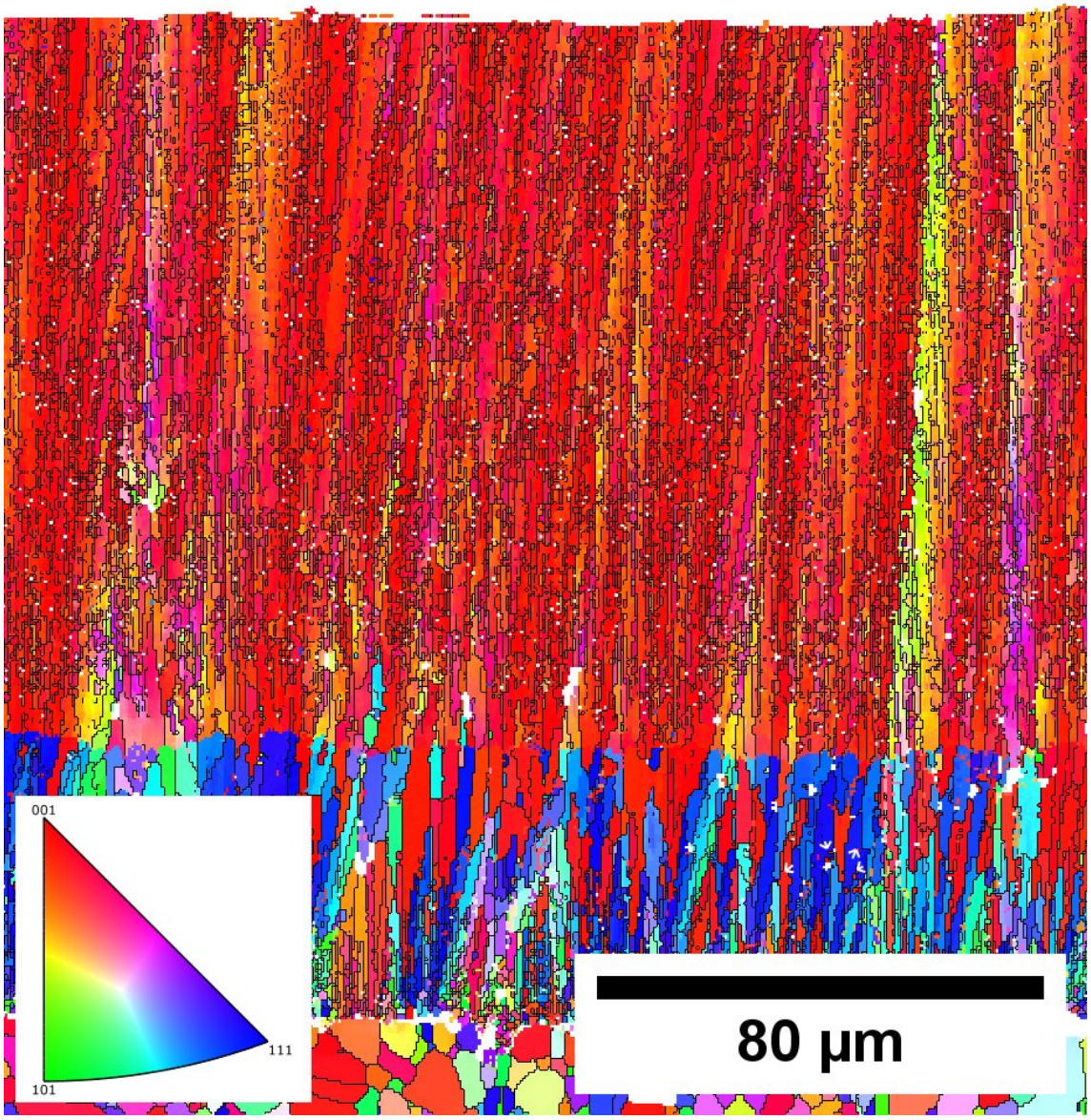


Figure B.11: GZO-LR AD

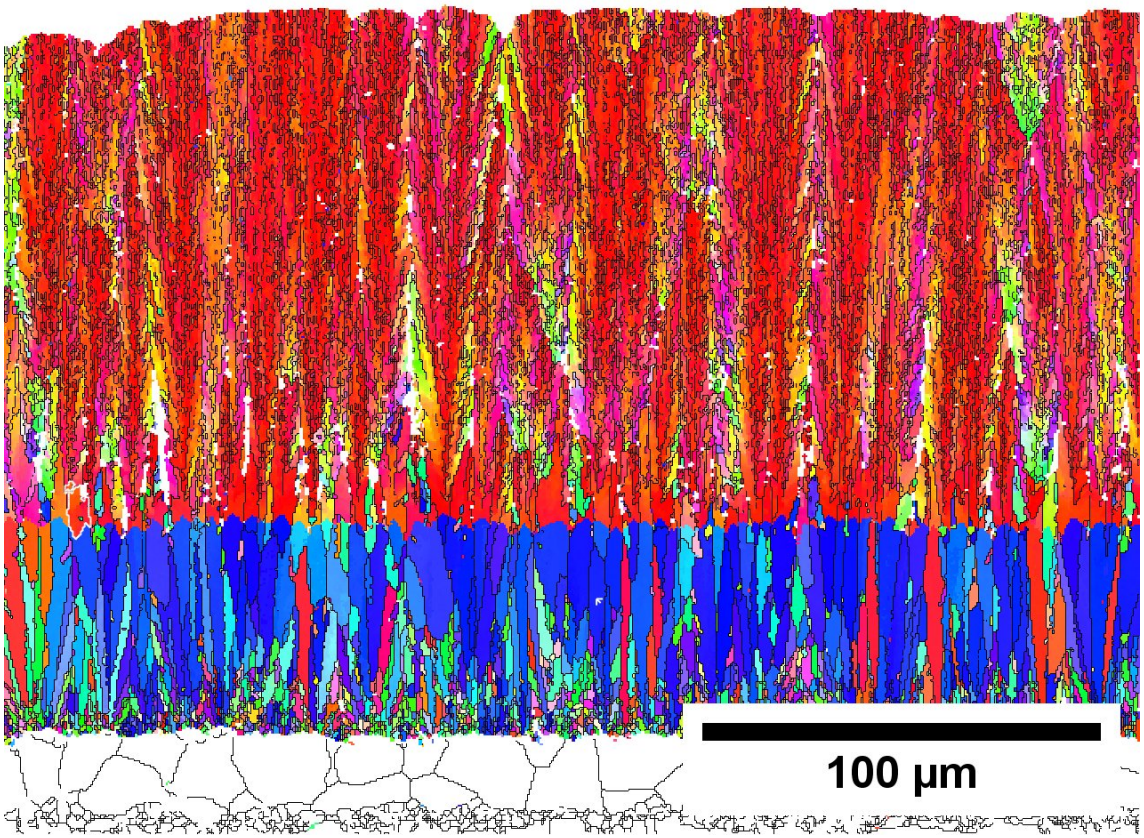


Figure B.12: GZO-LR N75



Figure B.13: GZO-LT AD

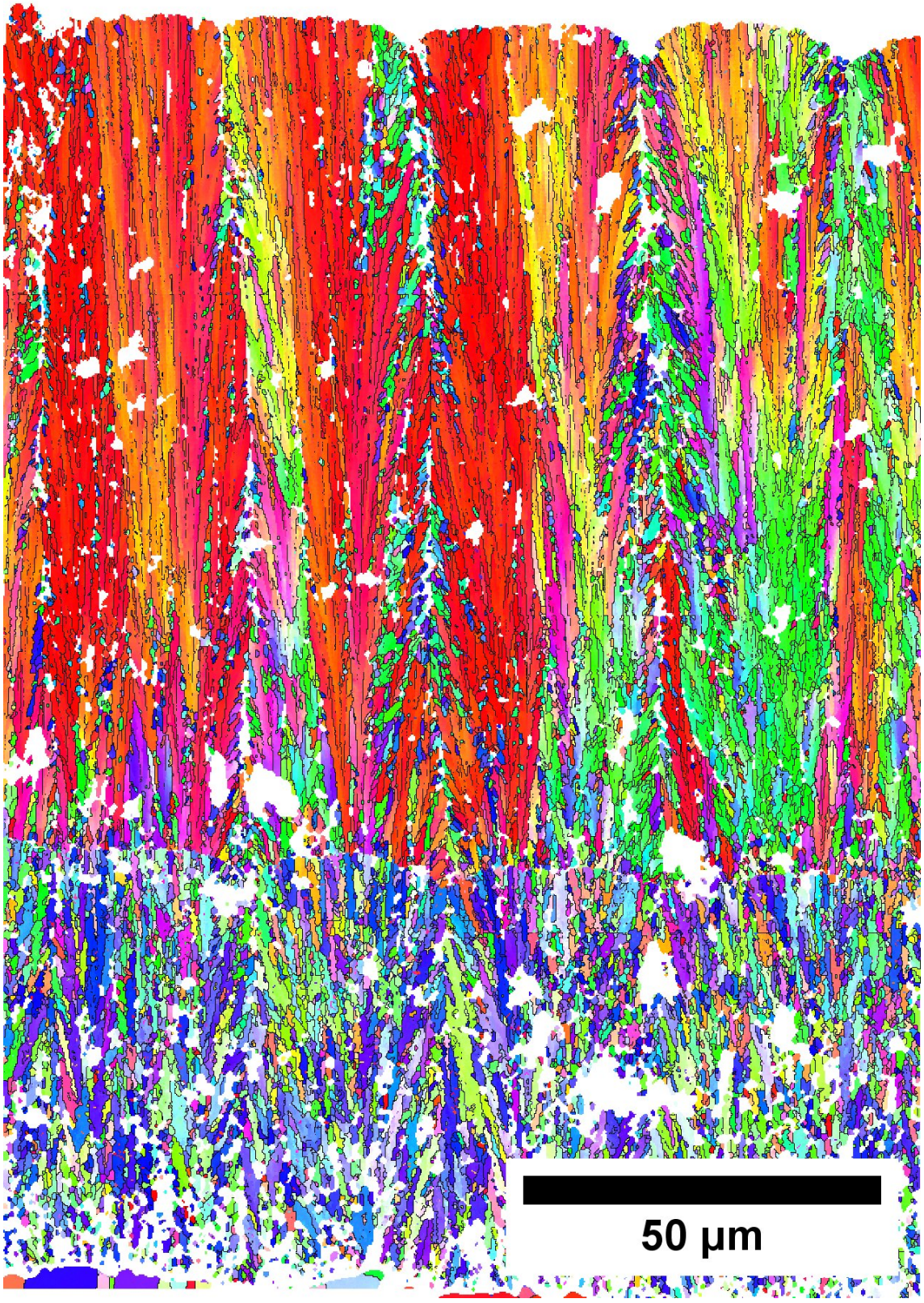


Figure B.14: GZO-LT N75

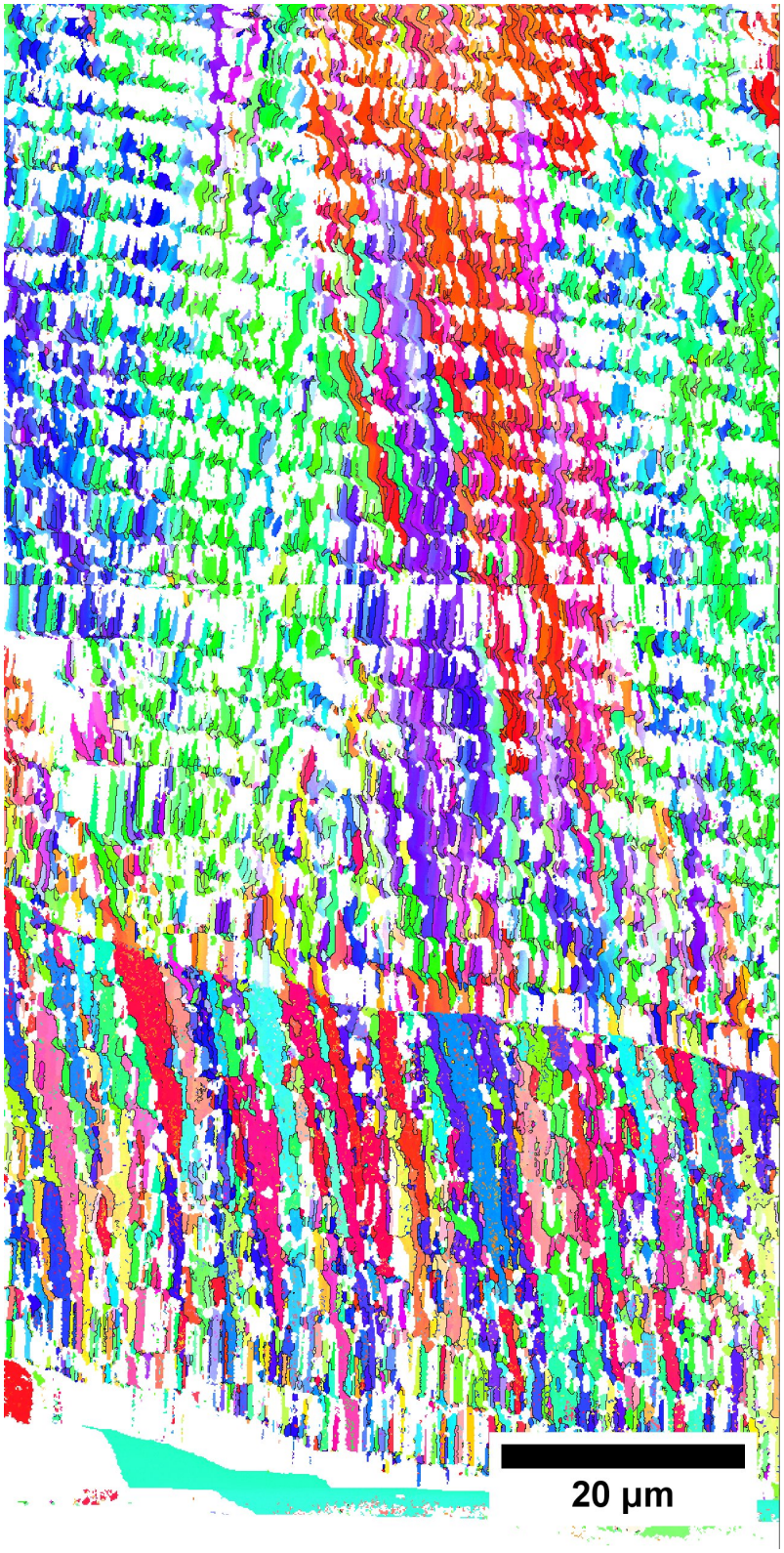


Figure B.15: GZO-LTLR AD

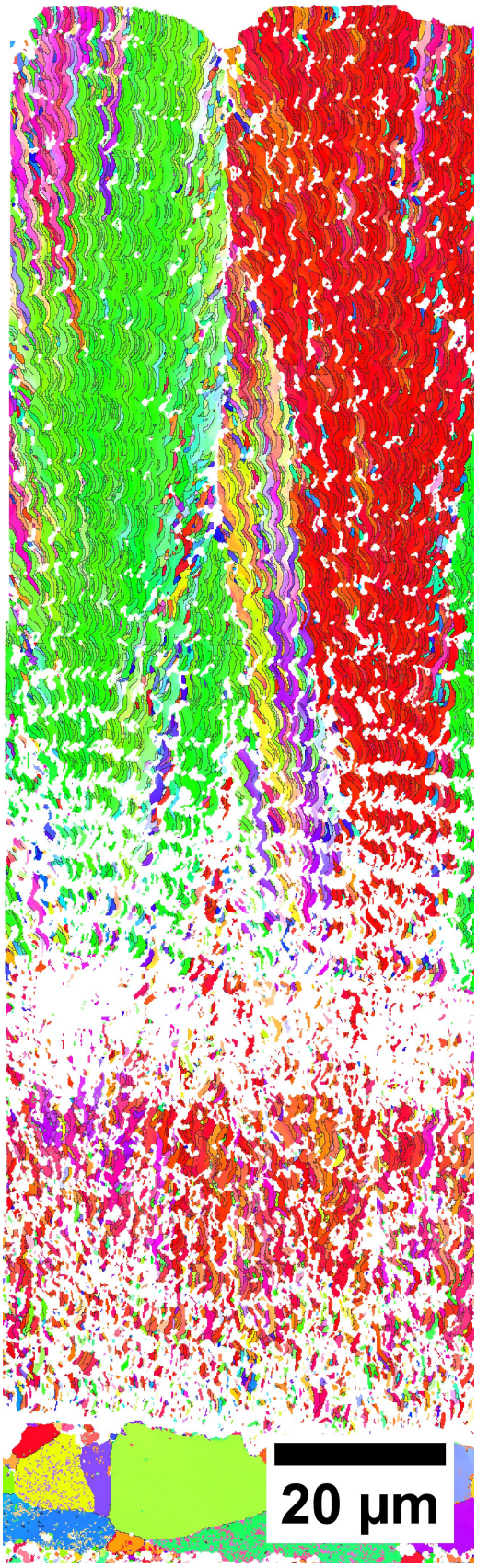


Figure B.16: GZO-LTLR N75

Appendix C

Enlarged images of erosion damage.

The images presented in Figure 5.2 and 5.4 are presented in enlarged format in this appendix for better observation of the microstructural damage details.

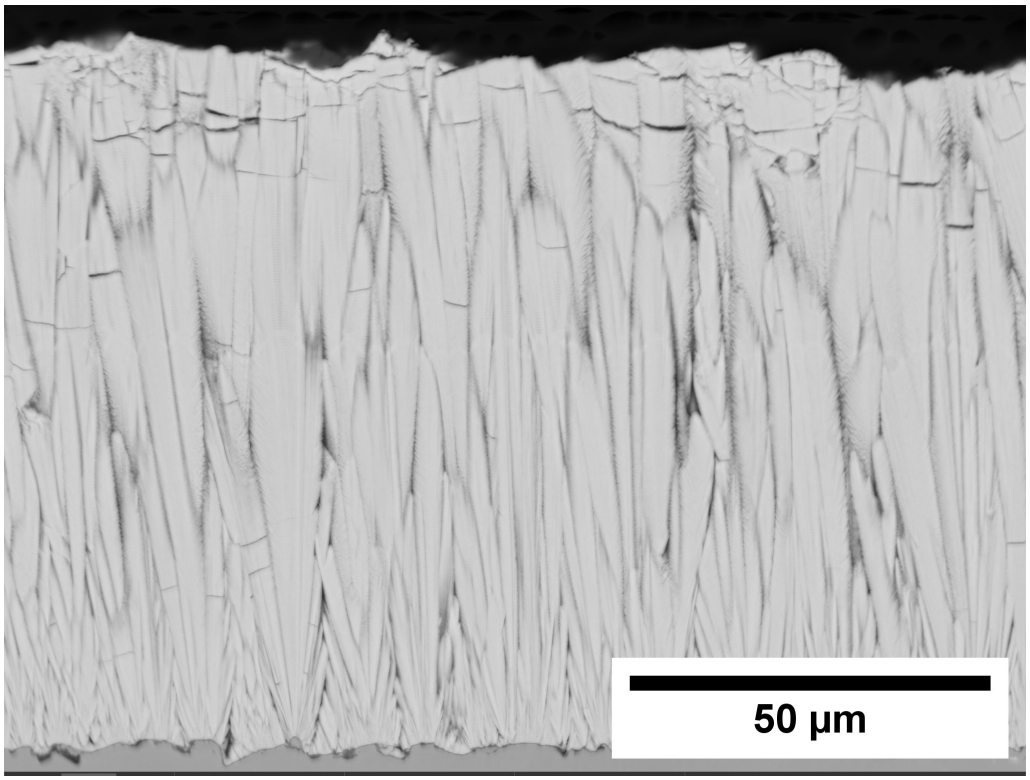


Figure C.1: LowK-Nom. cracked.

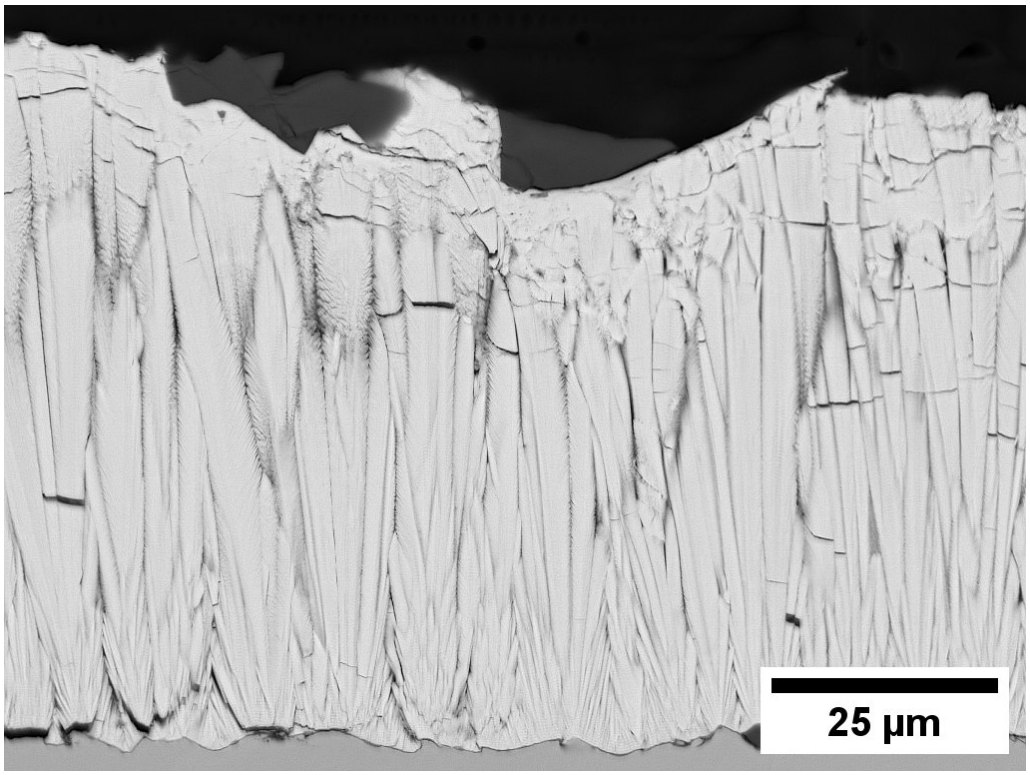


Figure C.2: LowK-Nom. cracked & densified.

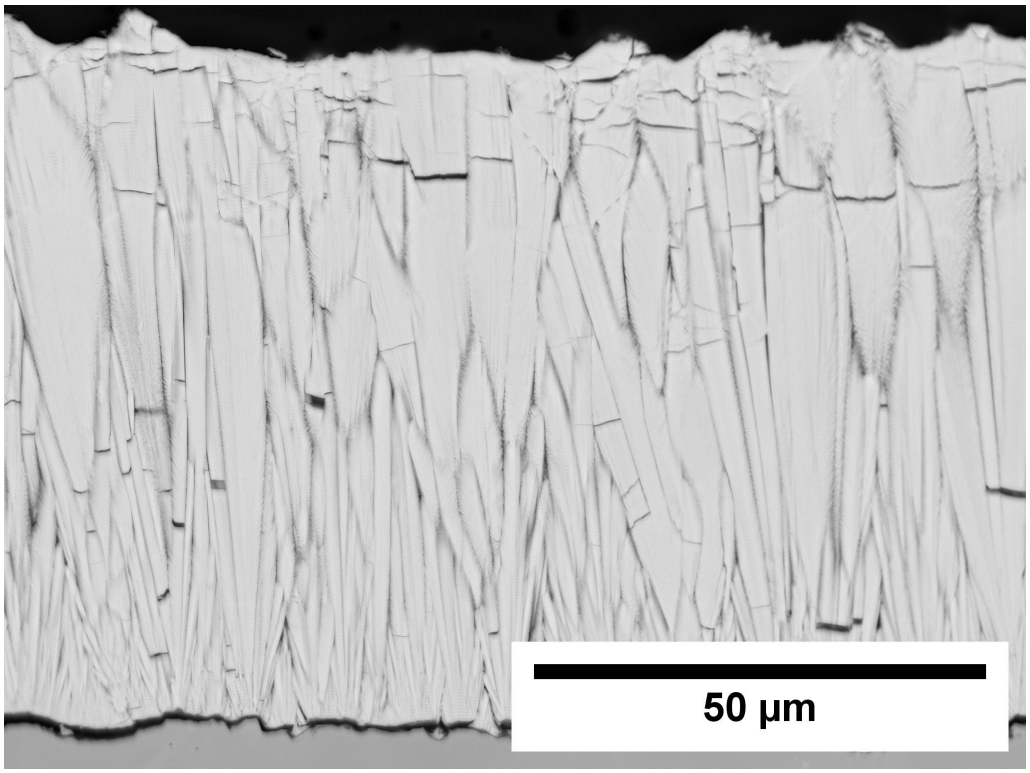


Figure C.3: LowK-Nom. cracked & delaminated.

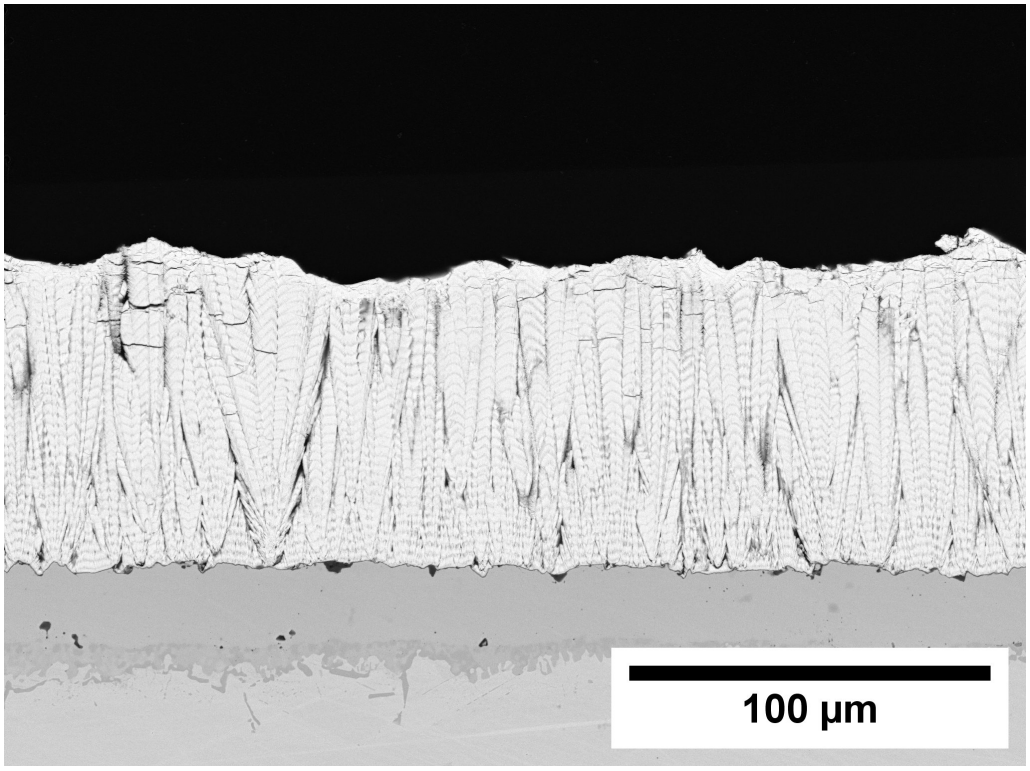


Figure C.4: LowK-LR. cracks.

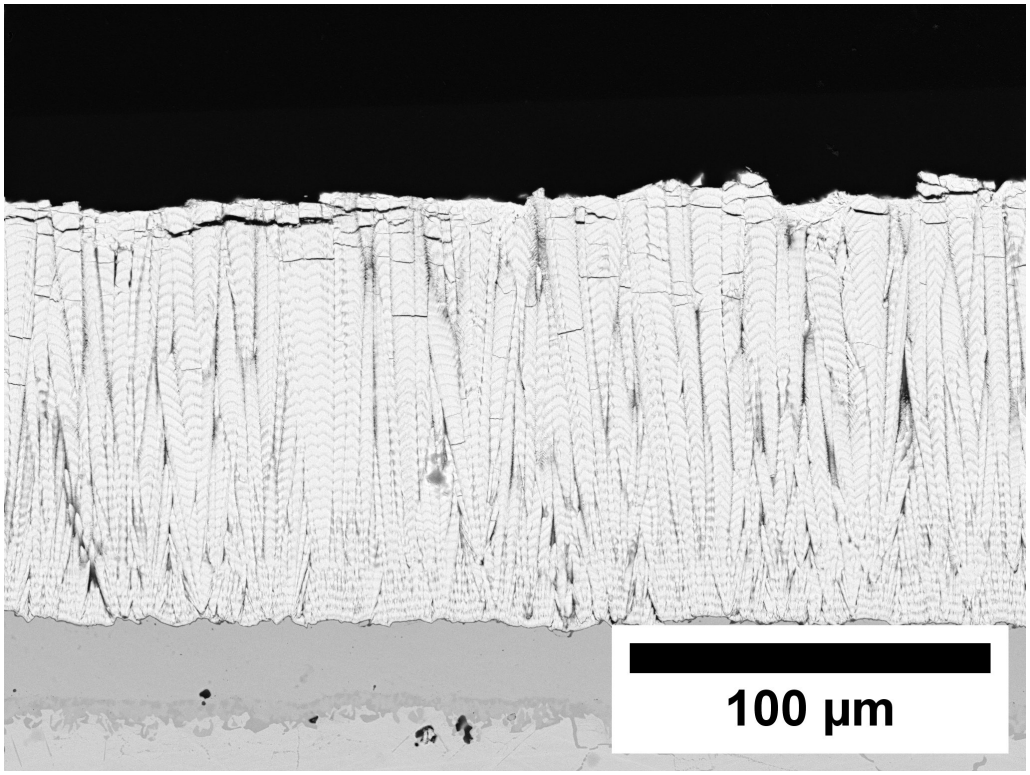


Figure C.5: LowK-LR. cracks.

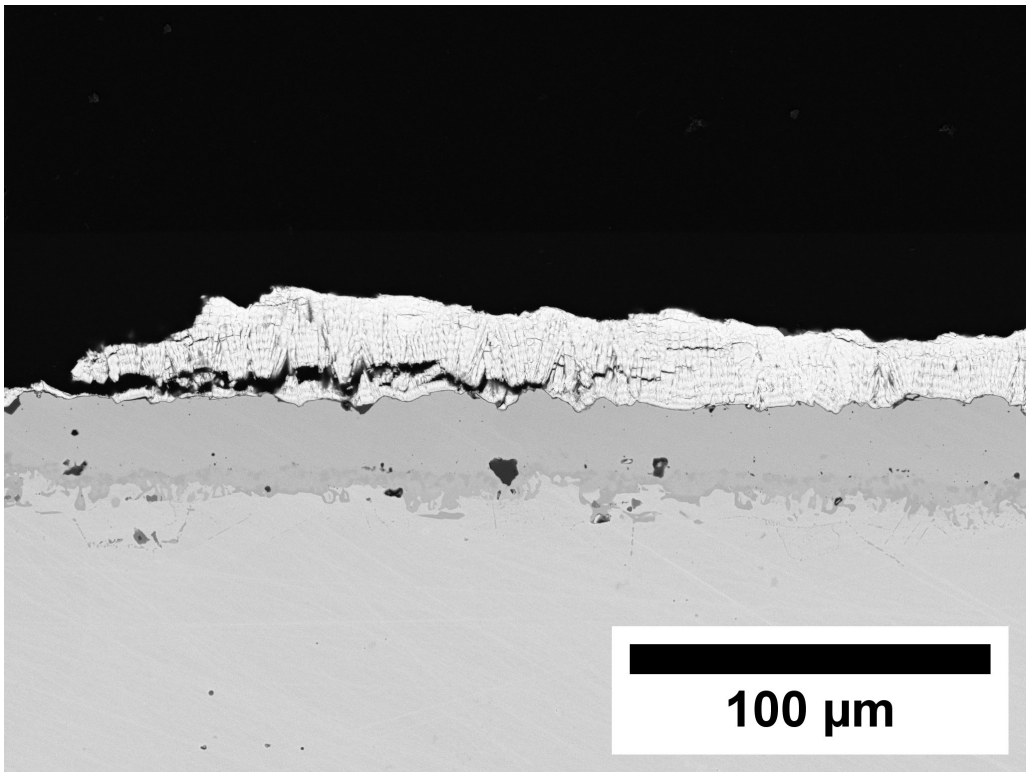


Figure C.6: LowK-LR. cracks & densified.

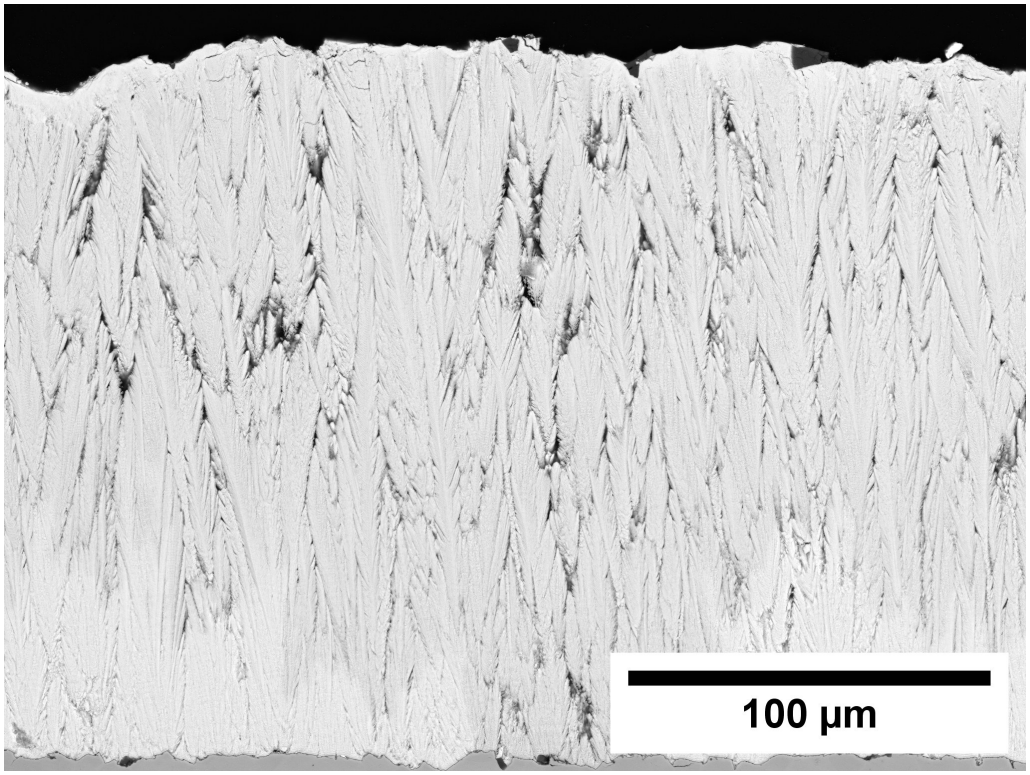


Figure C.7: LowK-LT. cracks & densification.

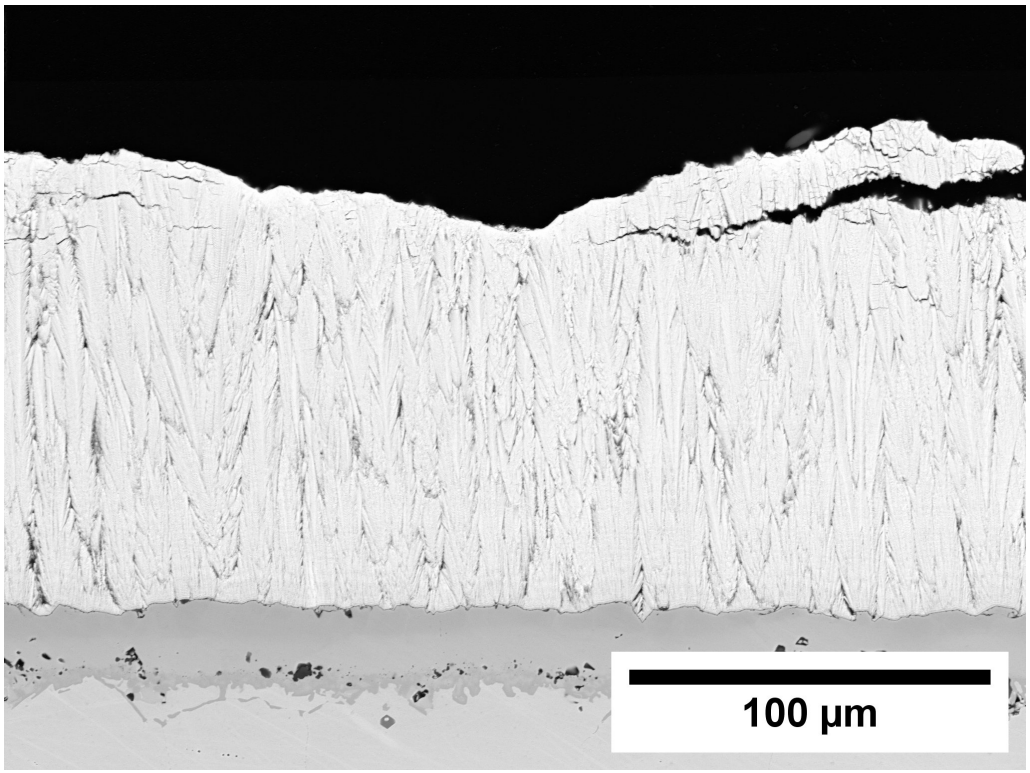


Figure C.8: LowK-LT. delamination

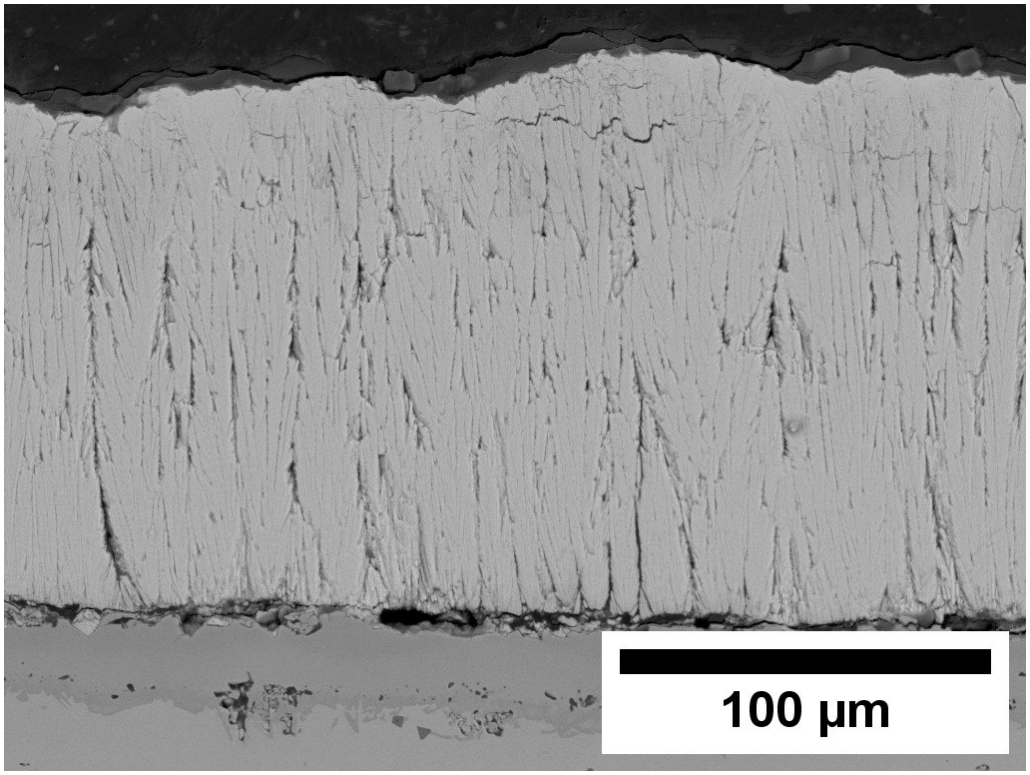


Figure C.9: LowK-LT. interface delamination

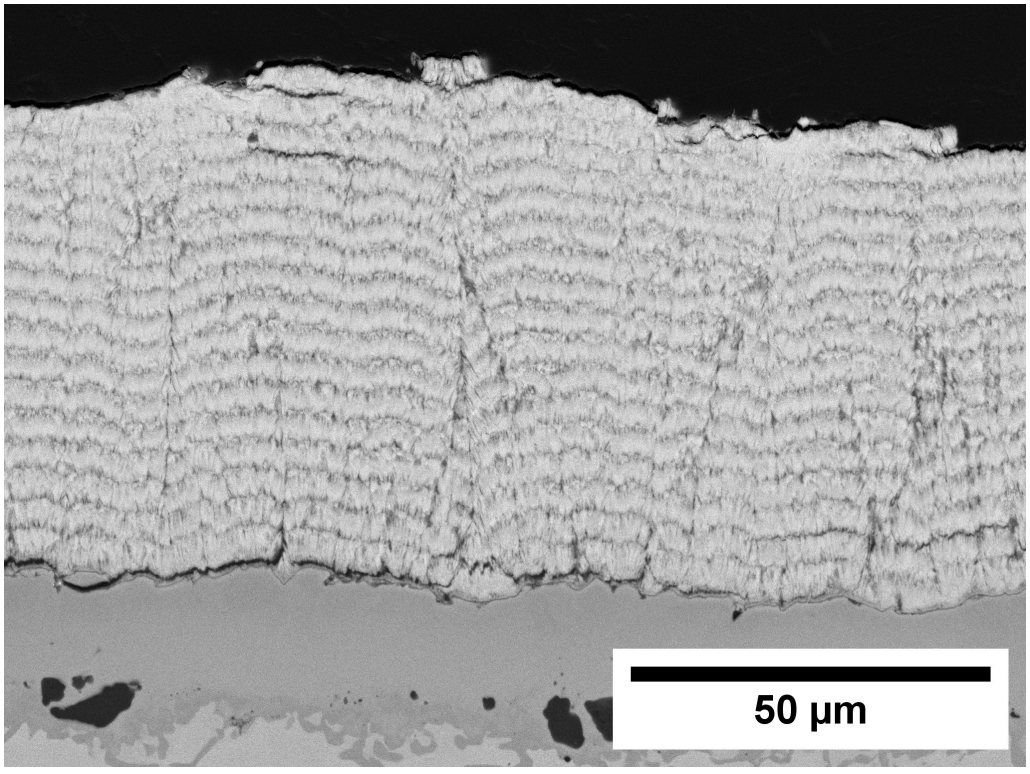


Figure C.10: LowK-LTLR. delaminated.

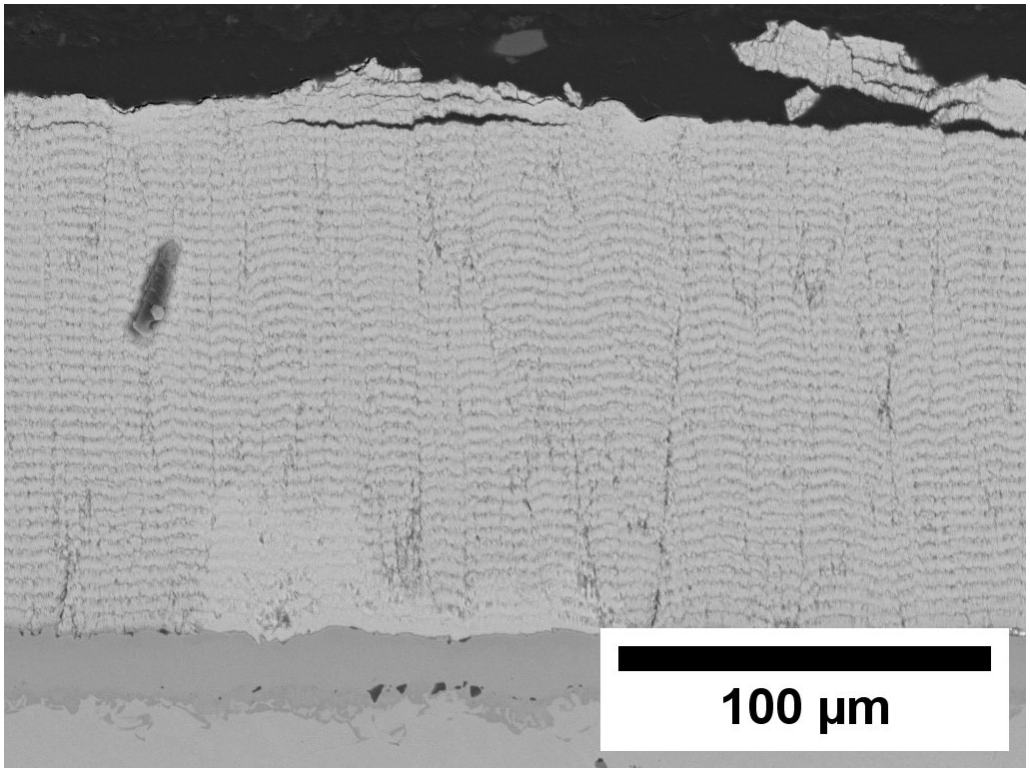


Figure C.11: LowK-LTLR. cracked & delaminated.

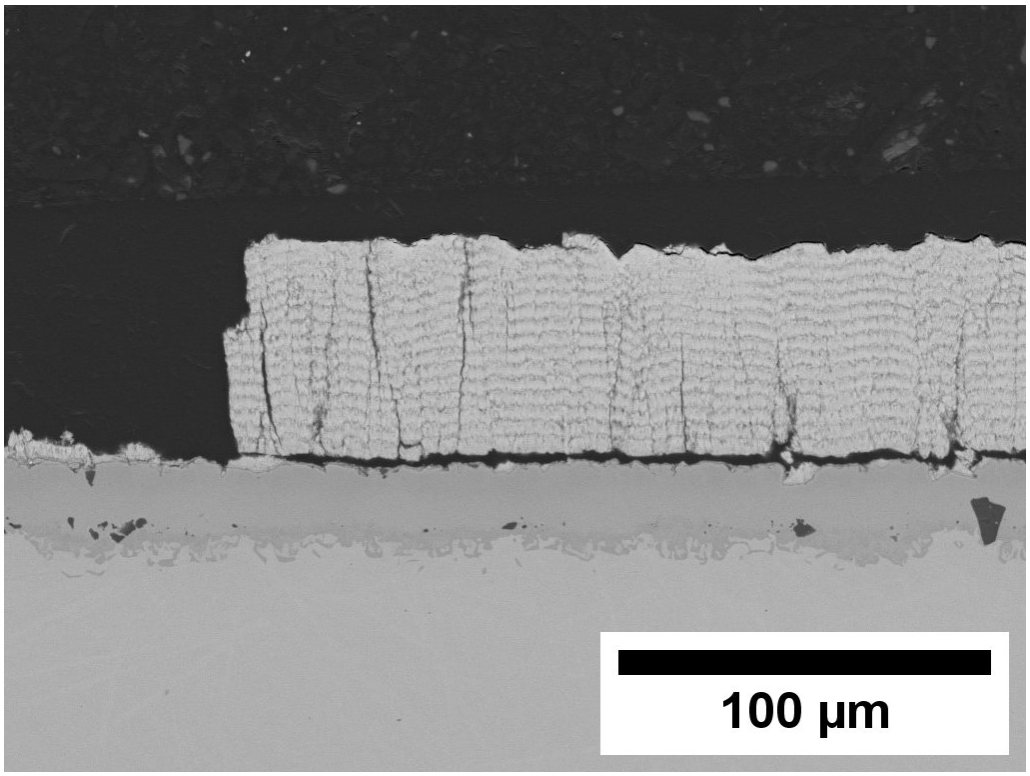


Figure C.12: LowK-LTLR. erosion scar edge.

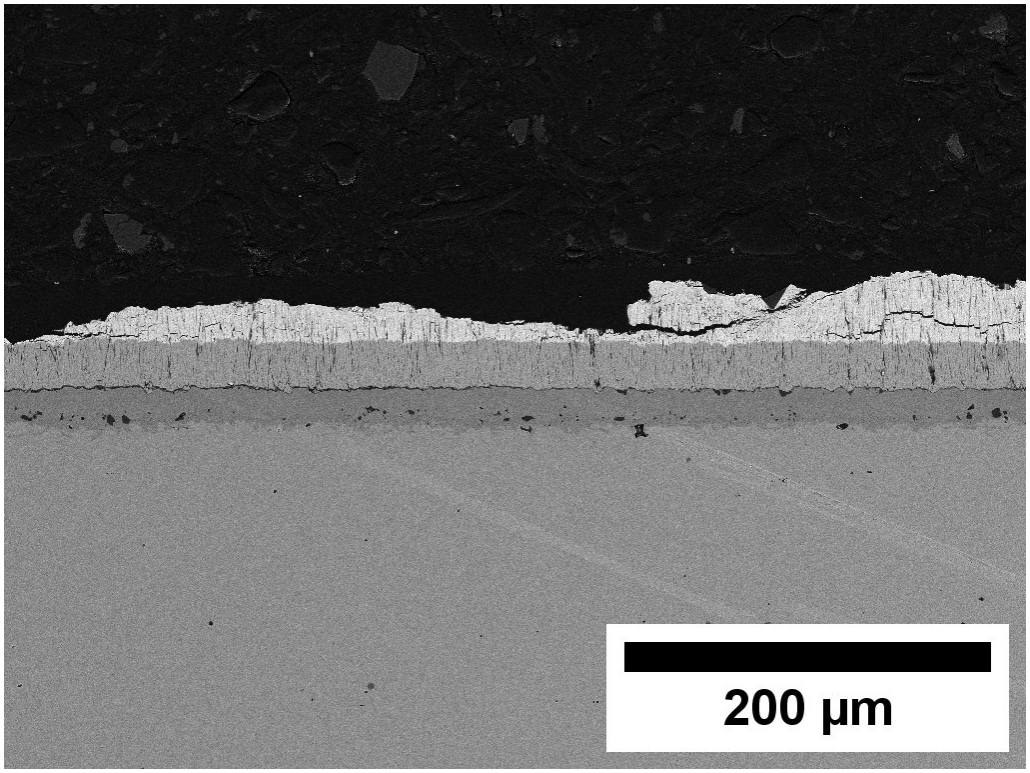


Figure C.13: GZO-Nom. damage overview.

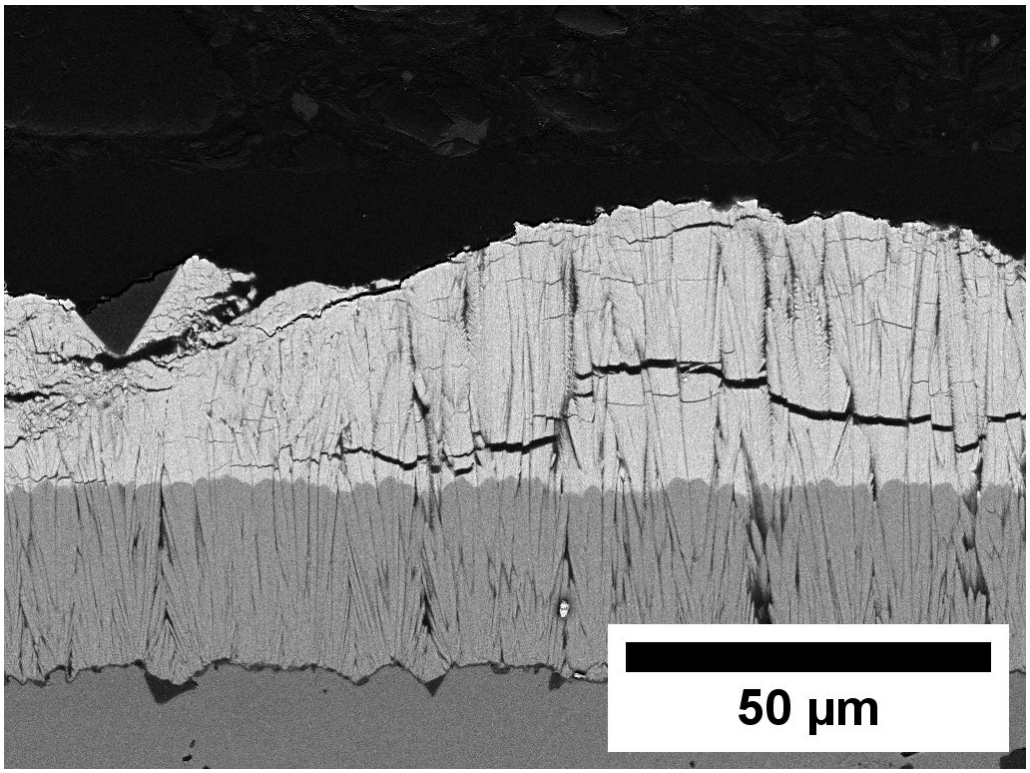


Figure C.14: GZO-Nom. cracked

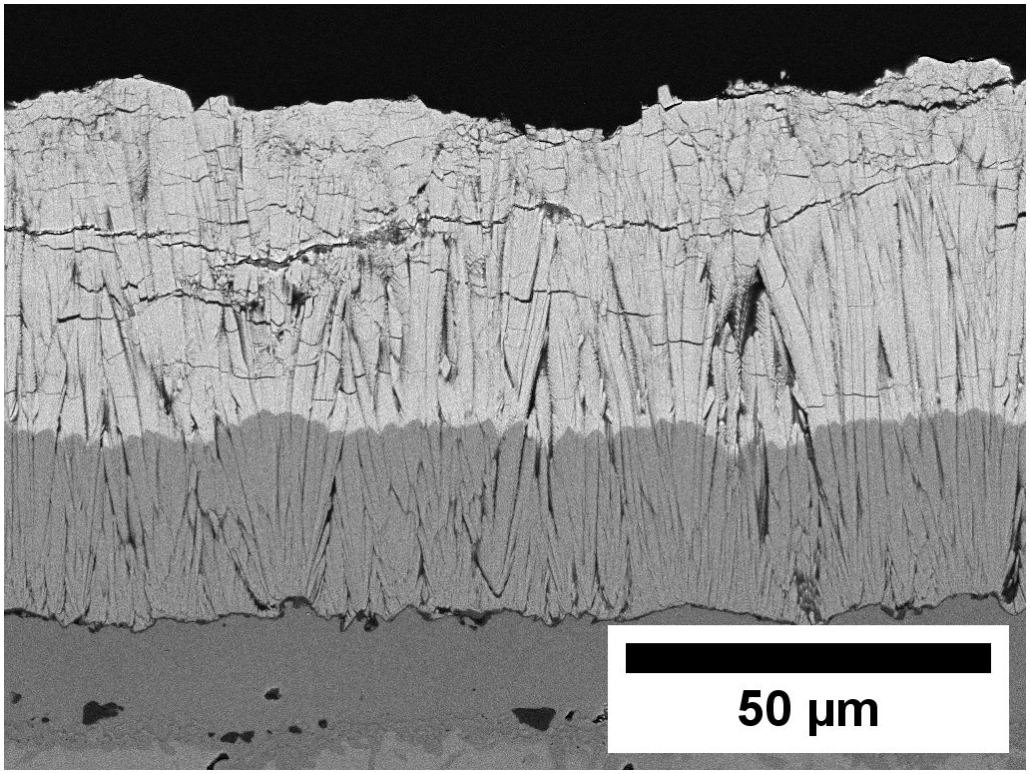


Figure C.15: GZO-Nom. extensively cracked

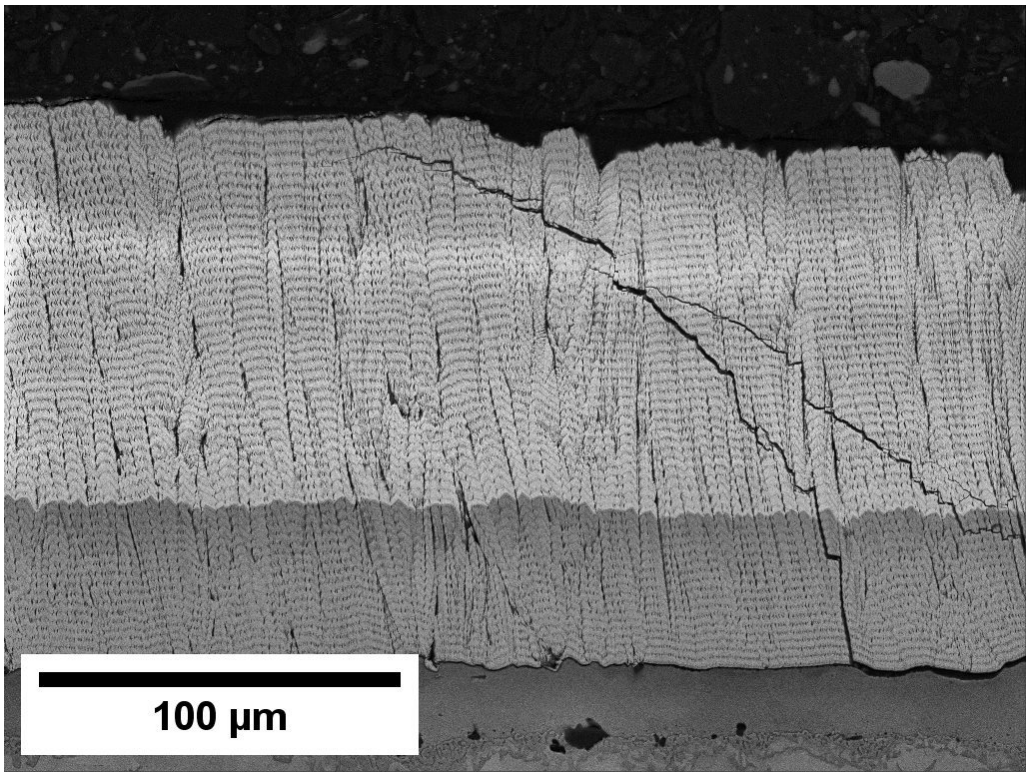


Figure C.16: GZO-LR delaminated

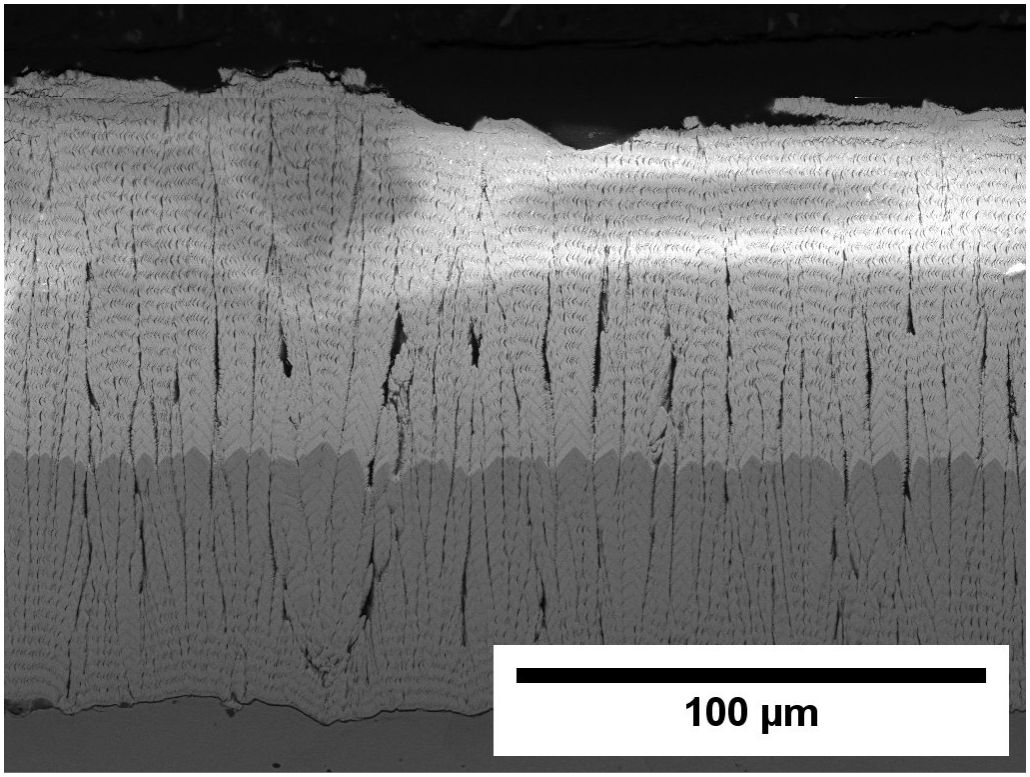


Figure C.17: GZO-LR densification

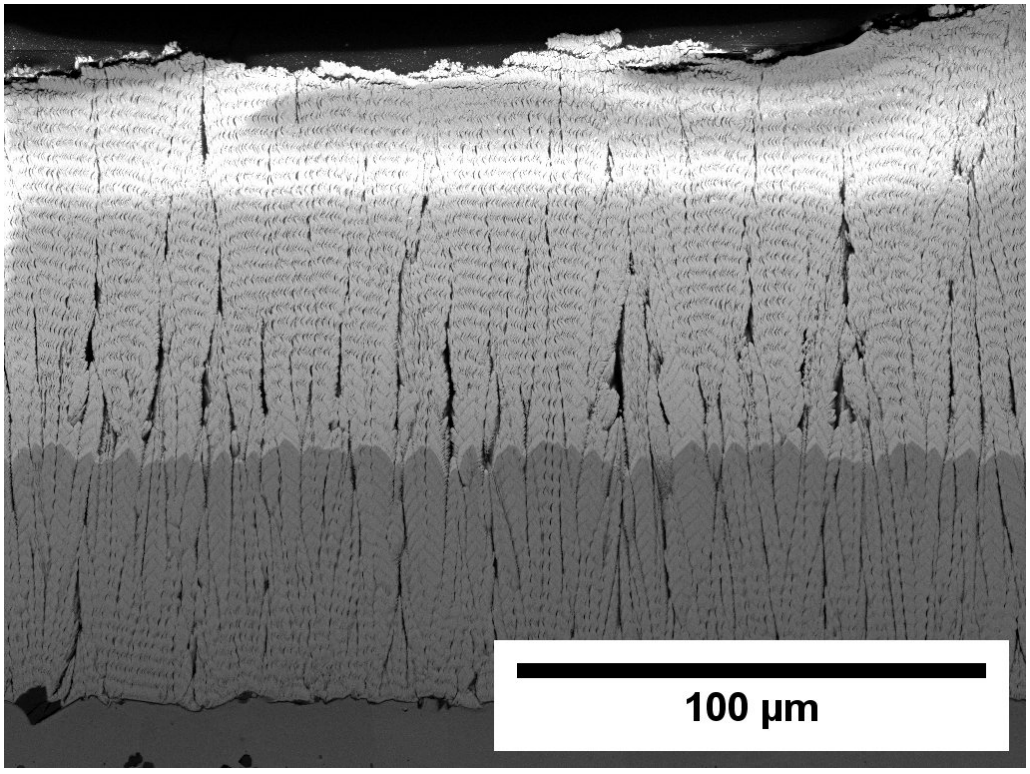


Figure C.18: GZO-LR damage detail

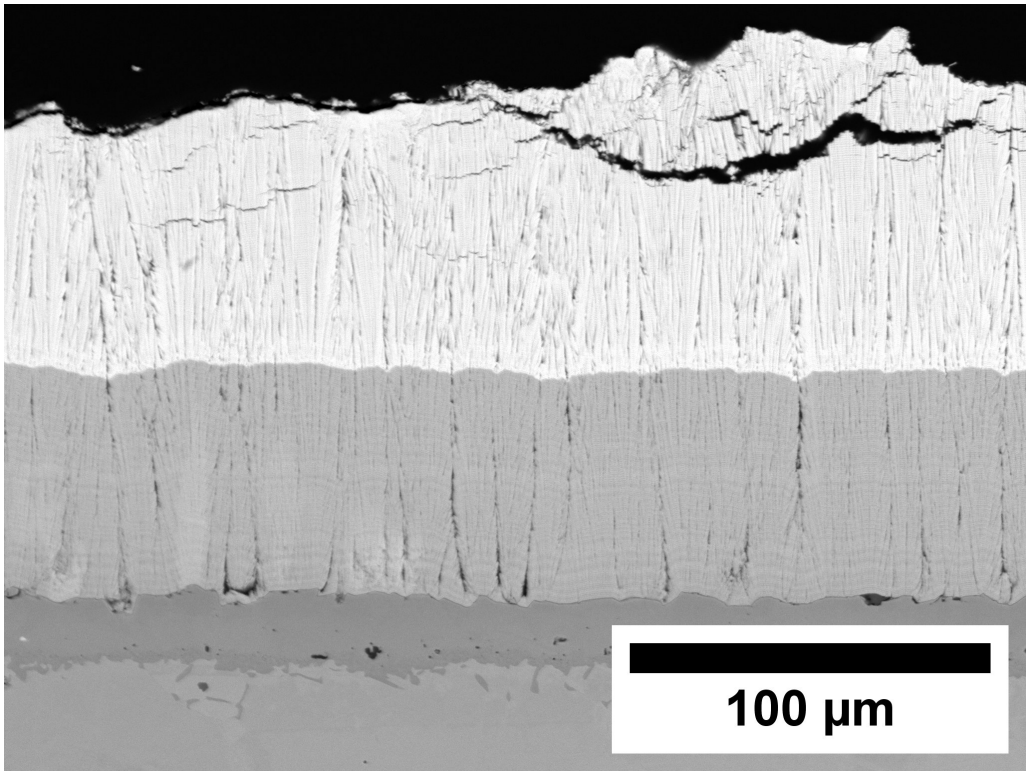


Figure C.19: GZO-LT cracked

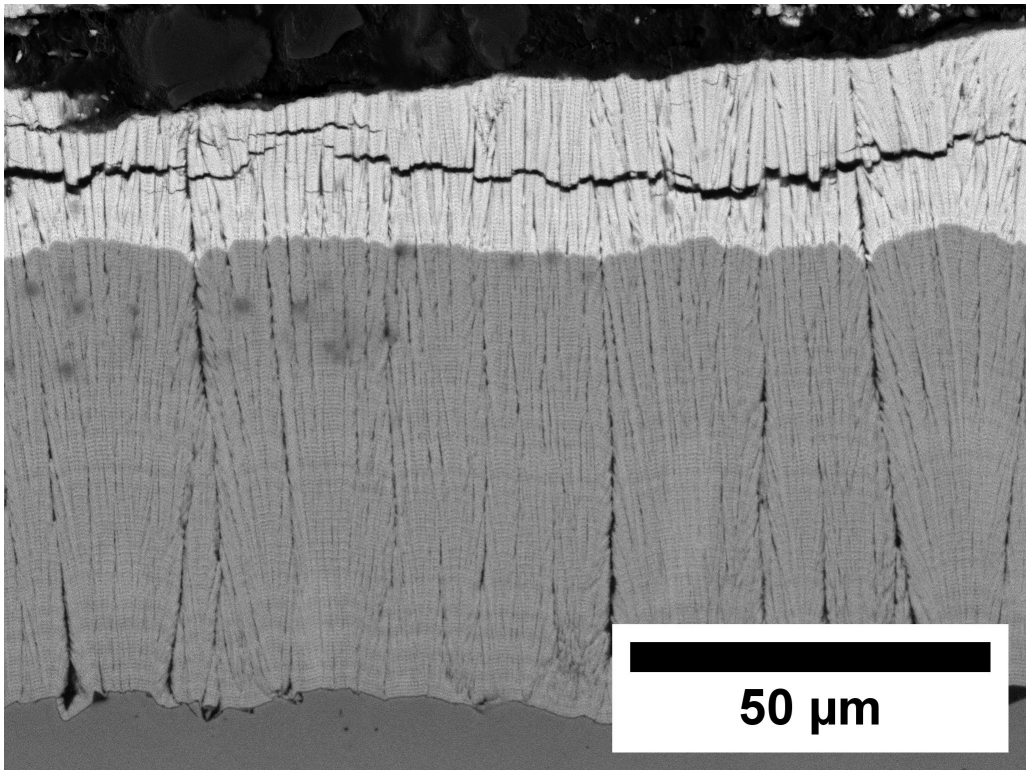


Figure C.20: GZO-LT cracked at interface

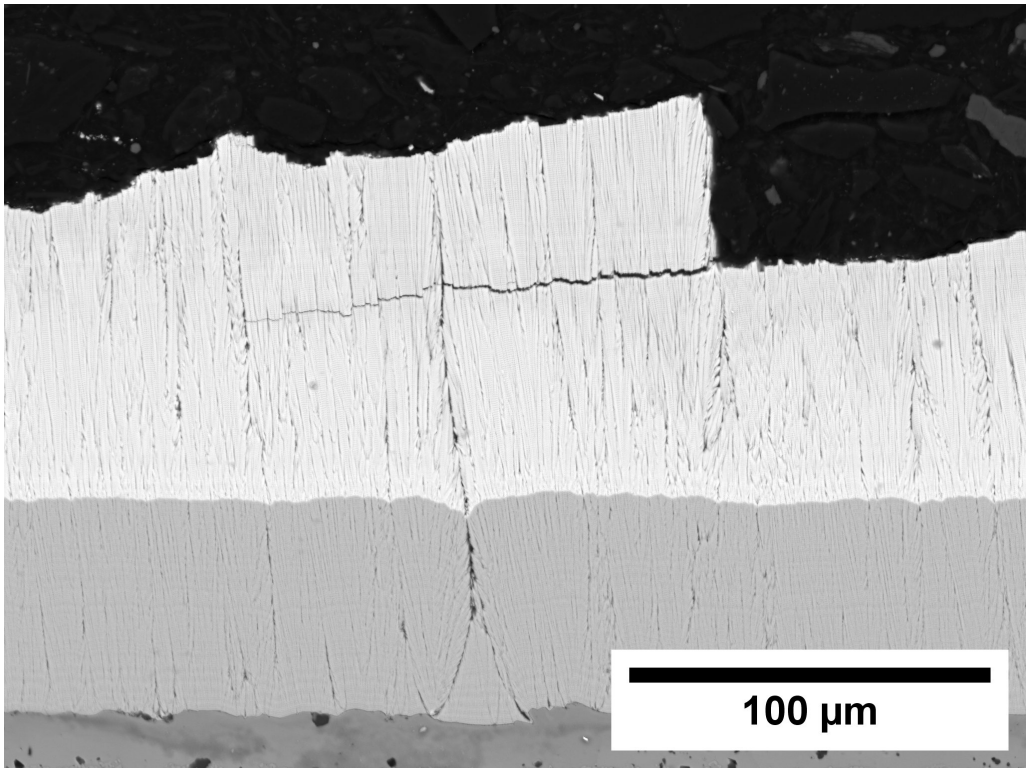


Figure C.21: GZO-LT delaminated

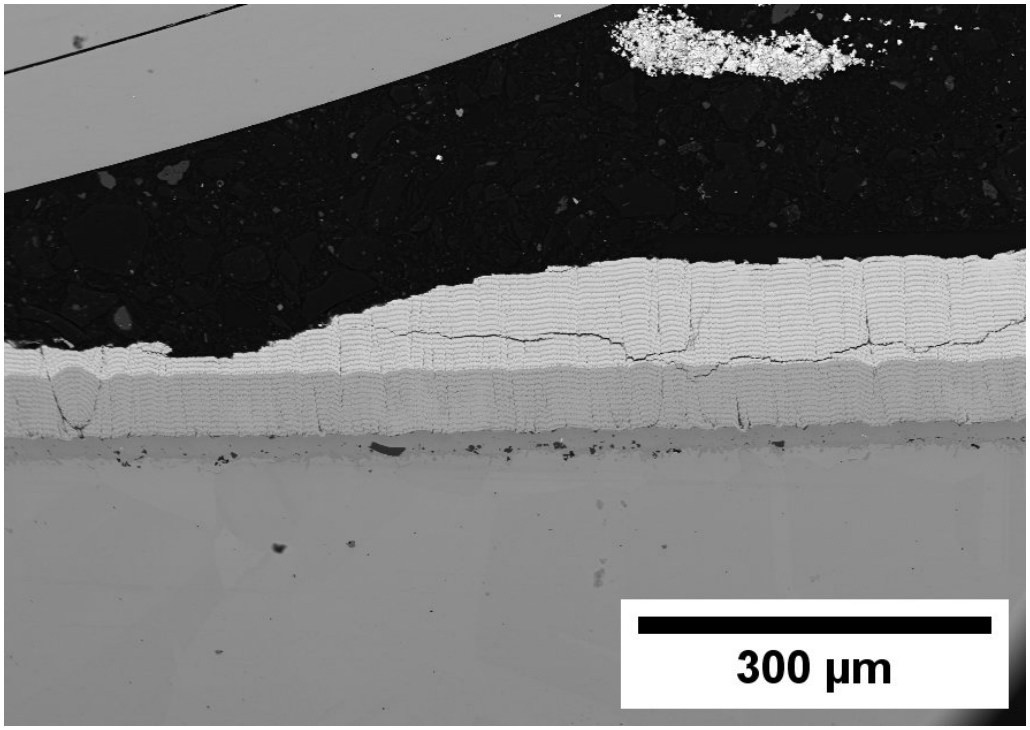


Figure C.22: GZO-LTLR - damage overview

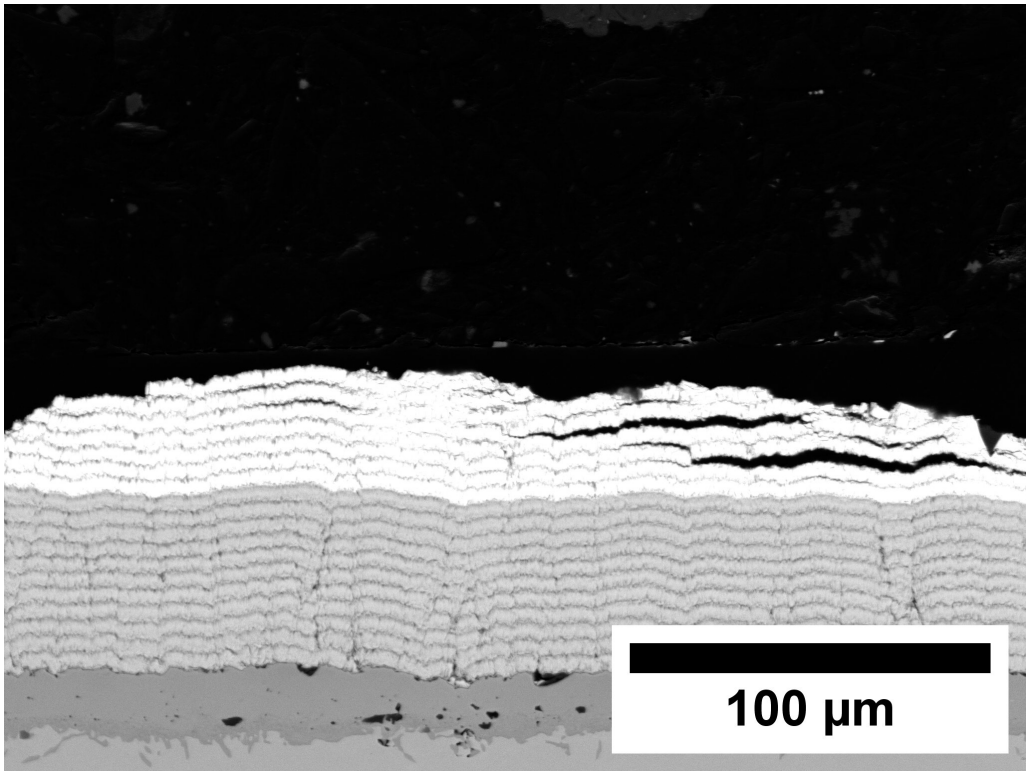


Figure C.23: GZO-LTLR - cracked

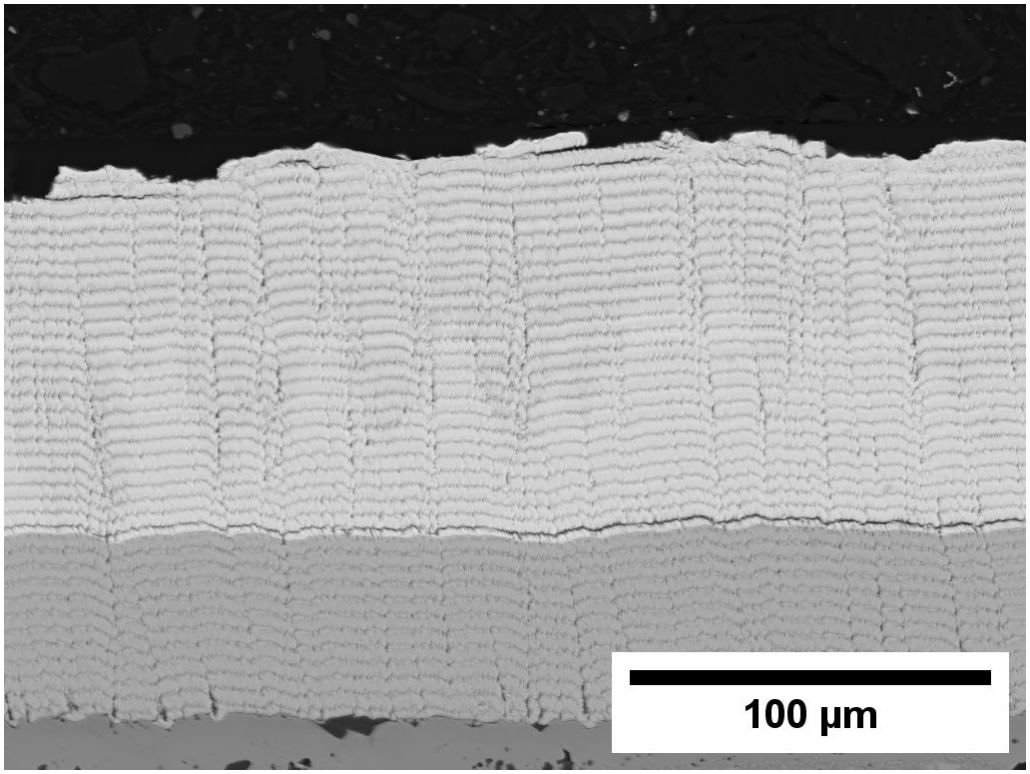


Figure C.24: GZO-LTLR delaminated